

Ice Crushing Pressure on Non-Planar Surface

By

© **Hyunwook Kim, B.Sc., M. Sc.**

A thesis submitted to the School of Graduates Studies

In partial fulfillment of the requirements for the degree of

Doctor of Philosophy

Faculty of Engineering and Applied Science

Memorial University of Newfoundland

October 2014

St. John's Newfoundland

Abstract

The objective of this study is to investigate ice-structure interaction and develop a numerical model to predict the changes of ice loads and pressure during ice-structure interaction on non-planar surfaces.

It is important to understand the sequential ice pressure and load development during ice-structure interaction. This is particularly true for non-planar surfaces as most ships and many offshore structures are composed of near-flat panels that may be dented as part of in-service loading leading to panels that are concave. An important question is whether these concave surfaces act as load-increasers for subsequent ice interaction. Most laboratory and field trial tests have been performed based on the assumption that the structural shape is flat. Therefore, little information is available for cases where the structure is concave due to plastic deformation, or specific areas with intentional structural concave shapes.

In support of this objective, a series of laboratory-scale ice crushing tests were performed. Force, time and displacement data were measured. It was observed that ice crushing on concave shape indenters induced higher ice loads and pressure magnitudes compared to flat indenters. As part of the experimental program, techniques to use pressure measurement film were adopted to obtain ice-structure contact location, actual contact area, and changes of magnitude of pressure within the contact region. Following the experimental program a numerical model of ice crushing for concave surfaces was developed. In order to achieve valid numerical simulation results, a crushable foam model was modified by adding failure criteria. This followed the effect of indenter shape, level of confinement, test speed and cone angle to be evaluated in the numerical model and compared with the experimental results.

The numerical model is shown to be valid for the flat indenter cases and the wedge and conical-shaped indenter cases. The findings from this study show that the shape of the indenting surfaces does influence ice forces and pressure and that generally, concave indentation surfaces lead to increases in pressure and force arising from ice crushing. These effects can be qualified globally and locally using the pressure measurement film, and the effects can be modeled numerically. This work demonstrates that the assumption of ice loads associated with flat or convex shapes may lead to under design for concave shapes or may lead to structural overload in cases where structures previously that have been indented.

Acknowledgements

I would like to express my deepest and sincere gratitude to my supervisor, Prof. Claude Daley, who continuously oriented me in the correct research direction and guided me to complete this study. His wide knowledge and constructive comments have been very important to complete this study. I will never forget his encouragement, understanding and supporting during my Ph.D program.

I owe an incalculable debt of gratitude to my co-supervisor, Prof. Bruce Colbourne. He was always encouraging me to do this study with a smile and kindness. Throughout this study, his supports and thoughtful suggestions guided me to complete my thesis and research.

I would like to express sincere thanks to Prof. Arisi S.J. Swamidas at Memorial University. His vast knowledge and useful guidance provided enormous help to complete this thesis. A warm thank goes to Dr. Jungyong (John) Wang at IOT who provided a chance to study here and help me with valuable discussions at various stages of this study. Special thanks are extended to Mr. Craig Mitchell, who spared a lot of time to help me with valuable discussions and supports during a cold room experiment for this thesis.

This research was funded by STePS² project (Sustainable Technology for Polar Ship Structures). The financial support during the program was also provided by NSERC CREATE and RDC-ABS HETC.

Finally, I would like to dedicate this thesis to my family, especially my wife Saetbyul Cha, for her love, patience, encouraging and understanding. She allowed me to spend most of the time on this work and made this thesis possible.

Table of Contents

Abstract	ii
Acknowledgement	iv
Table of Contents	v
List of Tables	xi
List of Figures	xiii
List of Abbreviations and Symbols	xxiii
Chapter 1 Introduction	1
1.1. Motivation	1
1.1.1. The Challenges in the Arctic Region	1
1.1.2. Ice Loads/Pressure on Non-Planar Surface	2
1.2. Objectives	3
1.3. Approach and Methodology	5
1.3.1. Experiments in Cold Room	5
1.3.2. Numerical Simulations	6
1.3.3. Scope	7
Chapter 2 Literature Review	9
2.1. Ice Mechanics	9
2.1.1. Properties of Sea Ice	9
2.1.2. Ice-Structure Interaction	10
2.2. Effect of Confinement	12
2.3. Ship Structure Damage	16
2.4. Field/Medium/Laboratory Scale Experiments	21

2.4.1.	Field/Medium Scale Experiments	21
2.4.2.	Laboratory Scale Experiments	24
2.5.	Local Ice Pressure Measurement Method	26
2.5.1.	Pressure Panel	26
2.5.2.	Tactile Sensor	31
2.6.	Ice Loads on Podded Propulsor	37
2.7.	Numerical Simulation	42
2.7.1.	SPH Model	42
2.7.2.	CEM Model	45
2.7.3.	Crushable Foam Model	47
2.7.4.	Others	52

Chapter 3 Development of Methods for Investigation of Local Ice Loads Using Pressure

Measurement Film	55
3.1. Overview	55
3.2. Specification of Pressure Measurement Film	57
3.2.1. Pressure Measurement Film Specification	57
3.3. Methodology of Spatial Pressure-Area Curves Plotting	60
3.4. Verification of Resolution Sensitivity	61
3.4.1. Activated Area Comparison	61
3.4.2. Total Force Comparison	64
3.4.3. Pressure Distribution Comparison	67
3.4.4. Result of Resolution Sensitivity	68
3.5. Source of Error	69

Chapter 4 Ice Crushing Pressure on Non-Planar Surface: Experiments

4.1. Overview	72
4.2. Test Condition	73
4.3. Test Scenario	75

4.3.1.	Wedge Shape Indenter	75
4.3.2.	Conical Shape Indenter	77
4.4.	Test Setup	78
4.5.	Test Results	81
4.5.1.	Definition of Contact Area	81
4.5.2.	Crushed Ice Sample	87
4.5.3.	Section of ice sample	89
4.5.4.	Force-Displacement History/Process Pressure-Area Curve/Compressive Ice Strength Comparison	90
4.5.4.1.	25° Ice cone, 1mm/s Test Speed	90
4.5.4.2.	25° Ice Cone, 100mm/s Test Speed	94
4.5.4.3.	Cylindrical Ice, 1mm/s Test Speed	96
4.6.	Pressure Measurement Film	101
4.6.1.	Pressure Distribution Map: Cone-Shaped Ice Sample	101
4.6.2.	Pressure Distribution Map: Cylindrical Ice Sample	103
4.7.	Pressure Pattern Examination	104
4.8.	Spatial Pressure-Area Curve	107
Chapter 5	Experimental Data Analysis	111
5.1.	Contact Area/Pressure Comparison: Flat vs. Concave Shape Indenter	111
5.2.	Effect of Concave Shape Indenter	114
5.2.1.	Definition of Representative Load	114
5.2.1.1.	Linear Regression Equation as Representative Load	115
5.2.2.	Derivation of Regression Equation	118
5.2.2.1.	Regression curve comparison	118
5.2.2.2.	Determination of ICRI: Test Result	122
5.2.2.3.	Derivation of Regression Equation: Linear Relationship	124
5.2.2.4.	Assessment of Regression Equation: Power and Exponential Relationship	128
5.2.2.4.1.	Evaluation of Power Relationship	128

5.2.2.4.2.	Evaluation of Exponential Relationship	130
5.2.2.4.3.	Evaluation of Modified Exponential Relationship	132
5.2.3.	Effect of Structural Shape	135
5.2.4.	Effect of Cone Angle	138
5.2.5.	Effect of Test Speed	139
5.2.6.	Evaluation of the Effect of Ice Sample Shape	141
5.3.	Discussion	144
5.3.1.	Confinement Effect	144
5.3.2.	Verification of Suitability of Applying a Linear Relationship: Pressure-Area Relationship Perspective	147
5.3.2.1.	Definition of Cone-Shaped Ice Parameter	147
5.3.2.2.	Comparison of Regression Relationship: Linear vs. Exponential	148
Chapter 6	Numerical Analysis	153
6.1.	Overview	153
6.2.	Proposed Ice Model	153
6.3.	Simulation Results	156
6.4.	Parametric Study	157
6.4.1.	Mesh Size Sensitivity	158
6.4.2.	Value of Max. Principal Stress (failure criteria) Sensitivity	160
6.4.3.	Size of HPZ Sensitivity	162
6.5.	Results of Numerical Analysis: 10cm Diameter Ice Sample	167
6.6.	Application to Larger Model	176
Chapter 7	Conclusions	184
7.1.	Conclusions	186
7.1.1.	Ice Crushing Pressure/Load on Non-Planar Surface	186
7.1.2.	Numerical Simulation	189
7.2.	Recommendations	190
7.2.1.	Consideration of Structural Shape Effect	190

7.2.2.	Ice Crushing Pressure/Load Experiments on Non-Planar Surface	191
7.2.3.	Numerical Simulation	192
References		193
Appendix A Verification of Stepped Crushing Method		210
Appendix B Active vs. Activated Area		211
Appendix C Verification of Resolution Sensitivity		212
C.1.	Activated Area Comparison	214
C.2.	Total Force Comparison	217
C.3.	Pressure Distribution Comparison	222
Appendix D Comparison of Defined Contact Area		236
Appendix E Force-Displacement History/ Process Pressure-Area Curve/Compressive Ice Strength Comparison		239
E.1.	35° Ice Cone, 1mm/s Test Speed	239
E.2.	35° Ice Cone, 100mm/s Test Speed	242
E.3.	Cylindrical Ice, 100mm/s Test Speed	244
Appendix F Pressure Distribution Map		247
F.1.	Pressure Distribution Map: Cone-Shaped Ice Sample	247
F.2.	Pressure Distribution Map: Cylindrical Ice Sample	248
Appendix G Spatial Pressure-Area Curve (25cm Diameter Ice Sample)		250
Appendix H Contact Area/Pressure comparison: Flat vs. Concave Shape Indenter		254
H.1.	Results of Test against a Flat Indenter	254

H.2.	25cm Diameter Ice Sample Test against a concave shape indenter	256
Appendix I	Results of Numerical Analysis: 25cm Diameter Ice Sample	259
I.1.	Force-Displacement Curve	259
I.2.	Compressive Ice Strength	262

List of Tables

Table 2-1: Summary of the state-of-knowledge and application of the properties of sea ice (after Timco and Weeks, 2010)	10
Table 2-2: A summary of the hull damages (TRA means transverse framing system and LON means longitudinal framing system) (after Hänninen, 2005)	17
Table 3-1: Specification of the pressure measurement film	57
Table 3-2: Pressure range by film type	58
Table 3-3: Results of activated area: Step 3	63
Table 3-4: Results of total force: Step 1	67
Table 3-5: Results of total force: Step 4	67
Table 4-1: Test conditions	74
Table 4-2: Comparison of nominal and projected contact area	85
Table 4-3: Comparison of width and height of pressure pattern	106
Table 5-1: Results of using 10cm diameter ice cone test against flat indenter	112
Table 5-2: Results of using 25cm diameter ice cone test against concave shape indenter ...	113
Table 5-3: Results of using cylindrical ice test against concave shape indenter	114
Table 5-4: Results of ICRI	122
Table 5-5: Result of ICRI for the verification purpose	124
Table 5-6: Results of ICRI (Test data vs. Derived by regression equation)	126
Table 5-7: Comparison of calculated force (linear vs. modified exponential relationship) ...	134
Table 5-8: Comparison result: flat vs. wedge shape indenter	136
Table 5-9: Comparison result: flat vs. conical shape indenter	137
Table 5-10: Comparison result with test speed 1mm/s	138
Table 5-11: Comparison result with test speed 100mm/s	139
Table 5-12: Comparison result with 25° ice cone	140
Table 5-13: Comparison result with 35° ice cone	140
Table 5-14: Comparison of result by ice sample shape	143
Table 5-15: Definition of force, pressure and exponential term	149
Table 5-16: Test conditions (to extract 'P ₀ ' and 'ex' from pressure-area curve)	151

Table 6-1: Ice material properties and failure criteria	154
Table 6-2: Test condition (10cm diameter ice cone)	157
Table 6-3: Mesh size/No. element comparison (indenter and ice)	159
Table 6-4: Test condition (25cm diameter ice cone)	176
Table 7-1: Effect of indenter shape (at 1mm/s test speed)	188
Table 7-2: Effect of indenter shape (at 100mm/s test speed)	188
Table C-1: Results of activated area: Step 1	216
Table C-2: Results of activated area: Step 2	216
Table C-3: Results of activated area: Step 4	217
Table C-4: Results of total force: Step 2	221
Table C-5: Results of total force: Step 3	222
Table H-1: Results of using 10cm diameter ice cone test against flat indenter	254
Table H-2: Results of using 25cm diameter ice cone test against concave shape indenter ...	256
Table H-3: Results of using cylindrical ice test against concave shape indenter	257

List of Figures

Figure 2-1: Yield stress plotted against confining pressure (after Jones, 1982)	13
Figure 2-2: Observed pressure and calculated uni-axial compressive strength in the Resolute Tests (after Spencer and Timco, 2010)	14
Figure 2-3: Constrained (a) vs. unconstrained (b) ice indenter geom. (after Ulan-Kvitberg et al., 2012)	15
Figure 2-4: Force-penetration history of unconstrained ice cone (top) and constrained ice cone (bottom) at 100mm/s (after Ulan-Kvitberg et al., 2012)	15
Figure 2-5: Comparison of ice classes and ship types of damaged and undamaged ships (after Hänninen, 2005)	16
Figure 2-6: The damage occurred during the winter 1986 on area 1 of ship no. 35. (after Kujala, 1991)	19
Figure 2-7: The shape on the damage on area 1 of ship no. 35 (after Kujala, 1991)	20
Figure 2-8: Strain gauge layout (after Ritch et al., 2008)	23
Figure 2-9: The experimental set up (after Tuhkuri, 1995)	25
Figure 2-10: Schematic illustrating the operating principle of the pressure panel (after Gagnon, 2008)	27
Fig. 2-11: 1.0m diameter ice cone test using the pressure panel before and after (after Reddy Gudimetla et al., 2010)	28
Fig. 2-12: Progression of pressure profile in double angle cone test (after Reddy Gudimetla et al., 2010)	29
Fig. 2-13: Raw image and pressure distribution map by pressure panel (after Reddy Gudimetla et al., 2010)	30
Figure 2-14: Segmented indenter (after Sodhi et al., 2001)	32
Figure 2-15: Indentation test with four tactile sensors (after Sodhi et al., 2001)	32
Figure 2-16: Time-history plots of the ice force records at 0.3mm/s (after Sodhi et al., 2006)	33

Figure 2-17: Load – time record expanded for interval 40 to 70 seconds (after Frederking, 2004)	34
Figure 2-18: Contour plot of pressure at time 86.1 s, a time of peak load (after Frederking, 2004)	35
Figure 2-19: Tactile sensor mounted on a model ship (after Izumiyama et al., 2007)	36
Figure 2-20: Ice load distribution on a model ship bow (after Izumiyama et al., 2007)	36
Figure 2-21: Illustration of actual load cases to be considered (after DnV, 2011)	38
Figure 2-22: Ice load definition (after DnV, 2011)	39
Figure 2-23: Critical scenarios for ahead working ships (after BV, 2012)	40
Figure 2-24: Critical scenarios for astern working ships (after BV, 2012)	41
Figure 2-25: Experimental/numerical comparison of the impacts on rigid target – hemispherical projectiles at 15m/s (top) and 100m/s (bottom) (after Delsart et al., 2011)	43
Figure 2-26: Impact at 0° at time intervals of 0.66 m/s, video and SPH (after Lavoie et al., 2008)	44
Figure 2-27: FE model of cylindrical structure and ice floe interaction (after Konuk et al. 2009)	45
Figure 2-28: Cohesive element model results for infinite (left) and finite (right) ice floe cases (after Konuk et al. 2009)	46
Figure 2-29: Typical situation in front of lighthouse in the simulation (after Hilding et al. 2011)	47
Figure 2-30: Volumetric strain-stress relationship (after Gagnon, 2006)	48
Figure 2-31: View of the numerical model (after Gagnon, 2010)	49
Figure 2-32: Volumetric strain stress curves for the M1 (high-stress) and M2 (low-stress) crushable foam (after Gagnon, 2010)	49
Figure 2-33: Load time series for the IceCrush simulation (after Gagnon, 2010)	50
Figure 2-34: Two sets of images, set No. 1 (left) and set No. 2 (right), depicting what happens during one of the spalling events in the IceCrush simulation (after Gagnon, 2010)	51
Figure 2-35: Computed contact force at 500ft/sec, with high speed images of a ballistic test (after Carney et al., 2006)	52

Figure 2-36: Test analysis comparison at 500ft/s, normal orientation (after Carney et al., 2006)	53
Figure 2-37: Contact force during the crushing at speed vice=0.1 m/s (after Dorival et al., 2008)	54
Figure 2-38: Ice sheet damaged after crushing against the structure at speed vice = 0.1 m/s at time t=3.4236s/6.1677s/6.8994s/25s (after Dorival et al., 2008)	54
Figure 3-1: Structures of the pressure measurement film (Mono-sheet type)	59
Figure 3-2: Structures of the pressure measurement film (Two-sheet type)	59
Figure 3-3: Scattering of peak pressure	60
Figure 3-4: Comparison of activated area by pixel size (Test 1)	62
Figure 3-5: Comparison of activated area by pixel size (Test 4)	62
Figure 3-6: Comparison of total force by pixel size (Test 1)	64
Figure 3-7: Comparison of total force by pixel size (Test 4)	65
Figure 3-8: Pressure distribution of Test 1-Step 1	67
Figure 3-9: Pressure distribution of Test 1-Step 2	68
Figure 4-1: Picture of podded propulsor	75
Figure 4-2: Wedge shape indenters (left: 10° wedge, right: 30° wedge)	76
Figure 4-3: Drawing of wedge shape indenters (left: 10° wedge, right: 30° wedge)	76
Figure 4-4: Picture of dented structure	77
Figure 4-5: Conical shape indenter (10° conical)	78
Figure 4-6: Drawing of conical-shaped indenter (10° conical)	78
Figure 4-7: System of ice sample preparation	79
Figure 4-8: Illustration of test setup	80
Figure 4-9: Photo of test setup (35° ice cone, 10° wedge indenter)	81
Figure 4-10: Illustration of contact area (Anominal vs. Aproject)	82
Figure 4-11: Comparison of nominal and projected contact area	84
Figure 4-12: Crushed ice sample after tests	88
Figure 4-13: Section of ice sample appearing a HPZ (Test 1 & 3)	89
Figure 4-14: Force-displacement history (25° ice cone, 1mm/s test speed)	90
Figure 4-15: Process pressure-area curve (25° ice cone, 1mm/s test speed)	91
Figure 4-16: Contact area comparison (25° ice cone)	92

Figure 4-17: Contact area comparison (35° ice cone)	92
Figure 4-18: Compressive ice strength (25° ice cone, 1mm/s test speed)	93
Figure 4-19: Force-displacement history (25° ice cone, 100mm/s test speed)	94
Figure 4-20: Process pressure-area curve (25° ice cone, 100mm/s test speed)	95
Figure 4-21: Compressive ice strength (25° ice cone, 100mm/s test speed)	96
Figure 4-22: Force-displacement history (cylindrical ice, 1mm/s test speed)	97
Figure 4-23: Comparison of max. depth at each wedge indenter angle (10°, 20° and 30° wedge indenter)	98
Figure 4-24: Process pressure-area curve (cylindrical ice, 1mm/s test speed)	99
Figure 4-25: Comparison of contact area at each wedge indenter angle	100
Figure 4-26: Compressive ice strength (cylindrical ice, 1mm/s test speed)	101
Figure 4-27: Pressure distribution map of Test 1 (10° wedge indenter, 35° ice cone, 1mm/s test speed)	102
Figure 4-28: Pressure distribution map of Test 4 (10° wedge indenter, 25° ice cone, 100mm/s test speed)	103
Figure 4-29: Pressure distribution map of test 5 (30° wedge, cylindrical ice, 1mm/s test speed)	103
Figure 4-30: Pressure distribution map of test 9 (10° wedge, cylindrical ice, 1mm/s test speed)	104
Figure 4-31: Criteria of the width and height of pressure pattern	105
Figure 4-32: Spatial pressure-area curve of Test 1 (10° wedge, 35° ice cone, 1mm/s test speed)	108
Figure 4-33: Spatial pressure-area curve of Test 17 (20° wedge, 35° ice cone, 1mm/s test speed)	108
Figure 4-34: Spatial pressure-area curve of Test 5 (30° wedge, cylindrical ice, 1mm/s test speed)	109
Figure 4-35: Spatial pressure-area curve of Test 9 (10° wedge, cylindrical ice, 1mm/s test speed)	110
Figure 5-1: Determination of representative load using the linear regression equation (Case 1)	116

Figure 5-2: Determination of representative load using the linear regression equation (Case 2)	117
Figure 5-3: Comparison of regression curve (Flat Test 3: Flat, 35° ice cone, 100mm/s)	119
Figure 5-4: Comparison of regression curve (Test 24: 10° Conical, 25° ice cone, 1mm/s)	119
Figure 5-5: Comparison of regression curve (Test 19_Rep: 20° Wedge, 35° ice cone, 1mm/s)	120
Figure 5-6: Test result vs. regression equation result of force (linear relationship)	121
Figure 5-7: Test result vs. regression equation result of force (power relationship)	121
Figure 5-8: Test result vs. regression equation result (ICRI)	125
Figure 5-9: Test result vs. regression equation result using the power relationship (F_0)	129
Figure 5-10: Test result vs. regression equation result using the power relationship (ex)	129
Figure 5-11: Test result vs. regression equation result using the exponential relationship (F_0)	131
Figure 5-12: Test result vs. regression equation result using the exponential relationship (ex)	131
Figure 5-13: Test result vs. regression equation result using the modified exponential relationship (ex)	133
Figure 5-14: Test result vs. regression equation result of cylindrical ice (ICRI)	141
Figure 5-15: Comparison of confinement-formable space between ice and indenter (flat indenter)	145
Figure 5-16: Comparison of confinement-formable space between ice and indenter (wedge indenter)	146
Figure 5-17: Definition of cone-shaped ice parameter	147
Figure 5-18: Regression fit of force-displacement curve (linear vs. exponential relationship)	148
Figure 5-19: Variety behavior of the pressure-area curve depends on 'ex'	150
Figure 5-20: Pressure-area curve (including P_0 and ex)	151
Figure 6-1: Volumetric strain-stress relation of crushable foam (by Kim)	155
Figure 6-2: Layer of ice model (Blue: Ice material 1, Green: Ice material 2)	155
Figure 6-3: Numerical simulation model consists of ice specimen and a steel plate	156
Figure 6-4: Test set-up (30° ice cone)	157

Figure 6-5: Structure of the element composition in indenter part	158
Figure 6-6: Comparison of force-displacement curve by diverse mesh size	159
Figure 6-7: Comparison of the force-displacement curve by percentage of failure criteria (F.C) (100mm/s test speed)	161
Figure 6-8: Comparison of force-displacement curve by percentage of failure criteria (F.C) (1mm/s test speed)	162
Figure 6-9: Definition of layered ice model (front view)	163
Figure 6-10: Definition of layered ice model (top view)	163
Figure 6-11: Height/Ratio of layered ice model	164
Figure 6-12: Radius/Ratio of layered ice model	165
Figure 6-13: Comparison of force-displacement curves by Hice mat_1/Hice mat_2 (rice mat_1/rice mat_2) ratio (100mm/s test speed)	166
Figure 6-14: Comparison of force-displacement curves (1mm/s test speed)	168
Figure 6-15: Comparison of force-displacement curves (100mm/s test speed)	168
Figure 6-16: Comparison of process pressure-area curves (100mm/s test speed)	170
Figure 6-17: Comparison of process pressure-area curves (1mm/s test speed)	170
Figure 6-18: Spatial pressure distribution plots (100mm/s test speed)	172
Figure 6-19: Spatial pressure-area curves (1mm/s test speed)	173
Figure 6-20: Spatial pressure-area curves (100mm/s test speed)	174
Figure 6-21: Spatial pressure-area curves: Applying correction factor $\alpha = 2.0$ (1mm/s test)	175
Figure 6-22: Spatial pressure-area curves: Applying correction factor $\alpha = 2.0$ (100mm/s test)	175
Figure 6-23: Comparison of force-displacement curve on flat indenter (Test 1: 25cm ice cone, 1mm/s test speed)	177
Figure 6-24: Comparison of force-displacement curve on a 10° conical indenter (Test 6: 25cm ice cone, 100mm/s test speed)	178
Figure 6-25: Figure 6-25: Comparison of compressive ice strength on a flat indenter (Test 1: 25cm ice cone, 1mm/s test speed)	180
Figure 6-26: Comparison of compressive ice strength on a 10° conical indenter (Test 4: 25cm ice cone, 1mm/s test speed)	181

Figure 6-27: Comparison of compressive ice strength on a 10° wedge indenter (Test 5: 25cm ice cone, 100mm/s test speed)	182
Figure A-1: Comparison of ‘straight’ and ‘stepped’ crushing method (reproduced by Kim)	210
Figure B-1: Concept of ‘Active’ and ‘Activated’ area (reproduced by Kim)	211
Figure C-1: Comparison of activated area by pixel size (Test 2)	212
Figure C-2: Comparison of activated area by pixel size (Test 3)	213
Figure C-3: Comparison of activated area by pixel size (Test 4)	213
Figure C-4: Comparison of activated area by pixel size (Test 6)	214
Figure C-5: Comparison of activated area by pixel size (Test 7)	214
Figure C-6: Comparison of activated area by pixel size (Test 8)	215
Figure C-7: Comparison of total force by pixel size (Test 2)	218
Figure C-8: Comparison of total force by pixel size (Test 3)	218
Figure C-9: Comparison of total force by pixel size (Test 5)	219
Figure C-10: Comparison of total force by pixel size (Test 6)	219
Figure C-11: Comparison of total force by pixel size (Test 7)	220
Figure C-12: Comparison of total force by pixel size (Test 8)	220
Figure C-13: Pressure distribution of Test 1-Step 3	223
Figure C-14: Pressure distribution of Test 2-Step 1	223
Figure C-15: Pressure distribution of Test 2-Step 2	223
Figure C-16: Pressure distribution of Test 2-Step 3	223
Figure C-17: Pressure distribution of Test 3-Step 1	225
Figure C-18: Pressure distribution of Test 3-Step 2	225
Figure C-19: Pressure distribution of Test 3-Step 3	226
Figure C-20: Pressure distribution of Test 3-Step 4	226
Figure C-21: Pressure distribution of Test 4-Step 1	227
Figure C-22: Pressure distribution of Test 4-Step 2	227
Figure C-23: Pressure distribution of Test 4-Step 3	228
Figure C-24: Pressure distribution of Test 4-Step 4	228
Figure C-25: Pressure distribution of Test 5-Step 1	229
Figure C-26: Pressure distribution of Test 5-Step 2	229

Figure C-27: Pressure distribution of Test 5-Step 3	230
Figure C-28: Pressure distribution of Test 5-Step 4	230
Figure C-29: Pressure distribution of Test 6-Step 1	231
Figure C-30: Pressure distribution of Test 6-Step 2	231
Figure C-31: Pressure distribution of Test 6-Step 3	232
Figure C-32: Pressure distribution of Test 7-Step 1	232
Figure C-33: Pressure distribution of Test 7-Step 2	233
Figure C-34: Pressure distribution of Test 7-Step 3	233
Figure C-35: Pressure distribution of Test 7-Step 4	234
Figure C-36: Pressure distribution of Test 8-Step 1	234
Figure C-37: Pressure distribution of Test 8-Step 2	235
Figure C-38: Pressure distribution of Test 8-Step 3	235
Figure D-1: Comparison of Anom. vs. Aproj. (25° ice cone, 20° wedge indenter)	236
Figure D-2: Comparison of Anom. vs. Aproj. (35° ice cone, 10° wedge indenter)	237
Figure D-3: Comparison of Anom. vs. Aproj. (35° ice cone, 20° wedge indenter)	237
Figure D-4: Comparison of Anom. vs. Aproj. (25° ice cone, 10° conical indenter)	238
Figure D-5: Comparison of Anom. vs. Aproj. (35° ice cone, 10° conical indenter)	239
Figure E-1: Force-displacement history (35° ice cone, 1mm/s test speed)	240
Figure E-2: Process pressure-area curve (35° ice cone, 1mm/s test speed)	241
Figure E-3: Compressive ice strength (35° ice cone, 1mm/s test speed)	241
Figure E-4: Force-displacement history (35° ice cone, 100mm/s test speed)	242
Figure E-5: Process pressure-area curve (35° ice cone, 100mm/s test speed).....	243
Figure E-6: Compressive ice strength (35° ice cone, 100mm/s test speed)	243
Figure E-7: Force-displacement history (cylindrical ice, 100mm/s test speed)	245
Figure E-8: Process pressure-area curve (cylindrical ice, 100mm/s test speed)	245
Figure E-9: Compressive ice strength (cylindrical ice, 100mm/s test speed)	246
Figure F-1: Pressure distribution map of Test 2 (10° wedge indenter, 35° ice cone, 100mm/s test speed)	247
Figure F-2: Pressure distribution map of Test 3 (10° wedge indenter, 25° ice cone, 1mm/s test speed)	247

Figure F-3: Pressure distribution map of test 17 (20° wedge indenter, 35° ice cone, 1mm/s test speed)	248
Figure F-4: Pressure distribution map of test 18 (20° wedge indenter, 35° ice cone, 100mm/s test speed)	248
Figure F-5: Pressure distribution map of test 6 (30° wedge, cylindrical ice, 100mm/s test speed)	249
Figure F-6: Pressure distribution map of test 10 (10° wedge, cylindrical ice, 100mm/s test speed)	249
Figure G-1: Spatial pressure-area curve of Test 2 (10° wedge, 35° ice cone, 100mm/s test speed)	250
Figure G-2: Spatial pressure-area curve of Test 3 (10° wedge, 25° ice cone, 1mm/s test speed)	251
Figure G-3: Spatial pressure-area curve of Test 4 (10° wedge, 25° ice cone, 100mm/s test speed)	251
Figure G-4: Spatial pressure-area curve of Test 18 (20° wedge, 35° ice cone, 100mm/s test speed)	252
Figure G-5: Spatial pressure-area curve of Test 6 (30° wedge, cylindrical ice, 100mm/s test speed)	253
Figure G-6: Spatial pressure-area curve of Test 10 (10° wedge, cylindrical ice, 100mm/s test speed)	253
Figure I-1: Comparison of force-displacement curve (25cm ice cone, 100mm/s test speed)	256
Figure I-2: Comparison of force-displacement curve on a 10° wedge indenter (25cm ice cone, 1mm/s test speed)	260
Figure I-3: Comparison of force-displacement curve on a 10° conical indenter (25cm ice cone, 1mm/s test speed)	260
Figure I-4: Comparison of force-displacement curve on a 10° wedge indenter (25cm ice cone, 100mm/s test speed)	261
Figure I-5: Comparison of compressive ice strength on a flat indenter (25cm ice cone, 100mm/s test speed)	262
Figure I-6: Comparison of compressive ice strength on a 10° wedge indenter (25cm ice cone, 1mm/s test speed)	263

Figure I-7: Comparison of compressive ice strength on a 10° conical indenter (25cm ice cone, 100mm/s test speed)	263
---	-----

List of Abbreviations and Symbols

BV	Bureau veritas
CEM	Cohesive element method
CEMH	Cohesive element method with homogenization
σ	Compressive ice strength
CAM	Contour-averaging method
α	Cone-shaped ice angle
α_c	Correction factor
DOE	Design of experiments
DnV	Det norske veritas
DDePS	Direct design for polar ships
x	Displacement
F_0	Force index
Hice mat ₁	Height of ice material 1
Hice mat ₂	Height of ice material 2
HPZ	High pressure zone
k_1	Ice coefficient
k_2	Ice coefficient
E	Ice crushing energy
ICRI	Ice crushing resistance index
IACS	International association of classification societies
h_{ice}	Maximum ice sheet thickness

A_{nominal}	Nominal contact area
V	Nominal crushed volume
PPA_N	Nominal process pressure-area
M	Number of total elements of width
N	Number of total elements of height
ex	Power term
PMF	Pressure measurement film
PPA	Process pressure-area
$A_{\text{projected}}$	Projected contact area
r_f	Rafting factor
SPH	Smoothed particle hydrodynamics
SPA	Spatial pressure-area
SAM	Square-averaging method
STePS ²	Sustainable technology for polar ships structures
PPA_S	Trend of process pressure-area curve by square-averaging method
PPA_C	Trend of process pressure-area curve by contour-averaging method
UR	Unified requirements
σ_{ice}	Uniaxial compressive strength of ice
X_p	Unit Size of the element
UTM	Universal testing machine

Chapter 1 Introduction

1.1. Motivation

1.1.1. The Challenges in the Arctic Region

Since the 19th century, people have had an interest in the Arctic as an unexplored territory, and there have been many efforts to explore the Arctic. From the 1960s onwards, the Arctic region has been recognized as a resource area for offshore oil and gas reserves. Also, there was a need for opening a northern sea route to achieving faster and more economical navigation between the east and west countries neighboring this Arctic route. All these activities require that ships and other steel structures operate in ice-covered waters. Designing these structures requires knowledge of how ice loads develop during ice-breaking processes. In general better knowledge of ice induced loads leads to safer and more efficient designs for operations in arctic regions. In order to accomplish this goal of safe and efficient design, development of proper theoretical methods and at the same time, gathering of necessary data through experiments, is required to properly understand the process and characteristics of ice-ship structure interaction.

Ice class ships, equipped with data recording instrumentation, have been used to collect ice-ship collision data in the Arctic since there was a specific demand for full-scale data for practical design and research purposes. These types of field tests were started from 1970s by industries

and research institution from all around the world. Along with full and medium-scale tests in the field, laboratory ice experiments were also carried out by universities and research institutes. Based on the results of these series of experiments in full and model scale laboratory ice tests, the researchers were able to increase their understanding of ice mechanics.

1.1.2. Ice Loads/Pressure on Non-Planar Surfaces

Due to wide natural variations in sea ice, and the difficulty in determining exactly what kinds of ice conditions are ahead of a ship or offshore structure in the Arctic, some ice-going ships will periodically encounter ice loads above their design criteria. These overloads will commonly cause permanent deformations in plating and framing, which show up as permanent deformations (dents) in the surface. Besides the plastic structural behavior, the nature of the ice loads is also a factor. The plate deformation, which creates a dent into which the ice presses may well modify the ice pressures. There are little test data available concerning this situation. Almost all available test data from laboratory or field does not involve permanent structural deformation (unless not recorded). Thus, the scenario of ice impinging on a concave surface arising from previous minor damage is a common but virtually un-studied case. Therefore, there is a need for additional information and analysis for ice-ship collision scenarios, considering prior plastic deformation in the ship structure.

In addition to the cases of an ice load-induced dent, there are cases where ice strikes convex/concave surface locations on the ship such as at the intersection of an appendage and the main hull. Design ice loads for such locations are generally based on data derived from flat

surface tests and models. Current practice would be to use loads for the typical hull structure. Therefore, it is worth investigating the effect of surface shape (i.e. non-planar shapes) on ice-structure interaction loads.

In both cases mentioned above, the ice will be impacting a non-planar convex/concave shaped surface rather than a flat surface. The reason that a ‘concave’ shape might show much higher magnitude of ice load compared to a ‘flat’ surface is the influence of ice confinement. In the case of a flat surface, broken ice pieces (spalling) can be freely extruded during the ice crushing process. Therefore, flat surfaces will not contribute any additional extrusion resistance that might act to increase the ice pressure and thus the loads as part of the ice failure process. In contrast, broken ice pieces are expected to be trapped, or at least impeded, between the structure and deforming ice sample within a confined space, as would be in the case of a concave shape. It can be expected that trapped ice pieces here will increase the confinement and exhibit higher ice load.

1.2. Research Objectives

Most ice load measurements, whether in the lab or field have considered the structure to be a nearly rigid body, with only small elastic deformations. Therefore, ice pressure models and data have ignored the effects of surface structural deformations or local concavity. However, the nature of ice-structure interaction could be quite different when the permanent plastic deformation of the structure, or surface concavity is considered. During ice-structure interaction,

which involves ice spalling and fracture, the broken ice material must be extruded, and the ease of extrusion will depend partly on the shape of the surface.

It is expected that concave shapes will tend to trap the extruding ice, leading to greater confinement and possibly higher ice loads. As well, compared to the case when the surface is flat, the total contact area will likely be quite different along with the distribution of ice contact pressures. A change in ice load and pressure magnitudes is to be expected.

The objectives of this study are:

1. Investigate the effect of surface concavity in influencing ice loads and pressures during ice crushing using a series of systematic experiments on simplified concave shapes. Determine from the experiments if the load/pressure increases and if it does is the increase significant with reference to flat surface cases.
2. Adopt procedures, previously developed for using pressure measurement films on a flat surface, to shaped surfaces in order to determine variations in spatial ice crushing pressure as influenced by the shape of the crushing surface.
3. Develop a numerical model of the ice crushing process against a concave surface that correctly captures both the global load variation and the local and spatial pressure variation as a crushing event proceeds.

4. Develop preliminary recommendations as to whether existing standards concerning ice loads on planar surfaces should be modified to account for the concave surfaces that commonly arise in ships subject to denting from ice loads.

1.3. Approach and Methodology

This study applies to two structural cases; overload resulting in plate denting, and cases where the ship's surface geometry is intentionally concave, as would be the case adjacent to ship appendages and at specific locations on the hull.

The experimental study considers two types of scenarios;

- (i) Study of ice-structure interaction on concave shapes representative of deformed plating on the main hull; in this case, the focus is on load and plastic response in an overload condition.
- (ii) Study of ice-structure interaction on concave shapes representative of locations other than the main hull; in this case, the focus is on load and response at the design condition.

1.3.1. Experimental Program

In both cases, the test data will be compared to available ice pressure test data on undeformed (flat) rigid surfaces. The study will be carried out using available test equipment in a cold room,

using universal testing machine (UTM). Force data from the UTM will be used to measure the ‘global’ load and nominal contact area, to obtain the ‘process’ pressure-area relationship. Chemical pressure measurement film (PMF) is a potentially attractive option. The films used in this study have micron-scale resolution and leave pressure patterns that remain upon completion of an impact event. The pressure measurement film will be used to measure ‘local’ contact load/pressure and contact area, to obtain ‘spatial’ pressure-area relationship. Numerical analysis will be carried out in parallel with experimental studies to compare and as well to analyze the obtained test data, and ultimately to validate numerical simulations of such cases.

The purpose of this study is to investigate ice impacts with such a concave-shaped surface to determine if the structural shape of the impacting surface has an effect on the apparent ice loads and pressures. A new test apparatus was designed to research the characteristics of ice-structure interaction on non-planar surface.

1.3.2. Numerical Simulations

Many researchers have performed a simulation of ice-structure interaction using finite element software. Since, most of the numerical simulation models developed by an individual study tend to satisfy a particular test condition which means that the capability of expansion into a particular scenario was not considered. In addition, most of the numerical simulation models were developed in the case of the impact situation where the strain rate is relatively high. In reality, actual ice loading conditions are distributed from low to high strain rate conditions. Therefore,

there is a high demand of developing a numerical simulation model which can be applied in diverse conditions.

This study aims to develop a numerical simulation model and material properties of the ice that can be applied for cases experiencing low to high strain rates without any major modification, using LS-DYNA[®]. The crushable foam model with LS-DYNA[®] has been found to be a reasonable model for ice. This model was used with updated failure criteria, and maximum principal stress, to simulate the widely observed ‘sawtooth’ ice crushing load pattern. The material property of the steel indenter was assumed as a rigid body. Two separated element layers were adopted to consider a high and low pressure zone within the contact region. Validation of the numerical ice model was based on compressive ice test results done in a cold room using a 10cm diameter cone-shaped ice samples. Furthermore, the verification process for scalability was performed by applying the numerical simulation model to larger-scale ice samples up to 25cm diameter against flat and concave shape indenters.

1.3.3. Scope

Chapter 2 is a literature review of ice-related research covering experiments at laboratory scales and up to field trials and including numerical simulations of ice-structure interaction. Work on ice loads on podded propulsors is reviewed as these devices which are becoming widely used in icebreaking vessels are most likely to present concave surfaces to impinging ice loads. Methods of global and local ice load measurement are introduced. A different method to simulate the ice-structure interaction is reviewed (i.e SPH, CEMH). In Chapter 3, the technique for measurement

of localized pressure distribution and contact area using pressure measurement film is presented. Analysis of pixel size sensitivity of the pressure measurement film is conducted to decide the optimal pixel size for further study. In Chapter 4, the detailed procedure of ice crushing experiments using the 25cm diameter ice samples on a non-planar surface is introduced. Comparison of the force-displacement curves and pressure-area curves are made between flat and concave indenters. In Chapter 5, effects of shape and angle of concave shaped indenter, shape and angle of ice samples and test speeds are discussed. Furthermore, the theory and effect of the ice confinement effect in crushing events is discussed. In Chapter 6, a numerical model for ice-structure interaction is presented. The updated perspective of the model is addressed. Comparisons between numerical simulation results and experimental results are made. Finally, the conclusions of the present study are provided in Chapter 7.

Chapter 2 Literature Review

The objective of this chapter is to review the current state of the art in the four areas of ice-structure interaction science relevant to this study: 1) experimental studies investigating ice-structure interaction, 2) ship denting damage arising from ice interaction, 3) measurements of ice pressures during ice-structure interactions and 4) numerical analysis of ice-structure interaction studies.

Moreover, there is very little literature available related to ice-structure impact tests on the case of non-planar surfaces. What follows is a review of the relevant literature available on topics that will contribute to the experimental and numerical studies to be carried out in this study. Full-scale measurements, model tests and numerical simulation methods for the ice-structure interaction loads are reviewed herein.

2.1 Ice Mechanics

2.1.1. Properties of Sea Ice

The stage of knowledge and applications of the engineering properties of sea ice was reviewed by Timco and Weeks (2010). In this paper, the physical properties (includes microstructure,

thickness, salinity, etc.) and the mechanical properties (includes tensile, flexural, shear, uni- and multi-axial compression strength, etc.) are explored for both first-year sea ice, second- year and multi-year sea ice (expressed as “Old ice”). As author mentioned, many properties are still not fully understood, especially on old ice discussed by Timco and Weeks. Table 2-1 summarized the state-of-knowledge and application of the properties of sea ice.

Table 2-1: Summary of the state-of-knowledge and application of the properties of sea ice (after Timco and Weeks, 2010)

	Knowledge		Application
	First-year ice	Old Ice	
Microstructure	Good (but locally highly variable)	Reasonable	Controls strength and failure behaviour (especially multi-axial loading situations).
Ice thickness	Good	Limited	Extremely important property used in determining ice forces, ice failure behaviour, bearing capacity, ship resistance in ice, etc.
Salinity and porosity	Good (fairly systematic)	Reasonable	Controls strength and failure behaviour.
Density	Reasonable (consistent trends but many confusing values in the literature)	Limited	Influences strength (especially as the ice decays), buoyancy (ice pieces broken by an icebreaker interacting with a propeller), heights of ice rubble piles, etc.
Tensile strength	Limited	Limited	Important failure process for local and mesoscale failures.
Flexural strength	Good	Non-existent	Important failure process for local and mesoscale failures.
Shear strength	Poor	Non-existent	Important for icebreaker design and ride-up and pile-up processes.
Compressive strength	Good	Reasonable	Important failure mode for local failures.
Multi-axial strength	Reasonable	Poor	Important for ice crushing failures on structures, especially with large contact areas.
Borehole strength	Reasonable	Reasonable	Important for situations where ice failure occurs under confined conditions.
Creep behaviour	Poor	Non-existent	Important for bearing capacity, ice roads, landing strips, etc.
Elastic and strain modulus	Good (literature is full of confused terminology)	Poor	Important for bearing capacity behaviour.
Poisson's ratio	Poor	Non-existent	Used in bearing capacity calculations.
Fracture toughness	Reasonable	Non-existent	Important failure process for local and mesoscale failures.
Friction	Poor (many variables to consider)	Non-existent	Important for ice-ice interactions and ice-structures interactions, especially on sloping structures and vessels.

2.1.2. Ice-Structure Interaction

The role of fracture and spalling in ice-structure interaction was discussed by Zou et al. (1996). This paper revealed that fracture and spalling, which initiated from flaws at shear zones with low confining pressure and tensile zones, contribute as key roles in the formation of critical zones during ice-structure interaction.

The mechanics of different types of fractures observed from small- and medium-scale indentation tests were analyzed by Li and Jordaan (2006). ‘Radial’ crack and ‘Hertz-like’ crack was considered as the main types of fracture, which is an important feature during ice-structure indentation at high displacement rates. Both types of fracture will affect to reduce the interaction load directly, which will reduce the effective loading area resulting in a global pressure decrease. Details of mechanics of ice-structure interaction were discussed by Jordaan (2001). The most of the force is transmitted through small areas, which is termed as high-pressure zones. The main processes in the contact layer regarding a recrystallization was discussed. Concept of process have been reproduced in tri-axial tests on polycrystalline ice in laboratory, and finite element model simulation was performed incorporates damage mechanics.

Small-scale indentation tests were conducted with compliant structures using freshwater ice sheets by Sodhi (2001). Grid-based tactile pressure sensors at the ice-structure interfaces was installed to measure the pressure during an interaction. This study confirmed that the effective pressure measured during small-scale indentation tests to be close to those measured on full-scale structures when the indentation rate is high in both situations.

Extensive work done on interaction between sea ice/iceberg and ship structures was reviewed by Shunying and Shewen (2012), in respect of; (i) ice pressure and local load determination based on model and field tests, (ii) global ice loads on ships from full-scale field observations, model tests and numerical simulation models under diverse ice conditions (i.e. level ice, pack ice) and ship operation conditions, (iii) analytical solutions and numerical models of impact loads of icebergs on ships for the Arctic navigation.

2.2. Effect of Confinement

It is a well-known fact that ice failure pressure in a confined ice sheet, for example; in a thick multi-year ice, is much higher than in a thin ice (first-year ice) (Timco and Weeks, 2010). Fully-confined penetration can be defined as the stresses in the confined ice area cannot be released by edge spalling (flaking) or surface. Internal cracking is the only way of stress relief (Blanchet and Defranco, 2001).

Effect of confinement was emphasized by Croasdale (2001). Croasdale analyzed the indentation tests on multi-year ice walls at Byam Martin Channel tests in 1985. During these tests, there were significant differences between the results of the 1.0m^2 spherical and 1.0m^2 flat indenter tests on spherical ice. Pressure at the center was higher in the case of the spherical indenter loading against a flat ice surface than for the flat indenter loading against a spherical ice surface. Test results revealed that the confinement from the surrounding ice may be the main factor, which governed the maximum interaction pressure.

Jones (1982) performed ‘Triaxial’ tests on randomly oriented, laboratory grown, polycrystalline ice, between strain rates of 10^{-7} and 10^{-1} s^{-1} . In addition, Jones adopted a superimposed hydrostatic pressure up to 85MN/m^2 to investigate the effect of confinement. For comparison, additional tests were carried out at a pressure of 0.1 MN/m^2 , to simulate unconfined condition. More details about the test setup are given by Jones (1978). The significant result shown in this study is that (as shown in Figure 2-1), in higher strain-rates, the applied confining pressure prevents cracking, which leads the compressive strength to increase to a higher than the

unconfined compressive strength (more than twice) in general. The role of the confining pressure in this study is similar to confinement formed by crushed, but trapped ice in a certain location due to the geometrical shape of confinement provided by the surrounding ice.

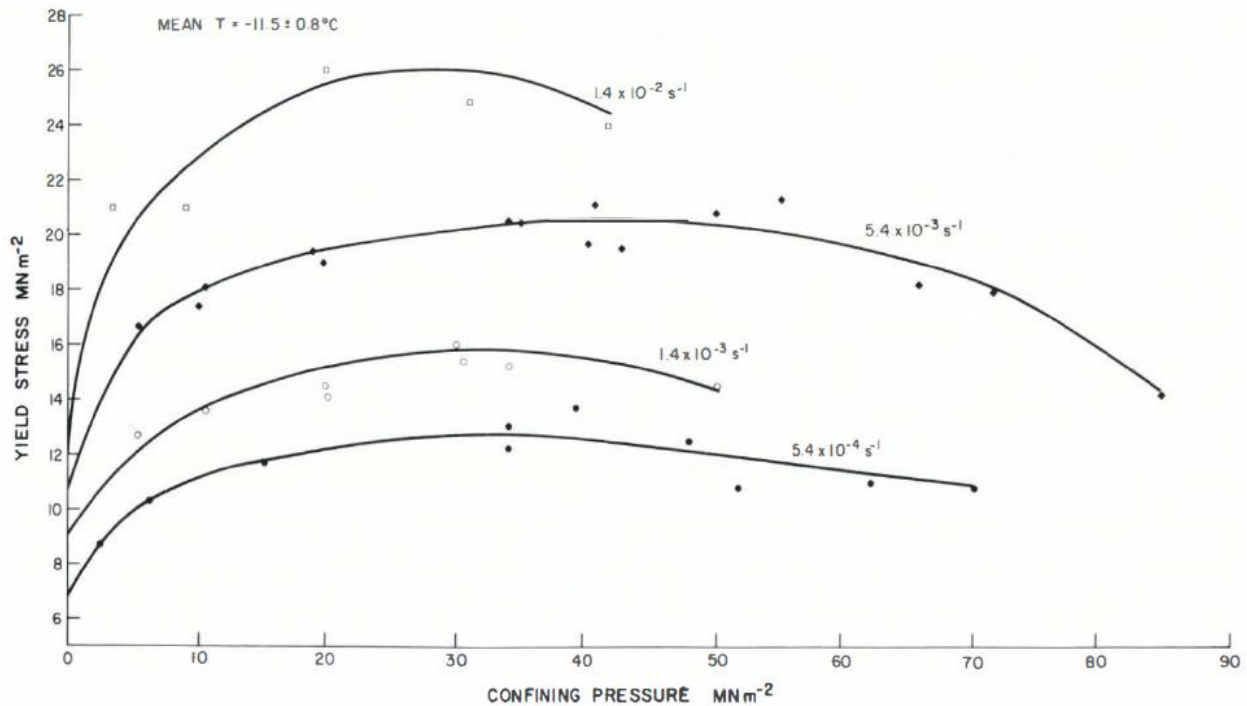


Figure 2-1: Yield stress plotted against confining pressure (after Jones, 1982)

Spencer and Timco (2010) reviewed the test results, which were conducted near Resolute Bay off Cornwallis Island in the Canadian Arctic during May 1993 (first-year sea ice, around 1.8m in thickness). A range of confinements to the flatjacks were varied by the depth of the flatjacks in different slot shapes. An ‘S-shape’ slot is a single-straight-vertical slot cut into the ice sheet, and this represents highly-confined test conditions. An ‘H-shape’ slot consists of three vertical slots (as the letter H) and the flatjack mounted in the middle of the section. Test with the ‘H-shape’ slot represents less-confined conditions.

Figure 2-2 shows a comparison of the Resolute Bay data to the calculated compressive strength. These higher values (with S-shape slot) reflect the confined state of the ice in the flatjack test.

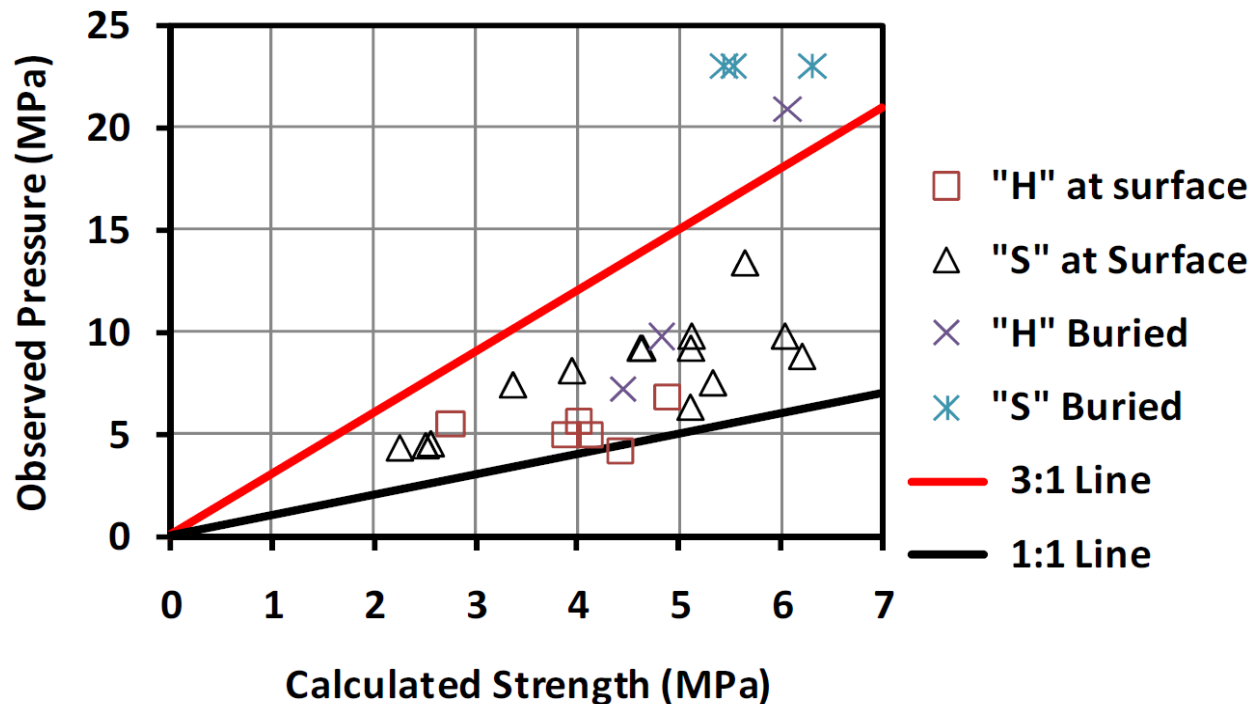


Figure 2-2: Observed pressure and calculated uni-axial compressive strength in the Resolute Tests (after Spencer and Timco, 2010)

Ulan-Kvitberg et al. (2011) examined the role of indenter (which represents a confinement) by adopting different indenter geometry shown in Figure 2-3. The level of confinement of the ice sample (size of exposed part) appears to determine the peak force as well as the expected process pressure-area trends at set speeds. Ulan-Kvitberg emphasized that the level of ice confinement is an important factor in considering design loads. Comparison of force-penetration history shows the effect of confinement (by steel indenter) clearly, as shown in Figure 2-4.

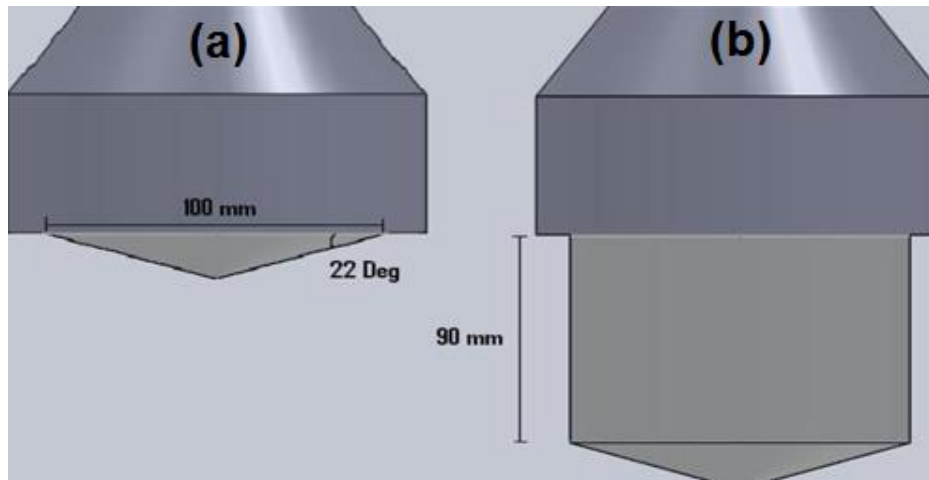


Figure 2-3: Constrained (a) vs. Unconstrained (b) Ice Indenter (after Ulan-Kvitberg et al., 2011)

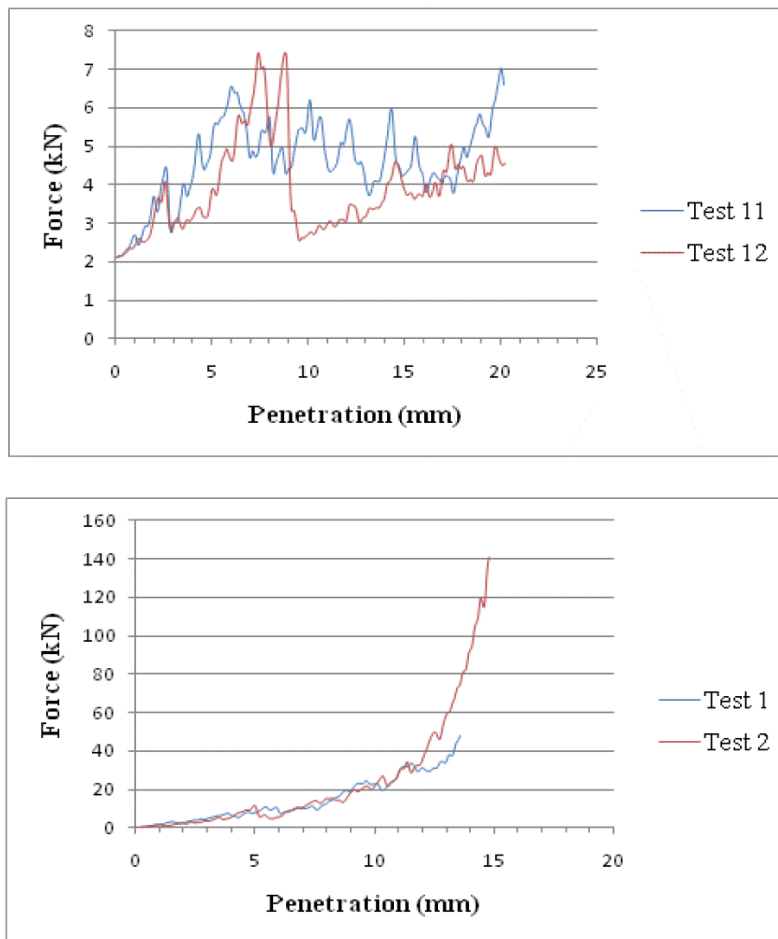


Figure 2-4: Force-Penetration History of Unconstrained Ice Cone (top) and Constrained Ice Cone (bottom) at 100mm/s (after Ulan-Kvitberg et al., 2011)

2.3. Ship Structure Damage

Hänninen (2005) introduced the list of ice-related incidents and accidents in the Baltic Sea winter during 2002-2003 (Table 2-2). The main purpose of this work was not only to collect hull damage, but also other ice-related damages. In the severe winter during 2002-2003, of the 62% of ship hull damages, 30% of the damages were caused by ice-ship interaction and 15% of hull damages occurred in the ice region under compression. The number of ships considered in this study was 111. The data were gathered from several sources. Within in these incidents, 30 cases included dents or ruptures due to ice-ship contact, and 23 cases included ship collisions due to heavy ice. A comparison between ice classes and ship types of damaged and undamaged ships are presented in Figure 2-5.

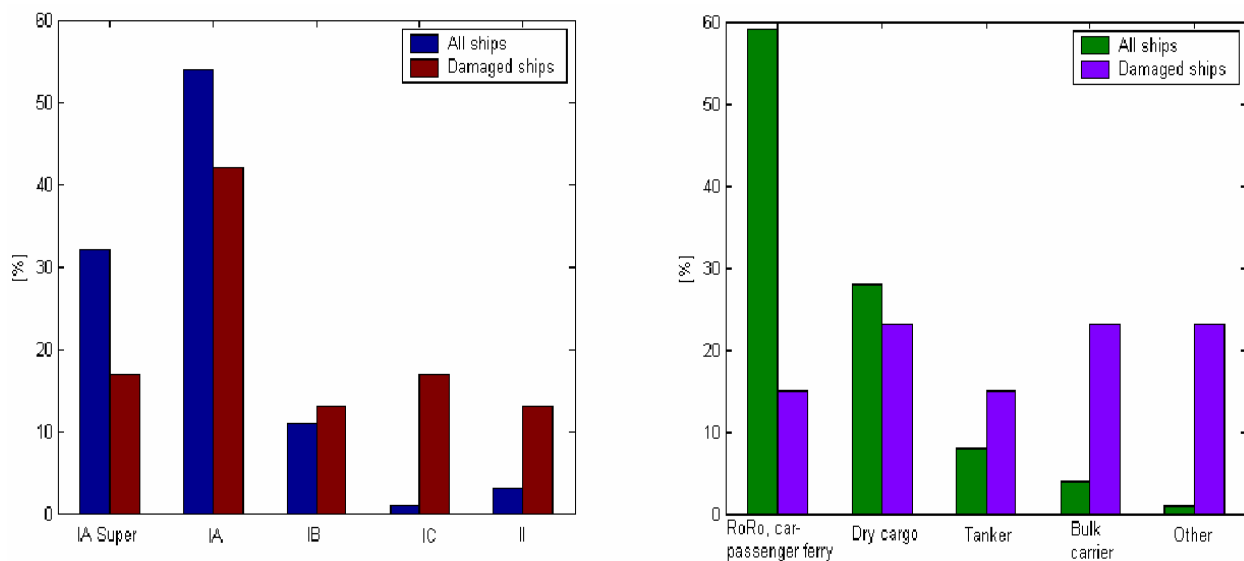


Figure 2-5: Comparison of ice classes and ship types of damaged and undamaged ships

(after Hänninen, 2005)

Table 2-2: A summary of the hull damages (TRA means transverse framing system and LON means longitudinal framing system) (after Hänninen, 2005)

Ship n:o	Framing	Horizontal location of the damage	Vertical location of the damage	Damage	Number of damaged frames /spacings	max. Dents [mm]	Horizontal extent [m]	Vertical extent [m]	Frac-tures	Frac-ture length [m]	Nearest harbour or ship's route
1	TRA	MID	below	bilge	-	-	-	-	-	-	Turku-Stockholm
9	TRA	MID	below	bilge	-	-	-	-	-	-	Turku
12	TRA	BOW	in ice belt	plating/frame	134	200	50	10	Yes	2	St. Petersburg
19	TRA	AFT	below	plating	-	-	-	-	-	-	-
28	-	-	-	ship sides	-	-	-	-	-	-	58°21'5N, 021°26'E
30	TRA	BOW,MID	all areas	plating, bilge	-	30	-	-	Yes	0.25	Vaasa-Umeå
32	-	-	-	plating	-	-	-	-	-	-	-
44	TRA/LON	BOW	on and below	plating/frame	-	30	-	-	-	-	St.Petersburg, Hanko
52	-	BOW	on ice belt	plating/frame	-	100	-	-	-	-	Pori
55	TRA/LON	BOW,MID	below	plating	-	50	-	-	-	-	-
63	-	BOW	on ice belt	ship sides	-	-	-	-	-	-	St. Petersburg
66	TRA	MID	on and below	plating/frame, bilge	12	20	2.4	1	-	-	Helsinki-Porvoo
67	-	BOW	on ice belt	ship sides	-	-	-	-	-	-	St. Petersburg
68	-	MID	on ice belt	plating	2	-	-	-	Yes	-	Loviisa
71	-	AFT	below	plating	1	-	-	-	Yes	0.15	Loviisa
75	TRA	BOW	below	plating	2	-	-	-	Yes	0.3	Loviisa
76	LON	MID	on ice belt	plating/frame	120	30	100	1.6	-	-	Suursaari
78	-	-	-	ship sides	-	-	-	-	-	-	Tallinn
81	-	-	-	ship sides	-	-	-	-	-	-	59°29'2N, 024°10'2E
83	TRA	BOW	below	plating	1	-	-	-	Yes	0.3	Saimaa
87	-	-	-	bilge	-	-	-	-	-	-	-
93	-	-	-	ship sides	-	-	-	-	-	-	-
95	-	-	-	ship sides	-	-	-	-	-	-	-
98	TRA	MID	on and below	plating	40	50	-	-	-	-	Luleå-Raahe
99	TRA	BOW	on and below	plating, bilge	-	20	-	-	-	-	Turku-Stockholm
100	TRA	BOW	on and below	plating, bilge	-	40	-	-	-	-	Helsinki-Tallinn
101	TRA/LON	MID	on ice belt	plating	3	30	4	1.4	-	-	Raahe

Kujala (1991) introduced damage statistics of ice-strengthened ships in the Baltic Sea from 1984 to 1987. This report includes 61 ships (31: 1A Super Class, 28: 1A Class, 2: 1C Class). All the longitudinally framed ships servicing in Bothnian Bay experienced sustained damages that was typically local, with minor denting of plating or frames. 26% of the 1A Super class and 54% of the 1A Class have experienced damage during the navigation. No damages resulting in leakages were found. Most of the reported damages appear to be at the mid-ship section while the ships have been stranded in compressive ice condition. Measurement of damages was made by visual observation as well as stereo photography. Figures 2-6 and 2-7 show the examples of ship damage (ship no. 35) and profile of the damaged area.



Figure 2-6: The damage occurred during the winter 1986 on area 1 of ship no. 35.

(after Kujala, 1991)

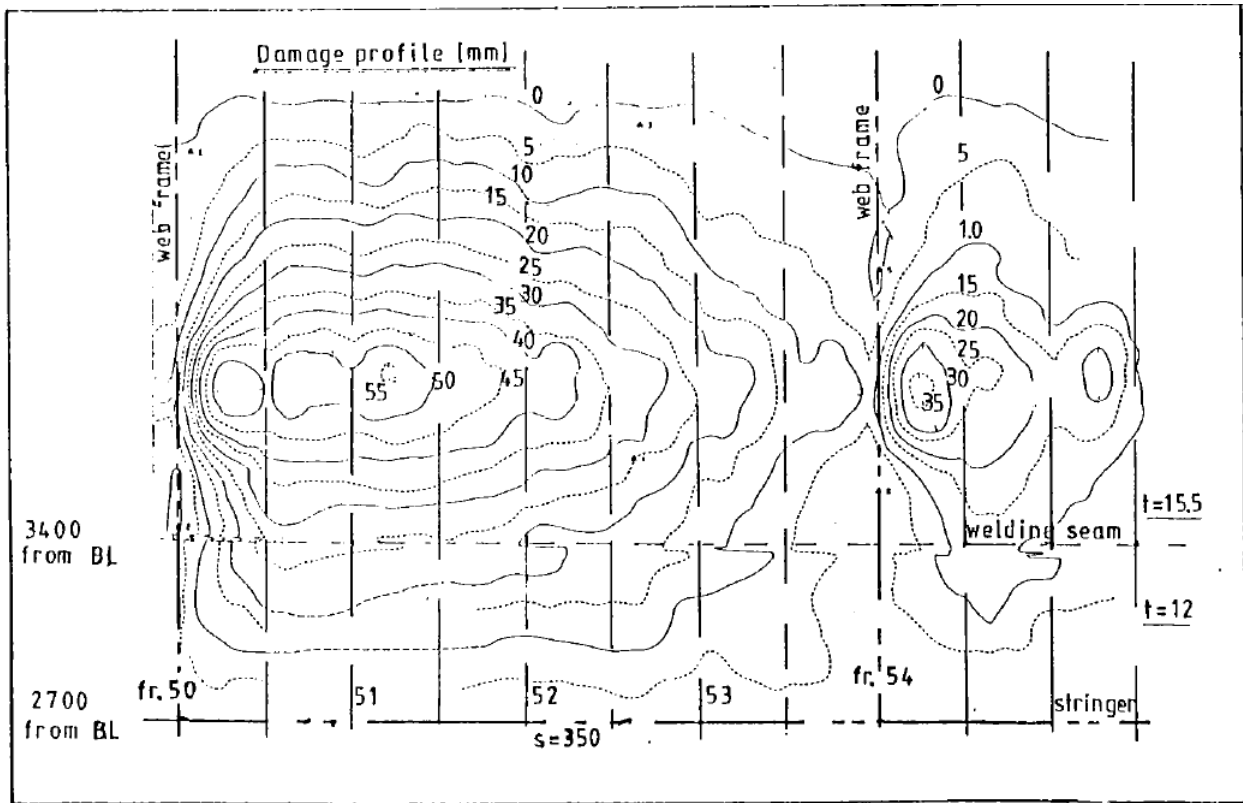


Figure 2-7: The shape on the damage on area 1 of ship no. 35 (after Kujala, 1991)

Clearly, a damaged (deformed) shape of the structure is a concave shape (the main interest in this study). However, this report was not intended to investigate any ice load/pressure variance in deformed area. Therefore, any further information, especially related to the ice load/pressure, was not available.

2.4. Field/Medium/Laboratory Scale Experiments

2.4.1. Field/Medium Scale Experiments

Daley (1994) compiled and analyzed data on field and medium-scale tests. Features of various field/medium-scale tests were illustrated and described in this report. One of the medium-scale experiments was at the Hobson's Choice ice tests, which were performed using the wedge-shaped and flat indenters pressed into a flat and shaped ice surfaces in an ice trench wall. In these cases, the ice surface was either flat or concave shaped and the indenter shapes were either flat or convex.

Field tests on the vessels Kigoriak, M.V. Arctic, and Polar Sea (Daley, 1994) aimed to measure direct ice loads acting on the ship structure. Frederking (2005) reported the local ice pressures on the Oden 1991 Polar Voyage. An area on the starboard of the ship was instrumented with strain gauges to measure local ice pressures, and the results show a significant relationship between ship speed and local ice pressures. He also examined local ice pressure data collected from the 1994 Polar transit of the Louis S. St. Laurent, and this provides an excellent data set for determining local average ice pressures as a function of the area (Frederking, 1999).

Strain-gauges were attached to selected parts of the structure and load data was acquired during ice impacts (Frederking, 1999). During the field tests, the ship structure may have experienced an extreme load condition leading to denting. However, as mentioned above, measuring the deformation of the structure was not the main focus of these tests since no record was made

regarding the deformation of the strain-gauged panel. Therefore, it is not clear whether any of these test data would have been for ice-structure interaction with the ship plating undergoing permanent structural deformations.

D.M. Masterson and R.M.W. Frederking (1993) also analyzed various field and medium-scale test data. They compiled the data on local ice pressures, and forces, which included a variety of indenter tests (Pond Inlet/APOA/Hobson's Choice) and field trial (M.V.Arctic/Kigoriak trial/USCGC Polar Sea). In addition, the data also contained tests on Molikpaq walls to investigate the global ice loads (which affects the overall stability of structures, in particular, and are associated with the total forces causing the bow print during a ship ram) and local ice loads (which determine the design of steel plate thickness plus spacing and size of stiffeners or concrete wall thickness and the amount of reinforcements). Through the test data, it was confirmed that the process pressure-area curve tends to decrease as the area of contact increases and design curves were suggested. However, there was no discussion or mention about structural shape effects (denting).

The main purpose of the previous tests was not to determine changes in ice loads and pressures associated with deformation of structural shapes. Therefore, it was not required to measure the effect of any permanent deformation in the structure itself; since the possibility of plastic deformation occurring in the structure was not expected. Furthermore, most of the location where strain gauges were attached had high rigidity (on the top side of the frame or close to the stiffened-frame). Ritch et al. (2008) reported a local ice pressure measurement on a strain gauge panel during the CCGS Terry Fox bergy bit impact test. A total of 178 impacts occurred between

the vessel and bergy bits, masses varying from 20-22,000 tones, and ship speeds varying from 0.2-6.5m/s. Maximum pressure measured was 11.3MPa on an area of 0.12m², and the maximum force of 5MN was measured.

Figure 2-8 shows the strain gauge layout of CCGS Terry Fox bergy bit impact trial test, using a total number of 120 strain gauges (Ritch et al., 2008). As one can see, most of the strain gauges were located on the top of the mainframe or stiffener which has high rigidity compared to other locations in the structure and provided a rigid structural panel of flat or slightly convex shape.

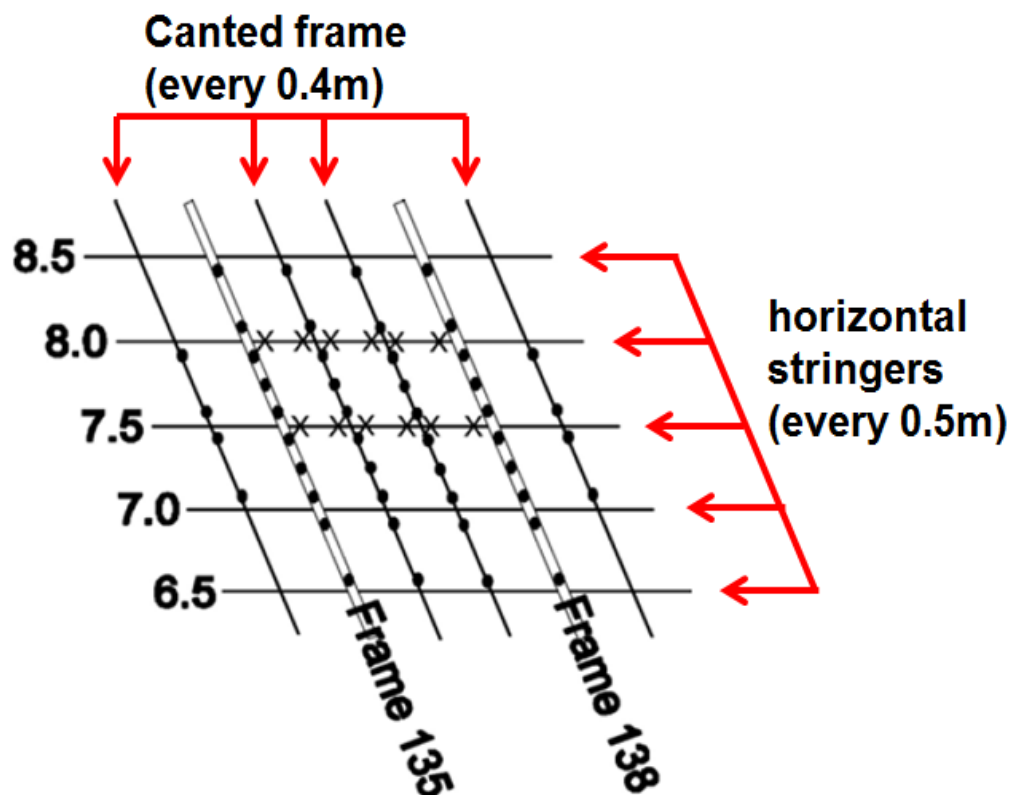


Figure 2-8: Strain gauge layout (after Ritch et al., 2008)

As part of a five-year program under the sponsorship of the Japan Ocean Industries Association (JOIA), medium-scale indentation test has been conducted on sea ice in the harbor of Lake Notoro, Hokkaido, by pushing a segmented indenter against the edge of floating ice sheets (Sodhi et al., 1988; Akagawa et al., 2001; Takeuchi et al., 2001; 2002; Frederking, 2004; Sodhi et al., 2006). The indenter was segmented, and measurements on each 10cm-wide segment include forces in three directions. More details about this program will be discussed in the next section.

2.4.2. Laboratory Scale Experiments

A series of laboratory scale experiments was done to observe ice-structure interaction more closely. Cole (1987) performed constant deformation-rate tests on laboratory-prepared polycrystalline ice to study strain-rate and grain-size effects in ice. Sayed and Frederking (1992) designed a series of experiments to understand the effects of extrusion of crushed ice during ice indentation. The experiments examined two-dimensional flow between two converging flat plates, and the entire process during the tests were observed through transparent side windows. As a result, local and average normal stresses and displacements were measured.

The brittle failures of polycrystalline ice were reviewed by Schulson (2001). Tensile cracking in ice was discussed in terms of the nucleation and propagation of cracks. In addition, the brittle compressive failure was also addressed. Daley (1992) employed ‘Chaos theory’ to analyze the behavior of the iterative sequence of cracks in analytical mode. Sodhi (2001) conducted small-scale indentation tests with compliant structures and freshwater ice sheet. The pressure generated

during the interaction was measured by tactile pressure sensors. It was revealed that the ductile ice behavior, present at low indentation speeds, and the continuous brittle crushing behavior observed at high indentation speeds were observed. The effective pressures measured during small-scale indentation tests were close to those measures on full-scale test structures.

Tuhkuri (1995) described the results of laboratory experiments, where a block of freshwater ice was crushed in a continuous manner against a compliant structure. Figure 2-9 shows the experimental setup.

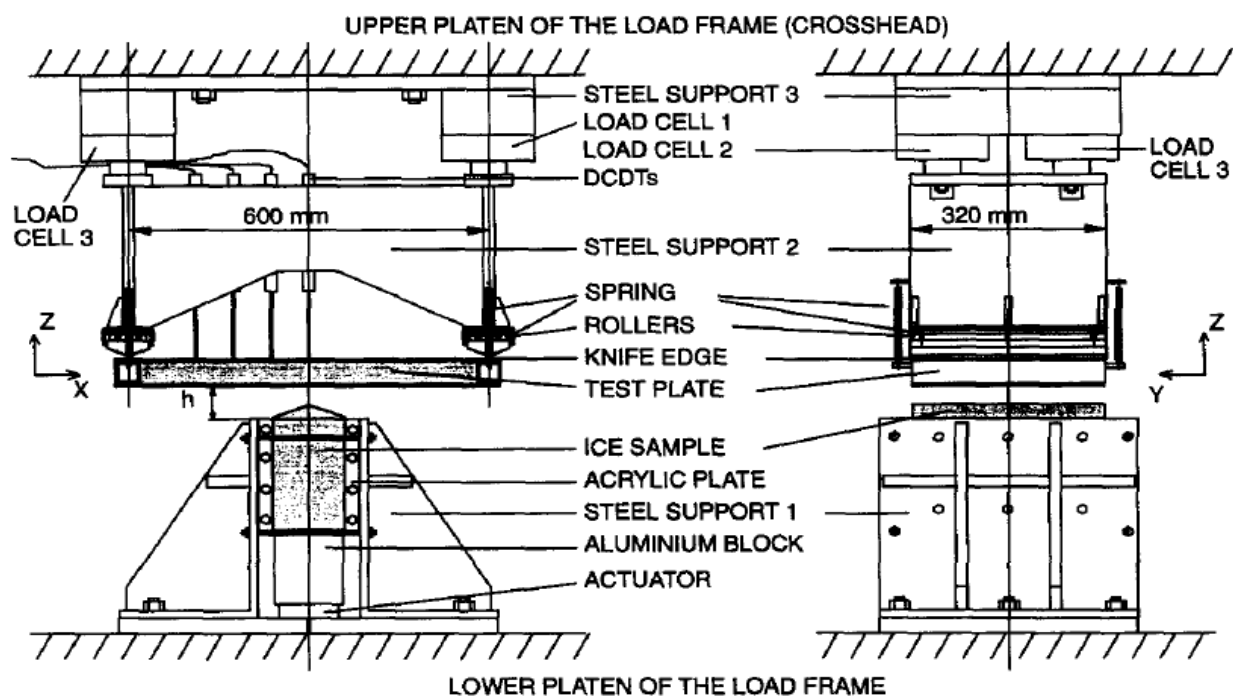


Figure 2-9: The experimental set up (after Tuhkuri, 1995)

The failure process, the ice-structure contact, and the ice loads were affected by the clearance between the test structure and the confinement box for ice that represented the role of confinement. In addition, test speed was not significant because the all tests were in brittle failure range. A wedge angle was not significant except the first peak loads.

2.5. Local Ice Pressure Measurement Method

Many researchers have conducted a large number of field trials and laboratory-scale experiments using a variety of instrumentation for ice-structure interaction tests to identify ice load/pressure and the actual contact area relationship, in real-time. As mentioned in the previous section, understanding of the spatial pressure-area curve, which describes that how local peak pressures relate to the area within the contact zone, is important to determine design loads on a local structure such as plating and framing. This section reviews the literature on local ice load measurements using pressure panels and tactile sensors.

2.5.1. Pressure Panel

Gagnon (2008) analyzed data from bergy bit impacts using a novel hull-mounted external pressure panel. A schematic of the pressure panel operating principle is illustrated in Figure 2-10. During the bergy bit impact test, data were acquired from impacts on the bergy bits of various sizes (10 - 22,000 tons) and over a range of ship speed (5 - 12kt). Through the image analysis, Gagnon observed that, (i) the ice contact area was irregular, where the pressure was high (8 - 20MPa) and roughly uniform; and (ii) is usually surrounded by a larger area of pulverized ice, where the pressure was relatively low (~2.5MPa). In addition, data showed that the trend of the pressure–area curve was somewhat increasing as discussed by Daley (2004; 2007).

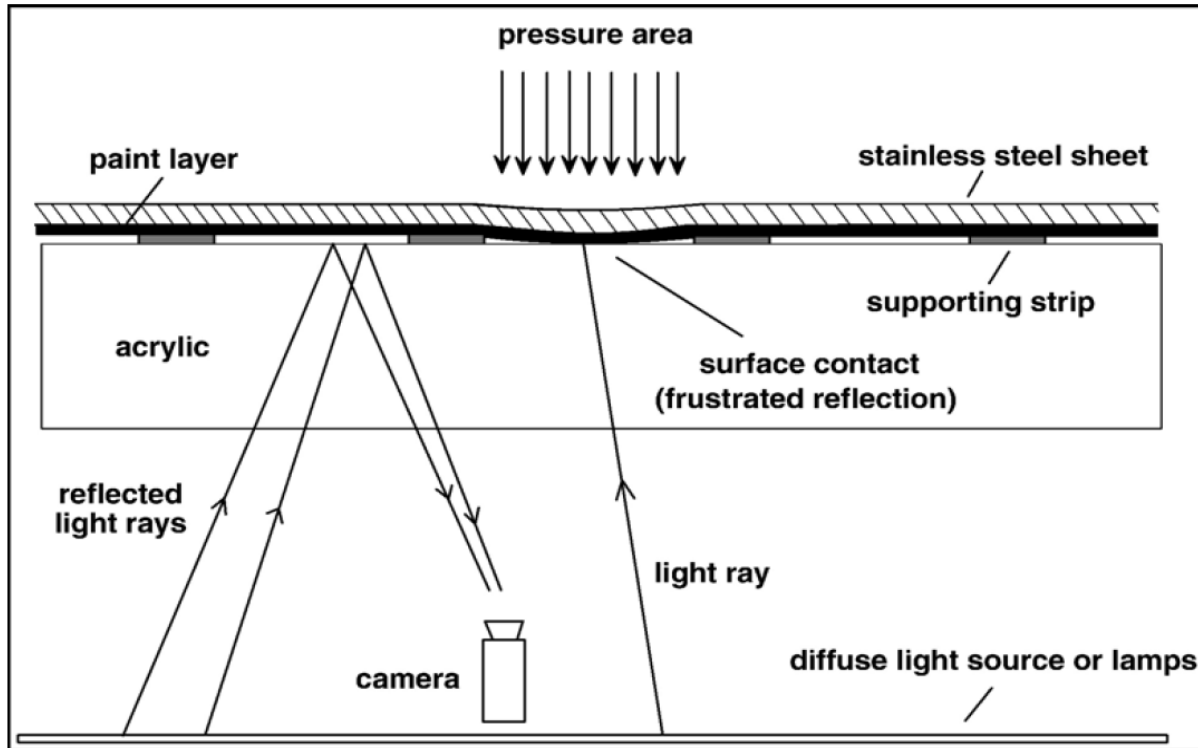


Figure 2-10: Schematic illustrating the operating principle of the Pressure Panel

(after Gagnon, 2008)

The pressure panel was extended to laboratory-scale tests using lab-grown ice sample and useful data were obtained (Gagnon, 2009; Reddy Gudimetla, 2012).

Figure 2-11 shows the 1.0m diameter ice cone test done by STePS² project using the pressure panel, which records pressure distribution in a real-time (Reddy Gudimetla et al., 2010). 1.0m diameter cone-shaped ice samples were being crushed against the above-mentioned laboratory-scale pressure panel. The aim of this test was to set the ice load conditions for the later quasi-static and dynamic tests to be carried out on the real-scale steel grillage. Figure 2-11 shows the ‘before’ and ‘after’ of the test.

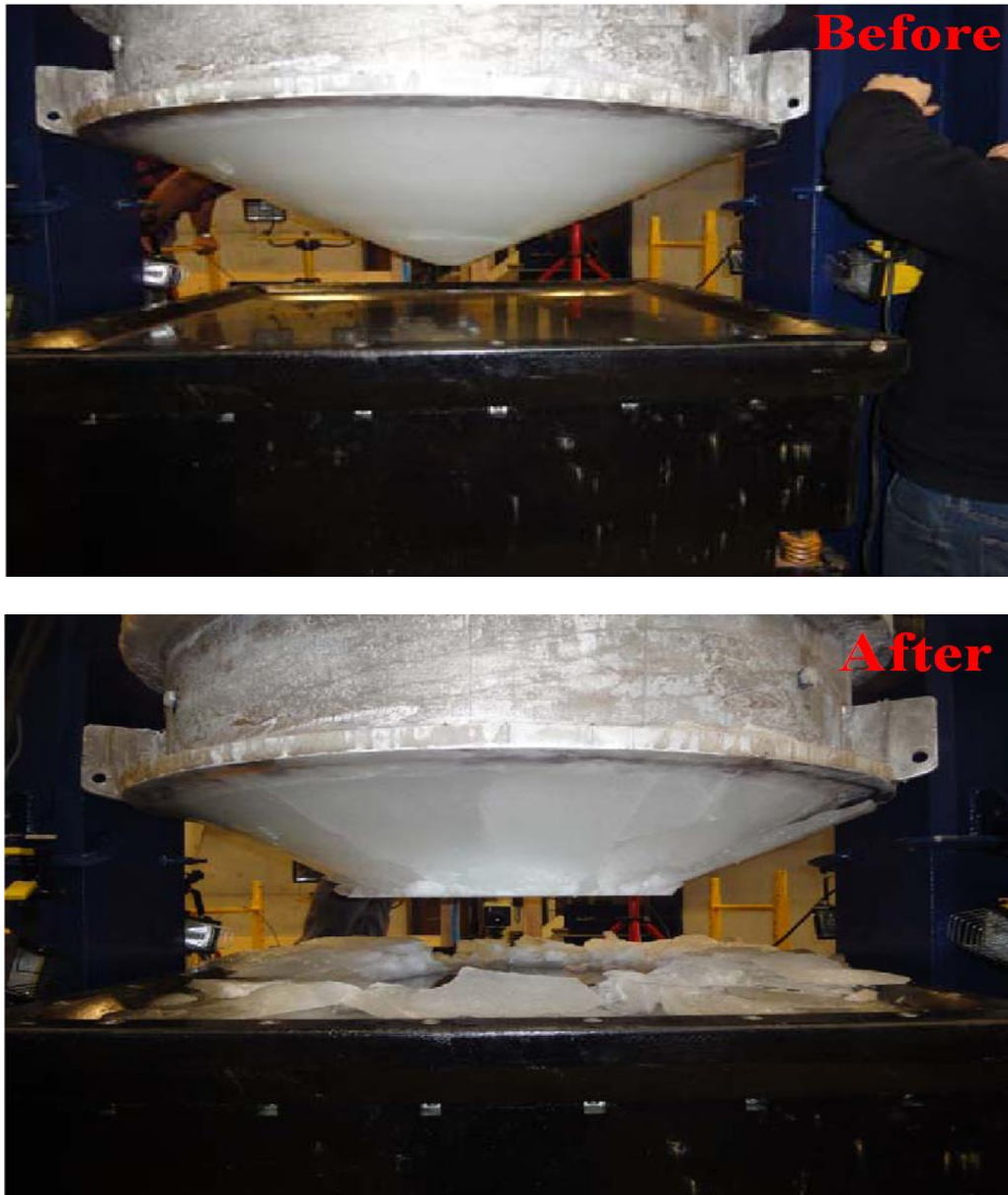


Fig. 2-11: 1.0m diameter ice cone test using the pressure panel before and after
(after Reddy Gudimetla et al., 2010)

Figure 2-12 shows the progression of pressure (contact area) profiles during the test. Obtained image from the pressure panel was analyzed to plot a pressure distribution map. An example of the analyzed image is shown in Figure 2-13.

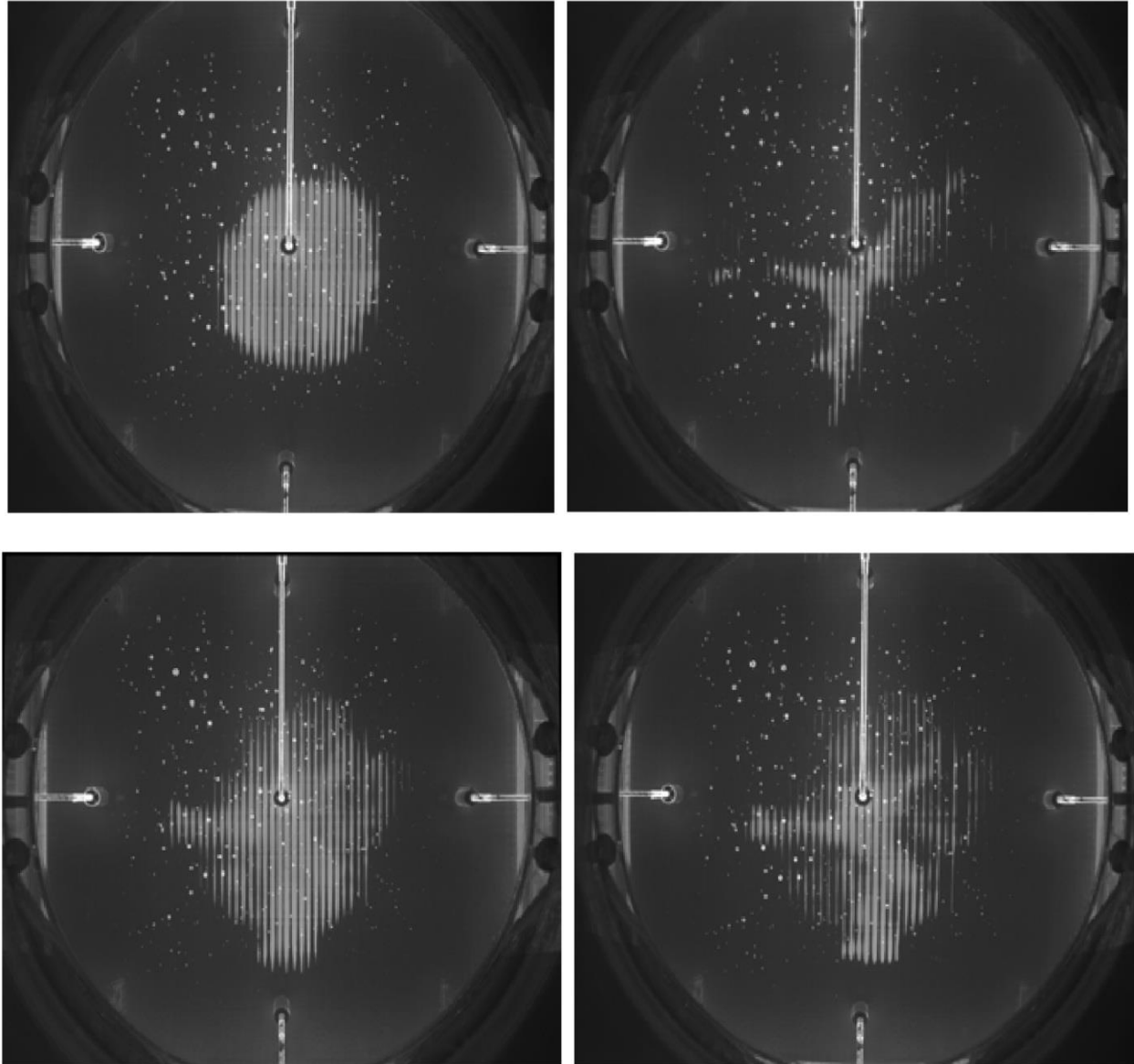
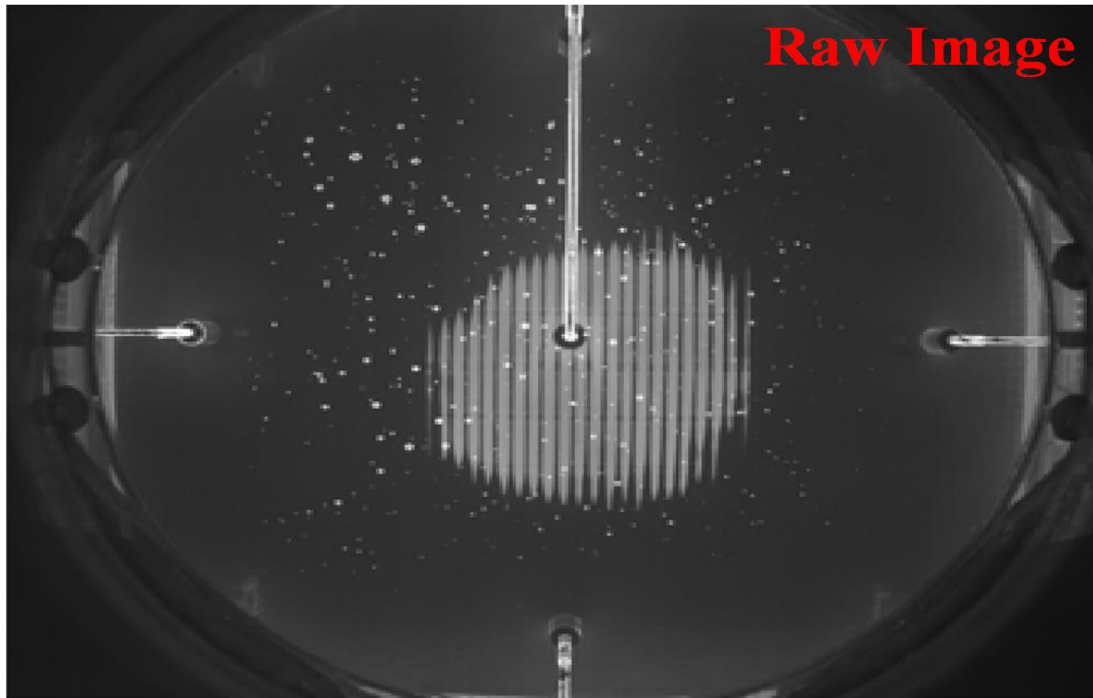
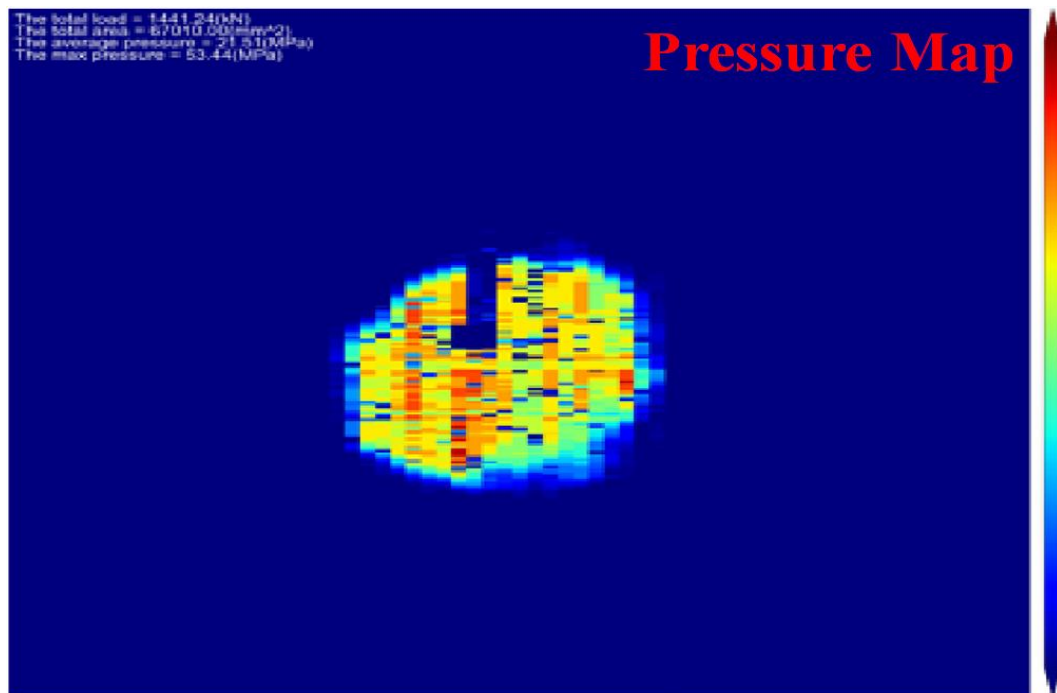


Fig. 2-12: Progression of pressure profile in double angle cone test

(after Reddy Gudimetla et al., 2010)



(a) Raw image obtained from pressure panel



(b) Plot of the analyzed pressure distribution map

Fig. 2-13: Raw image and analyzed pressure distribution map obtained from pressure panel tests

(after Reddy Gudimetla et al., 2010)

The advantages of using a pressure panel are: 1) pressure and contact area data are in real-time; and 2) simplicity of the measurement process. However, the response surface of the pressure panel acted as a flat rigid body (not allowing any deformation in the panel); so there are limitations in applying these results to this study that planned to measure the ice load and pressure distribution for a deformed or concave-shaped structure. In addition, installation of data acquisition system is still complex (i.e. instrumentation set-up and data-storage devices such as cables) and handling a large amount of recorded real-time data is not an easy task.

2.5.2. Tactile Sensor

A series of ‘Medium Scale Field Indentation Tests (MSFIT)’ have been performed by the Japan Ocean Industries Association (JOIA) program during 1996-2000. Results of tests were analyzed and published by many researchers (Takeuchi et al., 2001, 2002; Sodhi et al., 2001; Frederking, 2004; Sodhi et al., 2006). Takeuchi et al. (2001) examined the influence of a model structure width (W), ice thickness (h), indentation speed (V) and uni-axial compressive strength (σ_c) on ice loads. The global ice load (F_t) equation for level ice was derived from MSFIT data, and the equations were based on the main parameters V , h , W and σ_c . During tests; lots of local ice load data have been obtained using tactile sensors.

Sodhi et al. (2001) and Takeuchi et al. (2002) utilized tactile sensors during small-scale and medium-scale indentation tests and produced data on interfacial pressure generated during the ice-structure interaction. Obtained data were calibrated and compared with the small-scale indentation test results and full-scale measurement of ice forces on the Molikpaq structure.

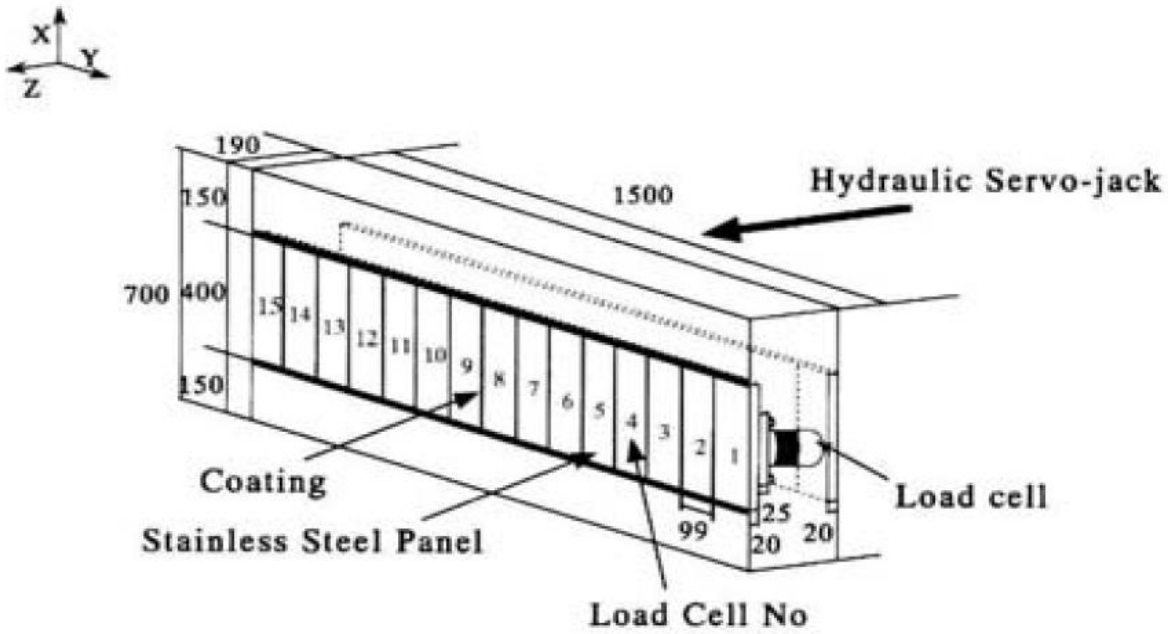


Figure 2-14: Segmented indenter (after Sodhi et al., 2001)



Figure 2-15: Indentation test with four tactile sensors (after Sodhi et al., 2001)

Calibration of the tactile sensor was done by comparing the load with load cell measurement data by Sodhi et al. (2006). A significant difference was shown between two measurement systems as shown in Figure 2-16.

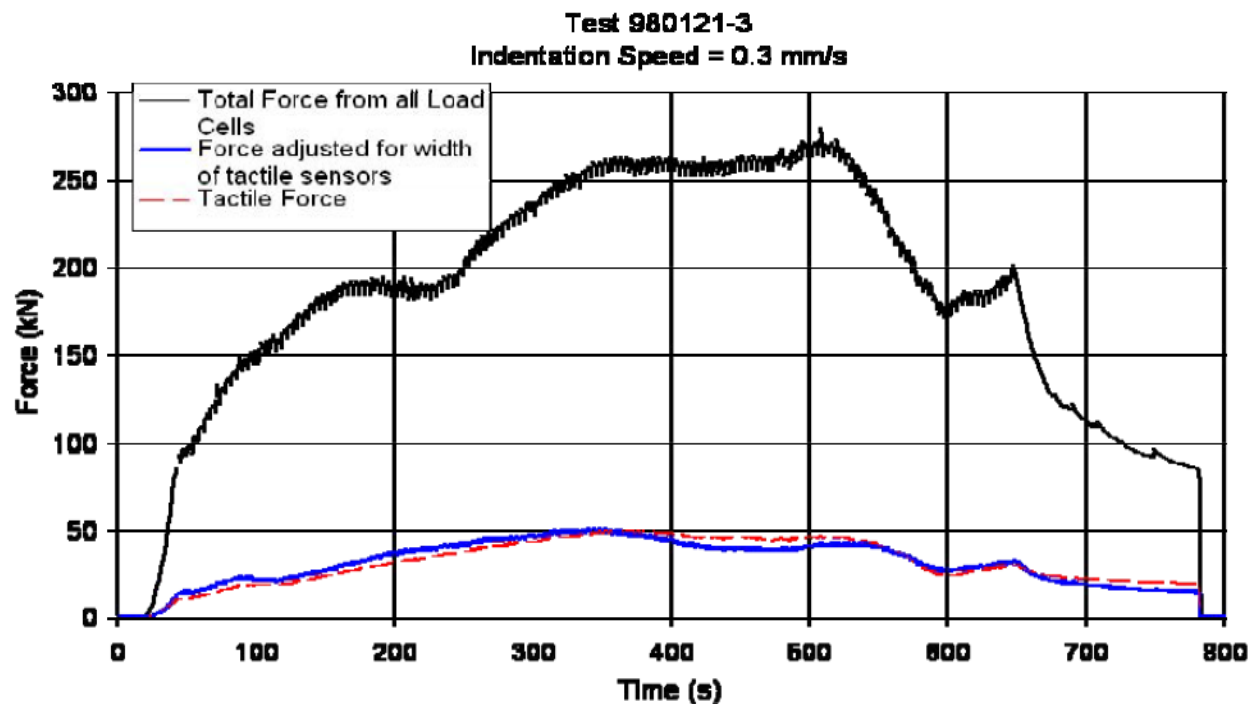


Figure 2-16: Time-history plots of the ice force records at 0.3mm/s (after Sodhi et al., 2006)

Frederking (2004) analyzed the indentation test data. He raised the issue that obtaining good measurement data on the pressure within the contact area is always a problem. If the sensor area was too large, the pressure was averaged over too large an area. On the other hand, if the sensor area was too small, there were usually insufficient sensors to determine the distribution of pressures. He observed that a load-time record between load cell and tactile sensor represented a good agreement for a particular period (see Figure 2-17).

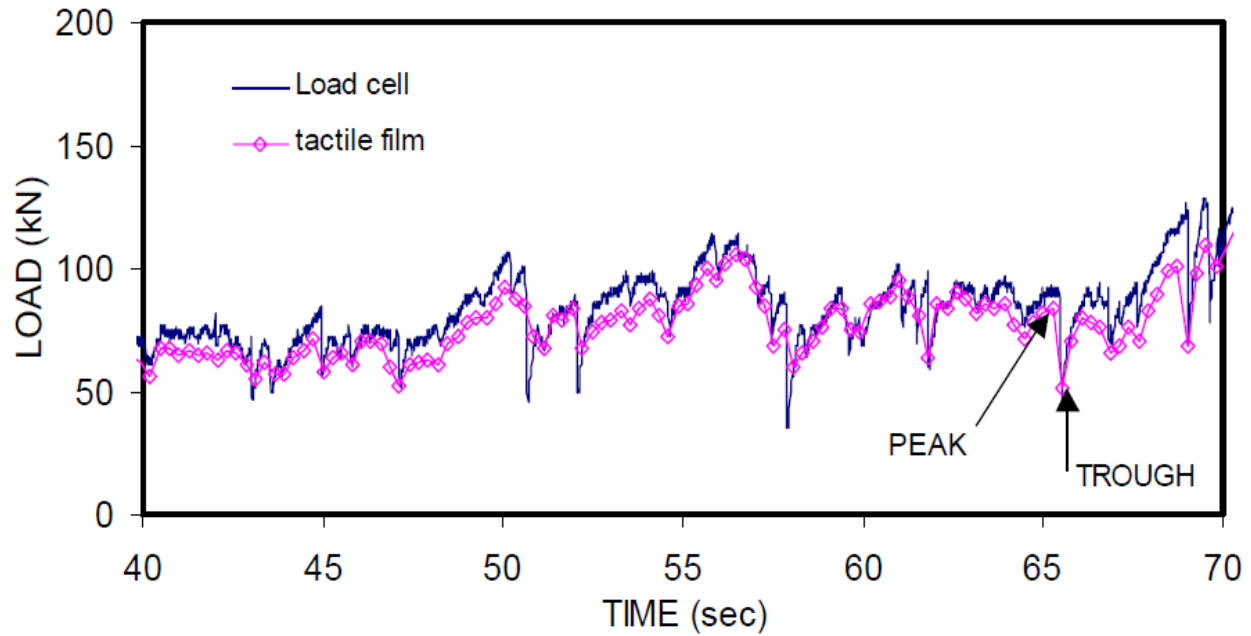


Figure 2-17: Load – time record expanded for interval 40 to 70 seconds (after Frederking, 2004)

Frederking realized that the contact between ice and structure represented ‘line-like’ load distribution with only about 10% of the ice edge experiencing any local pressure on all. In addition, a localized high pressure zone persisted up to 10 seconds (surprisingly long period).

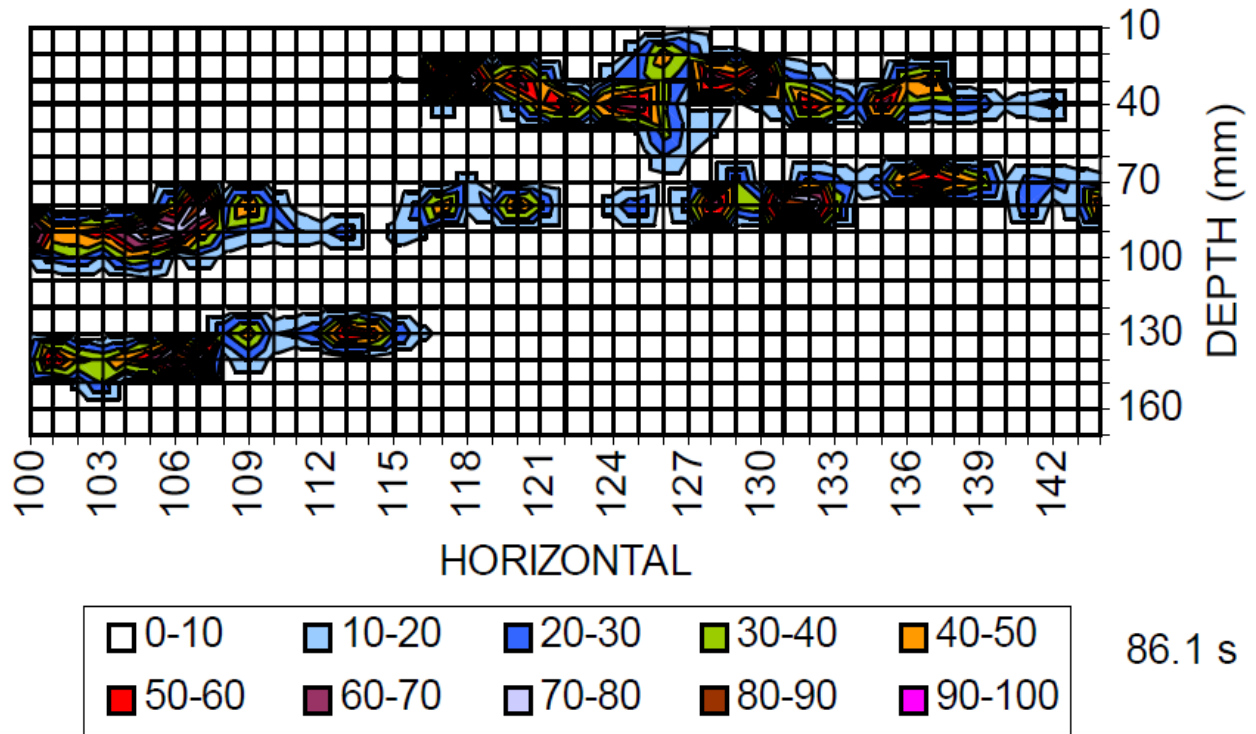


Figure 2-18: Contour plot of pressure at time 86.1 s, a time of peak load (after Frederking, 2004)

Tactile sensors were also used on a ship model test in the ice tank. A series of ship model test in level ice was performed with local ice load measurements (through tactile sensors) by Izumiyama et al. (2006; 2007) as shown in Figure 2-19. Spatial resolution of the tactile sensor was about 5.4mm, and data-acquisition rate were close to 100Hz. During the tests, data frequency was selected as 30Hz. The ice load distribution in the bow region was ‘broken-line-like’ fashion in which short load patches were aligned in a horizontal line and verified with the data in the full-scale conditions (Figure 2-20).

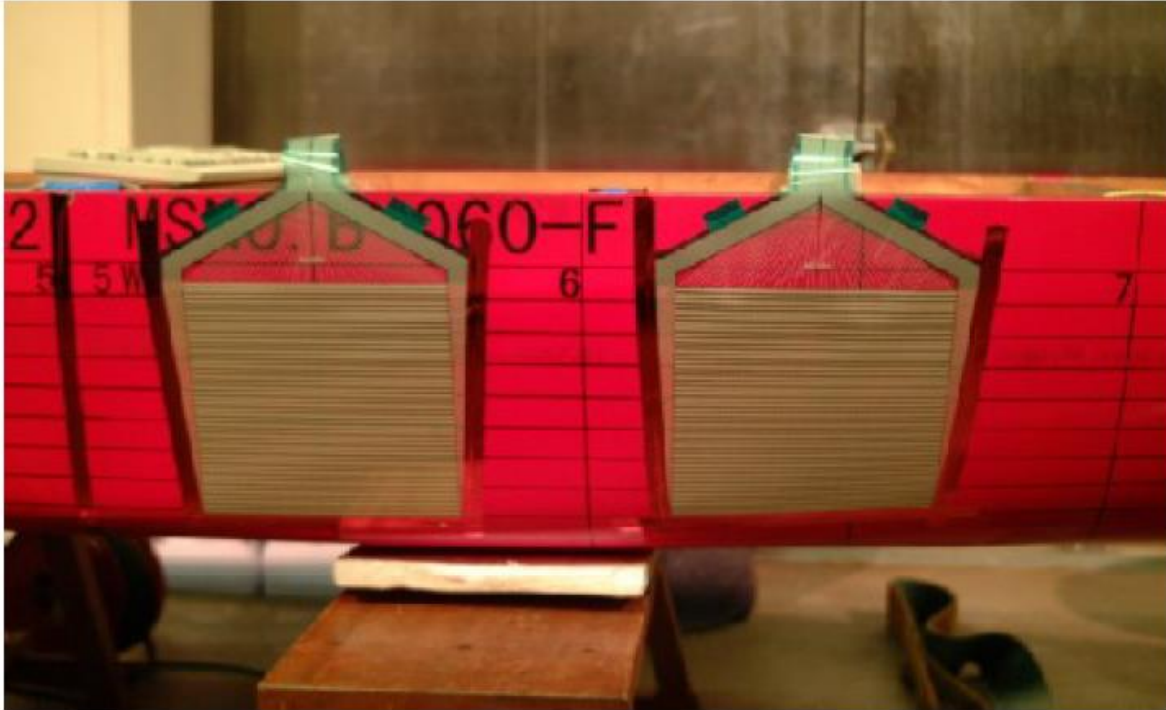


Figure 2-19: Tactile sensor mounted on a model ship (after Izumiyama et al., 2007)

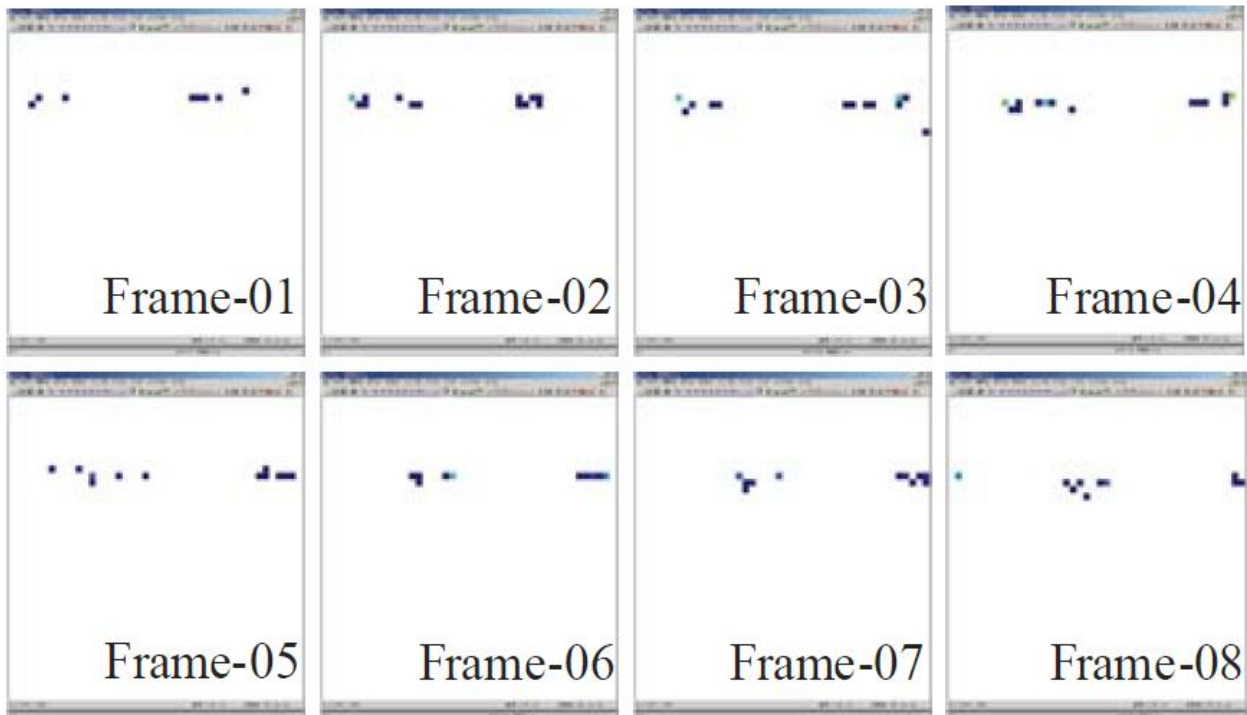


Figure 2-20: Ice load distribution on a model ship bow (after Izumiyama et al., 2007)

However, ice spalling events occur on an extremely short time; therefore, recording a real-time based contact area and pressure distribution is highly sensitive to the data-acquisition system's resolution and frequency of data recording. Even though tactile sensors represented a high capability for use in medium-scale and laboratory-scale tests, yet measuring all the phenomena occurring in an extremely short time is not practical, even with the tactile sensor equipment.

2.6. Ice Loads on Podded Propulsor

Most of the existing ice-ship structure collision test results have focused on primary ship's hull structure. This means that prepared ice samples were crushed against a flat plate. From these kinds of tests, magnitude of loads and distribution of pressures was obtained. However, investigation of damage at other locations due to direct impact or by broken ice piece impact is also significant.

A podded propulsor is chosen as the example of 'concave' shape structures in this study. A podded propulsor is likely to experience ice loads during service in the Arctic region. Therefore, each classification society is proposing their relevant rules to consider the ice load on the podded propulsor.

As shown in Figure 2-21, DnV (Det Norske Veritas) has proposed eight different impact scenarios that a podded propulsor can experience. In addition, DnV suggested equations to calculate the applied ice loads as indicated in Figure 2-22. Following the proposed equation, ice

pressure has been significantly simplified to give realistic magnitudes of ice pressures/loads compared to previous ice load calculation methods.

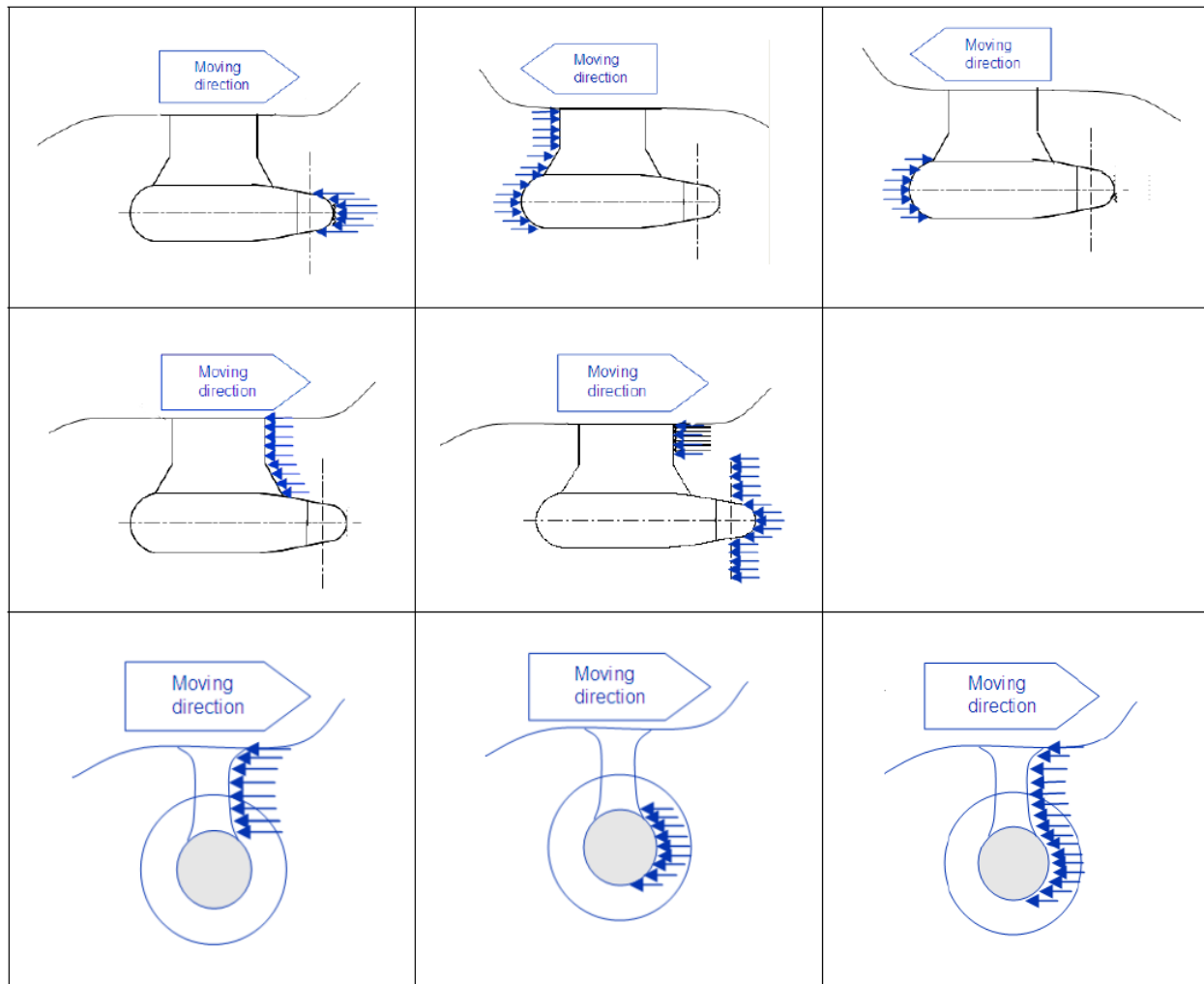


Figure 2-21: Illustration of actual load cases to be considered (after DnV, 2011)

$$F = p_o^{0.8} (A C^{0.3})^{\exp} C_1 C_2 C_3 C_4 \text{ [MN]}$$

where:

p_o = Ice pressure (MPa), see table 8.1

Table 8-1 Reference ice thickness and –pressure. Ref. technical background note and rules for IACS UR I2

<i>Ice Class</i>	<i>H_{ice} (m)</i>	<i>p₀ (MPa)</i>
PC-1	4.0	6
PC-2	3.5	4.2
PC-3	3.0	3.2
PC-4	2.5	2.45
PC-5	2.0	2
PC-6	1.75	1.4
PC-7	1.5	1.25

- A = considered projected area exposed to ice pressure in m² if less than 2H_{ice}²
= 2H_{ice}² otherwise
- exp = 0.3 when area is 1 m² and more
= 0.85 when A < 1 m²
- C = A / 2H_{ice}², or = min. 1
- H_{ice} = Reference ice thickness for machinery strength design, see table 8.1 D= propeller diameter
- C₁ = location and propeller type factor for hub and strut loads
= 1 in general
= 1.5 for pulling and pushing “front propeller” strut loads and pushing propeller axial pod loads
= 2.2 for pulling propeller axial load (“hub load”) calculated based on projected hub area
- C₂ = this factor reduces pod ice loads by 1/3 for under bottom mounted units
= 1 in general
= 2/3 for “deeply submerged” under bottom located propellers
- C₃ = ship type factor
= 1 in general
= 1.25 for icebreaker and ice management vessel
- C₄ = is statistical factor for expected maximum load during 20 years lifetime
= 1.2 in general.

Figure 2-22: Ice load definition (after DnV, 2011)

Alternately, BV (Bureau Veritas) has proposed 14 different scenarios to calculate the transverse and axial ice loads on a podded propulsor (BV, 2012). Twelve scenarios, except two blade failure scenarios by grounding, are possible ice loads as shown in Figure 2-23 and 2-24. BV rules are more detailed compared to DnV rules respect to determining various parameters such as adopting k_1 and k_2 (ice coefficient), h_{ice} (maximum ice sheet thickness), r_f (rafting factor), σ_{ice} (uniaxial compressive strength of ice).

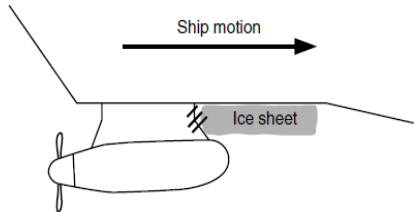
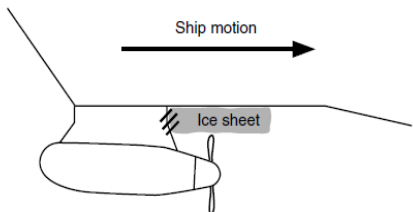
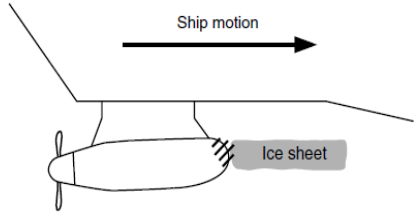
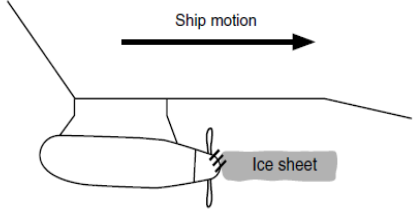
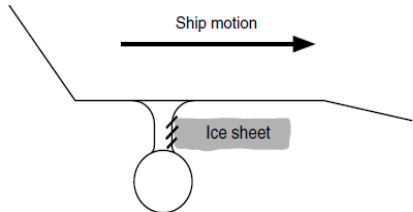
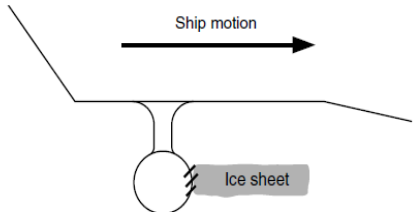
N°	Description	N°	Description
1a	Crushing ice sheet at bracket top 	1b	Crushing ice sheet at bracket top 
2a	Crushing ice sheet at propeller hub 	2b	Crushing ice sheet at propeller hub 
3	Crushing ice sheet at bracket, propulsor turned 90° 	4	Crushing ice sheet on propulsor, propulsor turned 90° 

Figure 2-23: Critical scenarios for ahead working ships (after BV, 2012)

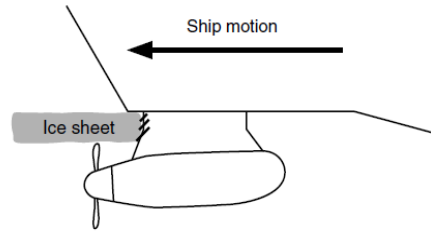
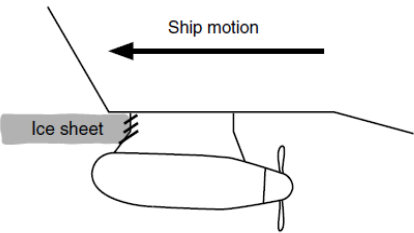
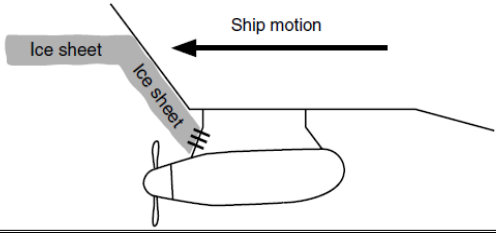
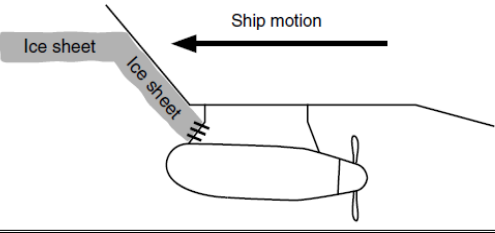
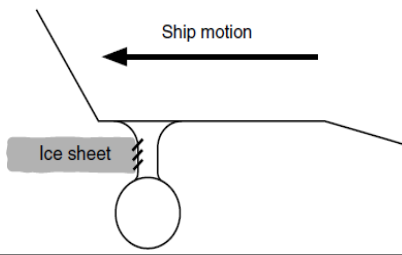
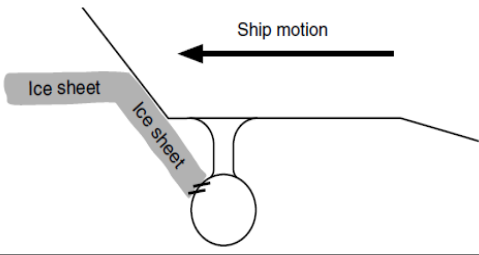
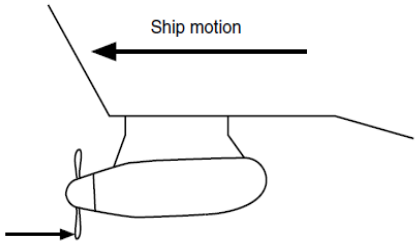
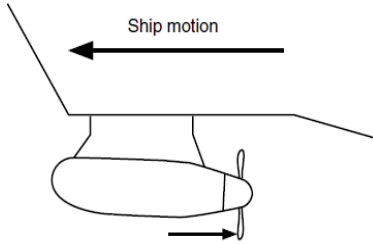
N°	Description	N°	Description
5a	Crushing ice sheet at bracket top 	5b	Crushing ice sheet at bracket top 
6a	Crushing ice sheet at lower bracket 	6b	Crushing ice sheet at lower bracket 
7	Crushing ice sheet on strut 	8	Crushing ice sheet on pod 
9a	Grounding (blade failure) 	9b	Grounding (blade failure) 

Figure 2-24: Critical scenarios for astern working ships (after BV, 2012)

However, it was impossible to find any procedure from DnV's and BV's references regarding how the proposed equations were specifically derived. In addition, information about whether the

proposed equations have undergone a series of verification processes such as field or model test or finite element analysis (not mentioned in the notes).

2.7. Numerical Simulation

Ice can exhibit a variety of behaviors as a function of strain rate in compression (in addition; temperature, grain size, etc.) from ductile to brittle. Large number of laboratory-scale ice experiments, as well as field trial tests, has been conducted to investigate the ice characteristics and ice-structure interaction. However, developing a valid numerical simulation method to explore a more diverse parametric condition is common in engineering due to the limitations of time and cost.

Diverse ice models have been developed to simulate the detailed behavior of ice during ice-structure interaction. In this section, simulation methods that are currently being applied are reviewed.

2.7.1. SPH Model

Smoothed particle hydrodynamics (SPH) is a ‘mesh-free’ particle method based on Lagrangian formulation. It has been widely applied to different areas in engineering topics (Johnson et al., 1996; 1998; Lavoie et al., 2008; Delsart et al., 2011). In SPH model, the behavior of the model is

represented by a series of particles, which possess material properties and interact with each other within the range controlled by a weight/smoothing function.

Delsart et al. (2011) addresses the development and validation of a numerical methodology to model the impacts of ice (see Figure 2-25). A preliminary experimental analysis, including ice material dynamic characteristics and impact tests on rigid and deformable targets were performed.

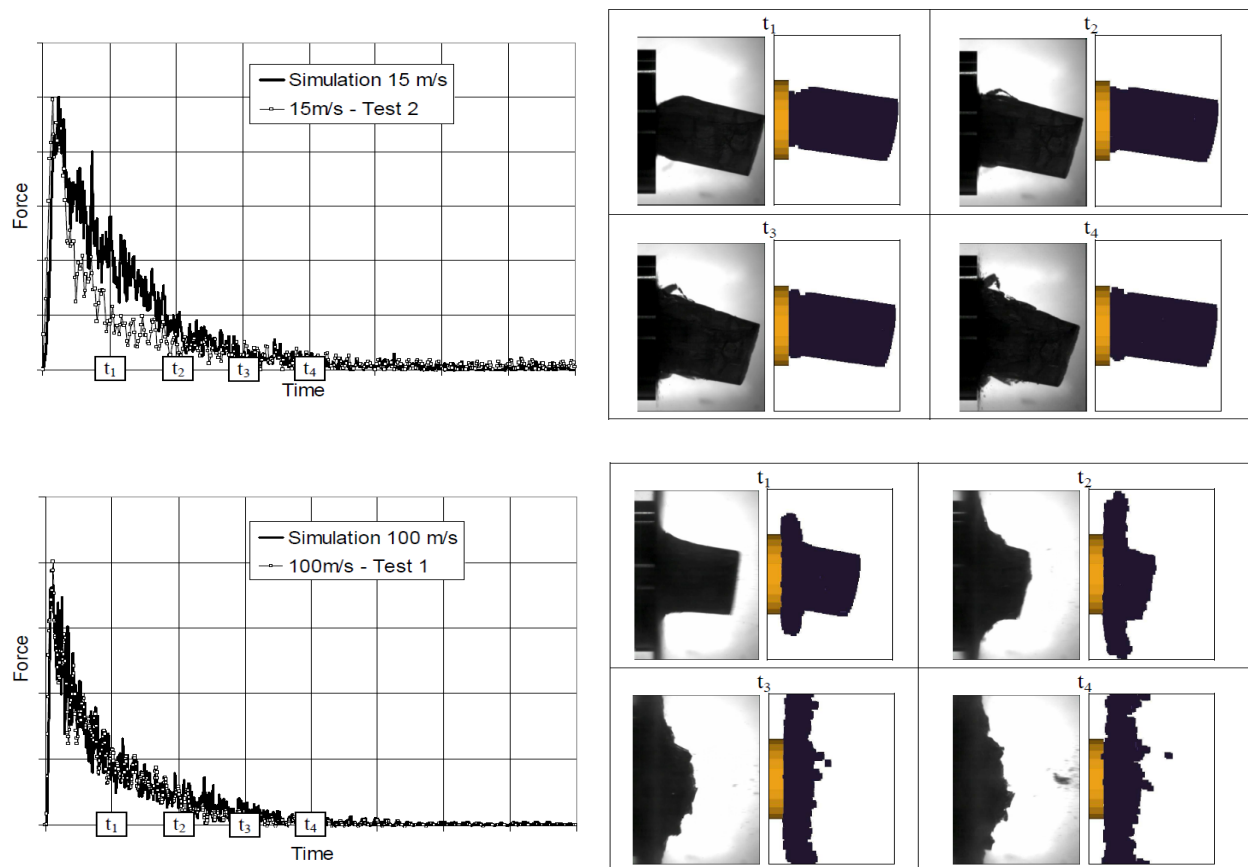


Figure 2-25: Experimental/numerical comparison of the impacts on rigid target – hemispherical projectiles at 15m/s (top) and 100m/s (bottom) (after Delsart et al., 2011)

Lavoie et al. (2008) demonstrated the accuracy of the method for ‘bird impact’ on rigid target. Validation test was performed using 1kg gelatin bird substitute material impacting against rigid thick steel plate at 95m/s velocity. Figure 2-26 shows the comparison results of snap shots and trend (a projectile of crushed section) of experimental and numerical simulation using SPH model. Both numerical and experimental are very similar.

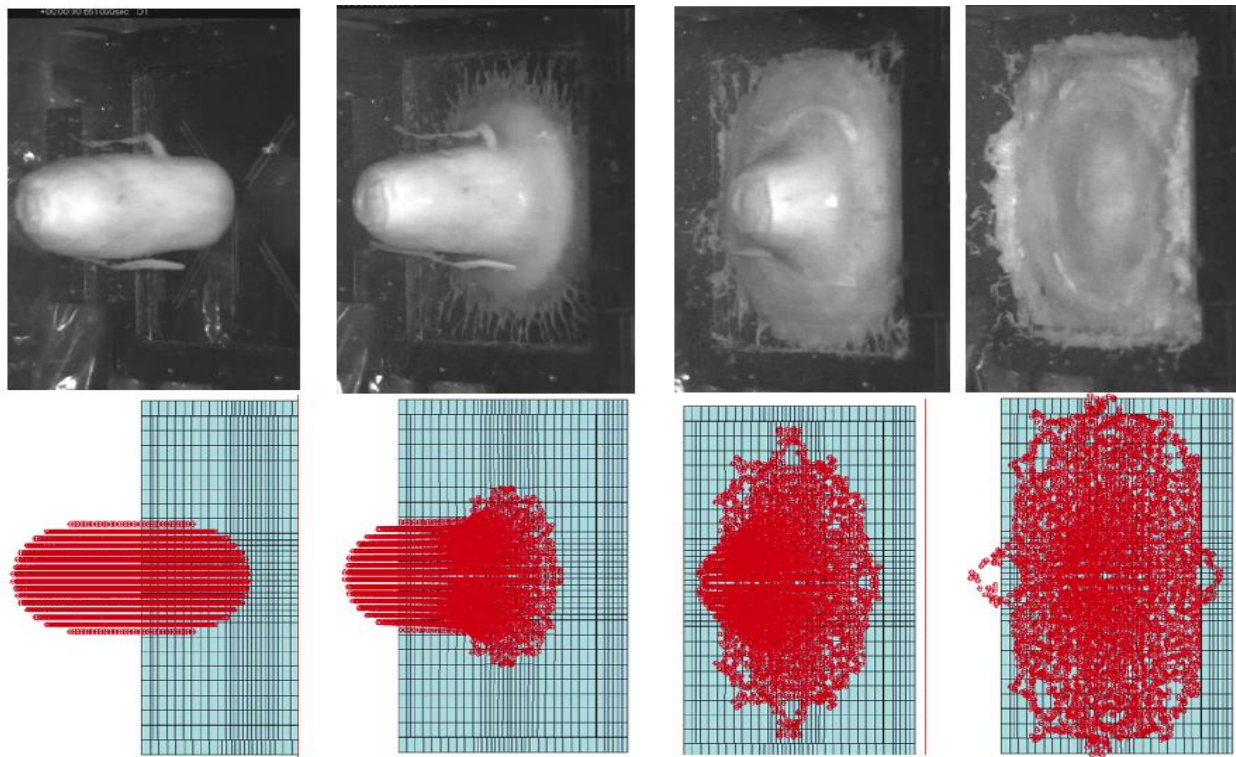


Figure 2-26: Impact at 0° at time intervals of 0.66 m/s, video and SPH (after Lavoie et al., 2008)

2.7.2. CEM Model

Konuk et al. (2009) developed a cohesive finite element (CEM) model of a pile and level ice interaction. In this model, ice floe is assumed to be either of a rectangular infinite strip or an infinite half plane (see figure 2-27). In both cases, the ice floe is assumed to have sufficient momentum to continue its linear movement at its ambient speed throughout the simulated ice-structure interaction process. This study emphasized the importance of fracture failures and rubble formations in simulating the ice-structure interaction processes.

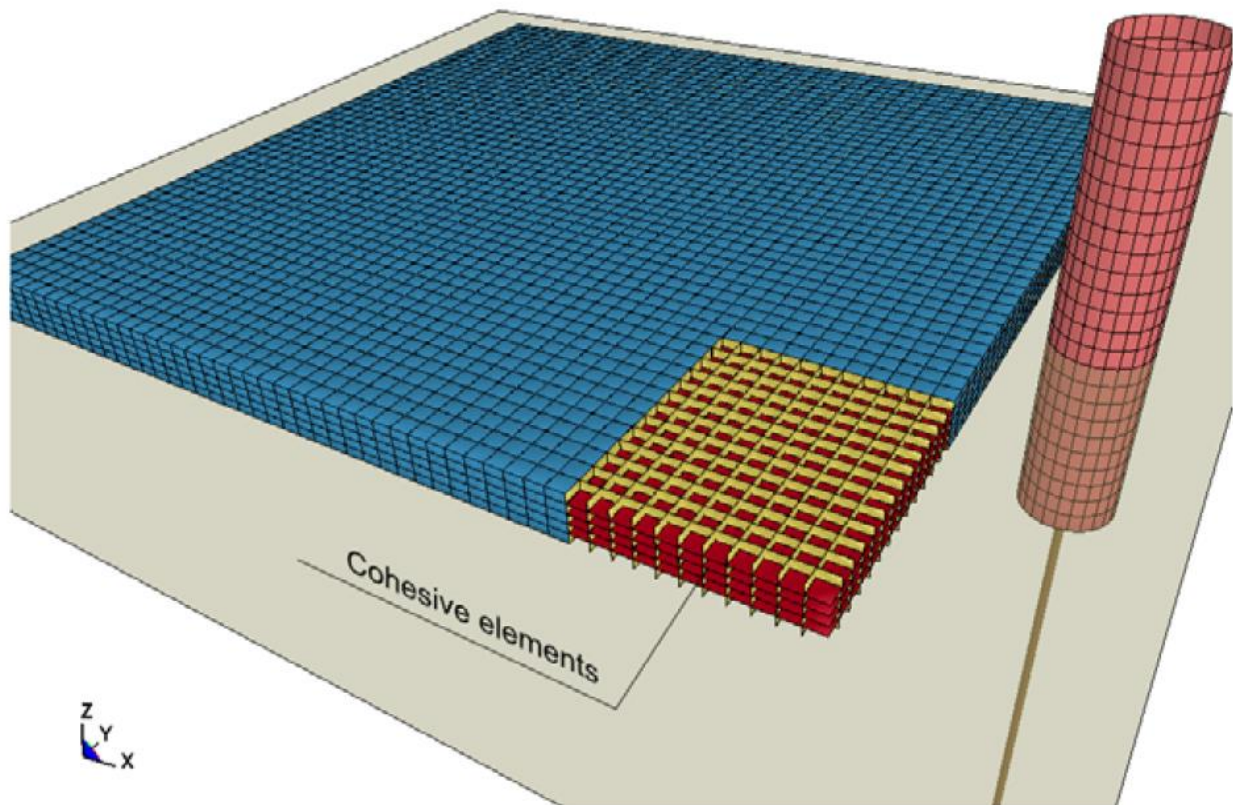


Figure 2-27: FE model of cylindrical structure and ice floe interaction (after Konuk et al. 2009)

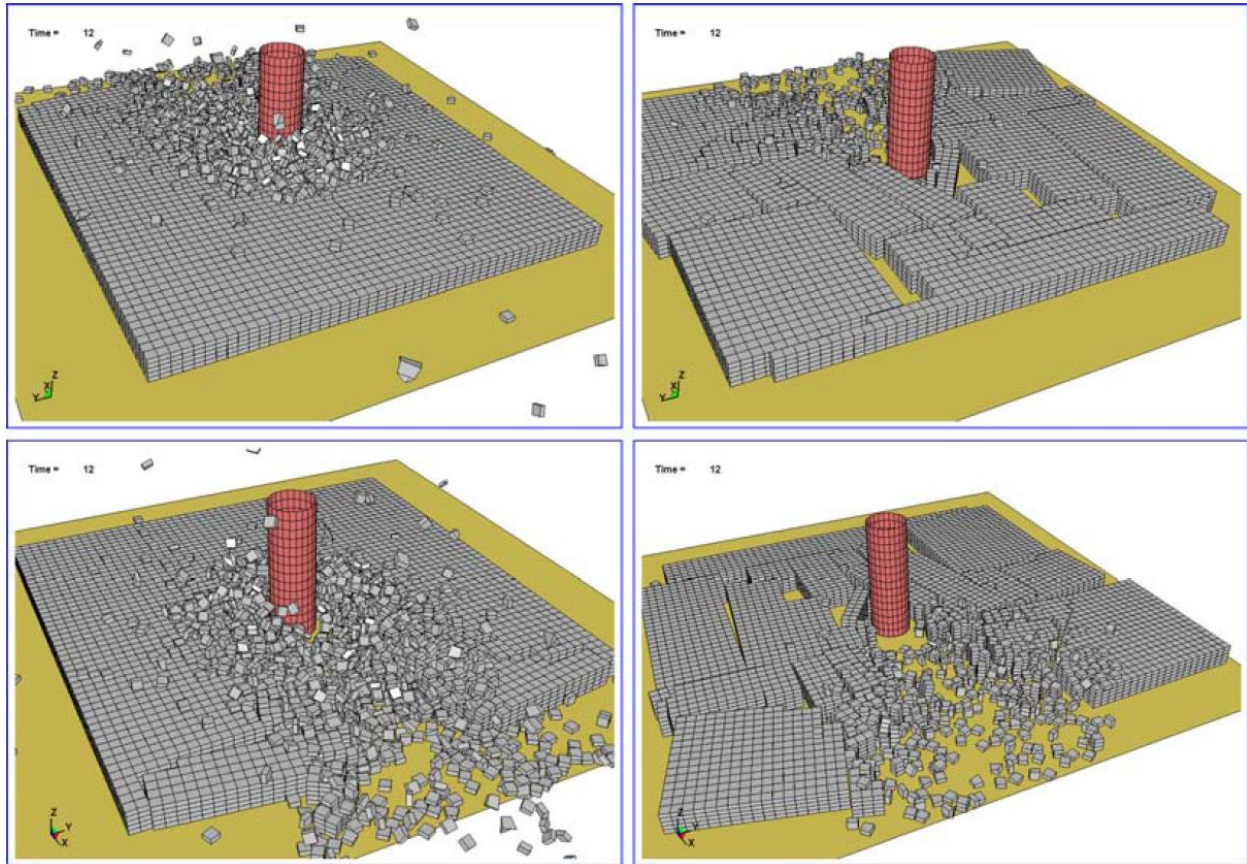


Figure 2-28: Cohesive element model results for infinite (left) and finite (right) ice floe cases
(after Konuk et al. 2009)

Hilding et al. (2011) performed a numerical simulation where the ice piles up in front of a lighthouse beneath the ice sheet using a cohesive element method with homogenization (CEMH), as shown in figure 2-29. The simulation results were compared with Norstromsgrund (in the Gulf of Bothnia) field test data. Comparison between experimental data and numerical analysis was similar quantitatively and qualitatively. In addition, numerical simulation demonstrated the feasibility of full-scale simulations of continuous crushing fracture mode of ice sheets against offshore structures.

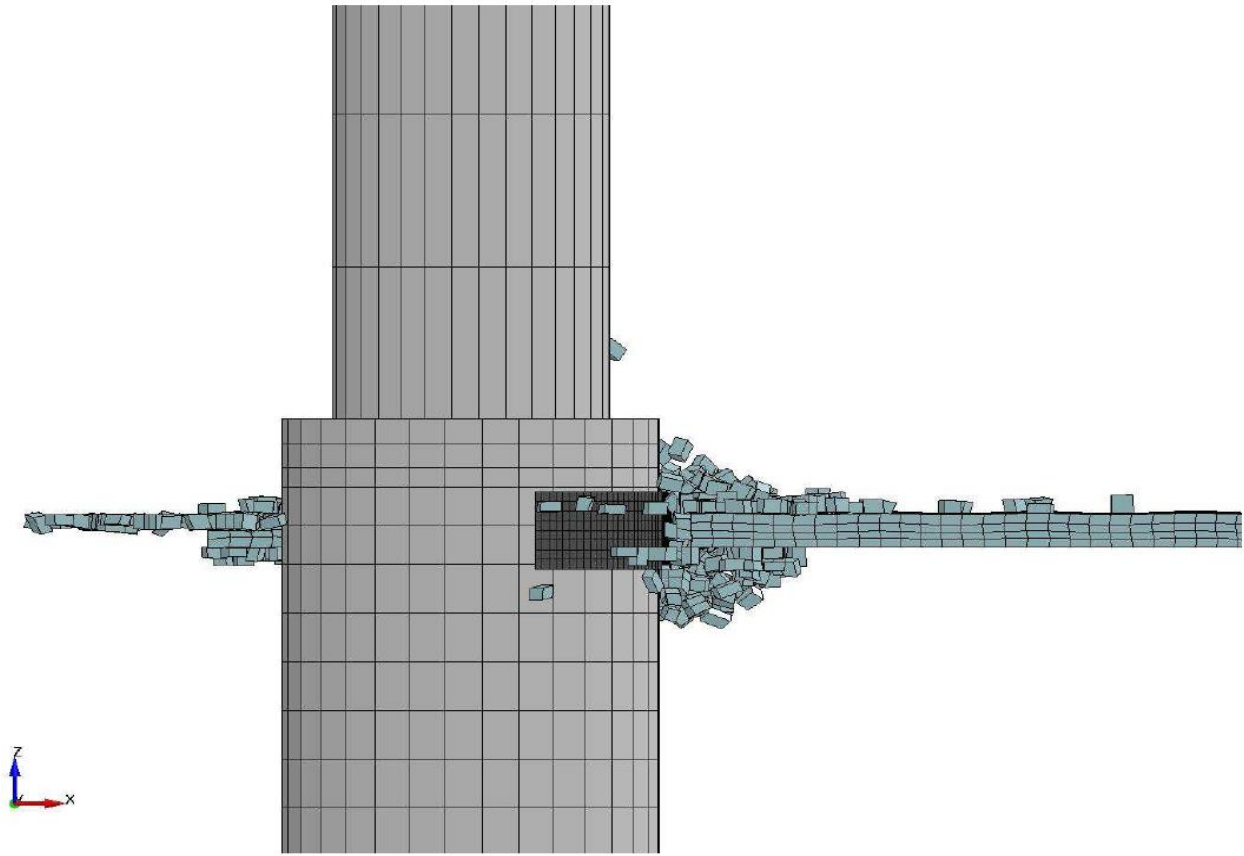


Figure 2-29: Typical situation in front of lighthouse in the simulation (after Hilding et al. 2011)

2.7.3. Crushable Foam Model

Ice material properties, which included a volumetric strain-stress relationship, of a crushable foam model (MAT 63) were calibrated by Gagnon (2006; 2007; 2012; 2011) through the bergy-bit field experimental data. For the numerical simulation, LS-DYNA[®] was chosen, and crushable foam was applied as an ice material. The deformation is mostly non-recoverable when the load is removed, hence the designation crushable foam. The behavior of the model using crushable foam is dominated by the volumetric strain-stress relationship. Dependency of the volumetric strain-stress relationships means that defining a proper volumetric strain-stress relationship is the most

important aspect in numerical simulation using crushable foam. Figure 2-30 shows a suggested and calibrated ‘volumetric strain-stress’ relationship.

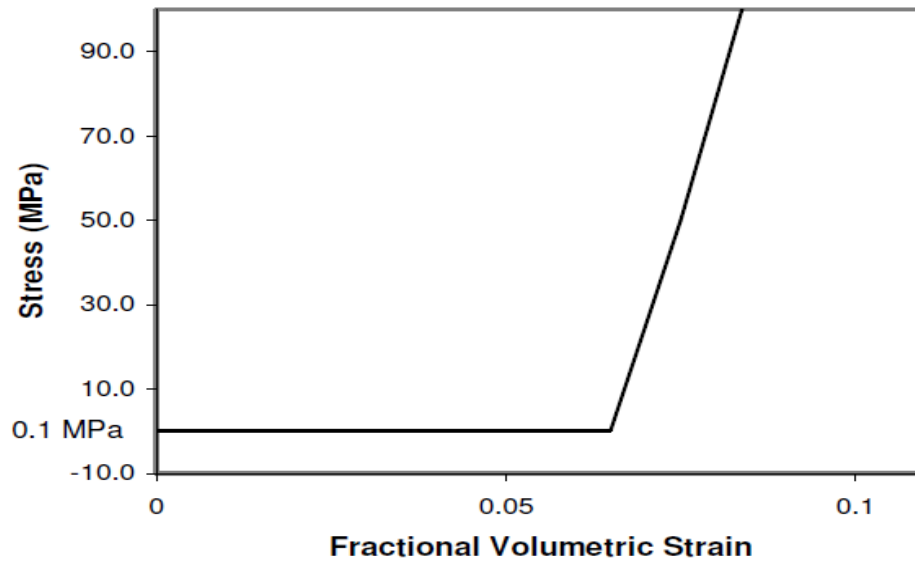


Figure 2-30: Volumetric strain-stress relationship (after Gagnon, 2006)

It is required to incorporate of a spalling behavior that leads to the frequently observed sawtooth load pattern in ice crushing and indentation test. Gagnon (2010; 2011) applied an updated methodology to simulate a sawtooth pattern, which is generally observed in the majority of the experimental performance, in respect of force-time history. The finite element model was composed layer by layer, and different material properties were assigned to each layer to create a ‘forced’ sawtooth pattern during simulation, as shown in Figures 2-31 and 2-32.

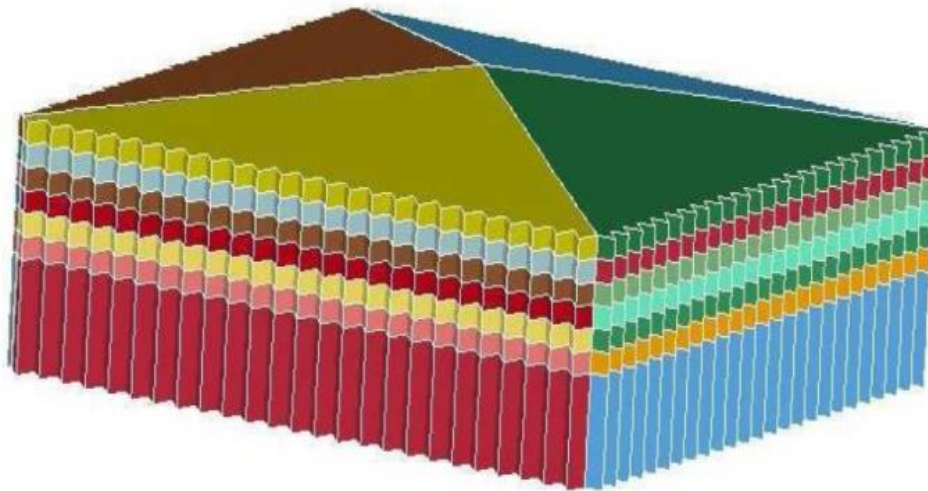


Figure 2-31: View of the numerical model (after Gagnon, 2010)

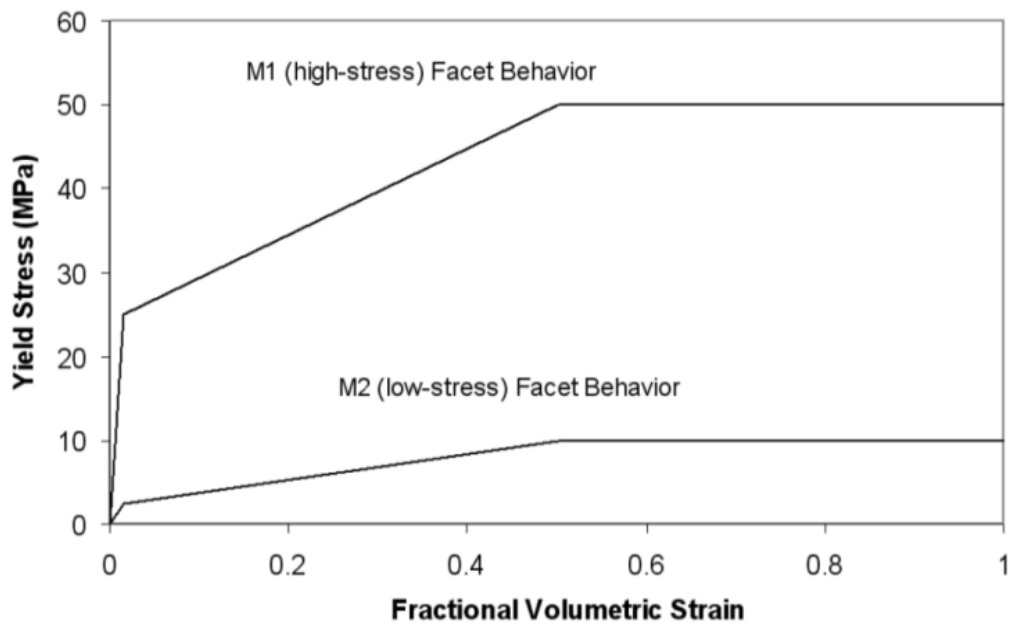


Figure 2-32: Volumetric strain stress curves for the M1 (high-stress) and M2 (low-stress) crushable foam (after Gagnon, 2010)

The updated model produces cyclic sawtooth load events and pressure distributions that are characteristic of observed ice behavior (see Figure 2-33). Due to the complexity of the problem and the variety of impact scenarios, it is desirable to have a more reliable numerical simulation model. The updated model introduced many stacked triangular facets to create a load pattern intentionally and demonstrated high and low pressure zone within the contact region, as shown in Figure 2-34.

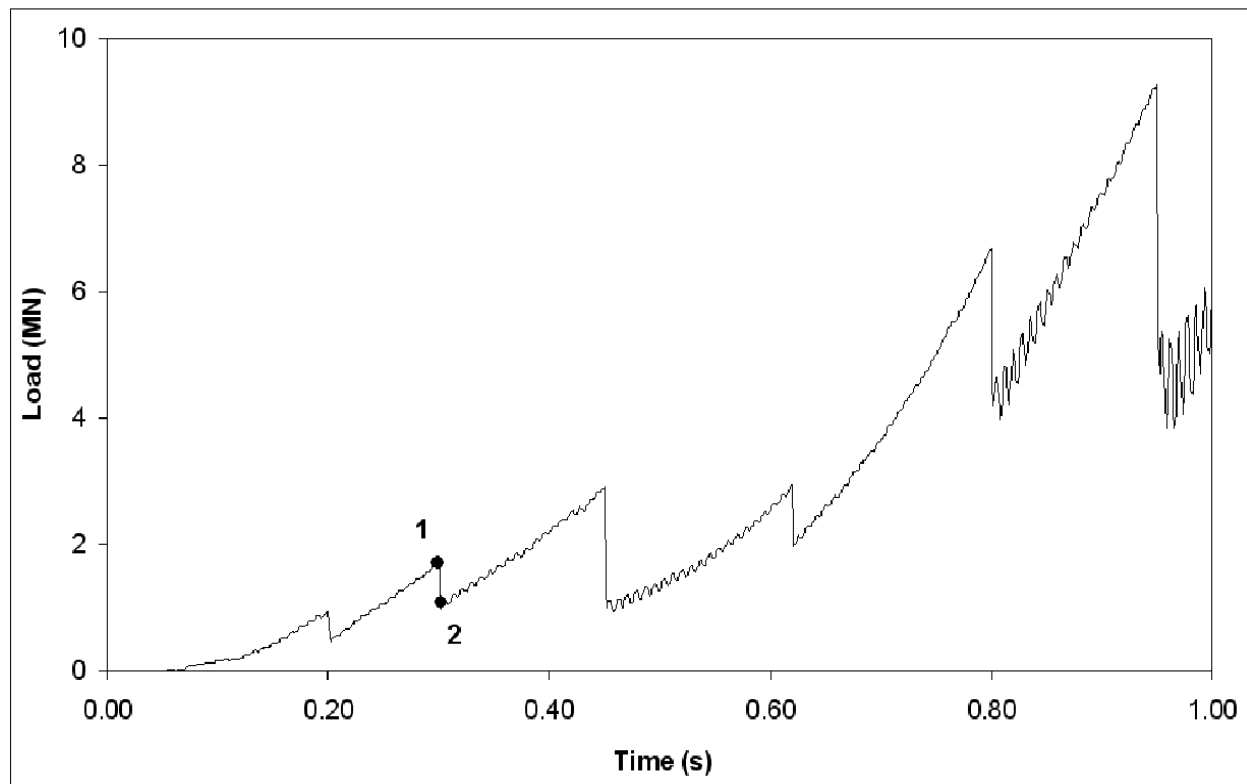


Figure 2-33: Load time series for the IceCrush simulation (after Gagnon, 2010)

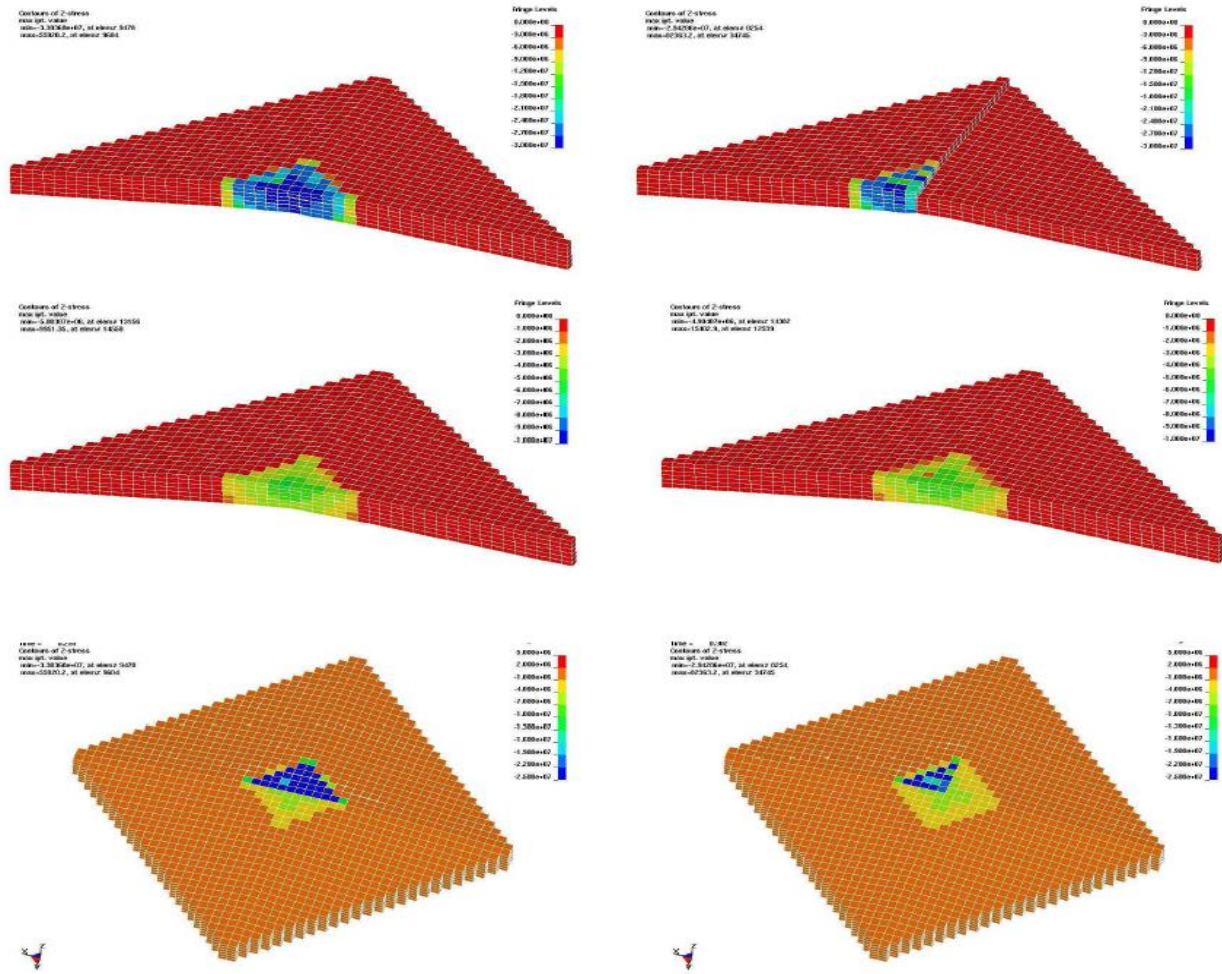


Figure 2-34: Two sets of images, set No. 1 (left) and set No. 2 (right), depicting what happens during one of the spalling events in the IceCrush simulation (after Gagnon, 2010)

Zong (2012) adopted different types of ice model by changing the material property using LS-DYNA[®]. As a result, the most appropriate ice model was proposed, which represented the best fit for ‘process’ pressure-area curves suggested by IACS Unified Requirements. The crushable foam and elastic-plastic model was tested during the simulation, and a modified crushable foam model was chosen. Restriction of Zong’s model is that it was only targeted for the Polar Class 3 as he described. Therefore, a general use of Zong’s model is highly restricted for various applications.

2.7.4. Others

Carney et al. (2006) conducted a numerical simulation between the space shuttle and ice block in circumstances of high strain-rate impact. A numerical model with failure criteria was developed to match experimental ballistic tests for high-velocity impact of ice. They used a simple isotropic elastic-plastic material model with a failure criteria and showed good agreement between simulation and experiments on the deformed shape of the projectile as well as time histories of the calculated and measured impact force, as shown in Figures 2-35 and 2-36.

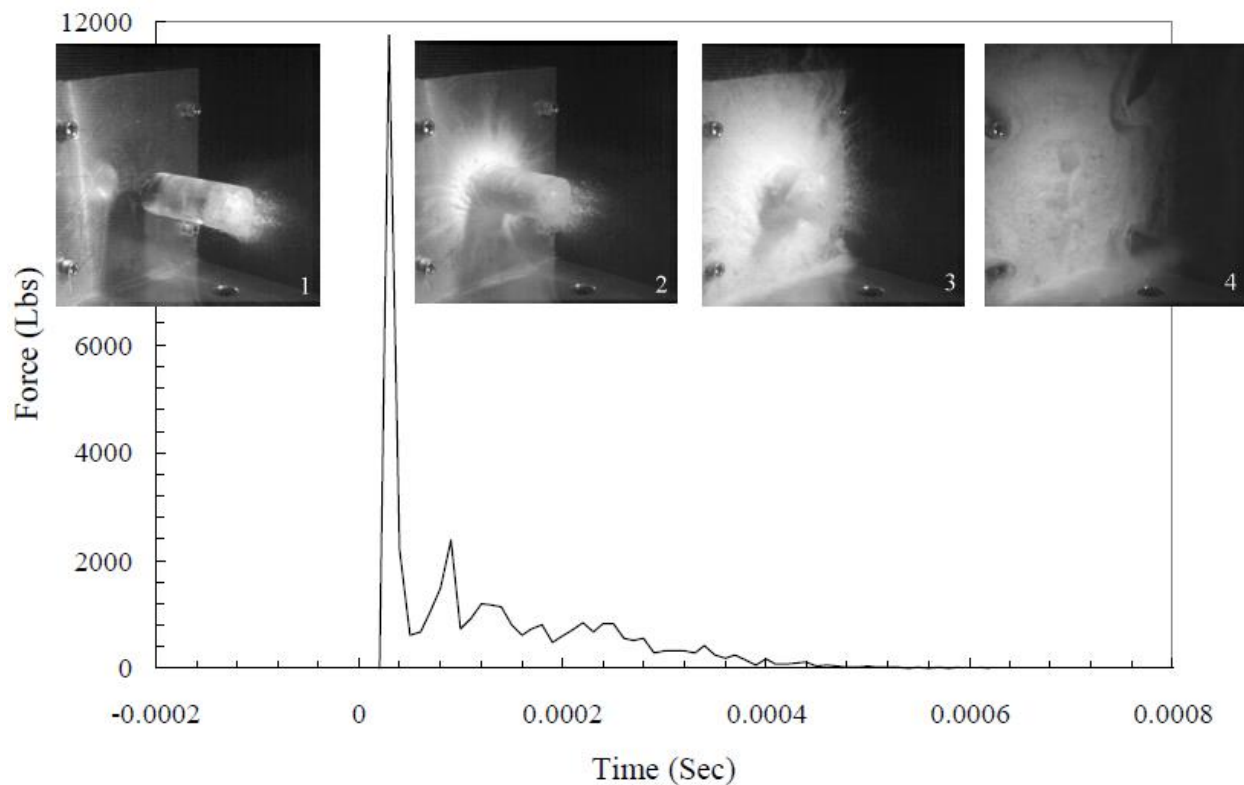


Figure 2-35: Computed contact force at 500ft/sec, with high speed images of a ballistic test
(after Carney et al., 2006)

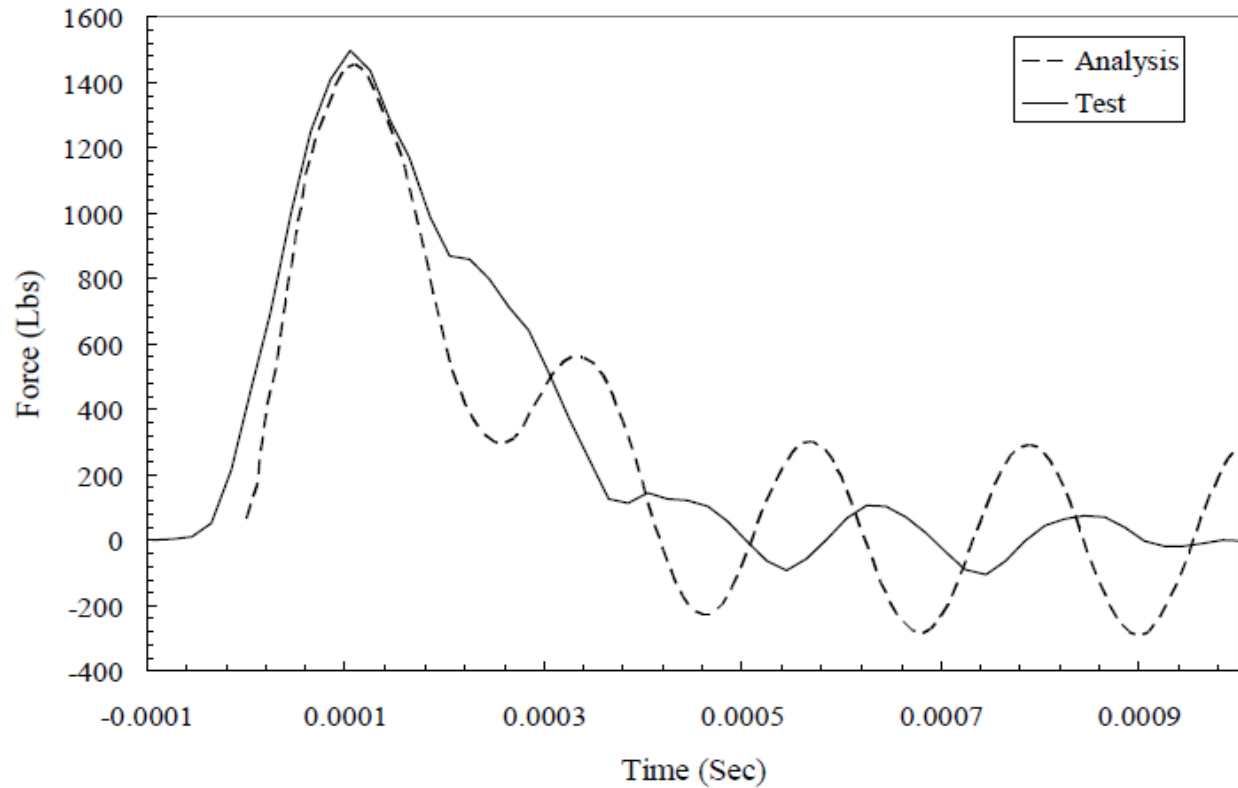


Figure 2-36: Test analysis comparison at 500ft/s, normal orientation (after Carney et al., 2006)

Dorival et al. (2008) examined a lattice model to simulate ice-structure interaction. The behavior of ice is modeled by a two-dimensional lattice model, in which inhomogeneity with the possible failure of ice incorporated. The simulation presented a lattice model for the investigation of interaction forces between an ice sheet and rigid structure. According to the numerical results shown in Figures 2-37 and 2-38, such a lattice model seems to be able to capture the main interaction scenarios involved in ice sheet cracking. Results are promising, but so far they are not sufficient for incorporating the complete ice-structure interaction process, due to the complexity of ice material.

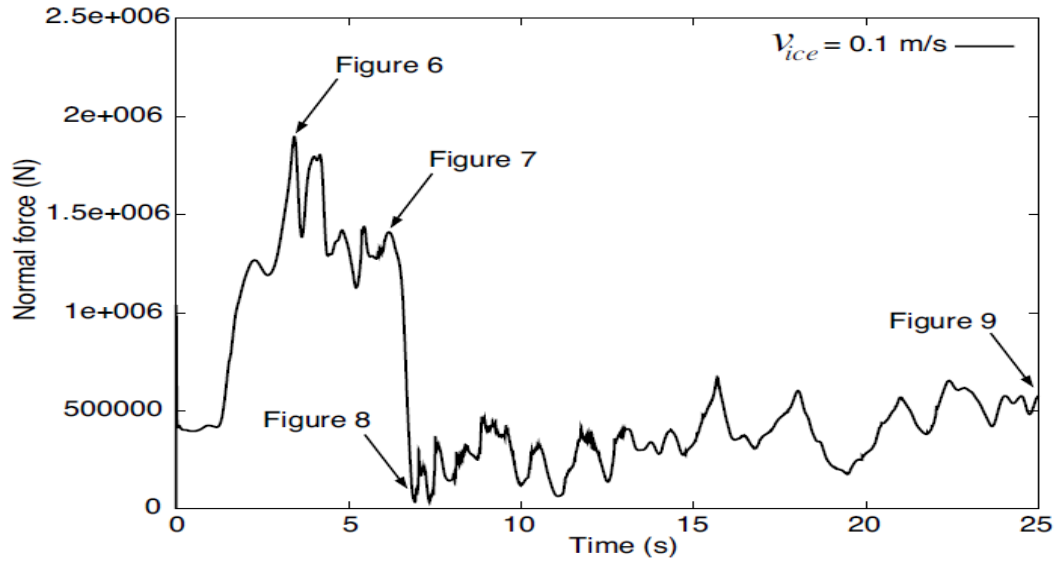


Figure 2-37: Contact force during the crushing at speed $v_{ice}=0.1 \text{ m/s}$ (after Dorival et al., 2008)

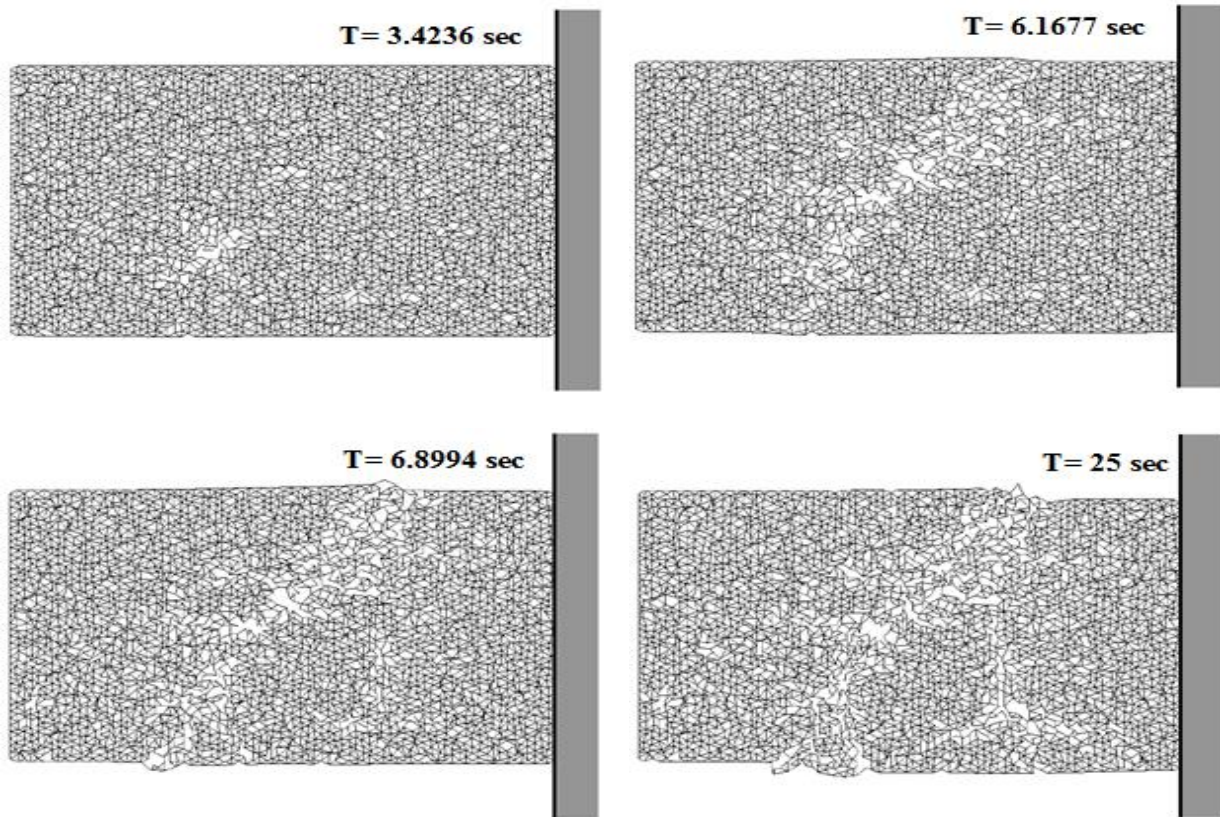


Figure 2-38: Ice sheet damaged after crushing against the structure at speed $v_{ice} = 0.1 \text{ m/s}$ at time $t=3.4236\text{s}/6.1677\text{s}/6.8994\text{s}/25\text{s}$ (after Dorival et al., 2008)

Chapter 3 Development of Methods for Investigation of Local Ice Loads Using Pressure Measurement Film

3.1. Overview

The pressure-area curve is the most common method to represent ice pressure data. There are two distinct types of pressure-area curves, which are named as a ‘Process’ pressure-area and ‘Spatial’ pressure-area curve (Frederking, 1999).

The process pressure-area curve describes the changes of average pressure across a nominal contact area and is determined from externally measured loads. In a typical example of a laboratory-scale ice crushing test, an ice specimen with a specific geometry which means that a nominal contact area is known, interacts against a known-shape surface. The ice loads are measured using some form of sensor. Typically, only the nominal contact area can be determined. From this data, the process pressure-area curve can be plotted. The process pressure-area curve describes how average pressure relates to a nominal contact area and is used to calculate the total collision loads in structures.

In contrast, the spatial pressure-area curve describes the changes of randomly distributed pressures within the contact area at a specific instant. A crushing event therefore, contains one process pressure-area curve and an infinite number (limited by measurement equipment) of spatial pressure-area curves. Daley (2007) suggested a connection between the two, with the terminus points of each spatial curve lying along the process curve. The spatial curve is useful for determining design loads on local structures, such as plating and framing.

However, determining the actual contact area at a given instant in time is not a simple task given the limitations of existing equipment because ice spalling events occur during an extremely short time. Studies have been done with varying levels of success using electronic devices (Frederking, 2004) or pressure panels (Gagnon, 2008). However, limited resolution, restricted rates of data acquisition and difficulty of calibration inhibit the usability of such techniques. Furthermore, a real time contact area and pressure distribution during an ice impact event change rapidly, thus it is requiring a high-resolution and high rate-of-data-acquisition system.

Chemical pressure measurement film (PMF) is a potentially attractive option. The films have micron-scale resolution and leave pressure patterns that remain upon completion of an impact event. High-resolution makes it possible to investigate the activated contact area and pressure distributions within the contact area at any particular time step of a collision event. Pressure distribution maps and spatial pressure-area curves are created using the pressure measurement films. Nominal process pressure-area curves are also created by the UTM data-acquisition system.

Image processing method and calibration process using pressure measurement film are discussed and described by Kim et al. (2012; 2013; 2014) and Ulan-Kvitberg (2012). In this section, a brief introduction of usage of pressure measurement film and verification of pixel size sensitivity are discussed.

3.2. Specification of Pressure Measurement Film

3.2.1. Pressure Measurement Film Specification

The Fujifilm Prescale[®] film was adopted in this study. Specifications of the pressure measurement film are shown in Table 3-1.

Table 3-1: Specification of the pressure measurement film

Physical Specifications			
Operating Temperature	5°C - 35°C (41°F - 95°F)	Spatial Resolution	5 to 15 microns
Humidity Range	20% to 90% RH	Substrate	Polyethylene Terephthalate (PET)
Accuracy	±10% visual, ±2% utilizing optional optical measurement systems		

There are seven types of the pressure measurement films; from ‘Extreme Low’ to ‘Super High’ categorized by a detectable pressure range for each film type. Prior to conducting a further study, pre-tests were performed to identify the most captured pressure ranges during an ice crushing test in a cold room to decide the suitable film types that will be used during this study. Results of preliminary tests using pressure measurement films were discussed by Ulan-Kvitberg (2012) and Kim et al., (2012; 2013; 2014). Pressure ranges between 2.5MPa to 50MPa were the most commonly detecting pressure range. Only a small portion of high pressure was captured (up to 80-100 MPa). Based on these results, three types of pressure measurement films (low, medium, and high) were adopted in this study. Table 3-2 represents the pressure ranges of each film type.

During the analysis, pressure values lower than 2.5MPa were regarded as zero-pressure due to the restriction of usage of the pressure measurement film. Ignored pressure value represents a potential source of error during the analysis process.

Table 3-2: Pressure range by film type

Film Type	Pressure Range
Low	2.5 – 10 MPa
Medium	10 – 50 MPa
High	50 – 130 MPa

There are two types of the pressure measurement films, which are the ‘Mono-sheet’ and ‘Two-sheet’ type. Structures of the pressure measurement film are illustrated in Figures 3-1 and 3-2.

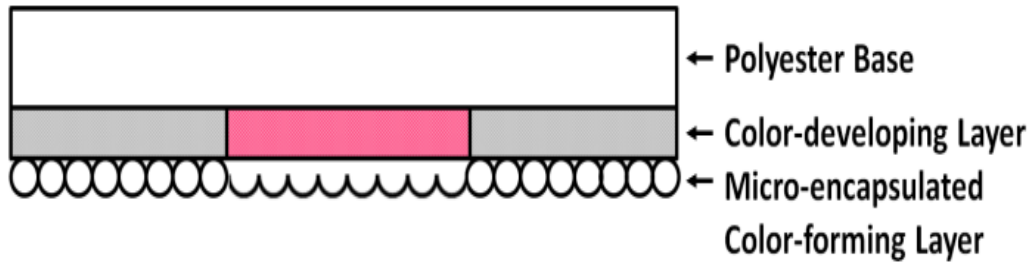


Figure 3-1: Structures of the pressure measurement film (Mono-sheet type)

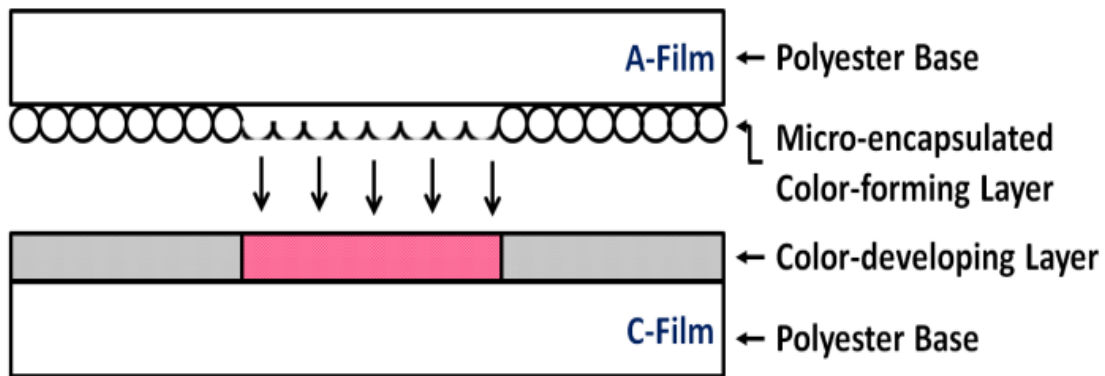


Figure 3-2: Structures of the pressure measurement film (Two-sheet type)

Mono-sheet type is composed of polyester base on which the color-developing material is coated, and the micro-encapsulated color forming material is layered on top. Two-sheet type is composed of two polyester bases. One is with a layer of the color developing material (C-Film) and the other is coated with a layer of micro-encapsulated color forming material (A-Film). When pressure is applied on the surface of the pressure measurement film, microcapsules are broken and the color forming material reacts with the color developing material (color turns as red as per the pressure applied). The microcapsules are designed to break depending on the magnitude of pressure, which means that the color density represents the specified pressure magnitude. When the color density gets darker, it indicates that a higher pressure is applied on the surface. The reaction mechanism is identical in both types of film.

3.3. Methodology of Spatial Pressure-Area Curves Plotting

There is no universal method of plotting spatial pressure-area curves. Daley (2004) plotted spatial pressure-area curves using data from the ‘Polar Sea’ field trials by starting at the highest pressure region and expanding it to include the contiguous areas to include lower pressure regions, around the starting location.

If there is only one peak pressure location within a contact area, Daley’s method is very adequate and simple for plotting spatial pressure-area curves. However, if there are several peak points as shown in Figure 3-3, it is hard to choose any specific starting location in the given spatial pressure-area curve. In addition, since the starting high pressure area cannot be expanded continuously; therefore, this method cannot be applied.

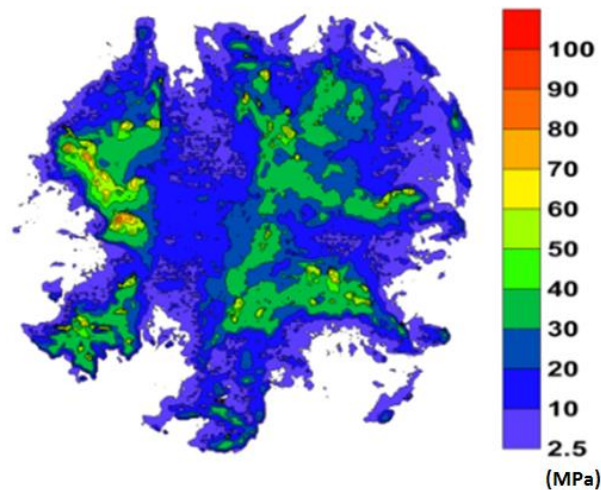


Figure 3-3: Scattering of peak pressure

In this study, two different methods for plotting spatial pressure-area curves, which are ‘Square-Averaging Method (SAM)’ and ‘Contour-Averaging Method (CAM)’, are employed. A detailed description of each method is introduced by Kim et al. (2012; 2014).

3.4. Verification of Resolution Sensitivity

Prior to analysis of the tested pressure measurement film used in subsequent studies (using the 25cm diameter ice sample), verification of the resolution (pixel size) sensitivity was performed to determine an optimal pixel size. Two main factors of plotting spatial pressure-area curves, the activated area and total force, were chosen for comparison purposes. In addition, the pressure distribution map was also chosen for further verification. For the analysis, test data of ice crushing test using the 10cm diameter ice cone were adopted. Test conditions and parameter were discussed earlier by Kim et al. (2012; 2013; 2014).

3.4.1. Activated Area Comparison

Figures 3-4 and 3-5 represent the activated area comparisons at each crushing step considering all five different resolutions (pixel size) available. The total activated area did not differ significantly according to varying resolution, except for step 3 of test 1, step 4 of test 4 in visualized figures. A more in-depth comparison of the data is presented in Table 3-3 at test step 3 of series of tests.

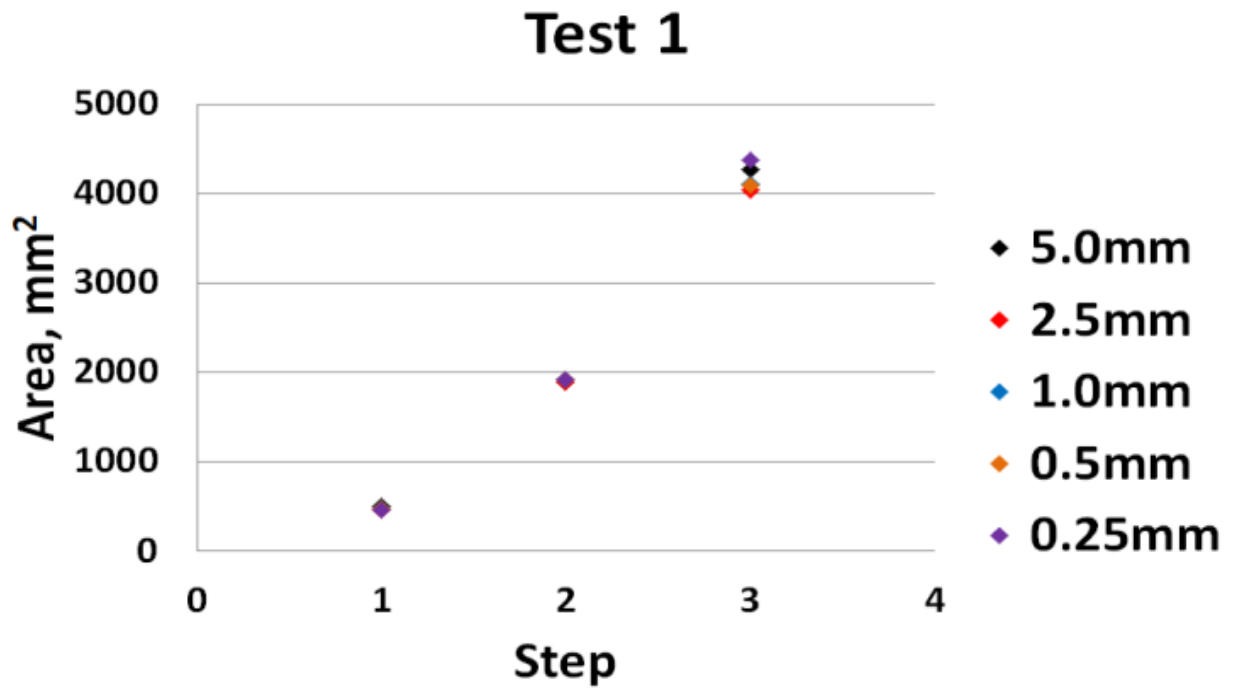


Figure 3-4: Comparison of activated area by pixel size (Test 1)

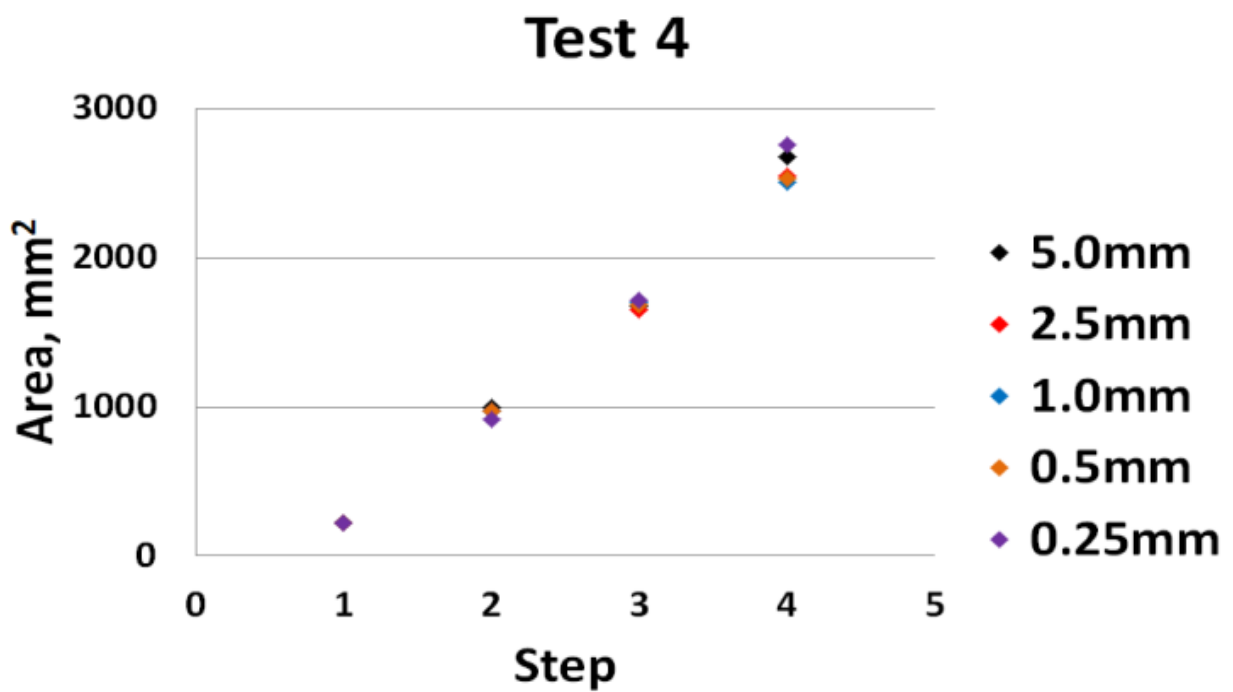


Figure 3-5: Comparison of activated area by pixel size (Test 4)

0.25 mm is chosen as the optimal resolution from this calibration study. All other resolutions are compared to 0.25mm pixel size. '+' sign indicates that obtained results were over-estimated. In contrast, '-' sign indicates under-estimation compared to the optimized resolution. The designated range is set as $\pm 5\%$ through the analysis. Pressure specified by 'bold-purple' (in Table 3-3) represent that obtained value was out of range of the selected designated range. In addition, the designated range expanded as $\pm 10\%$ and marked in 'bold-red'.

In the results given in Table 3-3, 25% of the data fall outside of the $\pm 5\%$ designated range, while none of the data fall outside of the $\pm 10\%$ designated range in step 3. Tests 1 and 7 show three pixel sizes were outside the designated $\pm 5\%$ range while the rest shows acceptable range across most of the considered resolution.

Table 3-3: Results of activated area: Step 3

Resolution (mm)	Test 1	Test 2	Test 3	Test 4	Test 5	Test 6	Test 7	Test 8
5.0	4275.0 (-2.2)	3550.0 (+0.3)	3225.0 (+1.7)	1675.0 (-2.4)	3675.0 (-4.9)	(-5.9) 3550.0	1900.0 (-0.5)	3025.0 (-2.1)
2.5	(-7.5) 4043.8	3518.8 (-0.6)	3137.5 (-1.1)	1650.0 (-3.8)	(-5.1) 3668.8	3643.8 (-3.4)	(-5.1) 1812.5	3000.0 (-2.9)
1.0	(-5.9) 4113.0	3482.0 (-1.6)	3157.0 (-0.5)	1699.0 (-1.0)	3686.0 (-4.7)	3619.0 (-4.1)	(-5.6) 1802.0	2979.0 (-3.5)
0.5	(-6.3) 4096.8	3507.3 (-0.9)	3165.0 (-0.2)	1681.8 (-2.0)	3696.8 (-4.4)	3584.5 (-5.0)	(-6.6) 1784.5	2983.5 (-3.4)
0.25	4370.1	3539.4	3172.6	1715.9	3865.9	3773.3	1909.9	3088.6

Overall, the percentage of 'out of designated range' for the $\pm 5\%$ range is decreased from 37.5% to 21.9% and 18.8% as a test step increased (see Figures 3-4 and 3-5). The sensitivity of resolution (pixel size) clearly decreased as the activated area increases. If the designated range is

expanded to $\pm 10\%$, the effect of changing pixel size quickly diminishes to zero after the middle of the ice crushing test.

3.4.2. Total Force Comparison

Figures 3-6 and 3-7 shows a comparison of the total load at each step of tests 1 and 4, at the varying resolutions. In contrast to the comparison of the activated area, the calculated total force shows high sensitivity to resolution (pixel size). Again, comparative tables for each step offer a more detailed look at the data and are shown in Tables 3-4 to 3-5.

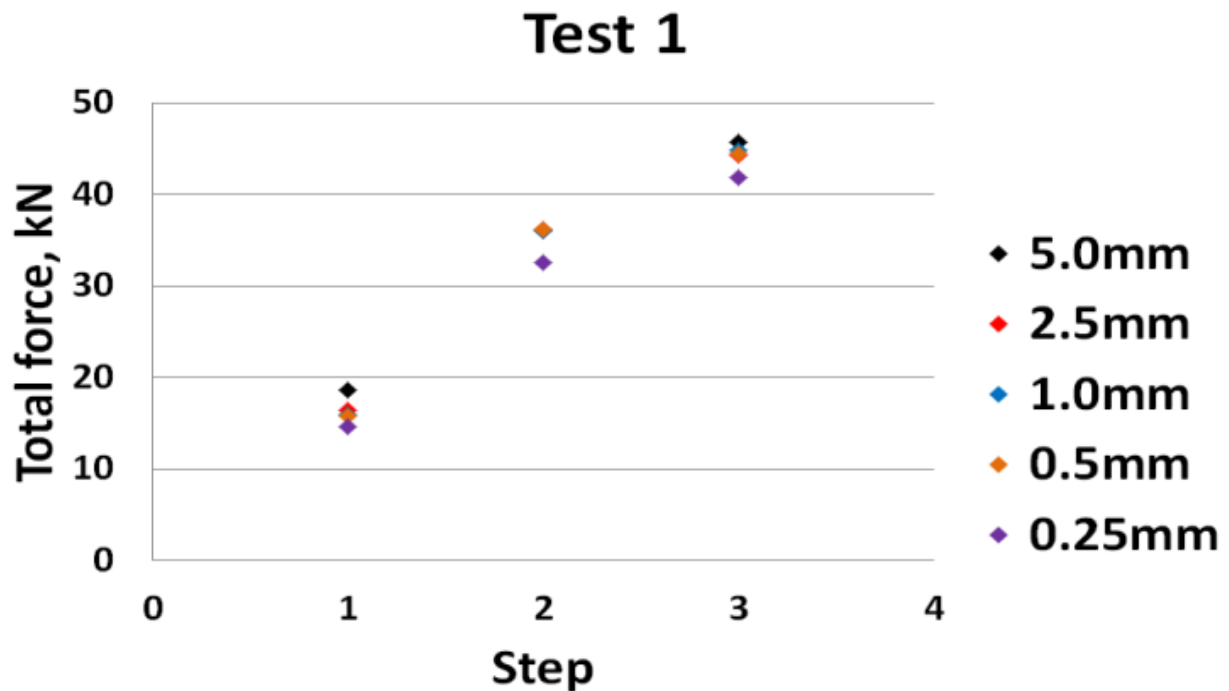


Figure 3-6: Comparison of total force by pixel size (Test 1)

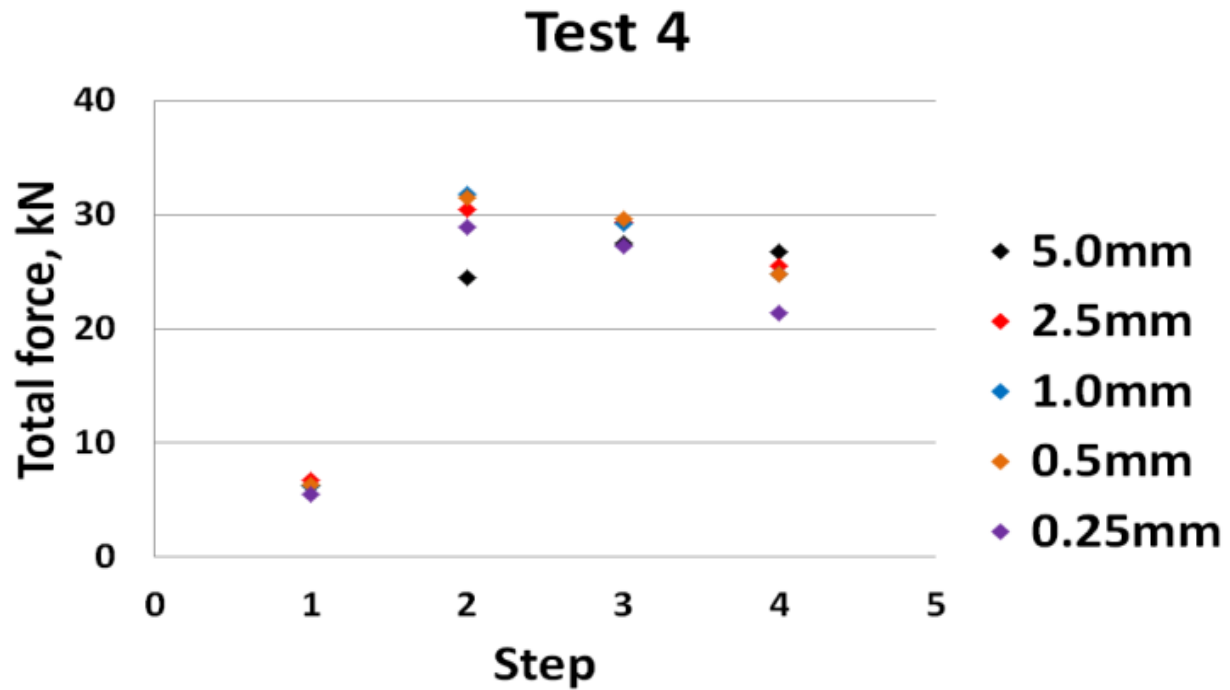


Figure 3-7: Comparison of total force by pixel size (Test 4)

As shown in Table 3-4, all of the pixel sizes for tests 1, 2, 4, 7 and 8 fall outside the $\pm 5\%$ designated range. Expanding to $\pm 10\%$ designated range still leaves test 4 and 8 outside of the range. Only test 3 falls within the designated range of $\pm 5\%$ of all resolutions. Approximately, 78.1% of the results fall outside of the $\pm 5\%$ range and 43.8% fall outside of the $\pm 10\%$ range. Clearly, the calculated total load using the pressure measurement film is more sensitive to the pixel size than the activated area.

Table 3-4: Results of total force: Step 1

Resolution (mm)	Test 1	Test 2	Test 3	Test 4	Test 5	Test 6	Test 7	Test 8
5.0	18.62 (+27.8)	16.19 (+8.8)	7.66 (+3.1)	6.19 (+12.3)	4.81 (+3.0)	13.61 (-0.1)	6.21 (+11.0)	7.06 (+20.7)
2.5	16.41 (+12.6)	16.00 (+7.5)	7.30 (-1.8)	6.78 (+23.0)	4.95 (+5.9)	13.91 (+2.0)	6.33 (+13.0)	7.02 (+19.8)
1.0	15.94 (+9.4)	16.15 (+8.5)	7.49 (+0.7)	6.28 (+13.9)	5.11 (+9.4)	14.98 (+9.9)	5.99 (+7.0)	7.26 (+24.0)
0.5	15.85 (+8.8)	16.07 (+8.0)	7.37 (-0.8)	6.35 (+15.2)	5.05 (+8.0)	15.01 (+10.1)	6.23 (+11.4)	7.24 (+23.7)
0.25	14.57	14.89	7.43	5.51	4.67	13.63	5.60	5.85

No significant improvements of the resolution sensitivity in the case of the calculated total load were made in step 4 (shown in Table 3-5). 75.0% of the results fall outside the $\pm 5\%$ designed range, while 37.5% fall outside the $\pm 10\%$ range. Clearly, the calculated total load from the pressure measurement film was, in contrast to the activated area, highly sensitive to the chosen analyzed resolution.

Table 3-5: Results of total force: Step 4

Pixel size (mm)	Test 3	Test 4	Test 5	Test 7
5.0	68.46 (+4.2)	26.75 (+25.1)	67.79 (+6.3)	57.33 (+13.0)
2.5	66.15 (+0.7)	25.53 (+19.3)	67.37 (+5.7)	56.73 (+11.8)
1.0	65.61 (-0.1)	24.82 (+16.1)	67.04 (+5.1)	54.27 (+7.0)
0.5	65.58 (-0.2)	24.84 (+16.1)	67.06 (+5.2)	54.11 (+6.7)
0.25	65.70	21.39	63.76	50.73

3.4.3. Pressure Distribution Comparison

Figure 3-8 shows the pressure distributions of test 1 from steps 1 to 3. Figure 3-8 (a) shows the original low-range pressure film scans for each step. Figure 3-8 (b) to (f) shows the pressure distribution for changing pixel size for each step. As it is expected, reducing pixel size increases fineness of the image and clarity of details. 5.0 mm pixel size does not give an adequate representation of the pressure pattern. 2.5 mm pixel size shows a significant improvement and the overall shape of the pressure pattern because distinguishable; however, the finer details are still not present. Clearly, improving the resolution improves the image, however, at a cost to computational efficiency. Figures 3-8 and 3-9 (and Figures in Appendix C.3) indicate that 1.0 mm pixel size gives sufficient information of the detailed pressure patterns.

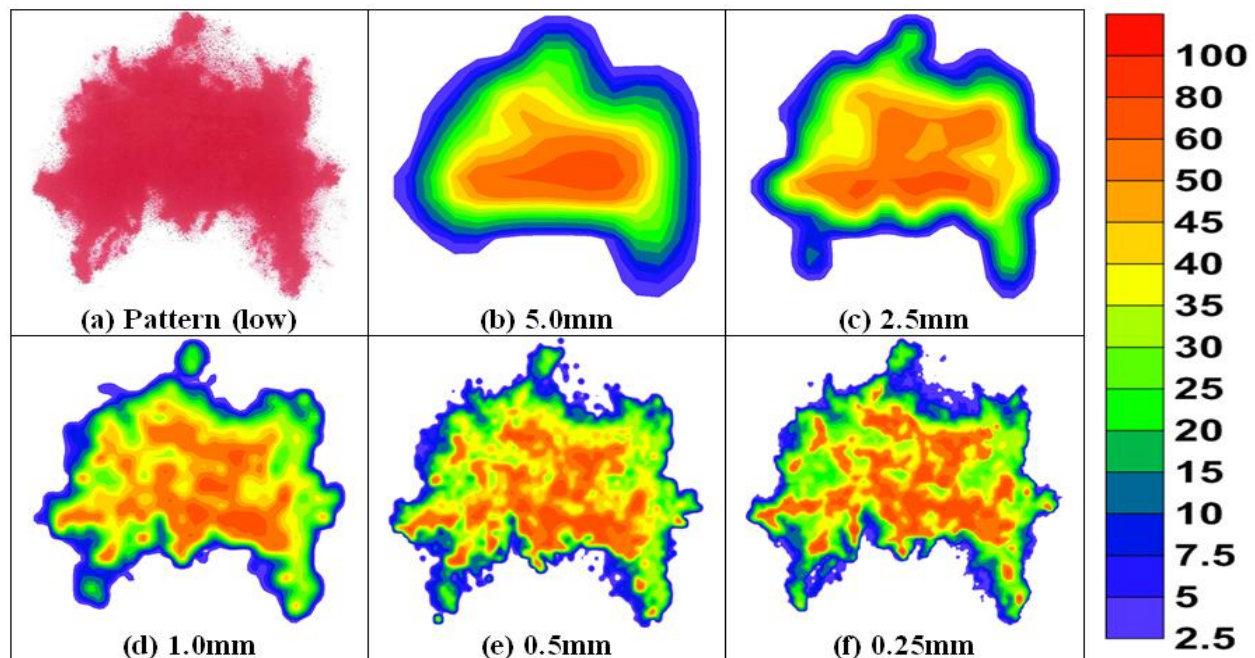


Figure 3-8: Pressure distribution of Test 1-Step 1

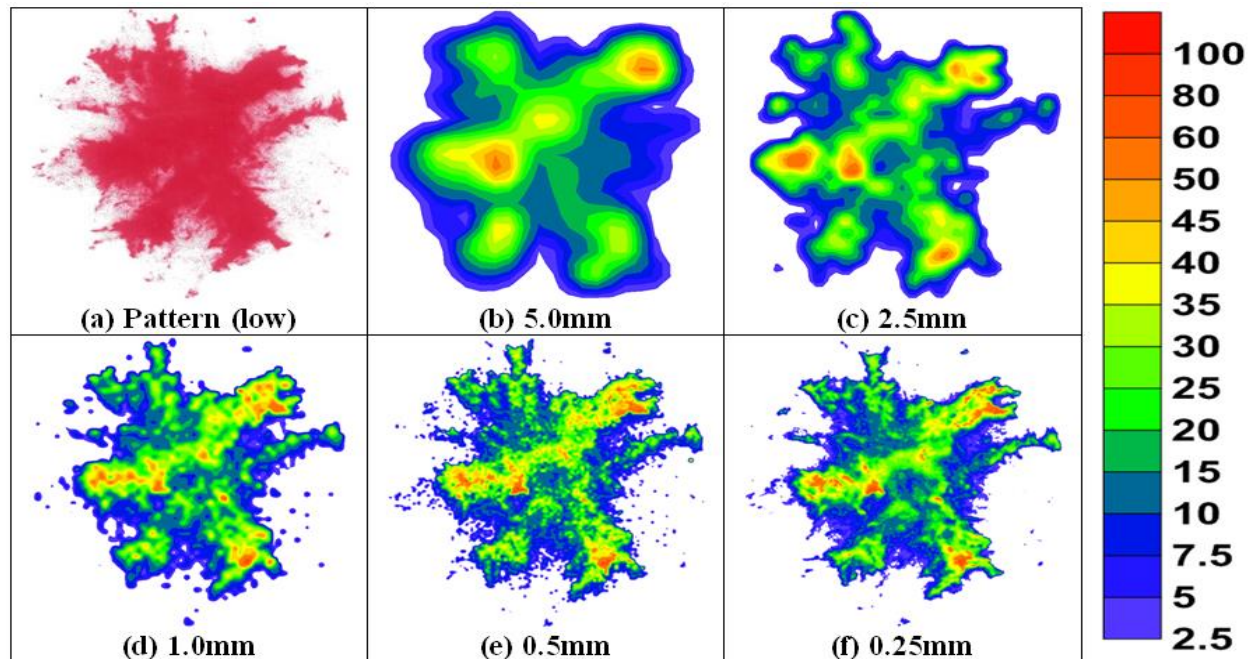


Figure 3-9: Pressure distribution of Test 1-Step 2

3.4.4. Result of Resolution Sensitivity

According to pixel size analysis results, the activated area was not sensitive using coarse pixel size (as mentioned above). In contrast, it was confirmed that the total force and the plot of the pressure distribution map were highly sensitive to the resolution of the analysis to obtain a reasonable result.

Therefore, analysis of further experiments using pressure measurement film will be applied to pixel size of 0.25mm, which is practically the smallest pixel size for the data analysis in this study.

3.5. Source of Error

The greatest advantages of using pressure measurement film are that the pressure distribution and contact area at the interface between two objects can be measured without the help of complicated measuring equipment in laboratory-scale tests.

However, using the pressure measurement film also has the following problems.

1) In order to measure the range of all possible pressures during the experiment, a variety of film types should be used. It is evident that the calibration for each film type requires a significant amount of time and effort. In addition, the number of increased data size after experiments, that need to be processed, is also a matter of concern.

2) Three different kinds of film type were applied in this study, and the lowest measurable pressure range was the value of 2.5MPa. In other words, even the pressure value below 2.5MPa can be captured during experiment; all the pressure values equal or less than 2.5MPa were considered as 'zero' due to the lack of the proper film type. Accordingly, such a loss of data can affect analysis results cannot be overlooked. Therefore, one needs to determine the effects of these practical data losses through the application of various film types in future studies.

3) Due to the nature of the pressure measurement film, all the contacts, which occurred before the replacement of film will be remained (obtained data might include overlapped pressure

pattern/ice pressure) on the surface of the film. Accumulation of pattern is also one of the disadvantages that need to be considered.

The advantage of using electronic equipment is the possibility of measuring of the contact area and pressure changes in a real time. On the other hand, the pressure measurement film should be replaced continuously in order to obtain a smooth pressure pattern or contact area. The concept of regarding this issue, accumulation of the contact area and load/pressure, was well described by Kim et al. (2012; 2014) as ‘Active vs. Activated’ area.

However, there are obvious limitations of unlimited use of pressure measurement film, according to the time issues (replacement of pressure measurement film too occasionally will interrupt a continuous test process) and financial issues (pressure measurement film is a one-time use, so that requires ongoing purchase).

4) Accumulation of the contact area and the load/pressure at a particular moment means that the analyzed results are likely to be exaggerated.

According to the experimental results published earlier by Kim et al. (2012), the contact area was uniform in case of low strain-rate experiments. Therefore, the source of error by using pressure measurement film was not significant in these studies. However, in case of high strain-rate experiments, it had a great effect due to the frequent spalling events (or flaking) and these indicated contact area in pressure measurement film to be relatively larger compared to the actual

contact area observed by visual inspection. In this case, the measured load also tended to be higher than the actual load applied at a particular instant.

5) Overall, it is difficult to state that using the pressure measurement film is completely novel and proved method to replace the earlier complex electronic measurement equipment because of the issues discussed above. However, it is an obvious advantage that gives the possibility of evaluating the contact area and load/pressure in a simple manner, instead of using complex instrumentation. Thus, there is a need to be aware of the facts that are mentioned above, while evaluating the experimental results obtained in this study by the pressure measurement film in this study.

Chapter 4 Ice Crushing Pressure on Non-Planar Concave Surfaces: Experiments

4.1. Overview

Ice-strengthened ships can encounter 'overload' conditions (rather than design load conditions) while navigating the Arctic region during their regular operational period. In this case, ship structures may be subjected to ice loads that exceeds the initial design loads. As a result, ship structures can be stressed beyond an elastic state and experience plastic deformation that was not intended. Occurrence of plastic deformation due to unexpected overload conditions is not the part of the present design condition and the most of the existing research and test data are available only for elastic conditions. Therefore, existing test data set are not sufficient and suitable to investigate ice-structure interaction scenarios considering plastic deformation state.

In addition, determination of ice loads and deformation that occur on locations other than the ship hull has become necessary for ships navigating the Arctic. For example, broken ice pieces may pass around the ship's propulsion system and impact the structures around the podded propulsors in ice-strengthened ship. Consequently, the structure can experience larger than expected ice impact loads.

In both cases mentioned above, ice will be impacting a convex or concave shape surfaces. There is some evidence that such structural shapes may increase ice loads (pressures) by increasing the confinement of the already extruded ice during impact. The purpose of this study is to investigate ice impact loads with such concave-shaped surfaces to determine whether the structural shape of the impacting surfaces has effects on the actual ice loads and pressures. A new test apparatus was designed to examine the characteristics of ice-structure interaction on non-planar surfaces.

The actual contact areas and magnitudes of ice loads/pressures during ice-structure interaction tests on concave-shaped surfaces were examined, using the pressure measurement film. In addition, force and displacement data obtained from the universal testing machine (UTM) was also utilized to measure the ‘global’ behavior during ice-structure interaction. In addition, it was also intended to determine the effects of indenter shapes on the contact pressures and areas. The analyzed indenter shape effects will be used to estimate ice loads or pressure on the different indenter shapes in this study.

4.2. Test Condition

Table 4-1 shows test conditions used in this study. Shape/angle of test indenter, shape/angle of ice sample and test speed were considered as controlled parameter. Additionally, stepped crushing method was adopted to obtain spatial pressure-area curves, pressure distribution and activated contact area using the pressure measurement film suggested by Kim et al. (2012; 2014); Ulan-Kvitberg (2012); and Kim and Daley (2013-a; 2013-b).

Table 4-1: Test conditions

Test No.	Shape/Angle of indenter (°)		Shape/Angle of ice sample (°)		Test speed (mm/sec)	Crushing method	No. of steps
1	Wedge	10	Cone	35	1.0	Stepped	4
2	Wedge	10	Cone	35	100	Stepped	4
3	Wedge	10	Cone	25	1.0	Stepped	3
4	Wedge	10	Cone	25	100	Stepped	3
5	Wedge	30	Cylindrical	0	1.0	Stepped	5
6	Wedge	30	Cylindrical	0	100	Stepped	5
7	Wedge	30	Cylindrical	0	1.0	Straight	-
8	Wedge	30	Cylindrical	0	100	Straight	-
9	Wedge	10	Cylindrical	0	1.0	Stepped	5
10	Wedge	10	Cylindrical	0	100	Stepped	5
11	Wedge	10	Cylindrical	0	1.0	Straight	-
12	Wedge	10	Cylindrical	0	100	Straight	-
13	Wedge	10	Cone	35	1.0	Straight	-
14	Wedge	10	Cone	35	100	Straight	-
15	Wedge	10	Cone	25	1.0	Straight	-
16	Wedge	10	Cone	25	100	Straight	-
17	Wedge	20	Cone	35	1.0	Stepped	3
18	Wedge	20	Cone	35	100	Stepped	3
19	Wedge	20	Cone	35	1.0	Straight	-
20	Wedge	20	Cone	35	100	Straight	-
21	Wedge	20	Cylindrical	0	1.0	Stepped	5
22	Wedge	20	Cylindrical	0	100	Stepped	5
23	Wedge	20	Cylindrical	0	1.0	Straight	-
24	Wedge	20	Cylindrical	0	100	Straight	-
25	Conical	10	Cone	35	1.0	Straight	-
26	Conical	10	Cone	35	100	Straight	-
27	Conical	10	Cone	25	1.0	Straight	-
28	Conical	10	Cone	25	100	Straight	-
29	Conical	10	Cone	35	1.0	Straight	-
30	Flat		Cone	25	1.0	Straight	-
31	Flat		Cone	25	1.0	Straight	-
32	Flat		Cone	25	100	Straight	-
33	Flat		Cone	25	100	Straight	-
34	Flat		Cone	25	100	Straight	-
35	Flat		Cone	25	100	Straight	-
36	Flat		Cone	35	1.0	Straight	-
37	Flat		Cone	35	1.0	Straight	-
38	Flat		Cone	35	1.0	Straight	-
39	Flat		Cone	35	100	Straight	-
40	Flat		Cone	35	100	Straight	-
41	Flat		Cone	35	100	Straight	-

4.3. Test Scenario

In this study, a series of tests were conducted to evaluate the behavior of ice-structure interaction, on concave-shaped surfaces. The tests were carried out considering two types of scenarios; 1) ice indentation on rigid ‘wedge’ shaped indenters and 2) ice indentation on rigid ‘conical’ shaped indenters, which represented ice loads caused by permanent deformation.

4.3.1. Wedge Shape Indenter

In the first scenario, the study of ice-structure interaction on concave shapes, representative of locations other than the main hull, was represented by ‘wedge’ shaped indenter. In this case, the body of podded propulsor was chosen as the target structure for the wedge shape. Figure 4-1 shows an actual picture of podded propulsor, which represents the assumed interaction surface used in this study.

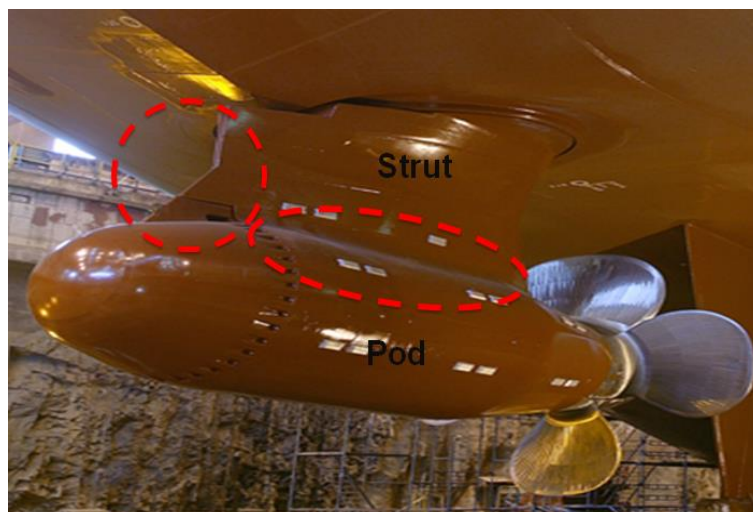


Figure 4-1: Picture of podded propulsor

Test apparatus was simplified as a wedge shape for the simplicity of the test. The wedge-shaped indenters, with two different angles (10° and 30°), shown in Figure 4-2 were designed and fabricated for this part of the study. 30° wedge-shaped indenter was modified into 20° wedge (after the tests) to extend the range of wedge angle variation. Figure 4-3 shows a detailed projection of the wedge-shaped indenters.

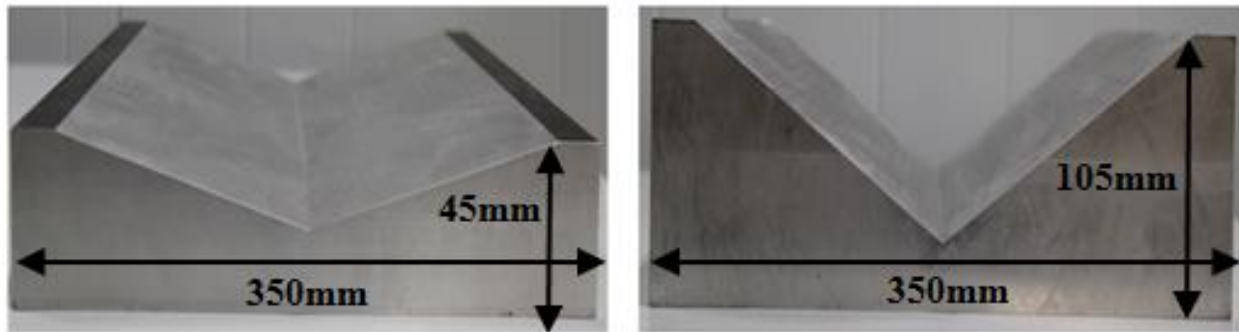


Figure 4-2: Wedge shape indenters (left: 10° wedge, right: 30° wedge)

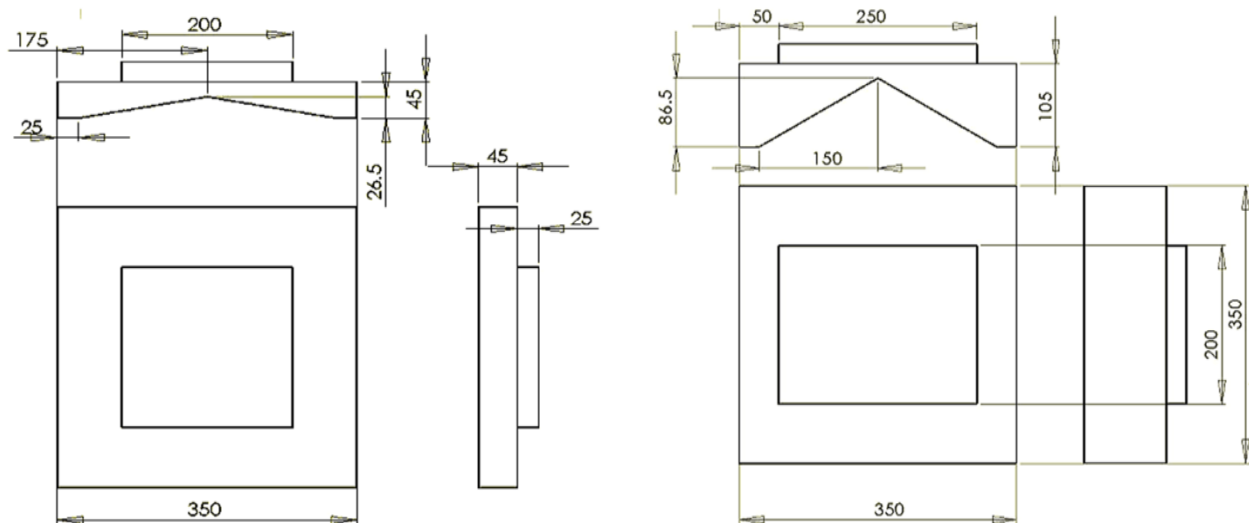


Figure 4-3: Drawing of wedge shape indenters (left: 10° wedge, right: 30° wedge)

4.3.2. Conical Shape Indenter

In the second scenarios, the study of ice-structure interaction on concave shapes, representative of deformed plating on the main hull, was modeled as ‘conical’ shaped indenter. The concave shape of the ship plating may be formed due to any unexpected overload applied on initially flat (or nearly flat) ship’s side structure, and remain as permanently deformed profile. Considering the plastic deformation in the ship structural side will possibly change the energy level during a collision, and this may cause extra ice loads on the structures (Daley and Kim, 2010). Figure 4-4 shows an example of dented structure on the hull of a ship.



Figure 4-4: Picture of dented structure

Test apparatus was simplified as conical shape for the simplicity of the experiment. The conical-shaped indenter with 10° , shown in Figure 4-5, was designed for this part of study. Figure 4-6 shows a detailed profile of a 10° conical-shaped indenter.

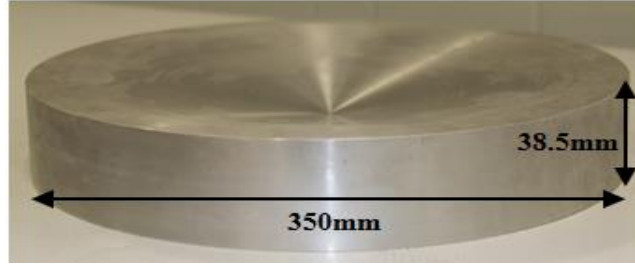


Figure 4-5: Conical shape indenter (10° conical)

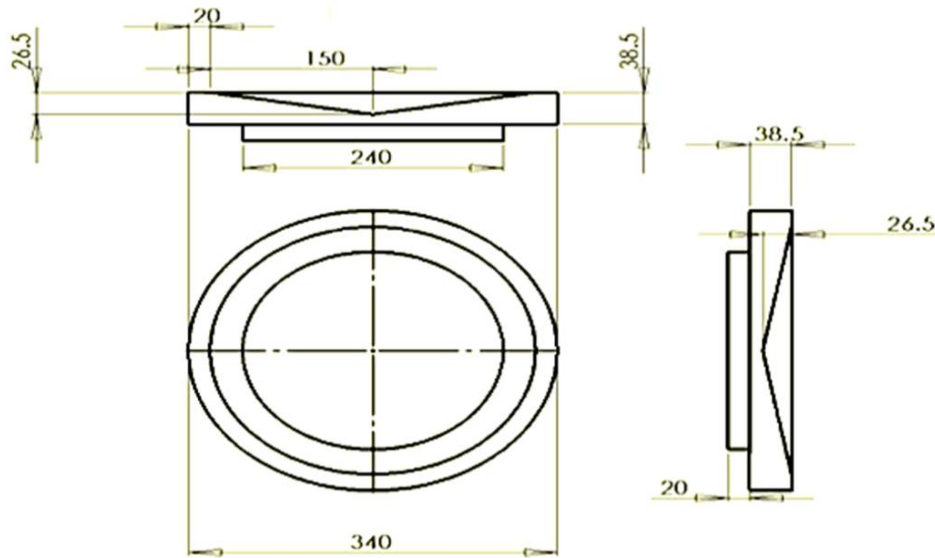


Figure 4-6: Drawing of conical-shaped indenter (10° conical)

4.4. Test Setup

The overall preparation method (see Figure 4-7) of ice sample is similar to a 10cm diameter ice sample. To increase the size of the ice sample up to 25cm diameter, ice preparation procedures were followed by utilizing the method proposed by Bruneau and Dillenburg (2012). This manufacturing method is used in STePS² project. The procedure to prepare ice sample is well

presented in this study. Normally, three days are required for the preparation of the test (two days for ice sample preparation and one day for ice shaving into a cone shape).



(a) De-aeration system



(b) Ice sample growing fridge

Figure 4-7: System of ice sample preparation

Test setup used in this study is illustrated in Figure 4-8. Wedge/conical shape indenter was attached to the top part (fixed side during the test), and ice sample (cone ice/cylindrical ice) was attached at the bottom (moving with a certain velocity control) of universal testing machine. In

addition, the pressure measurement film was attached to the face of the wedge indenter during the test. The pressure measurement films were utilized to obtain an activated contact area and pressure distribution at each step. Figure 4-9 represents a test setup used in a cold room with 10° wedge-shaped indenter.

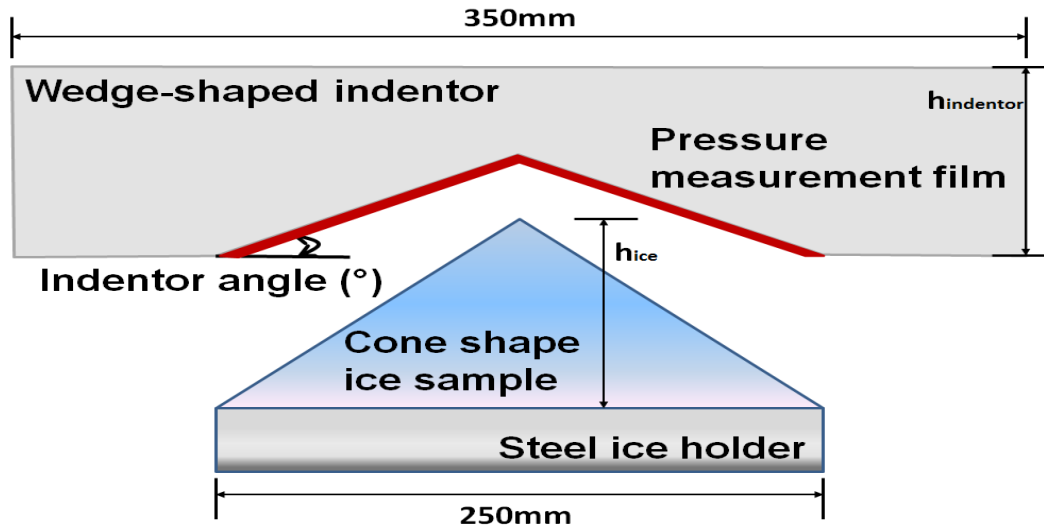
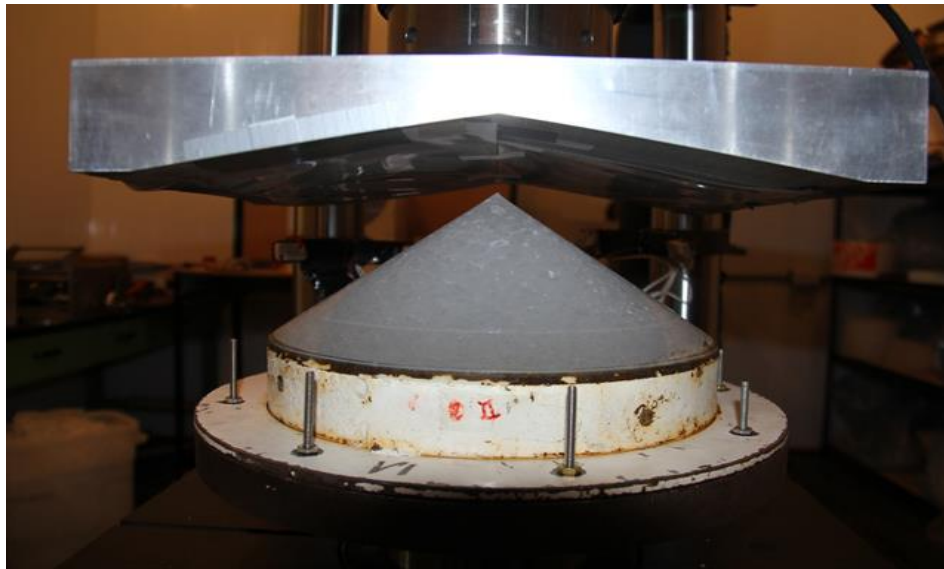
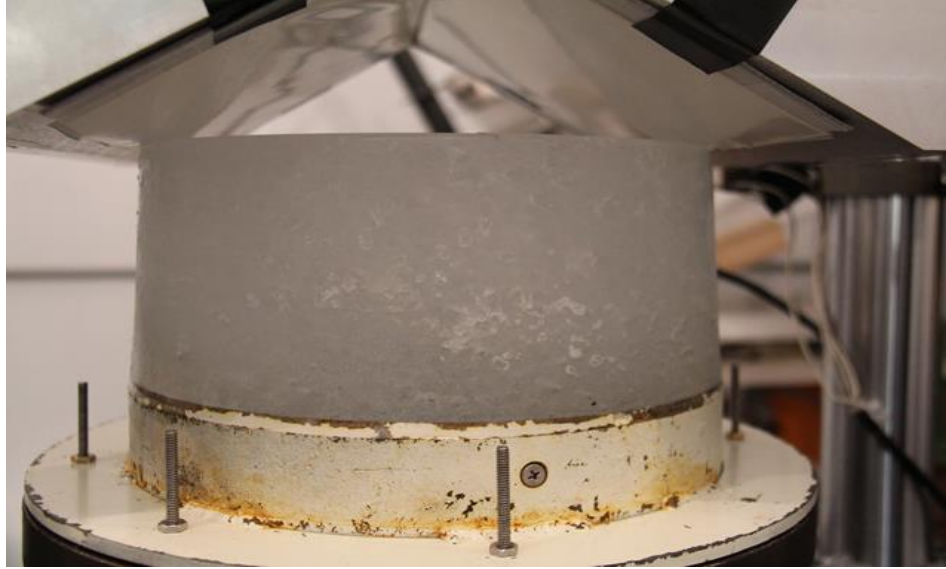


Figure 4-8: Illustration of test setup



(a) Photo of test setup (35° ice cone, 10° wedge-shaped indenter)



(b) Photo of test setup (Cylindrical ice sample, 30° wedge-shaped indenter)

Figure 4-10: Photo of test setup

4.5. Test Results

4.5.1. Definition of Contact Area

Understanding the external load, contact area and the overlapped area between the two interacting bodies, are essential to plot process pressure-area curves. The external loads can be obtained by the data-acquisition system of universal testing machine during the experiments. In addition, the contact area is easily determined through the initial geometry of the ice sample. In the case of flat indenter tests, simply the area overlapped between the ice sample and the indenter in any position during crushing is the contact area.

However, two different types of contact areas may be considered (exist) in the case of concave-shaped indenters, which are used in this study. First, a direct (overlapped) contact area between the ice sample and the concave-shaped indenter (A_{nominal}) can be considered as the contact area, which is similar to flat indenter case. Second, a projected contact surface area in normal direction (A_{project}) also can be used as a representative contact area. Concept of both contact areas are illustrated in Figure 4-10.

The contact area must be determined to plot process pressure-area curves using load data obtained through experiments. Daley (1999) defined the projected area (A_{project}) as the contact area to derive the equations followed by the energy-based method. The projected area can be applied as the contact area if considered interactions between two bodies in respect of the global viewpoint. Therefore, the projected area was used as representative contact area as the same manner in this study to plot process pressure-area curves.

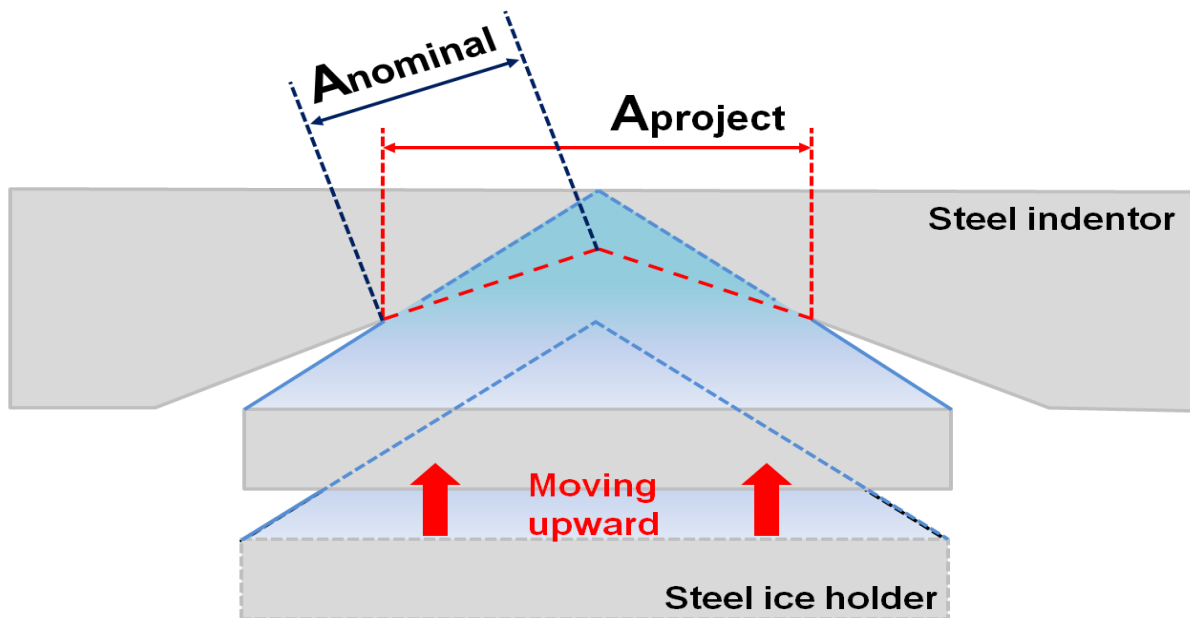
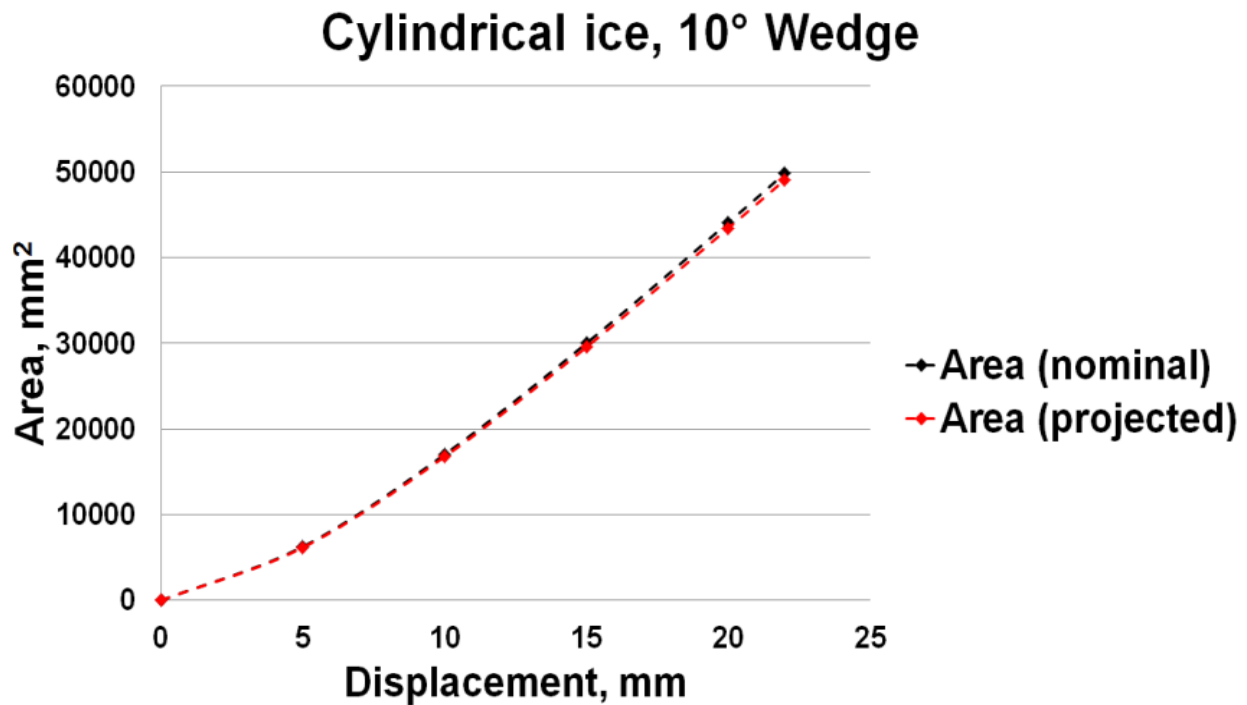


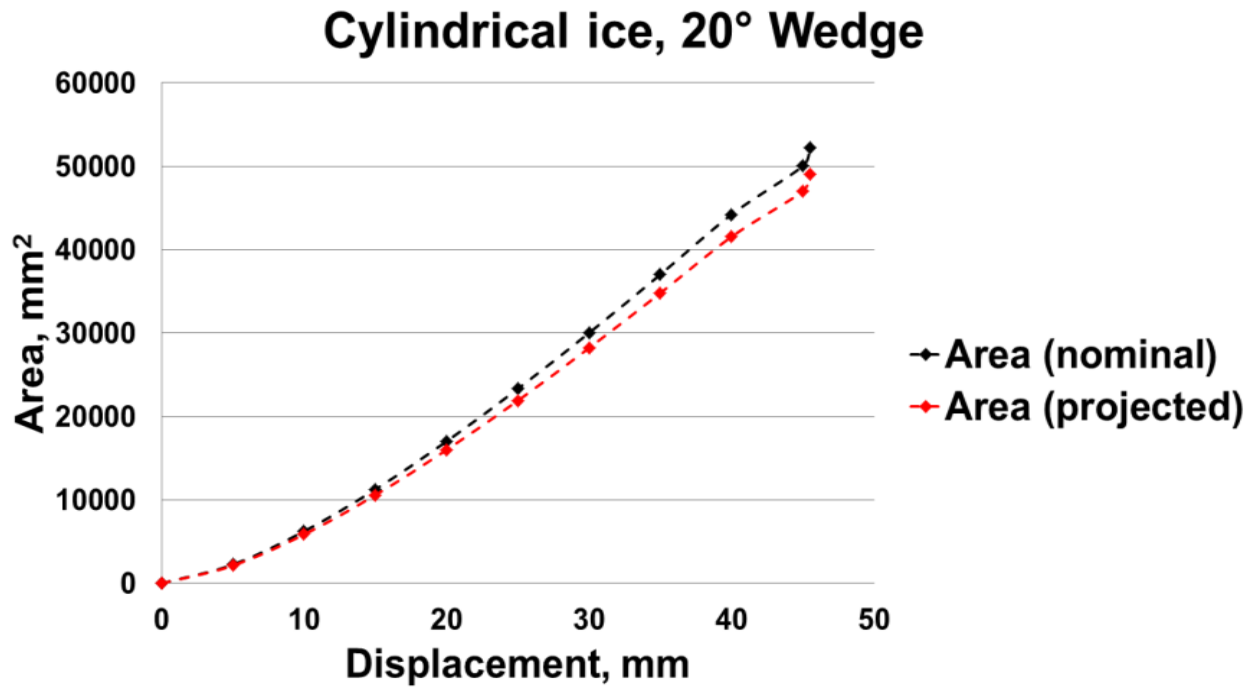
Figure 4-10: Illustration of contact area (A_{nominal} vs. A_{project})

A representative contact area was determined as projected area; however, there were practically no significant differences between the two defined contact areas. Comparison of nominal and projected contact areas between each test parameter (followed by the shape/angle of indenter and the shape/angle of the ice sample) were shown in Figure 4-11. As shown in Table 4-2, the only differences between two different defined contact areas were about 1-2% in total. In other words, the results will not be significantly affected whether selecting any contact area during an analysis.

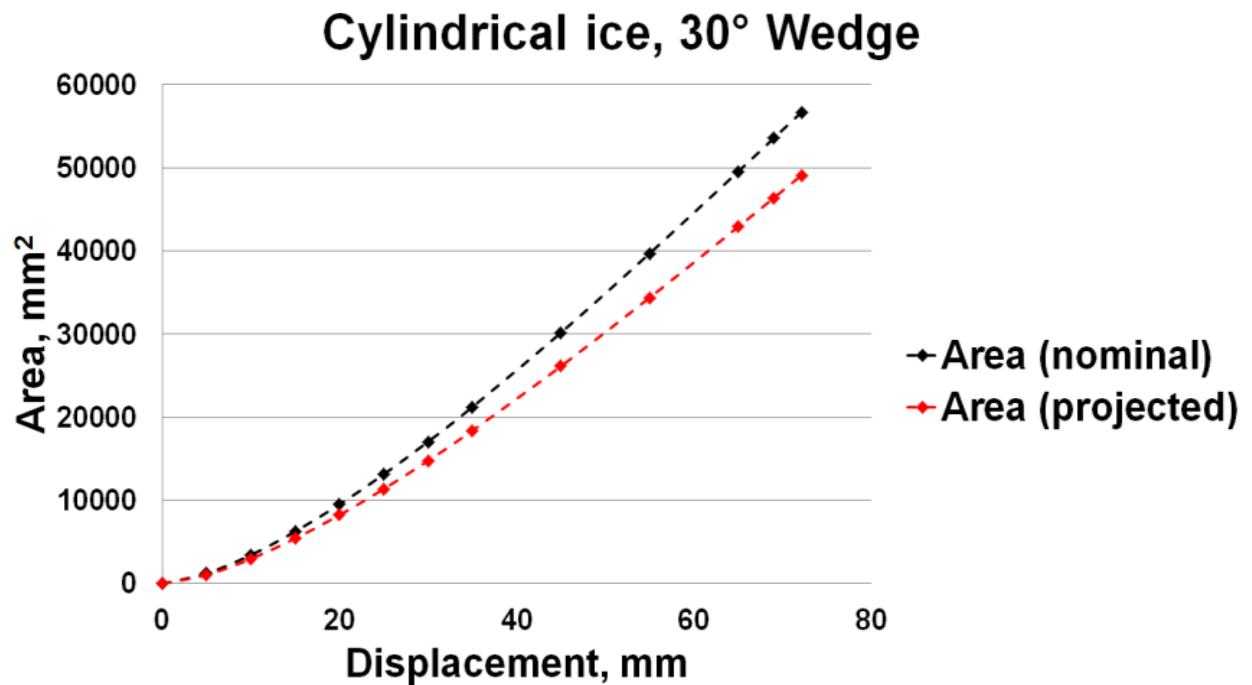
However, the case, where the test was done using a cylindrical ice sample against 30° wedge angle showed up to 15% difference between the nominal and projected area. Except for this case, the results did not show significant effect whatever contact area is used.



(a) Comparison of A_{nom} vs. A_{proj} (Cylindrical ice, 10° wedge indenter)



(b) Comparison of A_{nom} vs. A_{proj} (Cylindrical ice, 20° wedge indenter)



(c) Comparison of A_{nom} vs. A_{proj} (Cylindrical ice, 30° wedge indenter)

Figure 4-11: Comparison of nominal and projected contact area

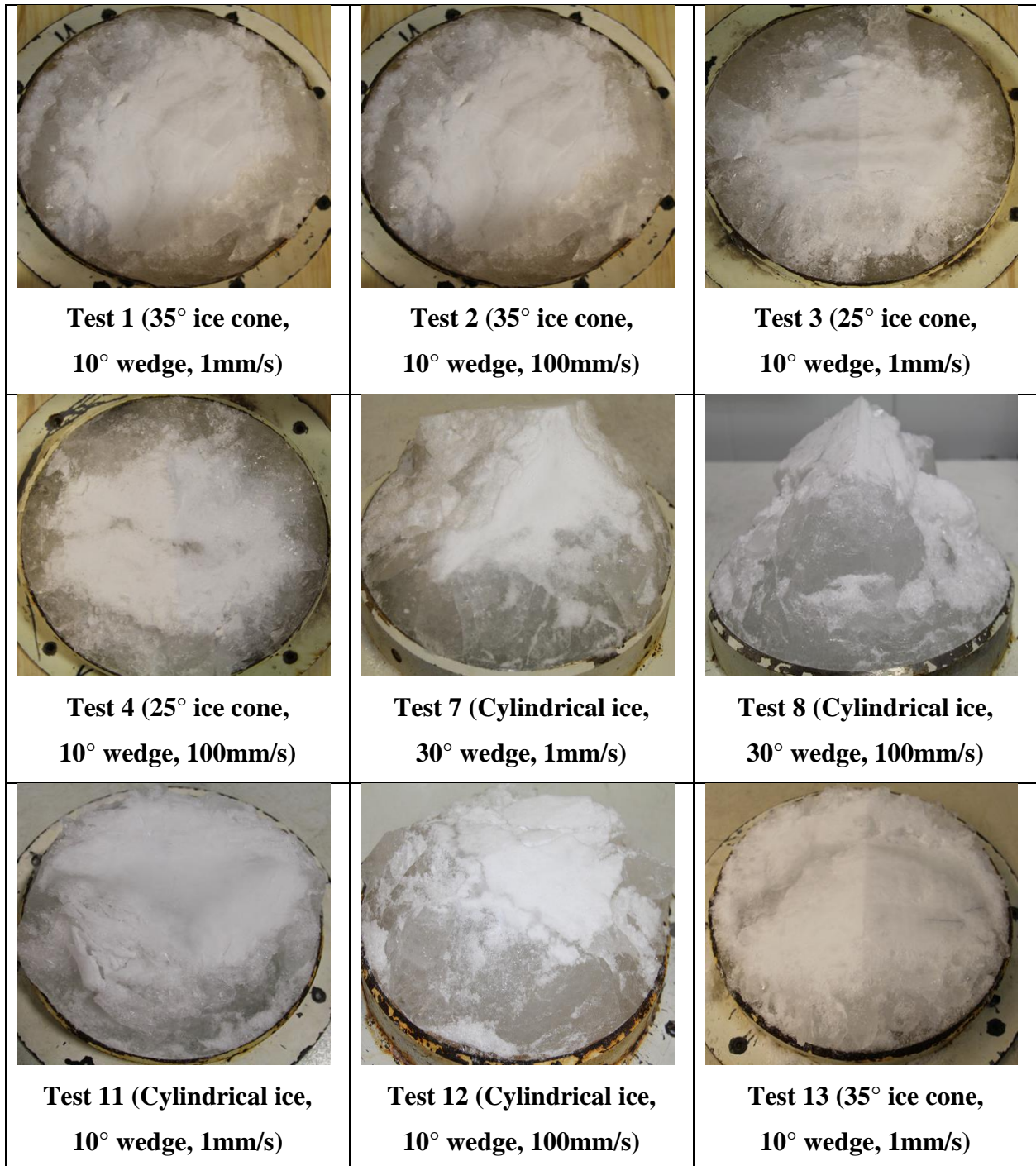
Table 4-2: Comparison of nominal and projected contact area

Cylindrical ice, 10° wedge					Cylindrical ice, 20° wedge			
Disp. (mm)	A _{nom} (mm ²)	A _{proj} (mm ²)	Ratio (A _{nom} /A _{proj})		Disp. (mm)	A _{nom} (mm ²)	A _{proj} (mm ²)	Ratio (A _{nom} /A _{proj})
5	6260	6160	1.02		5	2240	2120	1.06
10	17020	16760	1.02		10	6240	5860	1.06
15	30000	29540	1.02		15	1260	0580	1.06
20	44080	43420	1.02		20	17020	6000	1.06
22	49840	49080	1.02		25	23320	1900	1.06
-	-	-	-		30	30020	8220	1.06
-	-	-	-		35	37020	34800	1.06
-	-	-	-		40	44220	41560	1.06
-	-	-	-		45	50040	47020	1.06
-	-	-	-		45.5	52240	49080	1.06
Cylindrical ice, 30° wedge					25° ice cone, 10° wedge			
Disp. (mm)	A _{nom} (mm ²)	A _{proj} (mm ²)	Ratio (A _{nom} /A _{proj})		Disp. (mm)	A _{nom} (mm ²)	A _{proj} (mm ²)	Ratio (A _{nom} /A _{proj})
5	1240	1060	1.17		5	680	660	1.03
10	3440	2980	1.15		10	2720	2660	1.02
15	6260	5420	1.15		15	6100	6000	1.02
20	9520	8240	1.16		20	10840	10680	1.01
25	13140	11380	1.15		25	16960	16680	1.02
30	17060	14780	1.15		30	24400	24040	1.01
35	21240	18400	1.15		35	33220	32720	1.02
45	30180	26140	1.15		36.3	35740	35200	1.02
55	39700	34380	1.15		-	-	-	-
65	49540	42900	1.15		-	-	-	-
69	53540	46360	1.15		-	-	-	-
72.15	56680	49100	1.15		-	-	-	-

35° ice cone, 10° wedge					35° ice cone, 20° wedge			
Disp. (mm)	A _{nom} (mm ²)	A _{proj} (mm ²)	Ratio (A _{non} /A _{proj})		Disp. (mm)	A _{nom} (mm ²)	A _{proj} (mm ²)	Ratio (A _{non} /A _{proj})
5	240	240	1.00		5	440	420	1.05
10	940	940	1.00		10	1780	1680	1.06
15	2120	2100	1.01		15	4020	3780	1.06
20	3780	3720	1.02		20	7140	6700	1.07
30	8500	8380	1.01		25	11160	10480	1.06
40	15120	14900	1.01		30	16060	15100	1.06
50	23640	23280	1.02		35	21880	20540	1.07
60	34040	33520	1.02		40	28560	26840	1.06
65.5	40560	39940	1.02		41.5	30760	28880	1.07
25° ice cone, 10° conical					35° ice cone, 10° conical			
Disp. (mm)	A _{nom} (mm ²)	A _{proj} (mm ²)	Ratio (A _{non} /A _{proj})		Disp. (mm)	A _{nom} (mm ²)	A _{proj} (mm ²)	Ratio (A _{non} /A _{proj})
5	949	940	1.01		5	292	290	1.01
10	3790	3730	1.02		10	1164	1140	1.02
15	8522	8380	1.02		15	2617	2570	1.02
20	15145	14900	1.02		20	4652	4580	1.02
25	23660	23280	1.02		30	10463	10300	1.02
30	34066	33530	1.02		40	18595	18310	1.02
35	46363	45630	1.02		50	29056	2800	1.02
36	49049	48280	1.02		55	35157	34610	1.02
-	-	-	-		60	41838	41190	1.02
-	-	-	-		65	49101	48340	1.02

4.5.2. Crushed Ice Sample

Figure 4-12 shows the crushed section (top view) of the ice samples after the last step of tests.



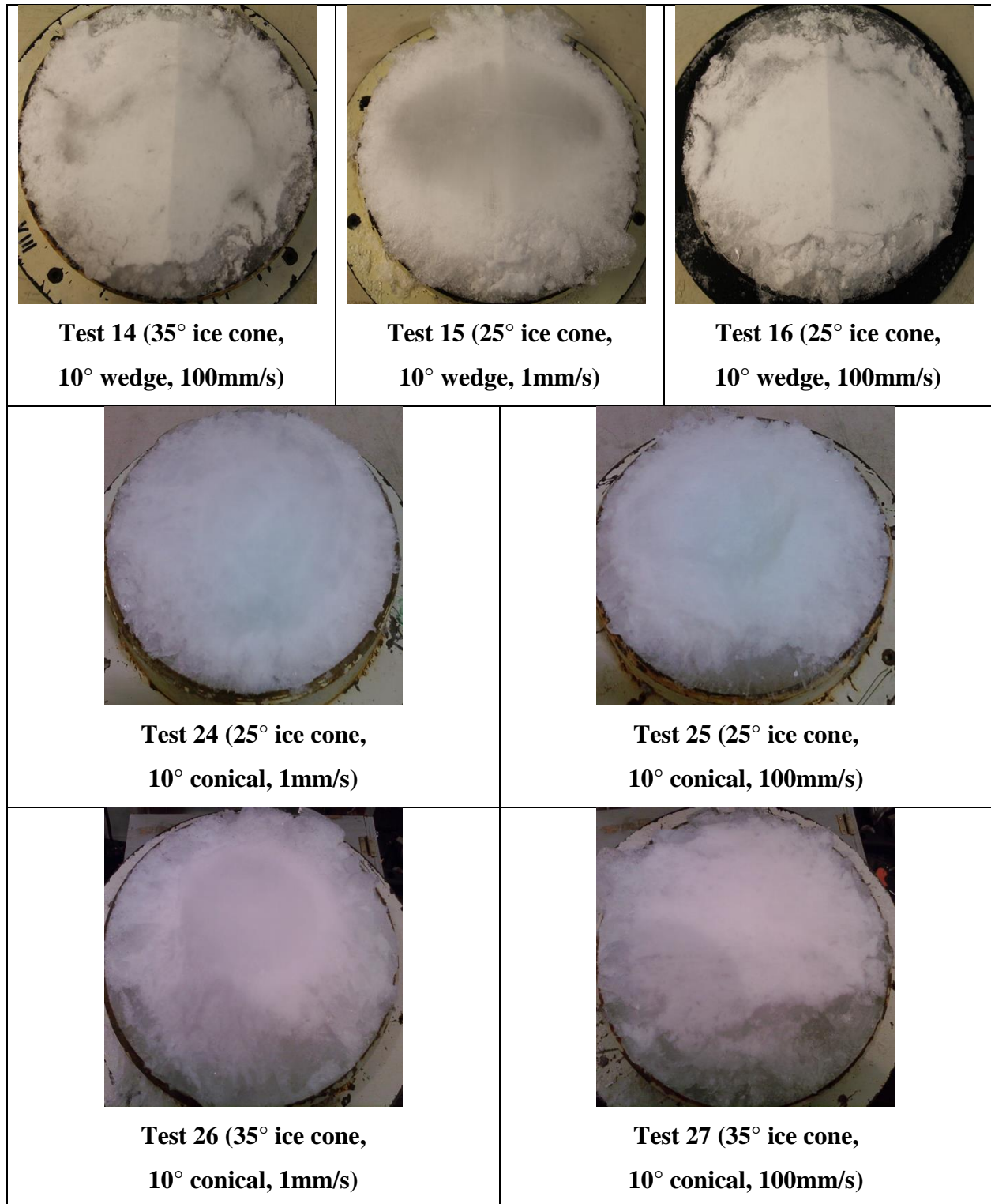


Figure 4-12: Crushed ice sample after tests

4.5.3. Section of ice sample

Figure 4-13 shows a section of the ice sample after the tests. As shown in Figure 4-13, high pressure zone (HPZ) which is marked as a red zone appeared clearly even at the low test speeds (Test 1 & 3). Blue zone represents the realistic contact area, including pulverized ice during the tests. It is different when compared with previous test results done by Kim and Daley (2013-a; 2013-b). They reported that the ice test results performed by the low test speed (1mm/s) did not show (or merely zero percent) HPZ after the tests. Appearance of HPZ is due to the effects of indenter shape (structural shape).

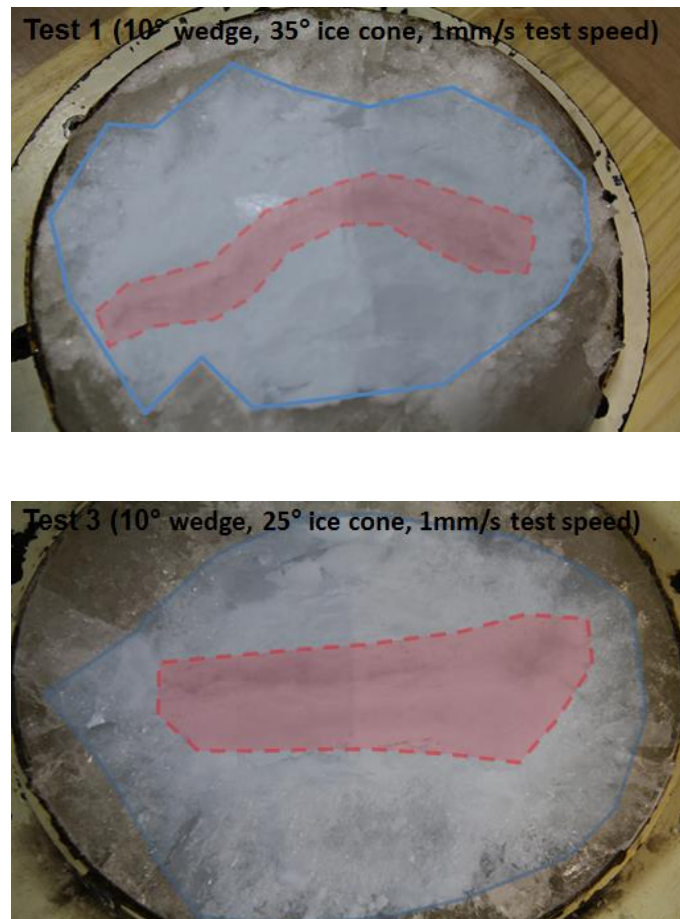


Figure 4-13: Section of ice sample appearing a HPZ (Test 1 & 3)

4.5.4. Force-Displacement History/Process Pressure-Area Curve/Compressive Ice Strength Comparison

Force-displacement history, process pressure-area curve and compressive ice strength depending on the test speed and the cone angle/cylindrical ice were compared after each test condition.

4.5.4.1. 25° Ice cone, 1mm/s Test Speed

Figure 4-14 shows the force-displacement history of 25° ice cone with 1mm/s test speed. As shown in Figure 4-14, 10° conical indenter test showed the highest ice loads compared to the flat and 10° wedge indenter tests. On the other hand, 10° wedge and flat indenter showed a similar ice load level.

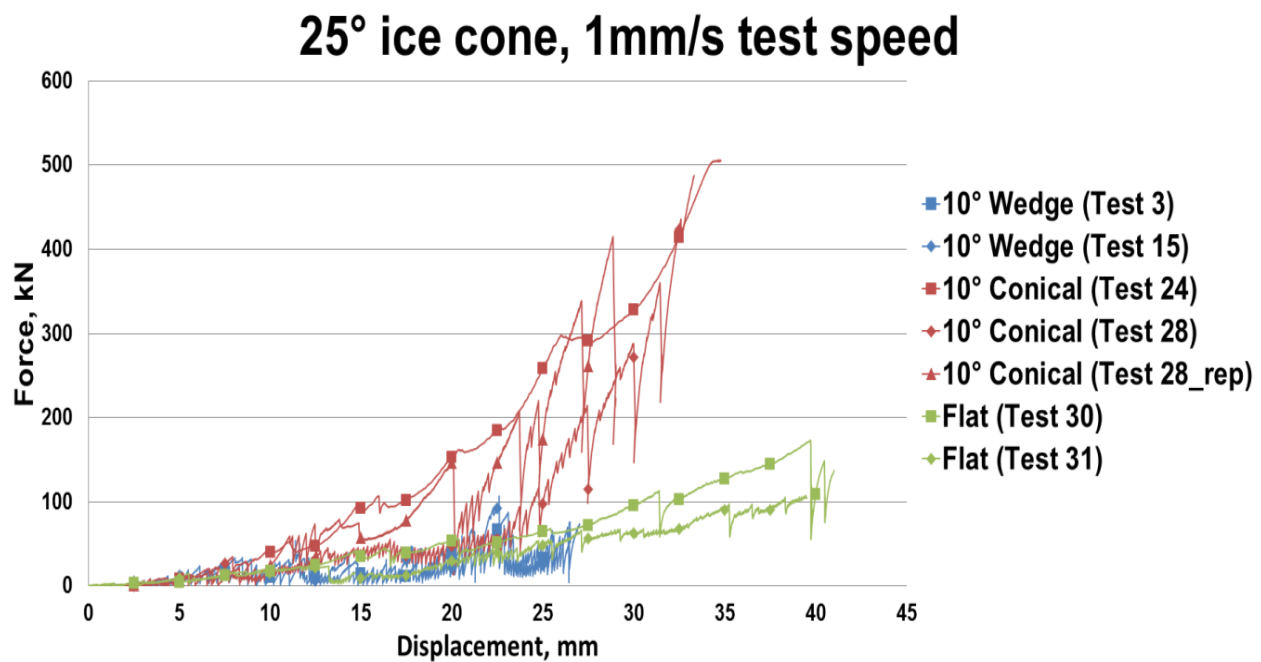


Figure 4-14: Force-displacement history (25° ice cone, 1mm/s test speed)

Figure 4-15 shows process pressure-area curves of 25° ice cone at 1mm/s test speed. Shown in earlier results of force-displacement history, 10° conical indenter showed the highest pressure in overall contact area. Comparison between the flat and 10° wedge indenter tests showed that pressure range of flat indenter was higher even the force-displacement history was similar because of the differences in indenter shape. As discussed, the contact area at the same displacement is larger in the case of conical and wedge indenter compared to flat indenter.

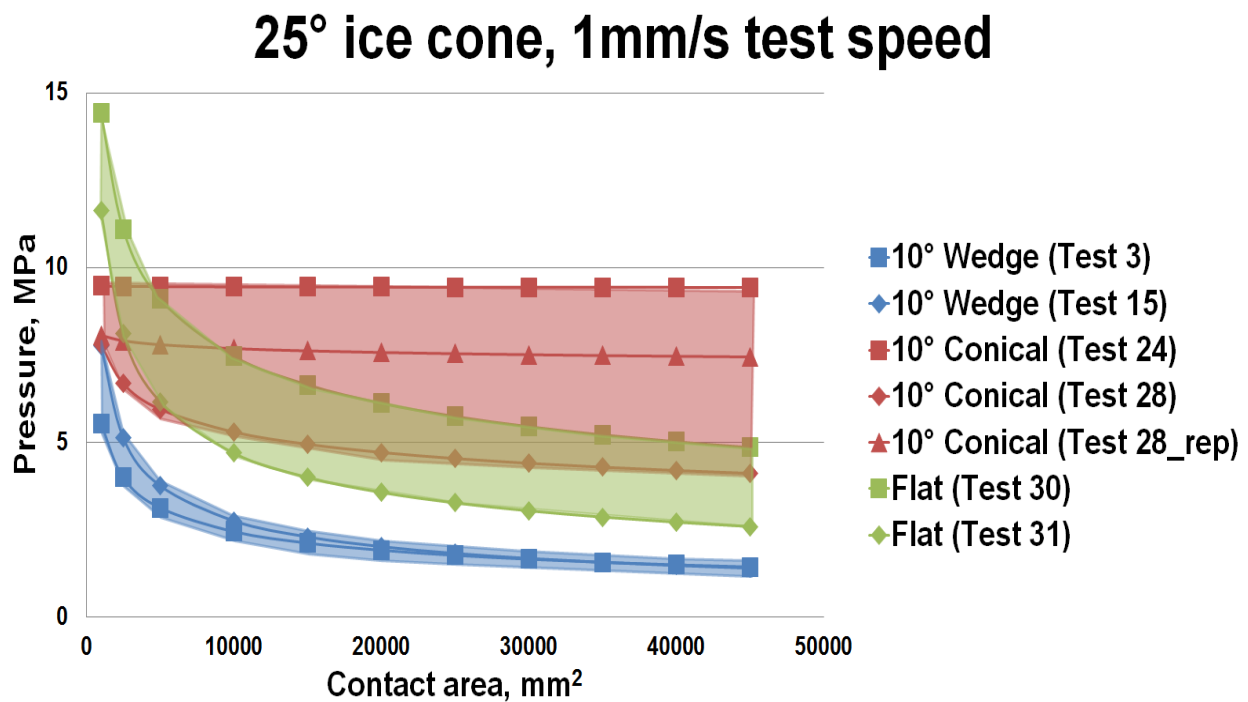


Figure 4-15: Process pressure-area curve (25° ice cone, 1mm/s test speed)

Contact areas of the indenter are shown in Figures 4-16 and 4-17. As mentioned earlier, the contact area is relatively larger in the case of the wedge or conical indenter compared to flat indenter as displacement increases. This increment in contact area will result to lowering the nominal pressure (Kim and Daley, 2013-b).

Contact area comparison (25° ice cone)

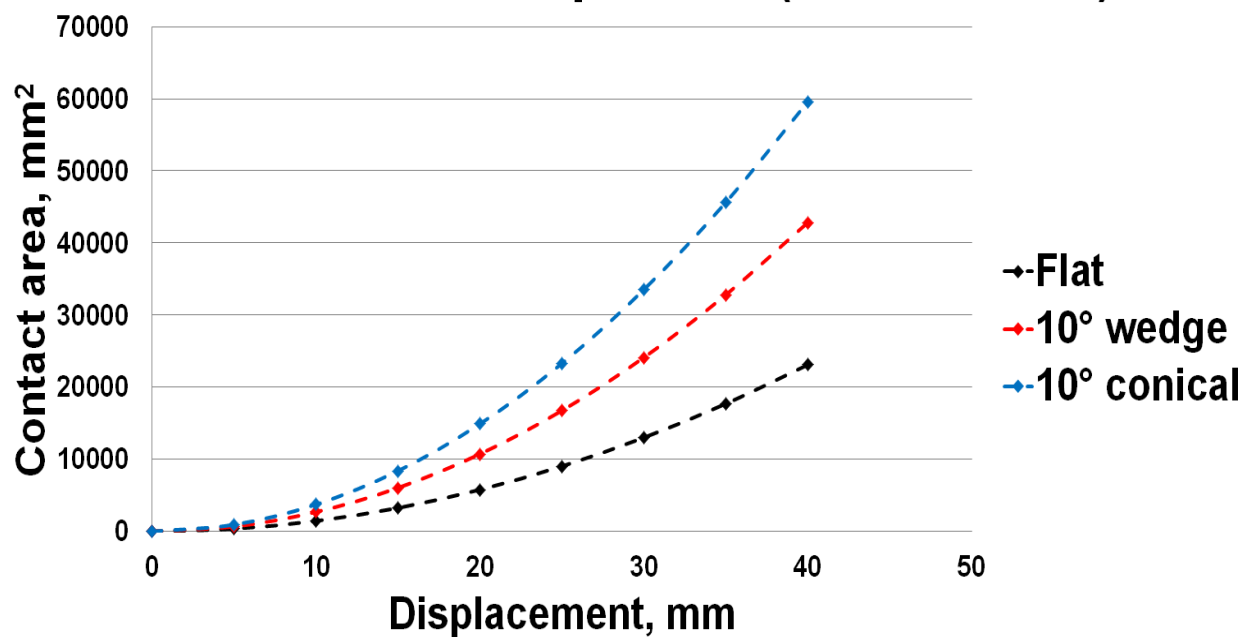


Figure 4-16: Contact area comparison (25° ice cone)

Contact area comparison (35° ice cone)

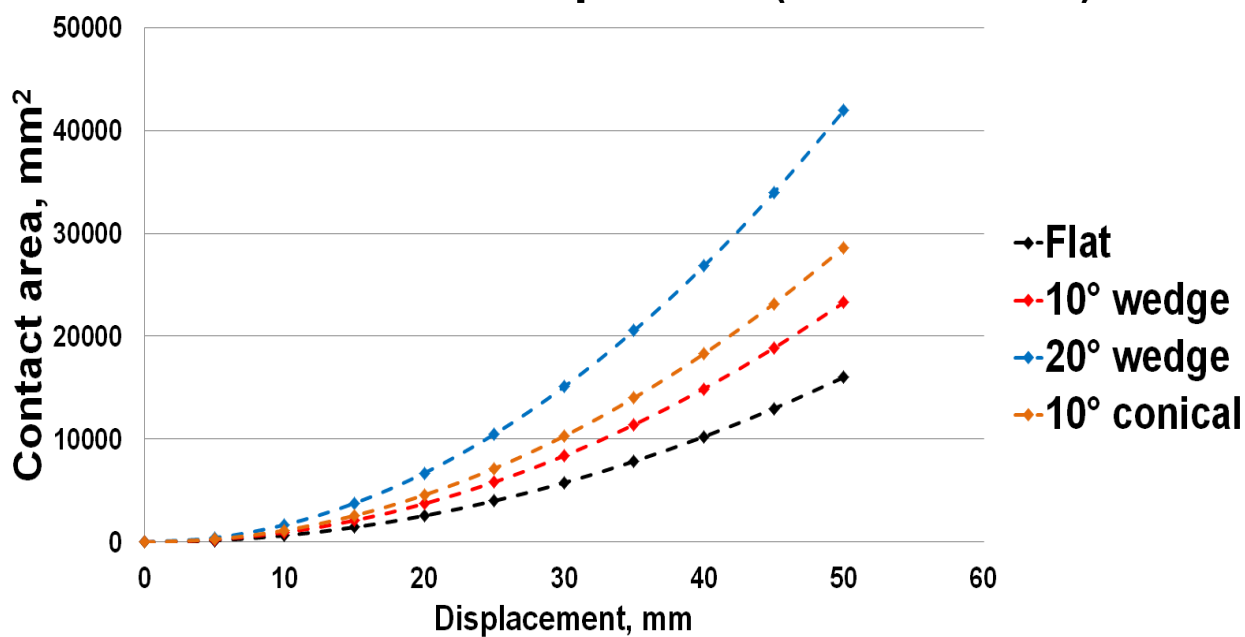


Figure 4-17: Contact area comparison (35° ice cone)

Additionally, compressive ice strength was compared for each test. Dillenberg (2012) suggested that 1) sum up total energy up to a certain displacement and 2) dividing by crushed volume to calculate the compressive ice strength of ice sample. Identical methodology was applied in this study.

Higher compressive ice strength values in y-axis means that more energy requires to crush the same volume of ice. It can be considered that the larger ice loads were applied against indenter. Therefore, the tendency of compressive ice strength is expected to show somewhat similar trend of the force-displacement history. Figure 4-18 shows the compressive ice strength comparison of 25° ice cone with 1mm/s test speed. As mentioned, 10° conical indenter case showed a significantly higher compressive strength level compared to two other cases.

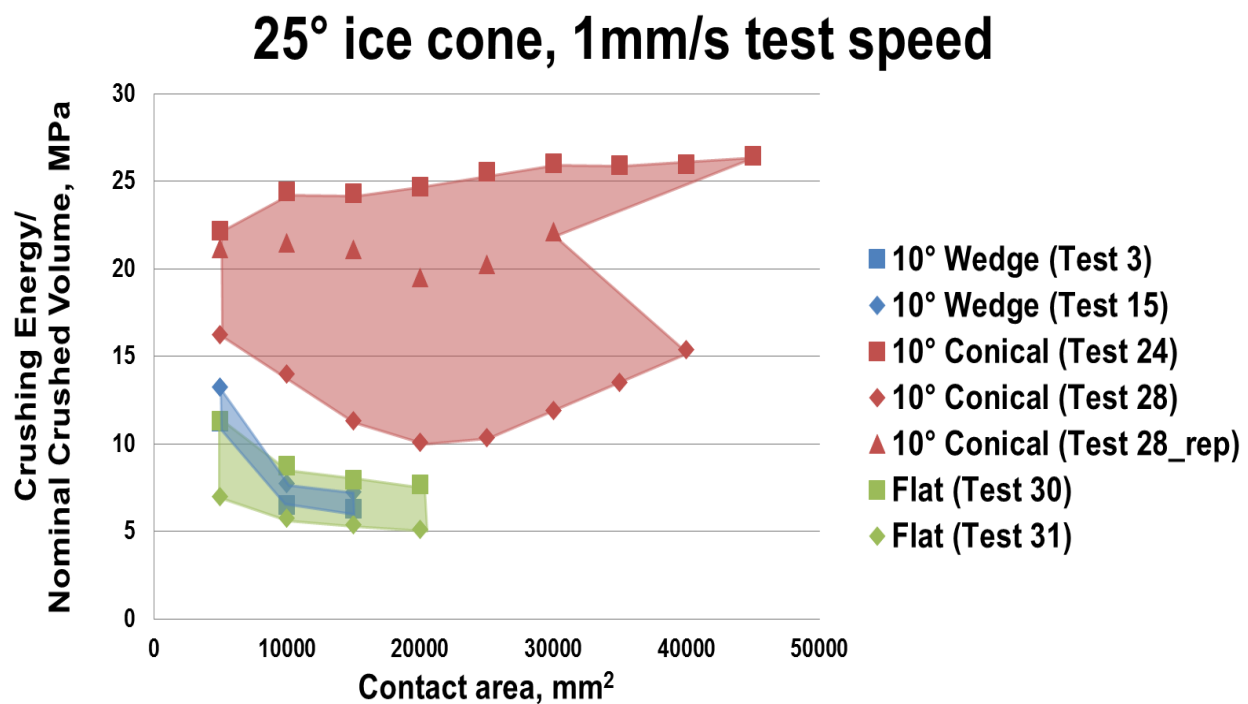


Figure 4-18: Compressive ice strength (25° ice cone, 1mm/s test speed)

4.5.4.2. 25° Ice Cone, 100mm/s Test Speed

Figure 4-19 shows the force-displacement history of 25° ice cone with 100mm/s test speed. 10° conical indenter test showed significantly higher ice loads compared to the flat and 10° wedge indenter test as shown in the previous 1mm/s test speed case. On the other hand, measured ice loads against 10° wedge represented relatively higher value than that for the flat indenter.

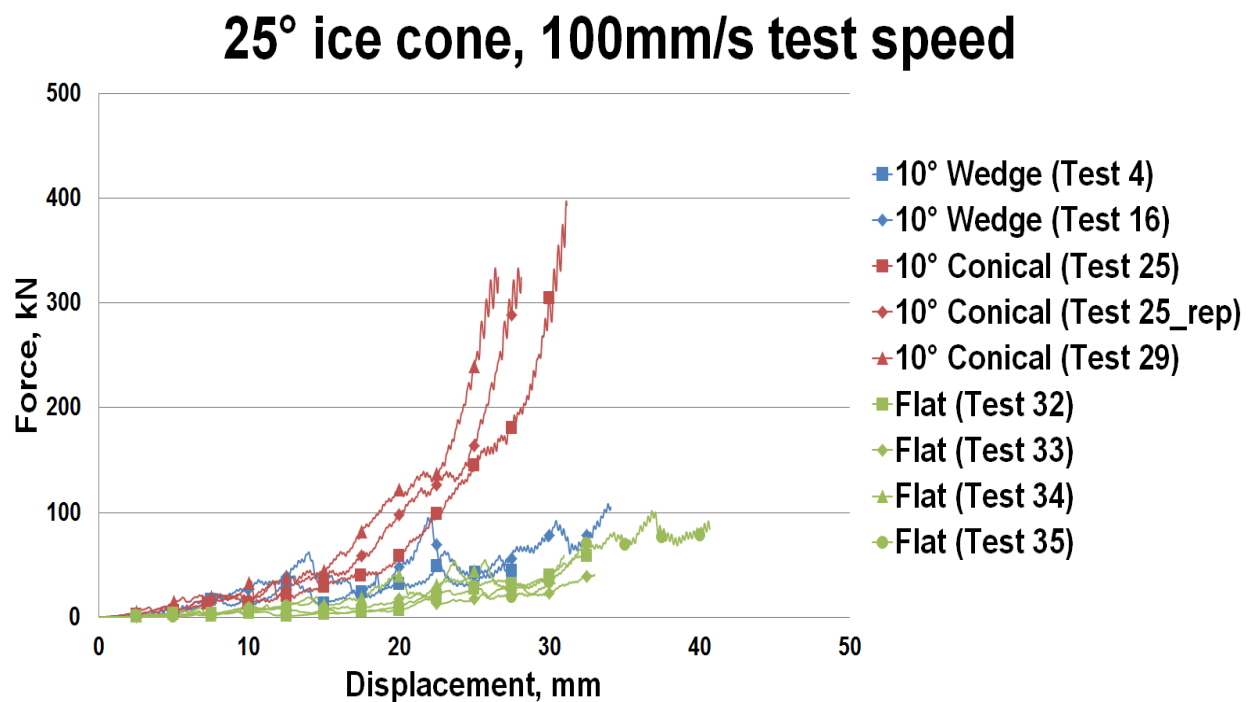


Figure 4-19: Force-displacement history (25° ice cone, 100mm/s test speed)

A similar tendency was observed in process pressure-area curves. 10° conical indenter represented the highest pressure level through the contact area. In addition, 10° wedge indenter test showed a relatively high pressure level at the first period of the area compared to flat

indenter. However, both curves are observed to be similar after a specific point as shown in Figure 4-20.

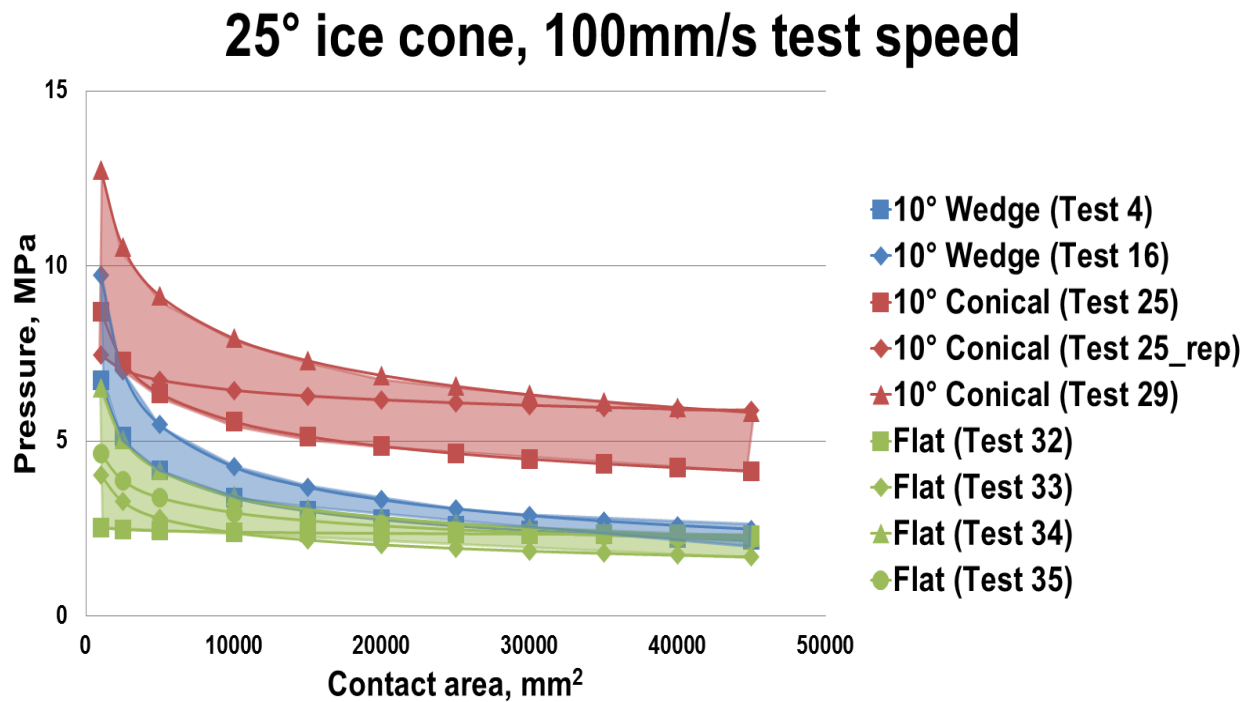


Figure 4-20: Process pressure-area curve (25° ice cone, 100mm/s test speed)

Figure 4-21 shows the results of compressive ice strength tests with 25° ice cone at 100mm/s test speed. As can be expected from the force-displacement history, 10° conical indenter test shows a large value of compressive ice strength and 10° wedge indenter also shown to higher than a flat indenter.

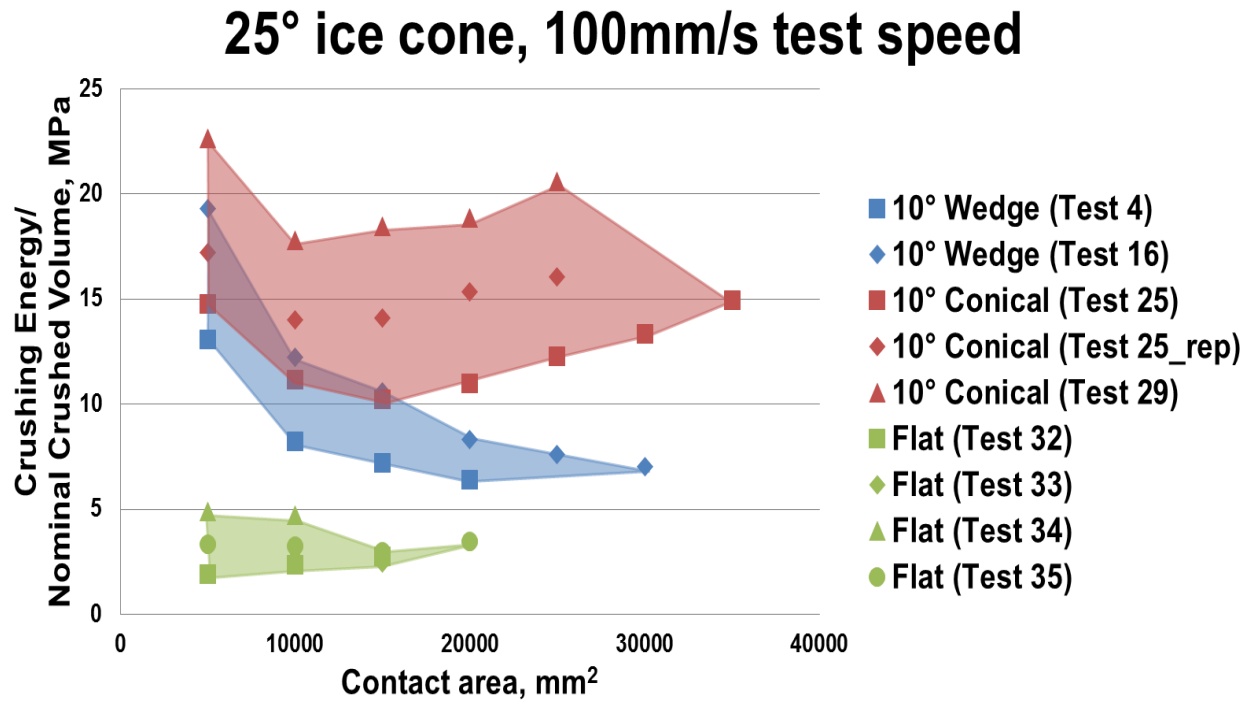


Figure 4-21: Compressive ice strength (25° ice cone, 100mm/s test speed)

4.5.4.3. Cylindrical Ice, 1mm/s Test Speed

Figure 4-22 shows the force-displacement history of cylindrical ice sample at 1mm/s test speed. As shown in the results, magnitude of ice loads was similar regardless of indenter angle. Note that the peak load occurred when the cylindrical ice reached the maximum penetration depth of each indenter, as represented in Figure 4-22 (as a dotted line).

Cylindrical ice, 1mm/s test speed

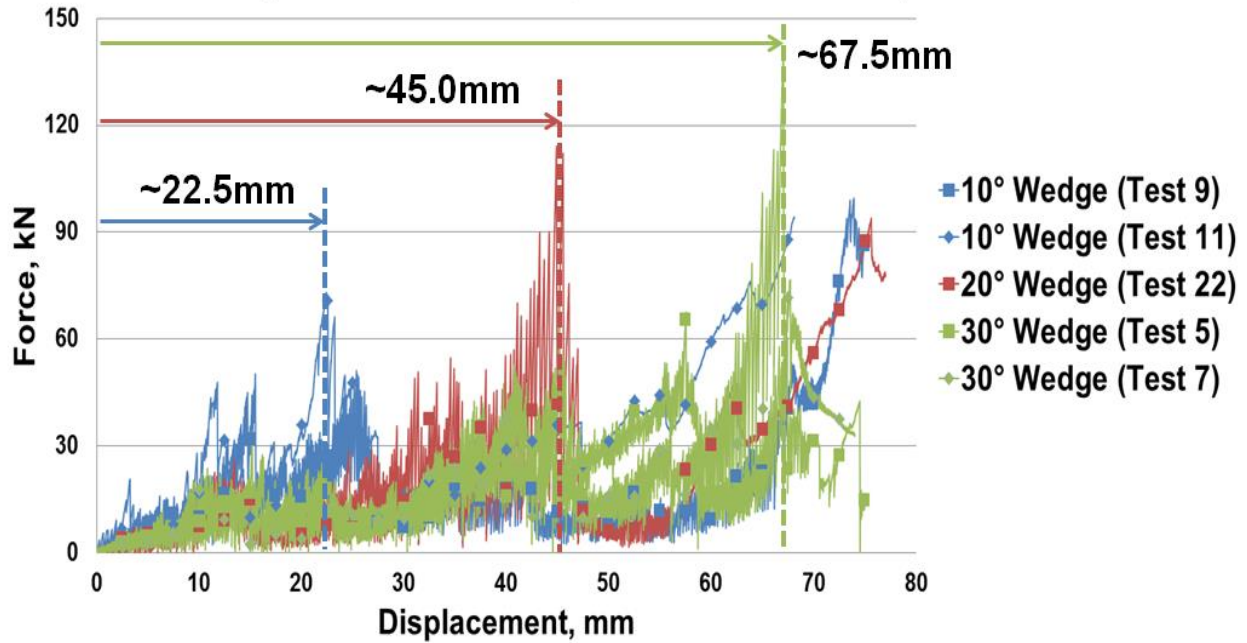
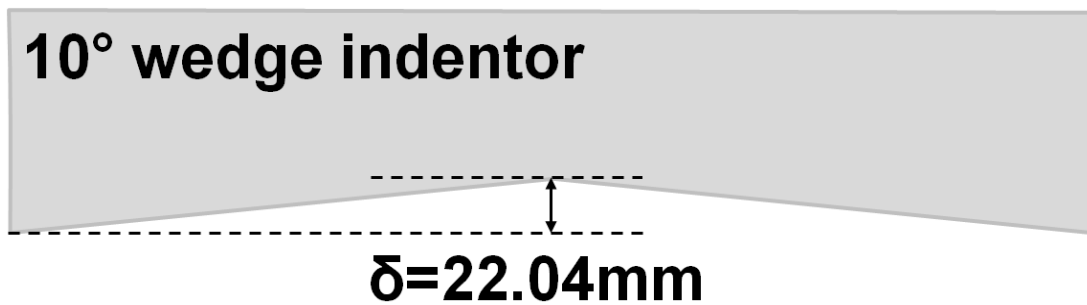
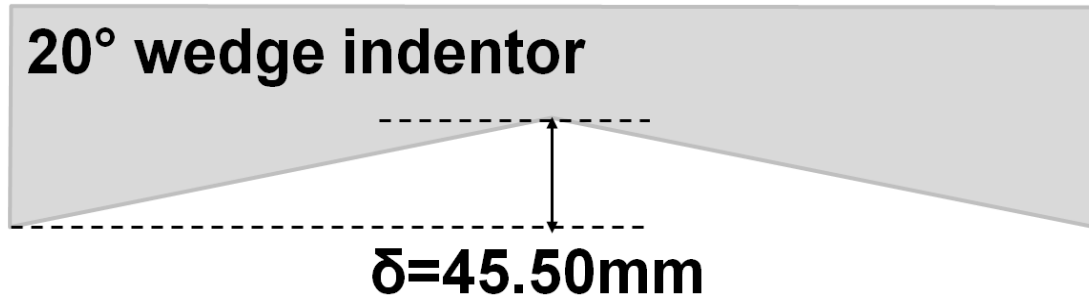


Figure 4-22: Force-displacement history (cylindrical ice, 1mm/s test speed)

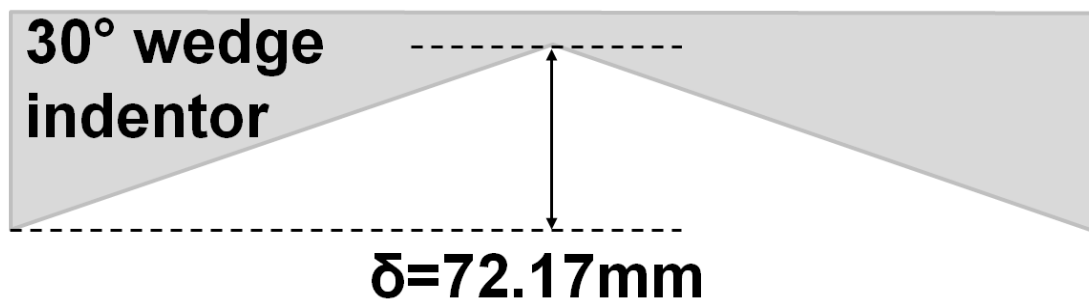
Figure 4-23 indicates the maximum penetration depth of the indenter at different wedge angles. In the case of 10° & 20° wedge indenters, the maximum penetration depth and the timing of the peak ice load was almost identical. Otherwise, in the case of 30° wedge indenter, the peak ice load occurred in the early (~93%) position, but still very close to the maximum penetration depth.



(a) 10° wedge indenter



(b) 20° wedge indenter



(c) 30° wedge indenter

Figure 4-23: Comparison of max. penetration depth at each wedge indenter angle

(10°, 20° and 30° wedge indenter)

Figure 4-24 shows the process pressure-area curve of cylindrical ice at 1mm/s test speed. As shown in force-displacement history, appreciable ice load dependency on the indenter angle was not observed. However, the overall contact area of 30° wedge indenter showed the relatively lower value according to the shape effects. As a result, larger ice pressure values were observed using 30° wedge indenter. Otherwise, the differences between the 10° and 20° wedge indenter were not significant.

Cylindrical ice, 1mm/s test speed

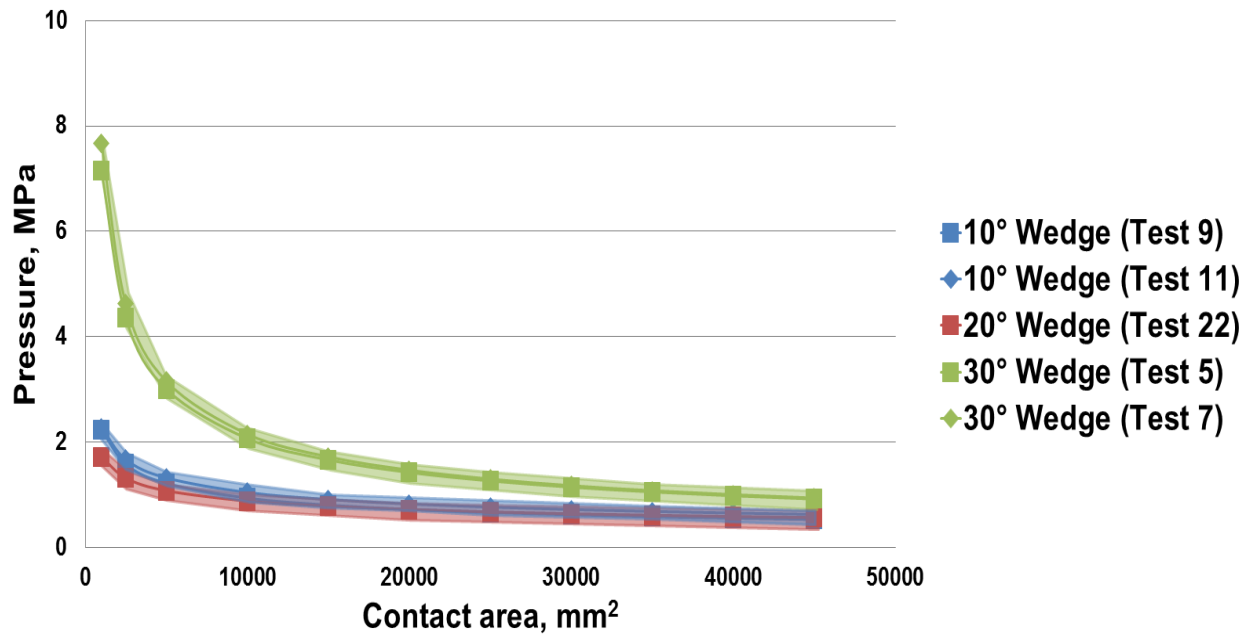


Figure 4-24: Process pressure-area curve (cylindrical ice, 1mm/s test speed)

Figure 4-25 represents a comparison of the contact area at a different indenter angle. As discussed, 30° wedge indenter showed the smallest contact area compared to 10° and 20° wedge indenters.

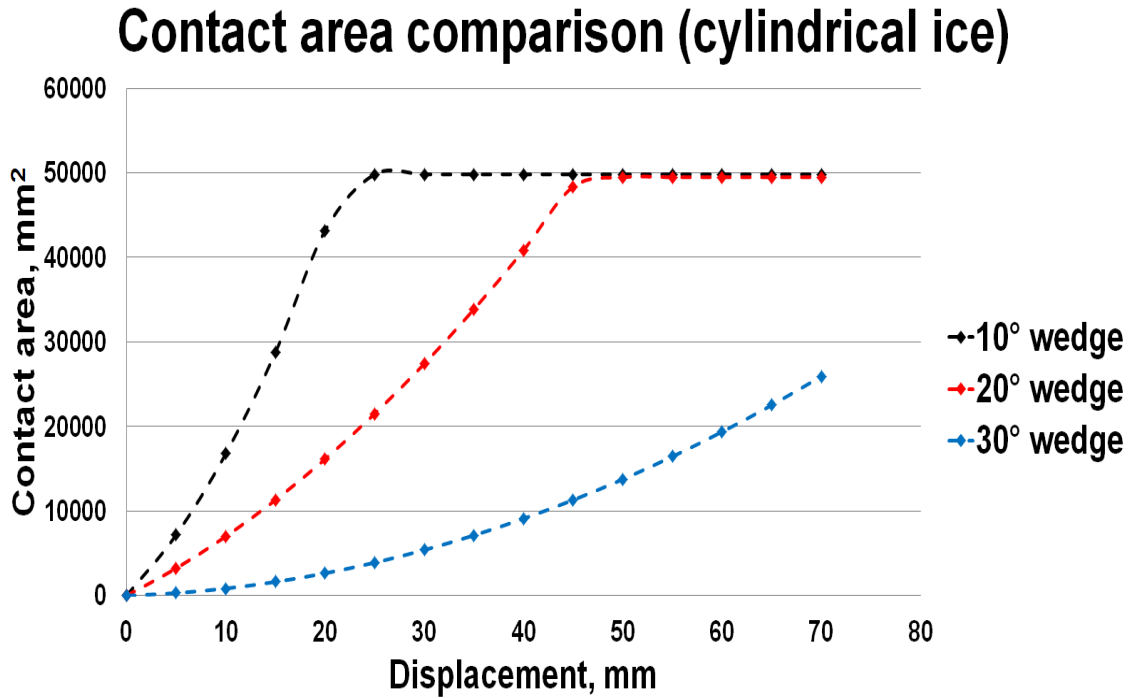


Figure 4-25: Comparison of contact area at different wedge indenter angle

Figure 4-26 shows the results of the compressive ice strength in case of cylindrical ice with 100mm/s test speed. Similar to pressure-area curve results, 30° wedge indenter test displayed a relatively larger compressive ice strength because of smaller contact areas (smaller crushed volume of ice) at the same displacement.

However, more important are the result of the magnitudes of compressive ice strengths using cylindrical ice. In a previous study, the average range of compressive ice strength was 5 - 25MPa using cone-shaped ice (Kim et al, 2012; Kim and Daley, 2013a; 2013b). In contrast, the results of cylindrical ice varied between 0.1 - 0.5MPa ranges, which is about 1/50 size of the results compared to the cone-shaped ice case.

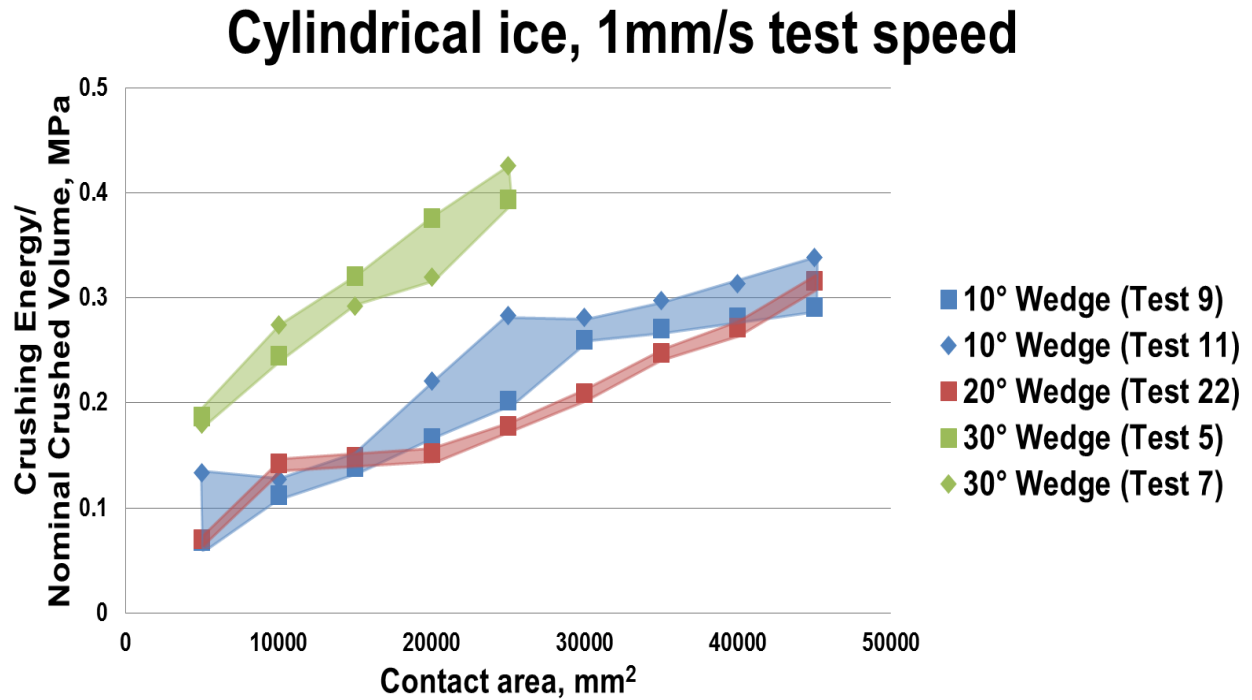


Figure 4-26: Compressive ice strength (cylindrical ice, 1mm/s test speed)

4.6. Pressure Measurement Film

4.6.1. Pressure Distribution Map: Cone-Shaped Ice Sample

Figure 4-27 shows the obtained pressure distribution at each test using the pressure measurement film. A total of 10 tests (6 tests: cone ice, 4 tests: cylindrical ice) was chosen to measure the activated contact area and pressure distribution (pattern) at designated step. Two characteristics of ice behavior were observed through the measured pressure pattern.

First, formation of pressure pattern against wedge-shaped indenter appeared in the normal direction of the indenter's centerline. In addition, shape of obtained pressure patterns were almost identical compared to the overlapped pattern between the cone-shaped ice and wedge indenter. However, more uniform pressure patterns were observed at low test speed (1mm/s) and randomized (and wide) pressure patterns were formed at high test speed (100mm/s).

Second, high pressure zones appeared even when the test speed was low, which was contrary to the conventional flat indenter test results. As observed by Kim and Daley (2013-a; 2013-b), nearly 10 - 20MPa average pressure was uniformly distributed within a circular contact area using cone-shaped ice sample against flat indenter. However, pressure range over the 40 - 80MPa was appeared clearly as 'line-like' shape against wedge-shaped indenter as shown in Figures 4-27 and 4-28 (Daley, 1992; Tuhkuri, 1995).

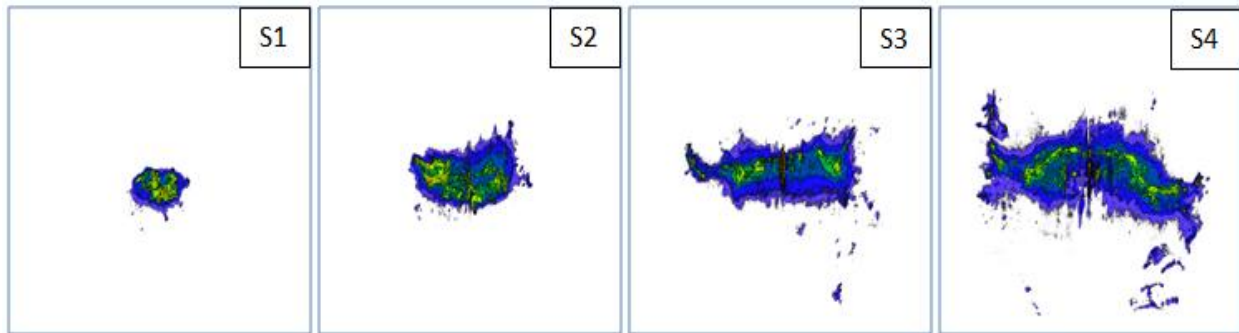


Figure 4-27: Pressure distribution map of Test 1
(10° wedge indenter, 35° ice cone, 1mm/s test speed)

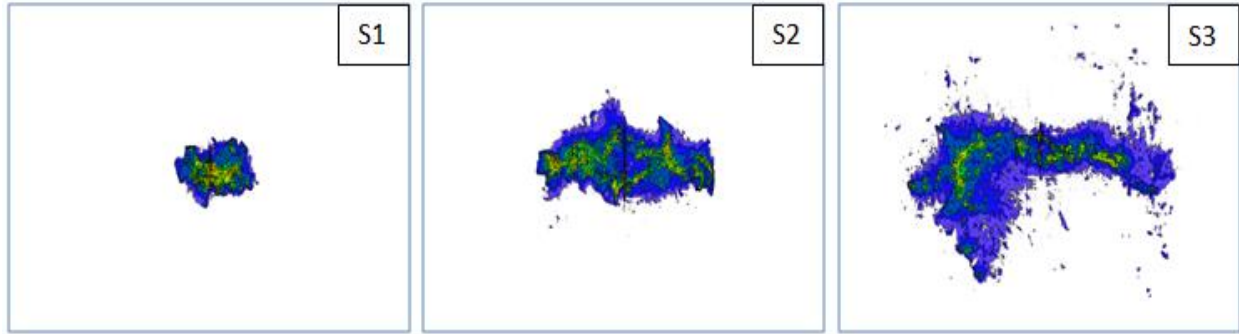


Figure 4-28: Pressure distribution map of Test 4
(10° wedge indenter, 25° ice cone, 100mm/s test speed)

4.6.2. Pressure Distribution Map: Cylindrical Ice Sample

In the case of cylindrical ice tests, the first contact location began not at the center of the wedge indenter, but at the side, unlike the case of cone-shaped tests. Figures 4-29 and 4-30 indicated that pressure patterns developed from the outer to inner as ice progressed. Speed of test did not have significant effects to form the pressure pattern during the tests using the cylindrical ice.

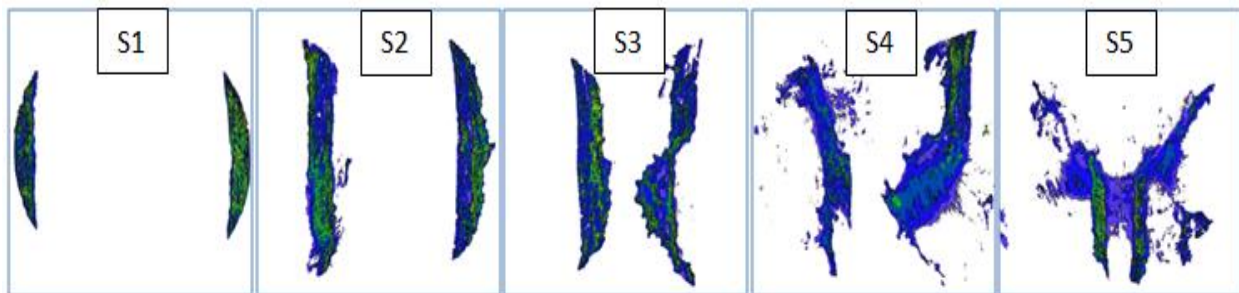


Figure 4-29: Pressure distribution map of test 5
(30° wedge, cylindrical ice, 1mm/s test speed)

Tests 9 and 10 shows the measured results against the 10° wedge indenter, and the cylindrical ice; it reached at the maximum depth of the indenter at step 2 (designed displacement of step 2 was 30mm). In this case, obtained pressure patterns on both indenter sides were opposite to the wedge-centerline as shown in Figures 4-29 and 4-30. More randomized pressure patterns were observed after step 2 by spalling events.

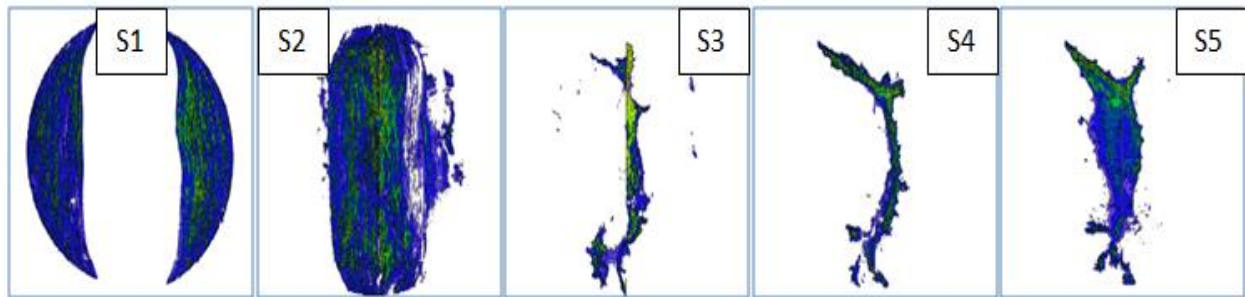


Figure 4-30: Pressure distribution map of test 9
(10° wedge, cylindrical ice, 1mm/s test speed)

4.7. Pressure Pattern Examination

Width and height of each test step were evaluated based on obtained pressure patterns by pressure measurement films. It may become applicable as an useful data to develop an ice load model to be used for the finite element analysis. Figure 4-31 represents the criteria of the width and height of each pressure pattern.

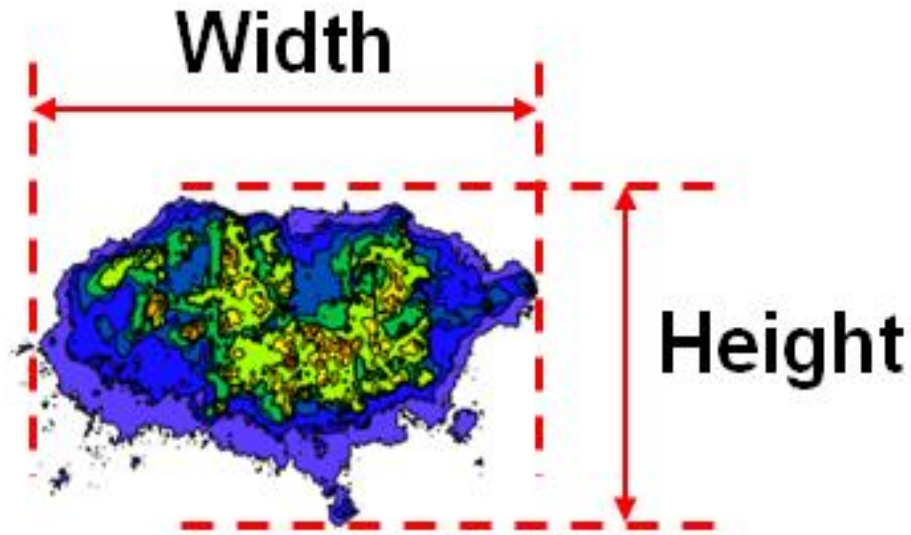


Figure 4-31: Criteria of the width and height of pressure pattern

Table 4-3 summarized the results of the width and height measurement after each test. It is remarkable that the width of each test case showed almost identical value, regardless of cone angles and test speeds. On the other hand, height of pressure pattern showed differences according to the test speed. Wider height (up to 70 - 80%) was observed in the case of high test speeds compared to low test speed due to more randomized pressure patterns occurring at high test speed; as discussed in the comparison of pressure pattern, in the previous section.

Table 4-3: Comparison of width and height of pressure pattern

Test 1 (10° wedge, 35° ice cone, 1mm/s)			Test 2 (10° wedge, 35° ice cone, 100mm/s)		
Step No.	Width (mm)	Height (mm)	Step No.	Width (mm)	Height (mm)
1	54.5	30.0	1	59.5	35.0
2	101.0	52.5	2	105.5	83.0
3	157.5	50.5	3	130.0	85.5
4	203.0	69.0	4	213.0	123.0

Test 3 (20° wedge, 35° ice cone, 1mm/s)			Test 4 (20° wedge, 35° ice cone, 100mm/s)		
Step No.	Width (mm)	Height (mm)	Step No.	Width (mm)	Height (mm)
1	55.0	39.0	1	55.0	35.5
2	108.0	51.5	2	120.0	61.5
3	173.5	63.0	3	180.5	104.0

Test 17 (20° wedge, 35° ice cone, 1mm/s)			Test 18 (20° wedge, 35° ice cone, 100mm/s)		
Step No.	Width (mm)	Height (mm)	Step No.	Width (mm)	Height (mm)
1	52.5	26.0	1	43.0	23.5
2	111.5	45.5	2	98.5	48.0
3	197.5	70.5	3	157.0	85.5

4.8. Spatial Pressure-Area Curve

Figures 4-32 to 4-35 show the spatial pressure-area curves for each test. Process pressure-area curves were plotted as ‘black-dotted’ line and spatial pressure-area curves for each step were plotted as ‘colored-dotted’ line. The curve labeled as ‘PPA (Process Pressure-Area) trend’ on the figures are the connection of the end points of spatial pressure-area curves at each step. Plotting the ‘PPA trend’ can be useful to understand the tendency of process pressure-area curve, when the information of an external load data or the contact geometry (nominal contact area) of two objects is not available. Daley (2004; 2007) examined the ‘Polar Sea’ trial data in this manner.

Kim and Daley (2012) suggested two different methods to plot the spatial pressure-area curves. In this study, the ‘Contour-averaging method’ was adopted for convenience.

As shown in Figures 4-32 and 4-33, overall trend of ‘PPA’ curves tended to decrease in the case of the cone-shaped ice tests. In a similar manner, PPA trend was analyzed using cone-shaped ice tests against flat indenter, both increasing and decreasing PPA were observed. However, decreasing trends were dominated in the case of the wedge indenter test.

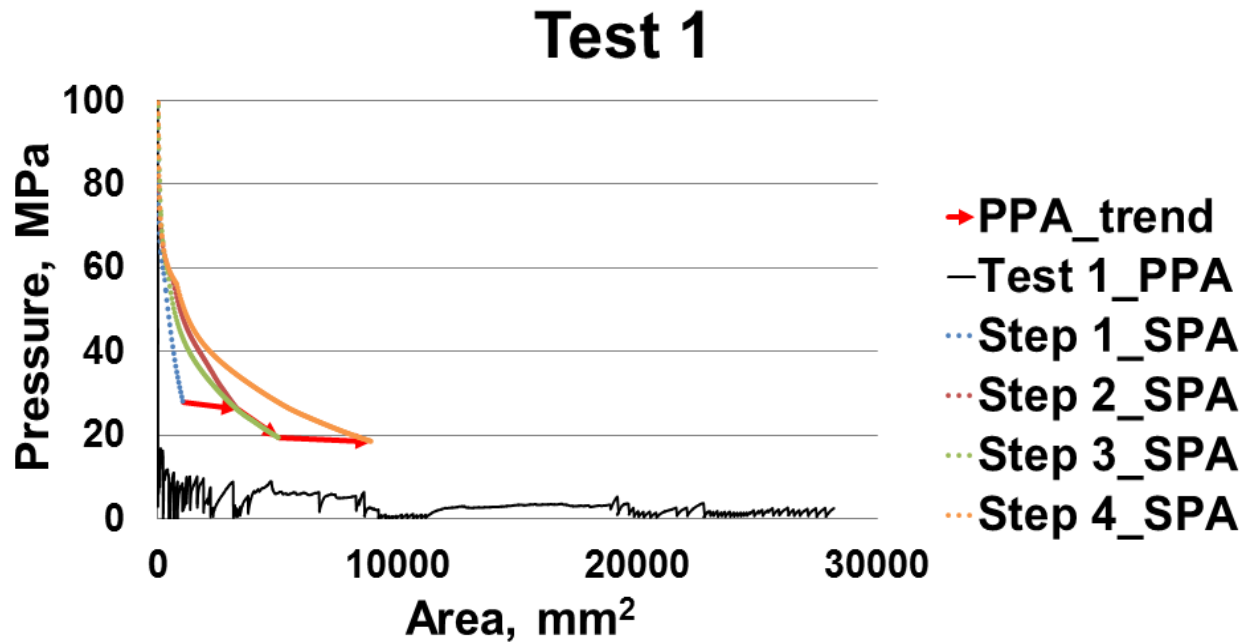


Figure 4-32: Spatial pressure-area curve of Test 1

(10° wedge, 35° ice cone, 1mm/s test speed)

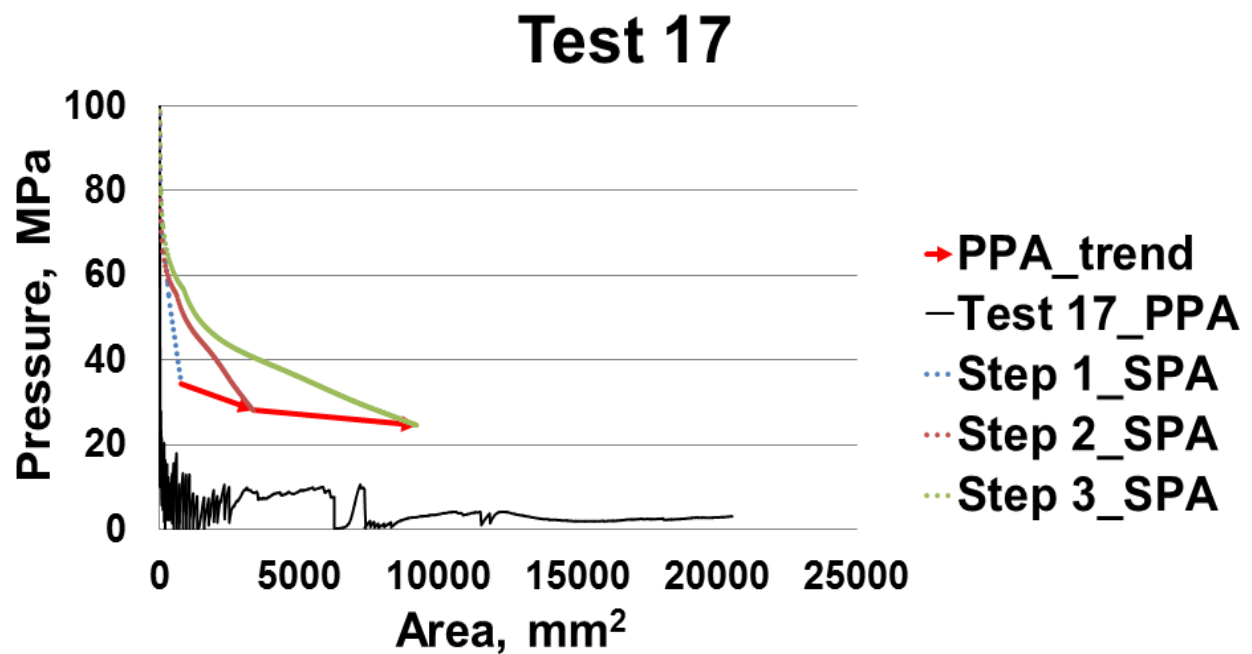


Figure 4-33: Spatial pressure-area curve of Test 17

(20° wedge, 35° ice cone, 1mm/s test speed)

The result of PPA trend using cylindrical ice tends to show more complexity as indicated in Figures 4-34 and 4-35. As confirmed by the pressure pattern in previous, the contact area was reduced extremely as test steps progressed in the case of cylindrical ice. These effects tended to decrease the contact area as test step progressed, and end points of each step showed a more complex pattern. These direction of arrows of PPA trend goes in a backward in most cases. However, the overall average pressures kept on decreasing.

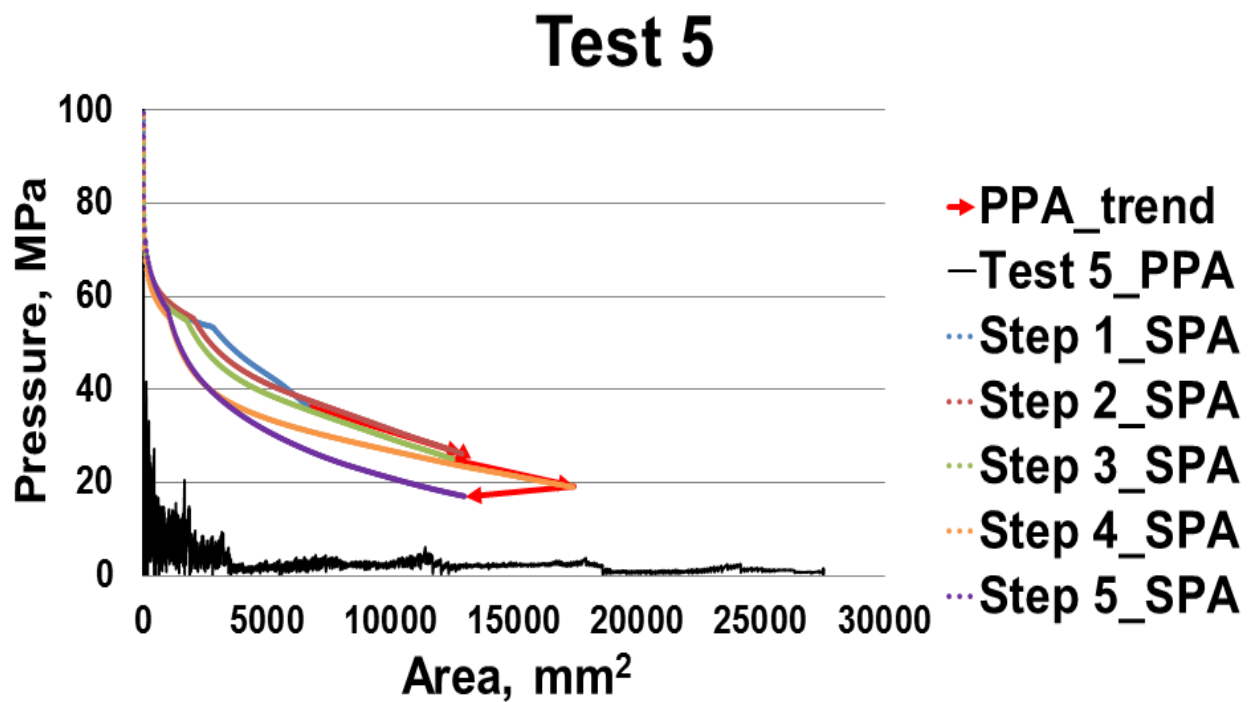


Figure 4-34: Spatial pressure-area curve of Test 5
(30° wedge, cylindrical ice, 1mm/s test speed)

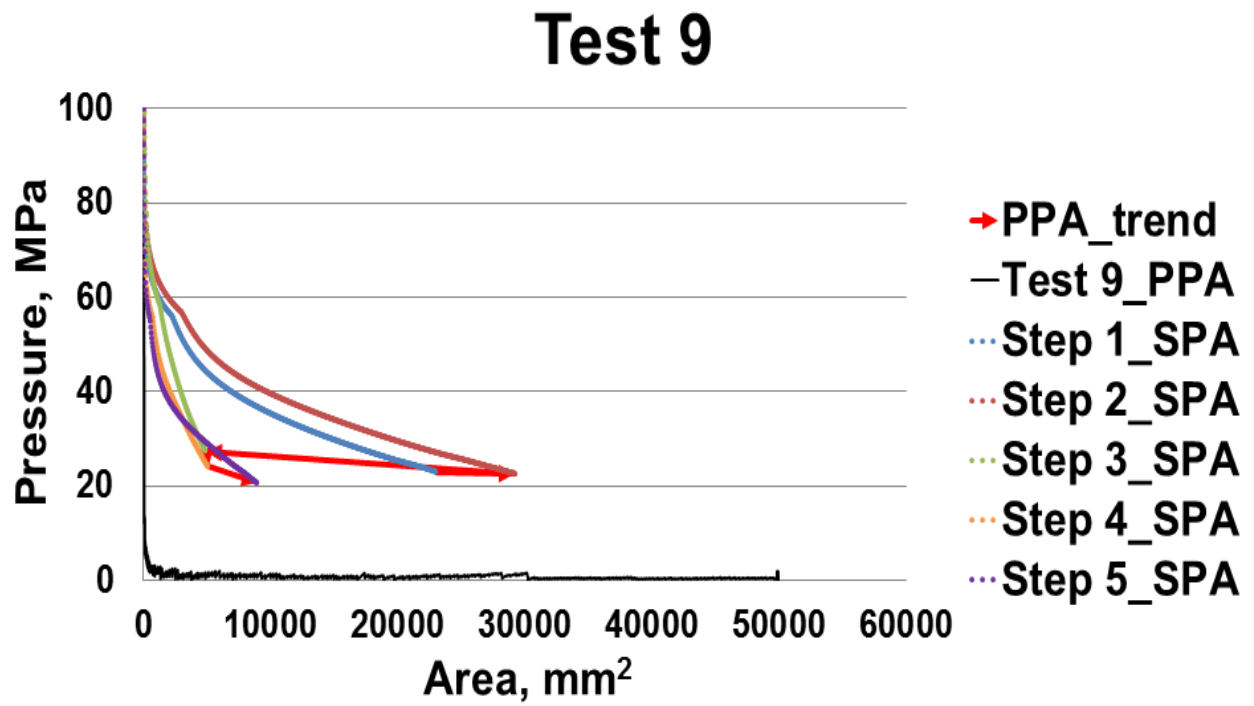


Figure 4-35: Spatial pressure-area curve of Test 9

(10° wedge, cylindrical ice, 1mm/s test speed)

Chapter 5 Experimental Data Analysis

5.1 Contact Area/Pressure Comparison: Flat vs. Concave Shape Indenter

For the evaluation of the effect of indenter shapes, the behavior of: 1) nominal vs. activated contact area and 2) nominal vs. activated pressure were compared at each test. The nominal contact area can be directly calculated by the shape of the prepared ice sample. In addition, obtained force data divided by nominal contact area is simply the nominal pressure. Activated contact area and activated pressure can be obtained using the pressure measurement film.

Table 5-1 shows the results of an earlier study using the flat indenter (Kim and Daley, 2012). The ratio between the activated and nominal contact area was about 60%. The value, 60% means that the measured value of activated area was less about 60% of the nominal contact area. The nominal contact area was larger than the activated contact area.

In contrast, comparison of the pressure showed the opposite trend. The percentage of activated pressure and the nominal pressure was about 500-600%, which means that the measured activated pressure was about 5-6 times higher (in average) compared to the nominal pressures. Less than 10MPa was the most approximate value in nominal pressures. However, the 10 -

30MPa pressure values were appeared in the activated pressure results. The difference was clearly shown when the test speed was high (100mm/s).

Table 5-1: Results of using 10cm diameter ice cone test against flat indenter

(a) Test 1 (30° ice cone, 100mm/s test speed)

Step no. (Disp.)	Nominal contact area (mm ²)	Nominal pressure (MPa)	Activated contact area (mm ²)	Activated pressure (MPa)	A _{act} /A _{nom} . (%)	P _{act} /P _{nom} . (%)
1 (9mm)	763.41	3.82	467.25	31.18	61.21	816.76
2 (18mm)	3053.63	8.82	1924.50	16.90	63.02	191.65
3 (27mm)	6870.67	2.06	4370.06	9.59	63.60	465.01
				Avg.	62.61	491.14

(b) Test 3 (50° ice cone, 1mm/s test speed)

Step no. (Disp.)	Nominal contact area (mm ²)	Nominal pressure (MPa)	Activated contact area (mm ²)	Activated pressure (MPa)	A _{act} /A _{nom} . (%)	P _{act} /P _{nom} . (%)
1 (15mm)	497.69	4.27	284.56	26.12	57.18	611.87
2 (30mm)	1990.76	4.49	1230.44	15.00	61.81	334.55
3 (45mm)	4479.21	6.10	3172.56	11.30	70.83	185.43
4 (55mm)	6691.17	11.65	5663.44	11.60	84.64	99.51
				Avg.	68.61	307.84

The differences of the contact area and pressure were even more increased using concave-shaped indenter as shown in Table 5-2. Overall, 1) average ratio of the contact area represented a value of 42.5% (less than half) and 2) pressure differences were about 40-70 times. The results of the contact area were smaller than the flat indenter tests. However, a significant difference relate to the pressures can be observed using concave-shaped indenter. Differences of pressure were decreased about 15 times lower than the cone-shaped ice tests (Test 1-4, 17, and 18). However, the results of the contact area were similar (about 42.5%).

Table 5-2: Results of using 25cm diameter ice cone test against concave shape indenter

(a) Test 1 (10° wedge, 35° ice cone, 1mm/s)

Step No. (Disp.)	Nominal contact area (mm ²)	Nominal pressure (MPa)	Activated contact area (mm ²)	Activated pressure (MPa)	A _{act.} /A _{nom.} (%)	P _{act.} /P _{nom.} (%)
1 (15mm)	2097.61	4.82	1050.50	27.84	50.08	577.24
2 (30mm)	8383.06	4.30	3318.13	26.24	39.58	610.42
3 (45mm)	18856.35	3.35	5024.69	19.43	26.65	579.76
4 (55mm)	28165.11	2.38	8908.94	18.51	31.63	778.26
				Avg.	36.99	636.42

(b) Test 18 (20° wedge, 35° ice cone, 100mm/s)

Step No. (Disp.)	Nominal contact area (mm ²)	Nominal pressure (MPa)	Activated contact area (mm ²)	Activated pressure (MPa)	A _{act.} /A _{nom.} (%)	P _{act.} /P _{nom.} (%)
1 (10mm)	1677.39	3.17	647.06	39.39	38.58	1242.08
2 (20mm)	6708.78	4.13	3088.19	35.58	46.03	860.72
3 (35mm)	20544.62	0.24	5203.13	22.53	25.33	9270.22
				Avg.	36.64	3791.01

The difference became larger in the case of the cylindrical ice tests as shown in Table 5-3. There were no significant differences about the contact area. However, more than 100 times (as an average) and up to 300 times pressure differences were obtained. Measured activated pressure remained as similar magnitude compared to cone-shaped ice tests. In contrast, the nominal pressure values were lower than 1.0MPa at the most of the test steps, and this result produced a significant relative pressure difference (up to 300 times higher).

Table 5-3: Results of using cylindrical ice test against concave shape indenter

(a) Test 6 (30° wedge, cylindrical ice, 100mm/s)

Step No (Disp.)	Nominal contact area (mm ²)	Nominal pressure (MPa)	Activated contact area (mm ²)	Activated pressure (MPa)	A _{act.} /A _{nom.} (%)	P _{act.} /P _{nom.} (%)
1 (15mm)	7251.11	11.23	6140.38	28.27	84.68	251.86
2 (30mm)	16976.55	2.86	10721.38	28.42	63.15	995.20
3 (45mm)	29176.31	2.41	15439.44	25.75	52.92	1068.11
4 (60mm)	43850.40	1.25	15140.69	22.97	34.53	1835.78
5 (75mm)	57630.00	0.02	3561.13	15.33	6.18	62781.92
				Avg.	48.29	13386.57

(b) Test 9 (10° wedge, cylindrical ice, 1mm/s)

Step No (Disp.)	Nominal area (mm ²)	Nominal pressure (MPa)	Activated contact area (mm ²)	Activated pressure (MPa)	A _{act.} /A _{nom.} (%)	P _{act.} /P _{nom.} (%)
1 (15mm)	28774.43	1.20	22971.31	23.10	79.83	1920.03
2 (30mm)	49828.00	0.20	29172.06	22.74	58.55	11647.98
3 (45mm)	49828.00	0.13	4851.25	27.38	9.74	21348.23
4 (60mm)	49828.00	0.22	5057.13	24.09	10.15	10938.61
5 (75mm)	49828.00	1.74	8910.81	20.70	17.88	1187.03
				Avg.	35.23	9408.37

5.2. Effect of Concave Shape Indenter

5.2.1. Definition of Representative Load

Three types of data are available; time (sec), displacement (mm), and load (kN) after the laboratory ice tests. Based on the obtained load and displacement (or time), the ‘force-

displacement' history curve can be plotted. Prior to analyzing the test data, the first step is defining the 'representative' load at each force-displacement history curves. A suitable representative load allows the results from the different cases to be compared based on a single parameter which reasonably defines the magnitude of the load and thus simplifies the comparison. In this study, two different load defining methods were evaluated.

The simplest way to determine the 'representative' load in the force-displacement history curve is using the mean (average) value. In this case, the mean value can be calculated easily, simply by averaging the measured load from a zero to the maximum displacement of the force-displacement history curve.

When the force-displacement curve is gradually increased, applying the mean value as the representative load is reasonable. However, it is insufficient to apply the mean value as a representative load for any force-displacement curves when the curve tends to increase dramatically. For this reason, applying the mean load as the representative load is a case sensitive. Therefore, a different approach needs to be considered.

5.2.1.1. Linear Regression Equation as Representative Load

Using a regression equation to determine a representative load was considered as an alternative method. Test data (applied in the previous section) were adopted for direct comparison in Figure 5-1. The slope of each test was expressed as 'Ice crushing resistance index (ICRI)' as the representative expression (unit: kN/mm). A term 'Resistance' defined as "*the capacity of a*

structure or component to resist the effects of loads” in the field of ‘Load and resistance factor design (LRFD)’ for structural steel design specifications and code (Arora and Wang, 2006). When the ICRI of the linear relationship is known, the load can be obtained by multiplying the desired displacement with the ICRI, if a direct comparison is to be made for any specific condition.

The value of the maximum load on the curve (see Figure 5-1) was measured as 63.3kN and the calculated value, followed by a linear regression equation, was 39.9kN (about 63.1%). The percentage, 63.1%, is still not an ideal result; however, the value obtained using a linear regression equation is more convincing compared to the simple average value.

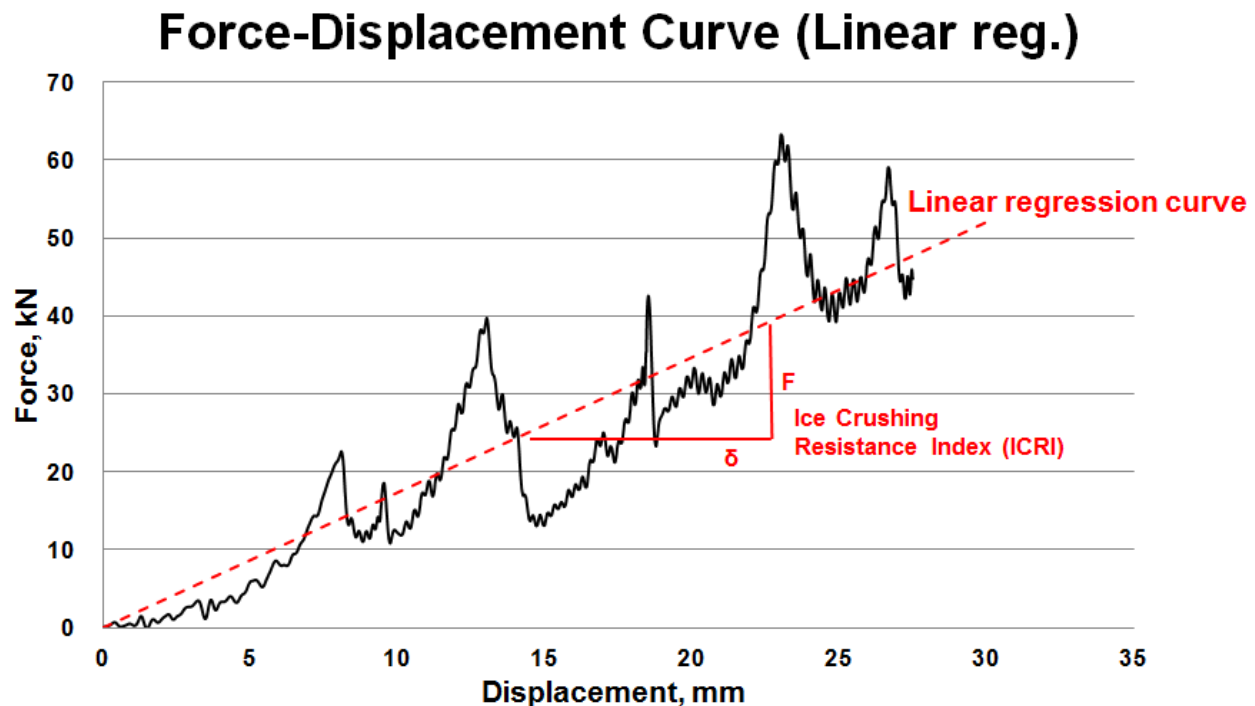


Figure 5-1: Determination of representative load using the linear regression equation (Case 1)

Force-displacement history curves where the load tends to increase rapidly, was also evaluated using the linear regression equation as shown in Figure 5-2. Similarly, the maximum load was compared. 396.9kN was measured as the maximum load in the force-displacement history curve, whereas the linear regression equation showed that it was 189.6kN (about 47.8%, which is close to 50%). The percentage difference between the linear regression computed equation and manually computed mean load was about double (increase in positive).

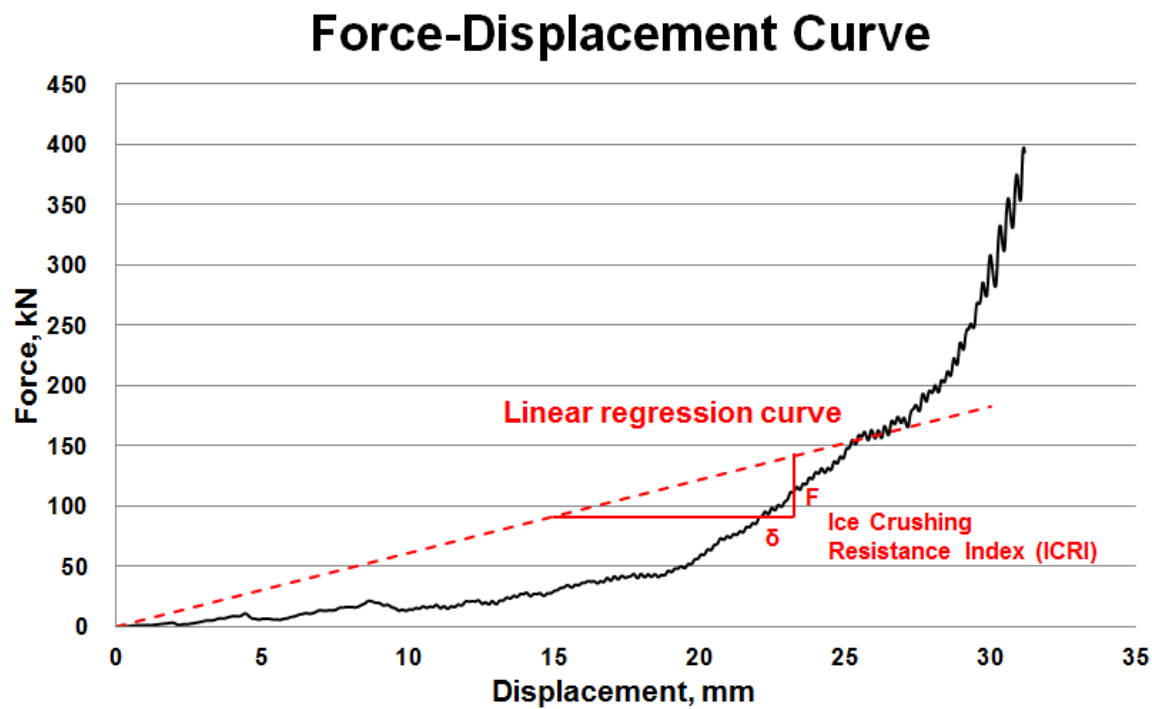


Figure 5-2: Determination of representative load using the linear regression equation (Case 2)

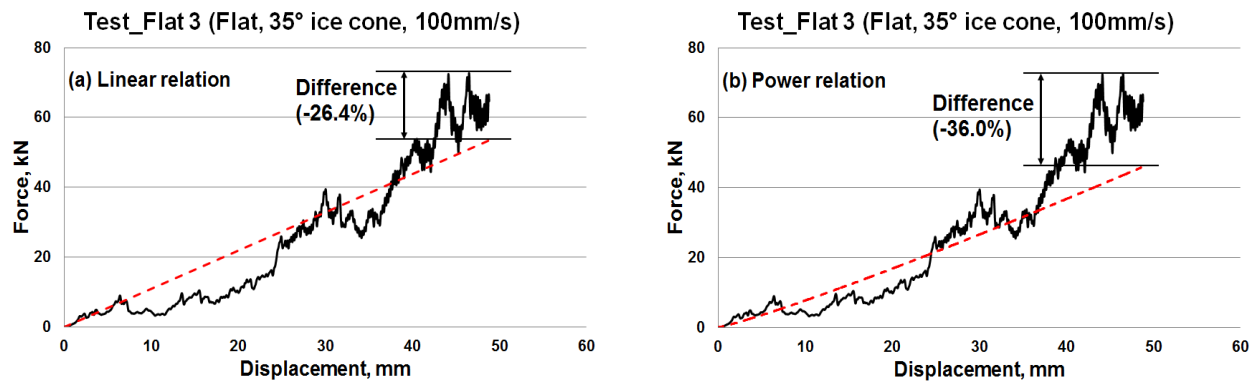
The purpose of not using power or exponential relationship to derive the regression equations was intended to reduce the number of variables required for the computation. There is only one variable, the ICRI, in the linear regression equation. However, there will be two variables, if the power or exponential regression equation was considered.

Adopting more variables will increase the complexity of regression equations and as well increase the source of error. Accordingly, the linear regression equation was applied in order to analyze the experimental data in the simplest way. The result of applying the power and exponential relationships will be also considered for the verification purpose of the feasibility of adopting the linear relationship, in subsequent section.

5.2.2. Derivation of Regression Equation

5.2.2.1. Regression curve comparison

Figures 5-3 to 5-5 show the comparison of regression curves followed by respective relationships, which are linear, power, exponential and modified exponential relationships (3 tests were selected, for each indenter shape). Primary evaluations of the results through Figures 5-3 to 5-5, the linear relationship regression equation was evaluated on the basis of this study. In addition to regression curve trends, comparison of the resulting values was obtained by regression equation, and the experimental results were performed to verify the feasibility of applying the linear relationship as a representative regression relationship.



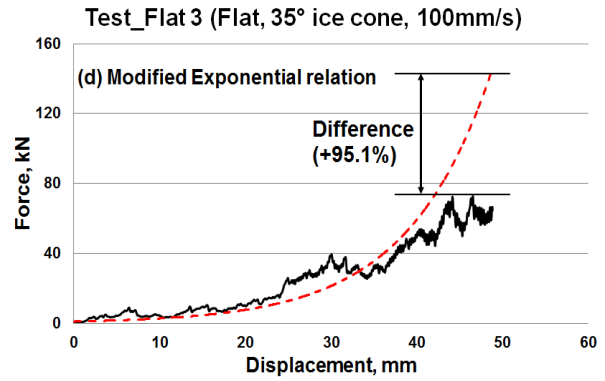
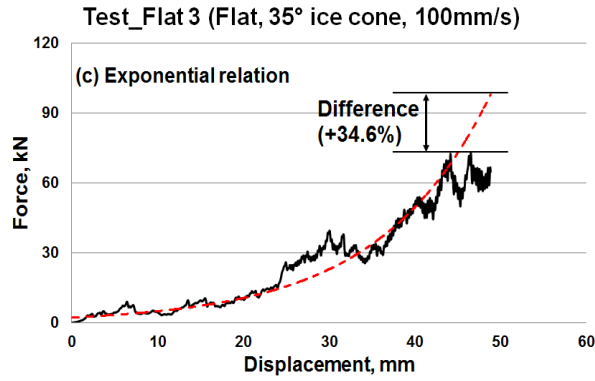


Figure 5-3: Comparison of regression curve (Flat Test 3: Flat, 35° ice cone, 100mm/s)

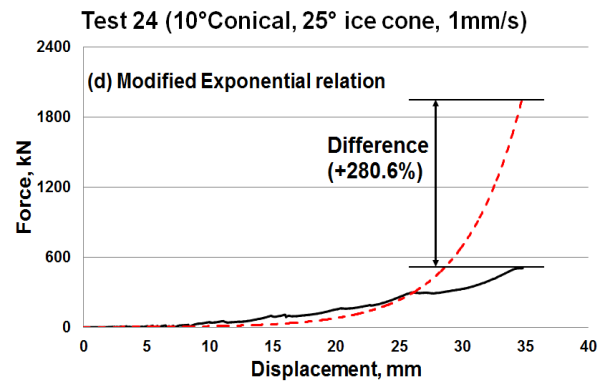
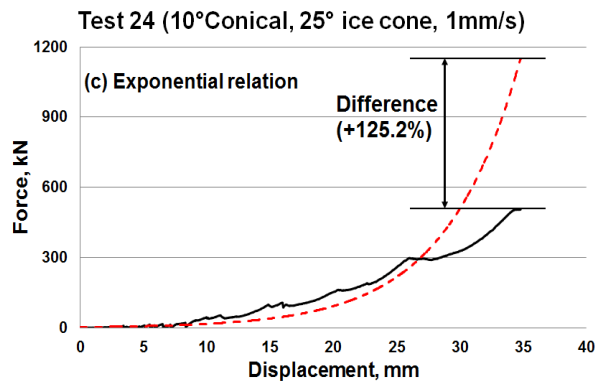
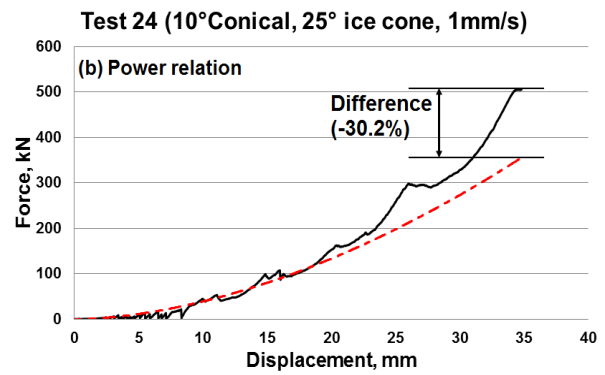
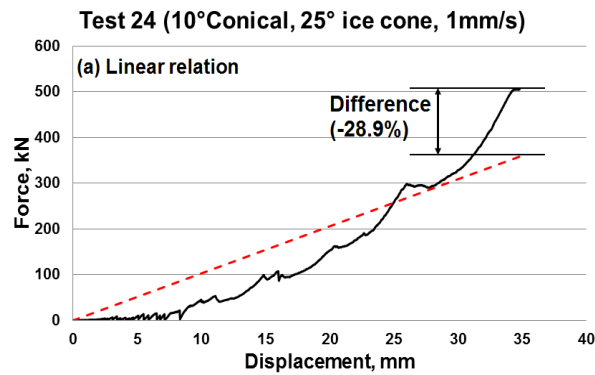


Figure 5-4: Comparison of regression curve (Test 24: 10° Conical, 25° ice cone, 1mm/s)

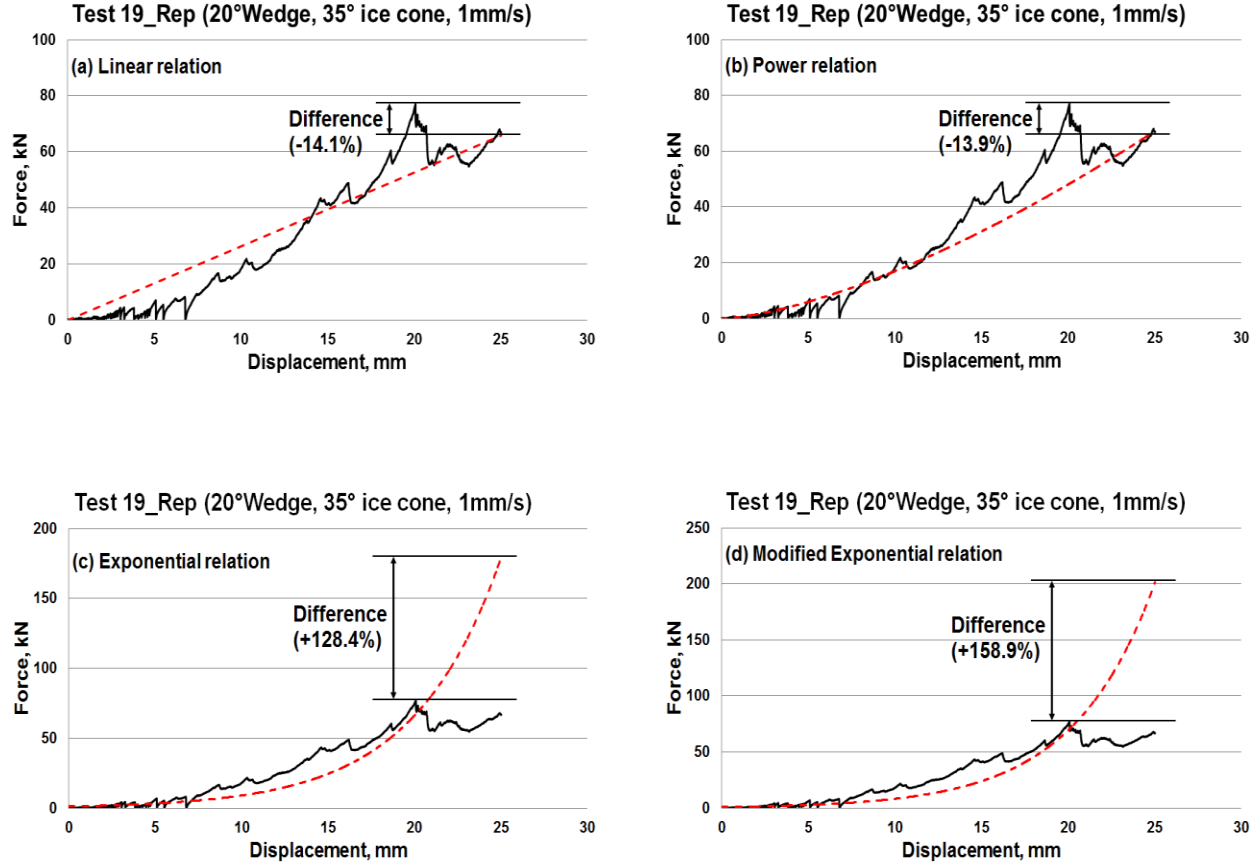


Figure 5-5: Comparison of regression curve (Test 19_Rep: 20° Wedge, 35° ice cone, 1mm/s)

Comparison of regression curves showed that the linear and power relationships were the most similar regression curves compared to experimental results. However, the difference between the two relationships was less than 10%, respectively. Therefore, a further evaluation was conducted through each regression parameter from derived regression equations.

In this section, comparison of the load at particular displacement ($\delta=40\text{mm}$, which is randomly chosen) was carried out to verify the validity of applying the linear relationship (Figures 5-6 and 5-7).

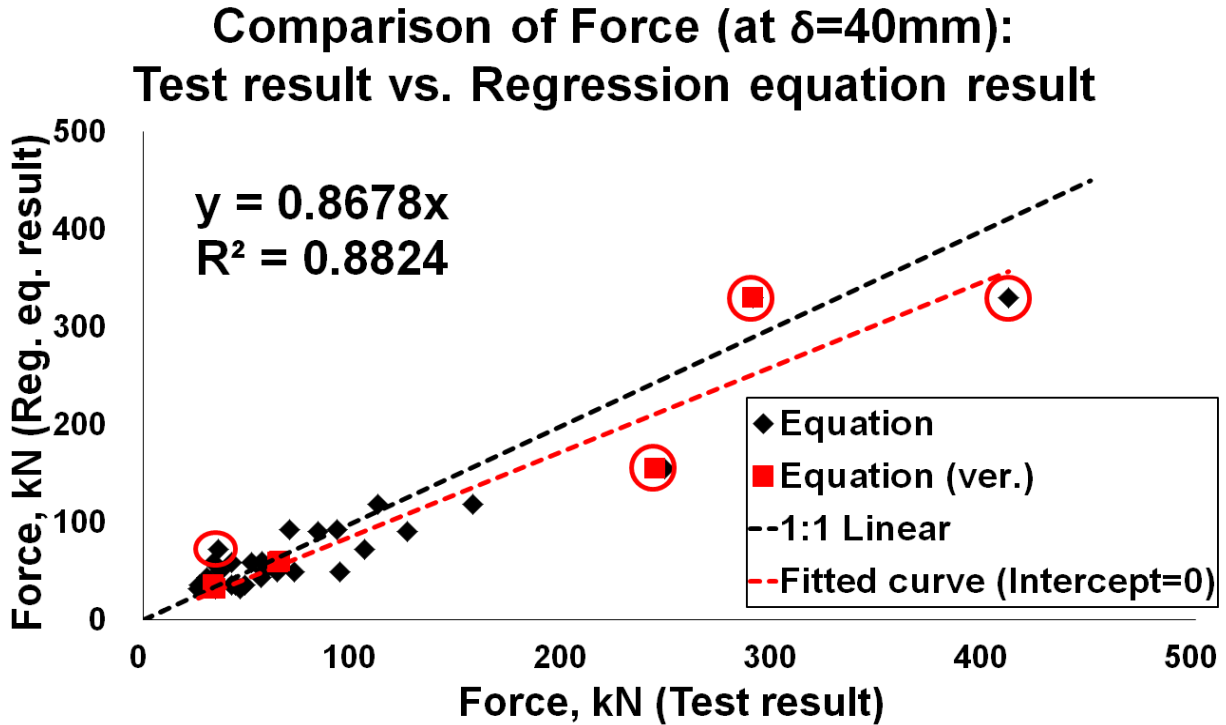


Figure 5-6: Test result vs. regression equation result of force (linear relationship)

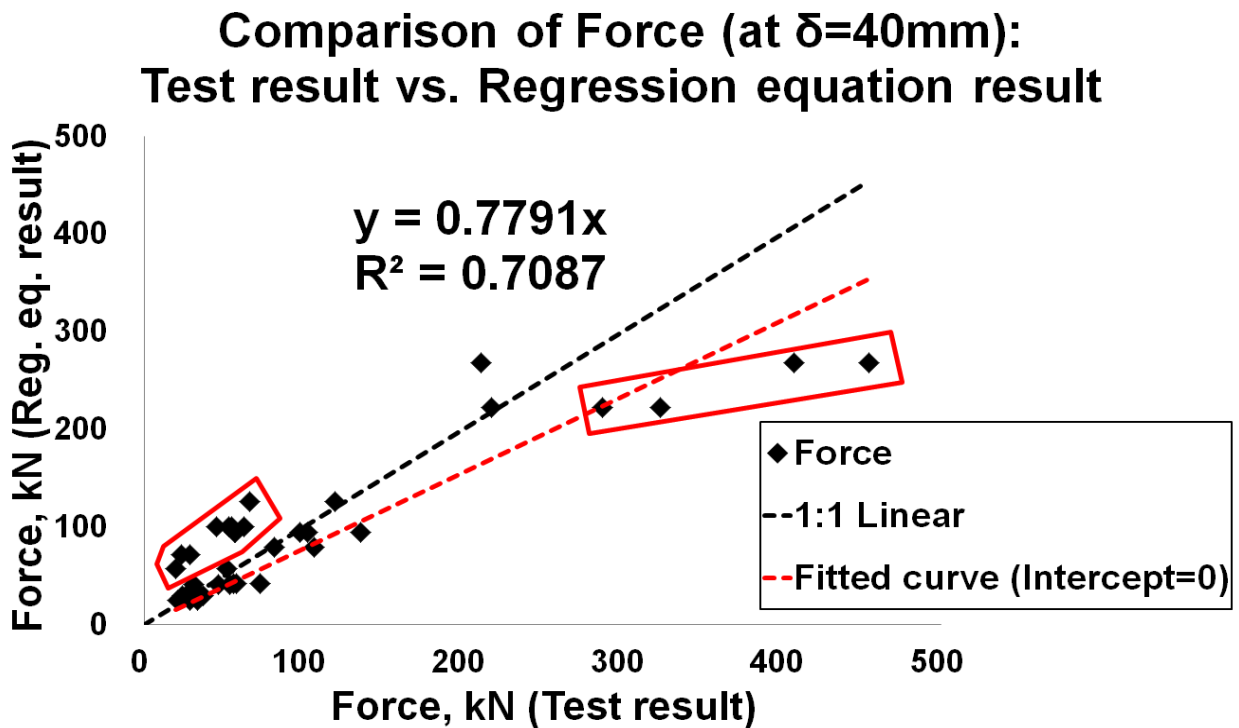


Figure 5-7: Test result vs. regression equation result of force (power relationship)

According to the comparison of force values (see Figures 5-6 and 5-7), the result of linear relationship, rather than the power relationship, confirmed that the force can be predicted relatively accurately compared to the experimental results. Therefore, analysis was performed applying the linear relationship in this study.

5.2.2.2. Determination of ICRI: Test Result

Table 5-4 shows the results of determined ICRI using the linear regression equation.

Table 5-4: Results of ICRI (Test result)

Test No.	Indenter shape	Indenter angle (°)	Cone angle (°)	Test speed (mm/s)	ICRI (Test result)
-	Flat	0	25	1	3.13
-	Flat	0	25	1	2.07
-	Flat	0	25	100	1.04
-	Flat	0	25	100	0.84
-	Flat	0	25	100	1.28
-	Flat	0	35	1	1.59
-	Flat	0	35	1	1.80
-	Flat	0	35	1	2.34
-	Flat	0	35	100	0.67
-	Flat	0	35	100	0.86
-	Flat	0	35	100	1.10
Test 24	Conical	10	25	1	10.28
Test 28	Conical	10	25	1	6.21
Test 25	Conical	10	25	100	6.08

Test No.	Indenter shape	Indenter angle (°)	Cone angle (°)	Test speed (mm/s)	ICRI (Test result)
Test 25_Rep	Conical	10	25	100	6.19
Test 29	Conical	10	25	100	6.78
Test 26_Rep	Conical	10	35	100	3.91
Test 27	Conical	10	35	1	0.87
Test 27_Rep	Conical	10	35	100	0.89
Test 3	Wedge	10	25	1	1.40
Test 4	Wedge	10	25	100	1.73
Test 16	Wedge	10	25	100	2.31
Test 1	Wedge	10	35	1	0.92
Test 13	Wedge	10	35	1	1.44
Test 17	Wedge	20	35	1	1.40
Test 19	Wedge	20	35	1	0.76
Test 2	Wedge	10	35	100	0.85
Test 14	Wedge	10	35	100	1.05
Test 14_Rep	Wedge	10	35	100	1.20
Test 19_Rep	Wedge	20	35	1	2.63
Test 18	Wedge	20	35	100	0.65
Test 20	Wedge	20	35	100	1.15

Prior to deriving a regression equation, six randomly chosen test results were excluded to be utilized for verification purposes at later on. The excluded six test results are shown in Table 5-5.

Table 5-5: Result of ICRI for the verification purpose (Test result)

Test No.	Indenter shape	Indenter angle (°)	Cone angle (°)	Test speed (mm/s)	ICRI (Test result)
-	Flat	0	25	100	1.60
-	Flat	0	35	100	0.83
Test 15	Wedge	10	25	100	1.62
Test 20_Rep	Wedge	20	35	100	0.85
Test 28_Rep	Conical	10	25	1	7.24
Test 26	Conical	10	35	1	2.78

The Design - Expert[®] program was adopted to derive the regression equations considering each of the variables. Originally, test plans were not set up for ‘Design of Experiment (DOE)’ in this study. Therefore, evaluation of the interaction between individual factors cannot be performed for further analysis. However, it is possible to use the Design-Expert[®] software only for the purpose of the derivation of regression equations.

5.2.2.3. Derivation of Regression Equation: Linear Relationship

The regression equation was derived based on the test data as shown in Table 5-4. Figure 5-8 shows the 1:1 plot of ‘Test result vs. Regression equation result’. Points marked as black-color represents the test results that were used to derive the regression equations. Points marked as red-color represents the selected data for verification purposes as mentioned.

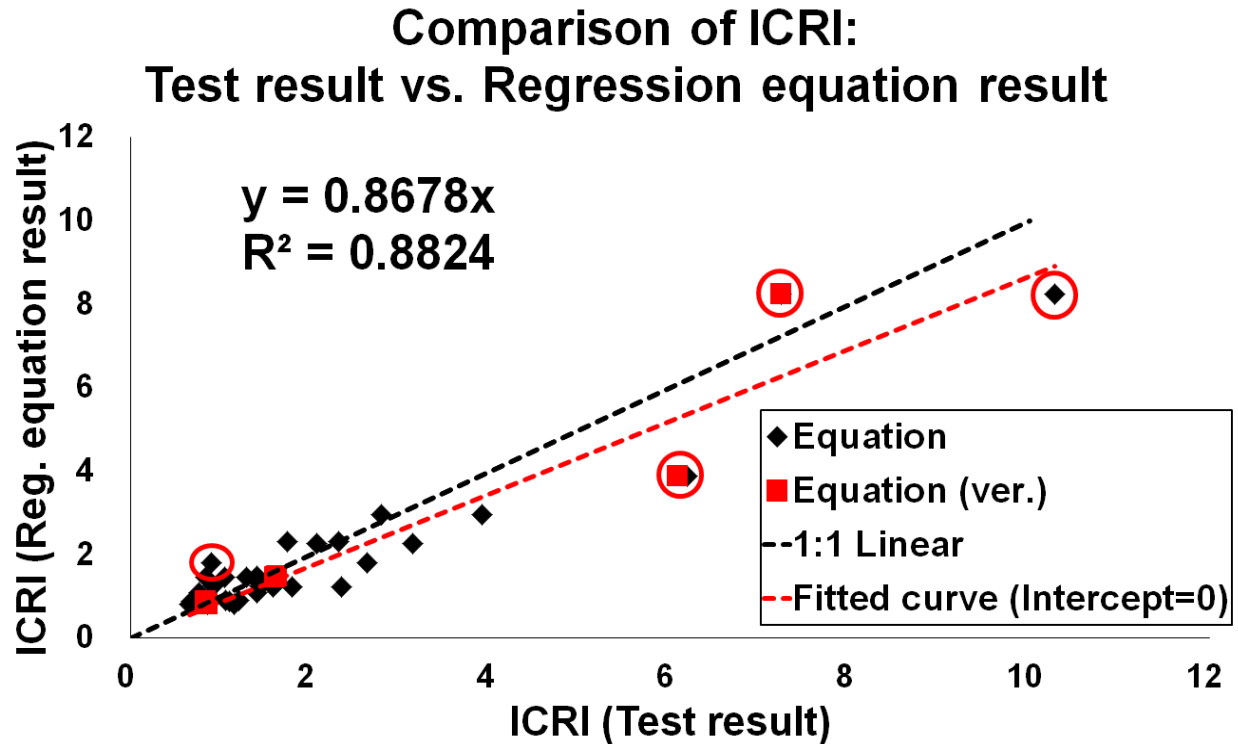


Figure 5-8: Test result vs. regression equation result (ICRI)

Results of obtained regression equations well predicted the ICRI, except the data points marked with a red circle. In addition, excluded test data points for the verification purpose also showed a good prediction by derived regression equations.

Equations (5-1) to (5-3) represents regression equations for each indenter shapes derived by using the Design-Expert®. In order to exclude the two-factor interactions, regression equations were solely composed by a single-factor term. The optimal results were acquired by the inverse square root transform.

$$1/\text{Sqrt}(\text{ICRI}_{\text{Flat}}) = (0.078692) + (6.10134\text{E} - 03 \times \text{Indenter angle}) + (0.023369 \times \text{Cone angle}) + (1.61709\text{E} - 03 \times \text{Test speed}) \quad (5-1)$$

$$1/\text{Sqrt}(\text{ICRI}_{\text{Wedge}}) = (0.011971) + (6.10134\text{E} - 03 \times \text{Indenter angle}) + (0.023369 \times \text{Cone angle}) + (1.61709\text{E} - 03 \times \text{Test speed}) \quad (5-2)$$

$$1/\text{Sqrt}(\text{ICRI}_{\text{Conical}}) = (-0.29881) + (6.10134\text{E} - 03 \times \text{Indenter angle}) + (0.023369 \times \text{Cone angle}) + (1.61709\text{E} - 03 \times \text{Test speed}) \quad (5-3)$$

Table 5-6 shows a comparison of ICRI between the test results and the derived regression equations.

Table 5-6: Comparison of ICRI (Test result vs. Derived by regression equation)

Indenter shape	Indenter angle (°)	Cone angle (°)	Test speed (mm/s)	ICRI (A) (Test result)	ICRI (B) (Reg. equation)	Ratio (A/B)
Flat	0	25	1	3.13	2.26	1.38
Flat	0	25	1	2.07	2.26	0.91
Flat	0	25	100	1.04	1.47	0.71
Flat	0	25	100	0.84	1.47	0.57
Flat	0	25	100	1.28	1.47	0.87
Flat	0	25	100	1.60	1.47	1.09
Flat	0	35	1	1.59	1.24	1.28
Flat	0	35	1	1.80	1.24	1.45
Flat	0	35	1	2.34	1.24	1.89
Flat	0	35	100	0.67	0.89	0.75
Flat	0	35	100	0.86	0.89	0.96
Flat	0	35	100	1.10	0.89	1.23
Flat	0	35	100	0.83	0.89	0.93

Indenter shape	Indenter angle (°)	Cone angle (°)	Test speed (mm/s)	ICRI (A) (Test result)	ICRI (B) (Reg. equation)	Ratio (A/B)
Conical	10	25	1	10.28	8.26	1.24
Conical	10	25	1	6.21	8.26	0.75
Conical	10	25	1	7.24	8.26	0.88
Conical	10	25	100	6.08	3.87	1.57
Conical	10	25	100	6.19	3.87	1.60
Conical	10	25	100	6.78	3.87	1.75
Conical	10	35	1	2.78	2.95	0.94
Conical	10	35	1	3.91	2.95	1.32
Conical	10	35	1	0.87	2.95	0.29
Conical	10	35	100	0.89	1.82	0.49
Conical	10	35	100	2.63	1.82	1.45
Wedge	10	25	100	1.40	1.49	0.94
Wedge	10	25	100	1.62	1.49	1.09
Wedge	10	25	1	1.73	2.30	0.75
Wedge	10	25	1	2.31	2.30	1.00
Wedge	10	35	1	0.92	1.26	0.73
Wedge	10	35	1	1.44	1.26	1.14
Wedge	20	35	1	1.40	1.10	1.27
Wedge	20	35	1	0.76	1.10	0.69
Wedge	10	35	100	0.85	0.90	0.94
Wedge	10	35	100	1.05	0.90	1.16
Wedge	10	35	100	1.20	0.90	1.33
Wedge	20	35	100	0.65	0.81	0.81
Wedge	20	35	100	1.15	0.81	1.42
Wedge	20	35	100	0.85	0.81	1.06

5.2.2.4. Assessment of Regression Equation: Power and Exponential Relationship

As mentioned earlier, result values using the power and the exponential relationships were also compared for the further validation purpose.

5.2.2.4.1. Evaluation of Power Relationship

Power relationship can be defined as following Equation (5-4);

$$F_{\text{power}} = F_0 x^{\text{ex}} \quad (5-4)$$

Where,

F_0 = force index (kN)

x = displacement (mm)

ex = power term

There are two variables, F_0 and ex , which needs to be determined using power relationship.

Figures 5-9 and 5-10 show the 1:1 plot of ‘Test result vs. Regression equation result’ of each variable (F_0 and ex).

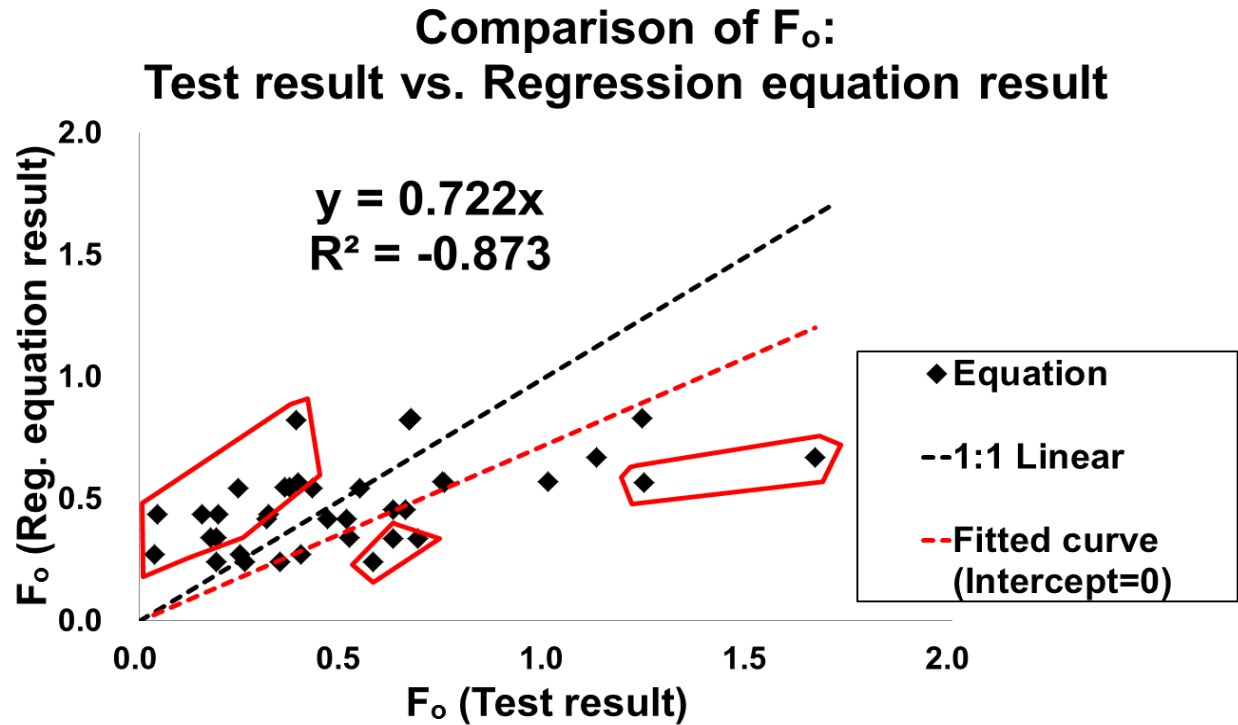


Figure 5-9: Test result vs. regression equation result using the power relationship (F_o)

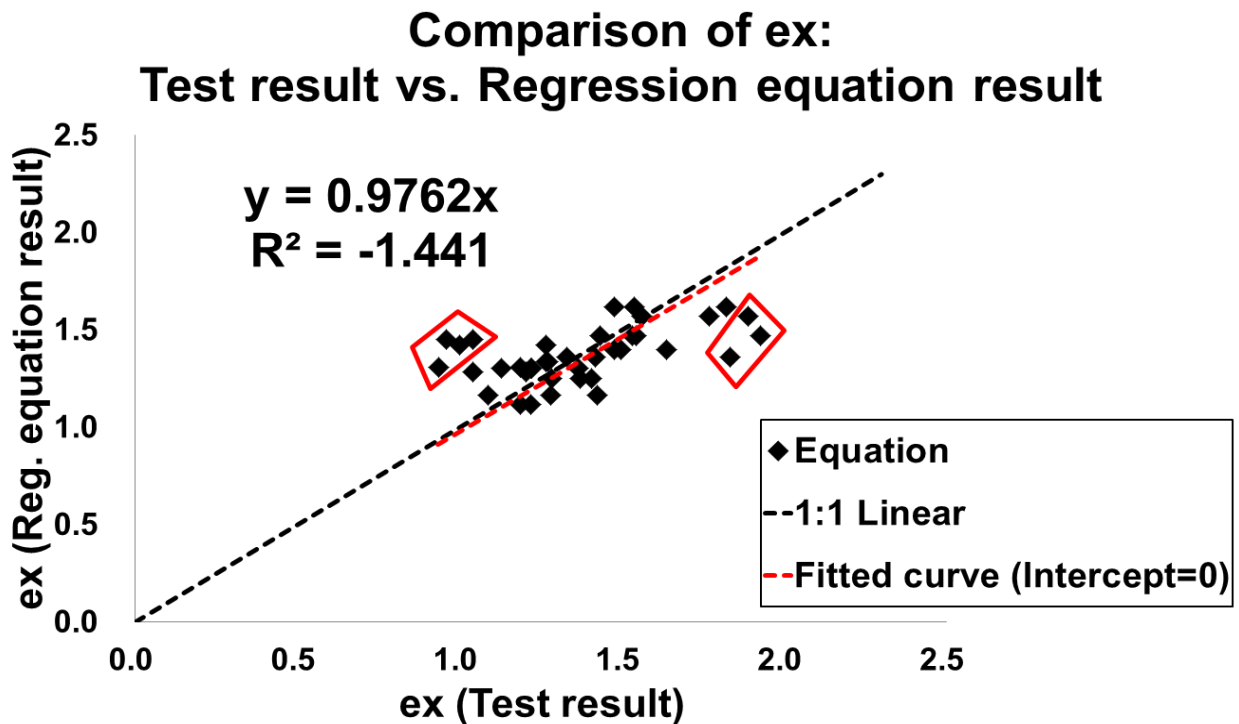


Figure 5-10: Test result vs. regression equation result using the power relationship (ex)

In the case of the term ‘ex’, comparison between test results and values derived by the regression equations showed a good agreement except at some points (marked within red boundaries), as shown in Figure 5-10. However, the difference of the term ‘ F_0 ’ showed a large variation as shown in Figure 5-9. As mentioned above, load value is determined by two variables, F_0 and ex using the power relation. Therefore, influence on one variable will tend to affect the other variable also. For this reason, the results obtained through the power relationship did not show a good comparison.

5.2.2.4.2. Evaluation of Exponential Relationship

The exponential relationship was also evaluated in the same manner. The exponential relation can be defined by following Equation (5-5);

$$F_{\text{exponent}} = F_0 e^{\text{ex} \cdot x} \quad (5-5)$$

Where,

F_0 = force index (kN)

x = displacement (mm)

ex = exponential term

F_0 and ex need to be determined in a manner similar as the power relationship. Figures 5-11 and 5-12 show the 1:1 plot of ‘Test result vs. Regression equation result’ of each variable, F_0 and ex.

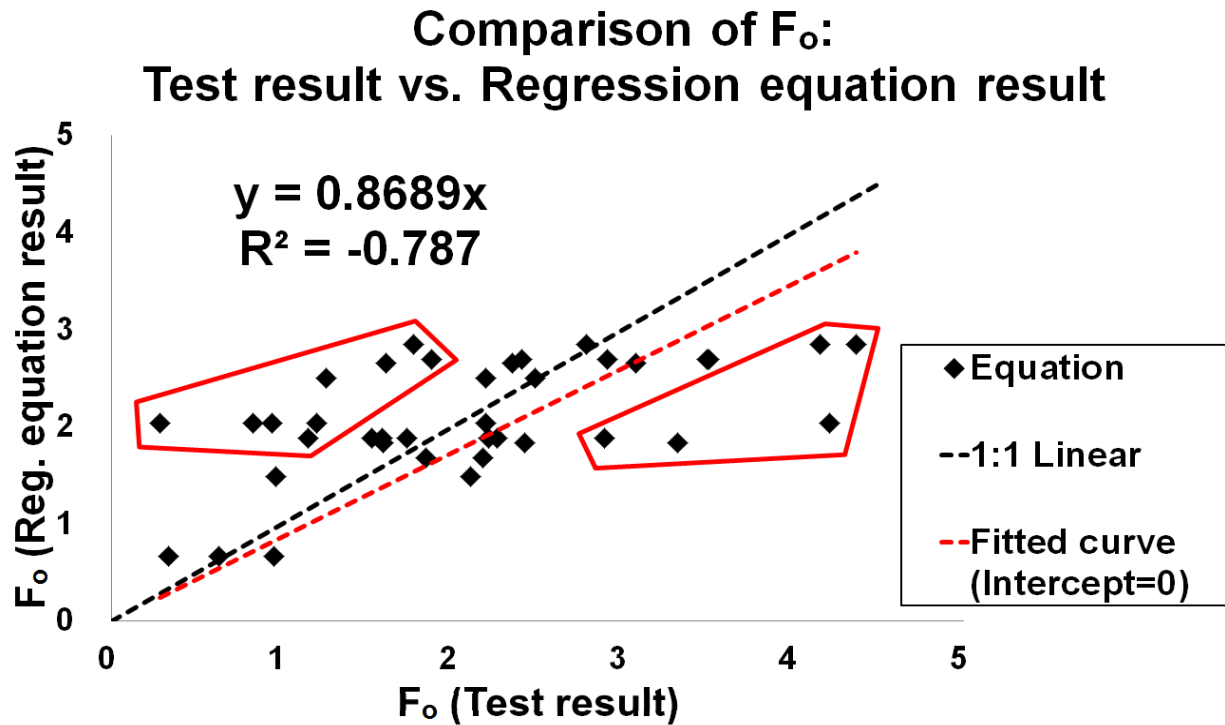


Figure 5-11: Test result vs. regression equation result using the exponential relationship (F_o)

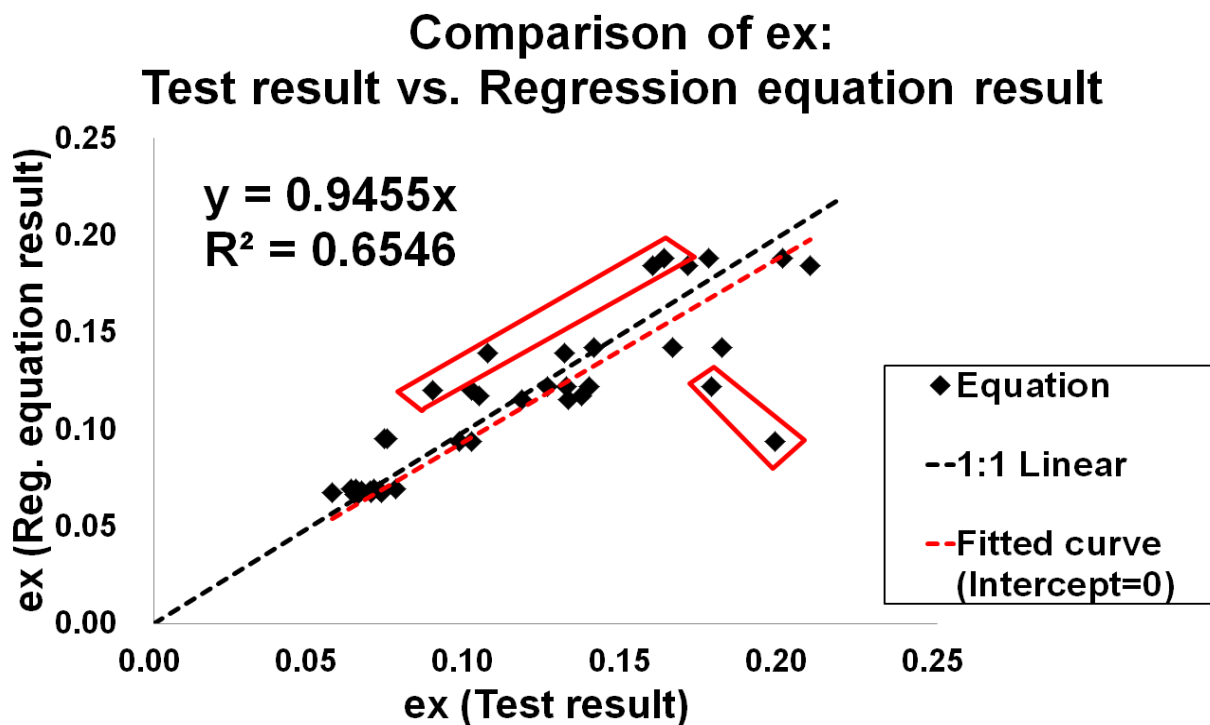


Figure 5-12: Test result vs. regression equation result using the exponential relationship (ex)

Similar to the power relationship, F_0 showed a significant difference using the exponential relationship. In addition, the total load (F_0) was not properly evaluated by the exponential relationship, since the scatter is large.

5.2.2.4.3. Evaluation of Modified Exponential Relationship

In addition, the modified exponential relationship was evaluated, where the term ' F_0 ' was fixed as '1.0'. In this case, a variable, which need to determine, was reduced as one (only ex) compared to the traditional exponential relationship (where the variables are two). The relationship equation is identical except that F_0 , which was fixed.

$$F_{\text{Exponent}} = F_0 e^{\text{ex} \cdot x} \quad (5-6)$$

Where,

F_0 = force index (kN) = 1.0 (fixed value)

x = displacement (mm)

ex = exponential term

As shown in Figure 5-13, comparison between test results and regression equation results has given a good agreement using the modified exponential relationship, unlike power and exponential relationships. In addition, the variable to be determined was also reduced as a single variable. Therefore, a further comparison between the linear and modified exponential

relationships is required to determine on the best method to obtain more effective and accurate result. For the comparison purpose, calculated total loads followed by the ICRI (linear relationship), and the exponential term (modified exponential relationship) at specific displacements were compared (in Table 5-7).

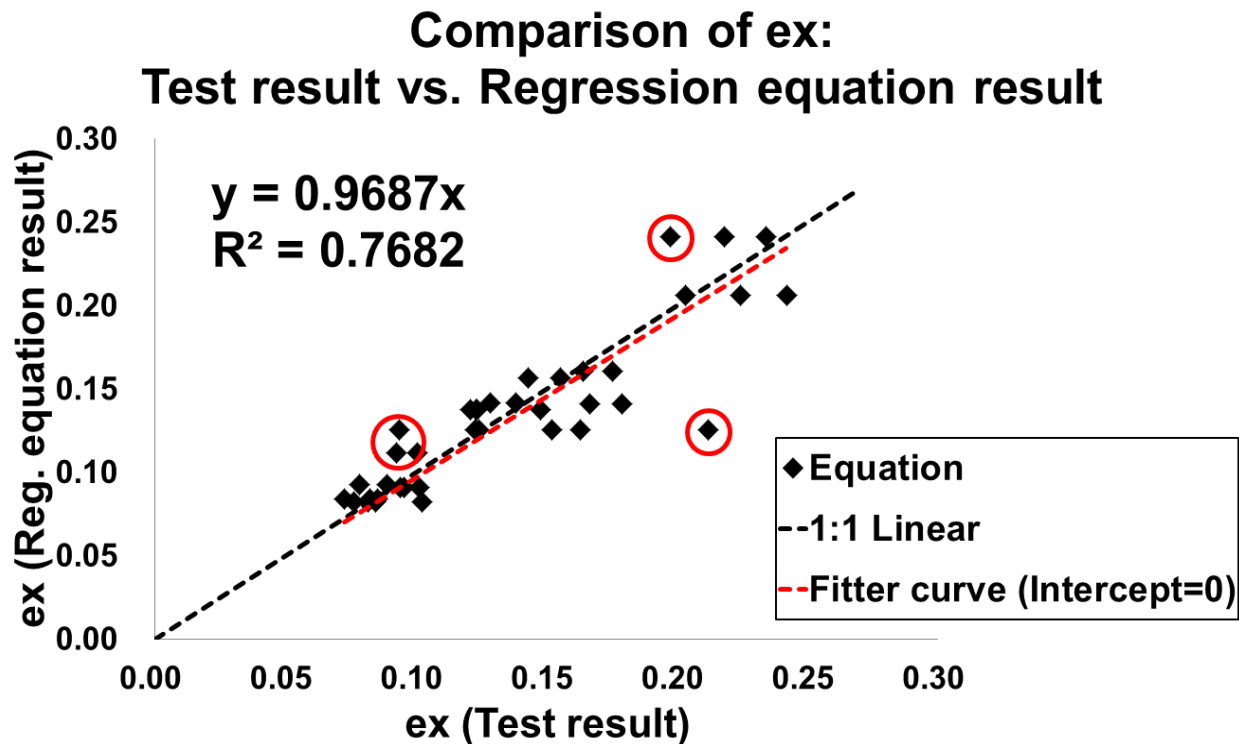


Figure 5-13: Test result vs. regression equation result using modified exponential relationship (ex)

Table 5-7 represents a direct comparison of derived total loads using the linear and modified exponential relationships at specific displacements.

Table 5-7: Comparison of calculated force (linear vs. modified exponential relationship)

Test condition	Load from linear relationship (kN)			Load from modified exponential relationship (kN)	
	at x=20mm	at x=40mm		at x=20mm	at x=40mm
Flat, 25° cone, 1mm/s	45.29	90.58		22.88	523.33
Flat, 25° cone, 100mm/s	29.41	58.82		15.70	246.55
Flat, 35° cone, 1mm/s	24.49	49.58		6.17	38.02
Flat, 35° cone, 100mm/s	17.86	35.71		5.20	27.04
Conical 10°, 25° cone, 1mm/s	165.10	330.21		125.17	15667.90
Conical 10°, 25° cone, 100mm/s	77.46	154.92		61.82	3821.34
Conical 10°, 35° cone, 1mm/s	59.10	118.20		12.30	151.29
Conical 10°, 35° cone, 100mm/s	36.34	72.69		9.36	87.67
Wedge 10°, 25° cone, 1mm/s	29.82	59.65		24.89	619.29
Wedge 10°, 35° cone, 100mm/s	46.08	92.15		16.83	283.25
Wedge 10°, 35° cone, 1mm/s	25.11	50.21		6.40	40.95
Wedge 10°, 35° cone, 100mm/s	18.05	36.10		5.37	28.83
Wedge 20°, 35° cone, 1mm/s	22.00	43.99		17.05	290.61
Wedge 20°, 35° cone, 100mm/s	16.13	32.25		12.30	151.41

As mentioned, any of methods cannot give relevant results for the evaluation of total loads. However, it is necessary to decide on the most suitable method to be used for subsequent analyses. As shown in Table 5-7, calculated total load magnitudes between two methods used represented a significant difference in most of the test, at chosen displacements. Modified exponential relationship demonstrated a good agreement in respect of the exponential term as shown in Figure 5-13. However, the results of total load shown in that column revealed the following issues (see Table 5-7);

- 1) Total load results using the 35° ice cone showed excessive low results at 20mm displacement.
- 2) Excessively large loads were derived, which was not measured during the actual tests, for some cases, For example, the maximum 15MN (using 25° cone ice with 1mm/s test speed) and 3MN (using 25° cone ice with 100mm/s test speed) was obtained for a conical-shaped indenter. However, it was observed that no test results which reached such high load values.

In addition, the results of the wedge-shaped indenter shows a high load value of 600kN, which was not measured in the actual test. In contrast, the derived results obtained from the linear relationship were closer to the measured test values. As a result, applying a regression equation using linear regression was judged to be the more appropriate method for further analysis.

5.2.3. Effect of Structural Shape

The regression equation (based on the linear relationship, as discussed in the previous section) was derived by including test parameters (indenter angle, test speed and ice cone angle). The effects of structural shape were evaluated using the regression equation.

Table 5-8 shows comparison results of 'Flat vs. Wedge shape' indenter. The resulting values of the ICRI were calculated using the Equation (5-1) and (5-2). The values in 'red-bold color' indicate the ratio obtained between flat and the 10° wedge indenters. The average ratio between flat and the 10° wedge indenters gave a value of 1.01. This states that the difference between two

indenter shapes is only about 1%. The 1% difference indicates that there were no significant effects between the two indenter shapes.

The values in ‘blue-bold color’ indicate the ratio obtained between the shapes of flat and the 20° wedge indenter. The average ratio between the flat and the 20° wedge indenter shows a value of 0.88, and this indicates that a greater ice load occurred for flat indenters compared to the 20° wedge indenter. In other words, the flat indenter showed a 12% larger load than wedge-shaped indenters.

Table 5-8: Comparison result: Flat vs. Wedge shape indenter

	Indenter angle (°)	Cone angle (°)	Test speed (mm/s)	ICRI	Ratio (B/A)	Ratio (C/A)		Ratio (C/B)
Flat (A)	0	25	1	2.26				
Wedge (B)	10	25	1	2.30	1.02			
Wedge (C)	20	25	1	1.93		0.85		0.84
Flat (A)	0	25	100	1.47				
Wedge (B)	10	25	100	1.49	1.01			
Wedge (C)	20	25	100	1.29		0.88		0.87
Flat (A)	0	35	1	1.24				
Wedge (B)	10	35	1	1.26	1.01			
Wedge (C)	20	35	1	1.10		0.89		0.87
Flat (A)	0	35	100	0.89				
Wedge (B)	10	35	100	0.90	1.01			
Wedge (C)	20	35	100	0.81		0.91		0.90
				Avg.	1.01	0.88		0.87

Table 5-9 shows comparison results of ‘Flat vs. Conical shape’ indenter. Unlike the previous (wedge-shaped indenter case), significant effects of indenter shapes were observed using conical-shaped indenter. The measured average ratio between the two indenter shapes recognized as 2.68 on average. This means that measured loads against conical indenter tends to show about 268% larger loads compared to the flat indenter.

Table 5-9: Comparison result: Flat vs. Conical shape indenter

	Indenter angle (°)	Cone angle (°)	Test speed (mm/s)	ICRI	Ratio (B/A)
Flat (A)	0	25	1	2.26	
Conical (B)	10	25	1	8.26	3.65
Flat (A)	0	25	100	1.47	
Conical (B)	10	25	100	3.87	2.63
Flat (A)	0	35	1	1.24	
Conical (B)	10	35	1	2.95	2.38
Flat (A)	0	35	100	0.89	
Conical (B)	10	35	100	1.82	2.04
				Avg.	2.68

Overall, significant effects between two indenter shapes can be found in Table 5-9 at a smaller cone angle and apparently low test speed. Again, it was confirmed that the effects of conical-shaped indenter was significant.

5.2.4. Effect of Cone Angle

Tables 5-10 and 5-11 show the comparison results of the effects of cone angle. As discussed, relatively larger loads occurred when the cone angle was smaller as shown in Tables 5-10 and 5-11. When the test speed was 1mm/s, the average ratio difference between the cone angles was 0.56, about the half. In addition, the difference between the two cone angles were 0.61 when the test speed was 100mm/s. Overall, higher ice loads are expected as the angle of cone decrease due to the behavior of ice-structure interaction (specifically, the magnitude of the loads), which is highly sensitive to the cone angle (which can be referred as the shape/size of ice sample).

Table 5-10: Comparison result at test speed 1mm/s

	Indenter angle (°)	Cone angle (°)	Test speed (mm/s)	ICRI	Ratio (B/A)
Flat (A)	0	25	1	2.26	
Flat (B)	0	35	1	1.24	0.55
Wedge (A)	10	25	1	2.30	
Wedge (B)	10	35	1	1.26	0.55
Wedge (A)	20	25	1	1.93	
Wedge (B)	20	35	1	1.10	0.57
				Avg.	0.56

Table 5-11: Comparison result at test speed 100mm/s

	Indenter angle (°)	Cone angle (°)	Test speed (mm/s)	ICRI	Ratio (B/A)
Flat (A)	0	25	100	1.47	
Flat (B)	0	35	100	0.89	0.61
Wedge (A)	10	25	100	1.49	
Wedge (B)	10	35	100	0.90	0.60
Wedge (A)	20	25	100	1.29	
Wedge (B)	20	35	100	0.81	0.63
				Avg.	0.61

5.2.5. Effect of Test Speed

Tables 5-12 and 5-13 show the comparison results of the effects of test speeds. As discussed, relatively large ice load was measured when the test speed was low, as shown in Tables 5-12 and 5-13, using the same cone angle.

When the cone angle was 25°, the average difference (ratio) between cone angles were about 0.66. In addition, the difference was about 0.72 when the cone angle was 35° with the same test speed, respectively. This result confirmed that the well-known understanding of ice mechanics, which is the low test speed (strain rate) induces a higher ice load compared to the high test speed.

Table 5-12: Comparison result using 25° ice cone

	Indenter angle (°)	Cone angle (°)	Test speed (mm/s)	ICRI	Ratio (B/A)
Flat (A)	0	25	1	2.26	
Flat (B)	0	25	100	1.47	0.65
Wedge (A)	10	25	1	2.30	
Wedge (B)	10	25	100	1.49	0.65
Wedge (A)	20	25	1	1.93	
Wedge (B)	20	25	100	1.29	0.67
				Avg.	0.66

Table 5-13: Comparison result using 35° ice cone

	Indenter angle (°)	Cone angle (°)	Test speed (mm/s)	ICRI	Ratio (B/A)
Flat (A)	0	35	1	1.24	
Flat (B)	0	35	100	0.89	0.72
Wedge (A)	10	35	1	1.26	
Wedge (B)	10	35	100	0.90	0.71
Wedge (A)	20	35	1	1.10	
Wedge (B)	20	35	100	0.81	0.74
				Avg.	0.72

5.2.6. Evaluation of the Effect of Ice Sample Shape

In this study, two different shapes of the ice samples were adopted to evaluate the effects of ice sample shapes (cone and cylindrical). Tests were conducted with identical conditions, and the effects were evaluated.

The regression equation based on the linear relation was derived in the same manner, and the ICRI of two different shapes of the ice sample was compared. Figure 5-14 shows the 1:1 plot of ‘Test result vs. Regression equation result’ of cylindrical ice. Overall, ICRI results were well predicted by the derived regression equation except for few points.

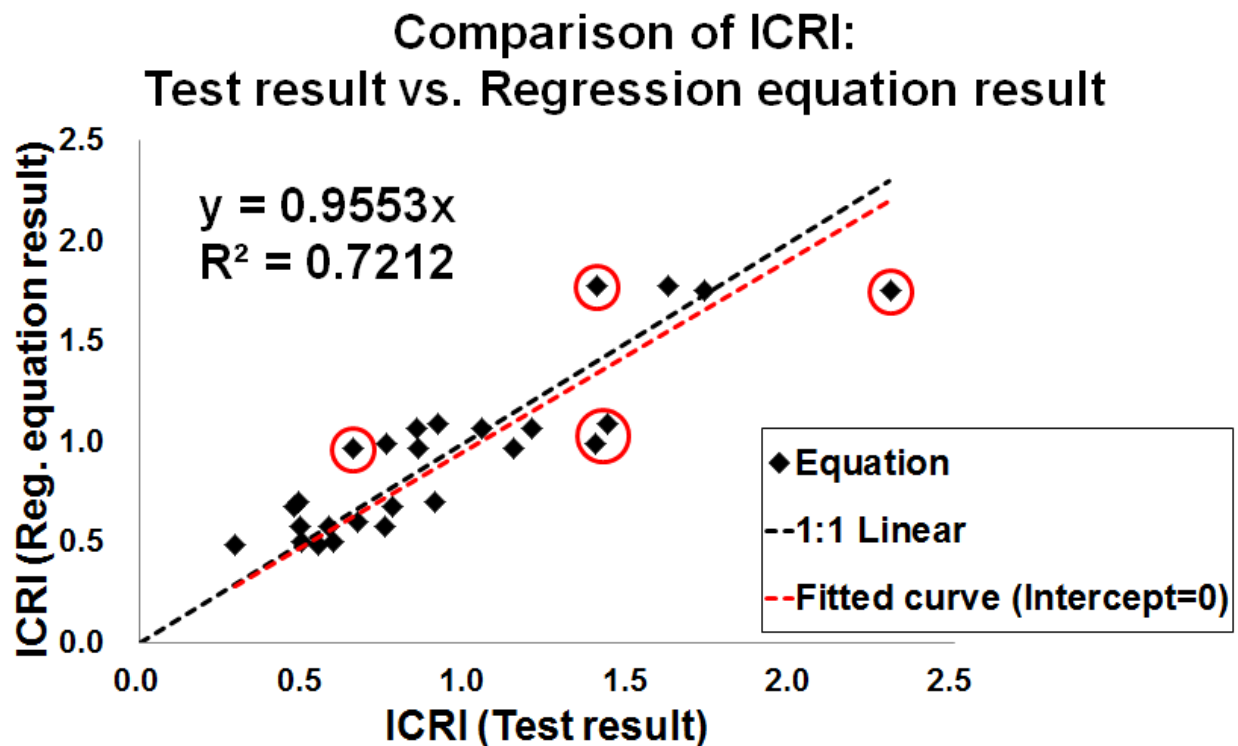


Figure 5-14: Test result vs. regression equation result of cylindrical ice (ICRI)

Table 5-14 shows the comparison of the ICRI between the ice sample shapes for each test condition. As shown in Table 5-14, cone-shaped ice sample showed a relatively large load compared to cylindrical ice. The values in ‘red-bold color’ indicate the ratio between 25° ice cone and cylindrical ice samples. The average ratio between the two ice sample shapes was obtained around 2.86. This indicates that the cone-shaped ice sample with a 25° cone angle produced nearly about 3 times larger loads compared to the cylindrical ice.

In addition, values in ‘blue-bold color’ indicate the ratio of the ICRI obtained for 35° ice cone and cylindrical ice samples. Results of load using cone-shaped ice sample represented larger loads (average ratio was 1.67) compared to the cylindrical ice sample at same test speeds. Values in ‘purple-bold color’ indicate the ratio between 25° and 35° ice cone. The average value was obtained about 0.59, and it can be seen that this is similar to that which was evaluated in the previous section.

Table 5-14: Comparison of results by ice sample shape

	Indenter angle (°)	Cone angle (°)	Test speed (mm/s)	ICRI	Ratio (B/A)	Ratio (C/A)	Ratio (C/B)
Cylindrical (A)	10	0	1	0.70			
Cone (B)	10	25	1	1.77	2.53		
Cone (C)	10	35	1	1.09		1.56	0.62
Cylindrical (A)	20	0	1	0.60			
Cone (B)	20	25	1	1.68	2.80		
Cone (C)	20	35	1	0.99		1.65	0.59
Cylindrical (A)	30	0	1	0.50			
Cone (B)	30	25	1	1.58	3.16		
Cone (C)	30	35	1	0.89		1.78	0.56
Cylindrical (A)	10	0	100	0.68			
Cone (B)	10	25	100	1.76	2.59		
Cone (C)	10	35	100	1.07		1.57	0.61
Cylindrical (A)	20	0	100	0.58			
Cone (B)	20	25	100	1.66	2.86		
Cone (C)	20	35	100	0.97		1.67	0.58
Cylindrical (A)	30	0	100	0.48			
Cone (B)	30	25	100	1.56	3.25		
Cone (C)	30	35	100	0.87		1.81	0.56
				Avg.	2.86	1.67	0.59

5.3. Discussion

5.3.1. Confinement Effect

The magnitude of ice loads and pressure developments are significantly influenced by the properties of ice (as a material) and as well by the confinement effect during the compressive ice crushing test. The term ‘Confinement’ mentioned here can be classified into two cases where, 1) confinement formed naturally by crushed (or broken piece of ice) ice during tests and 2) confinement artificially formed by a test apparatus. Ulan-Kvitberg et al. (2011) analyzed the effect of an ice holder as confinement during compressive ice tests, and compared the force-displacement curves. Figure 5-15 illustrates the formation of confinement in the case of flat indenters.

Using a ‘small cone angle’ ice sample represented higher ice loads (since larger amount of crushed ice has to be pushed transversely) compared to ‘large cone angle’ ice sample, as discussed in the previous section. The effects of the cone angle can be explained by the amount of available space between the ice sample and indenter (can be referred as confinement-formable space) as illustrated in Figure 5-15 (marked with the red color).

Crushed (or broken) ice during the collision may be removed immediately after ice-structure interaction. However, crushed ice can also remain in space between the indenter and the ice (marked in red color) due to re-freezing process or be confined by the remaining ice sample. This formation will keep contributing to the transverse load required to withstand additional ice loads.

In this respect, a wider-space between the two bodies means that the crushed ice can escape more freely compared to a narrow-space. For this reason, more crushed ice tends to get trapped between the space as illustrated in Figure 5-15 when the cone angles are relatively small, and this will result higher ice loads consequently.

The effect of confinement (by crushed ice) does not significantly affect, in the case of high speed (high strain rates) tests due to the frequent spalling events. A term spalling means that crushed ice did not tend to remain during the contact processes and removes quickly from ice-structure interaction location. In contrast, the effect of confinement of crushed ice was significantly higher at low test speeds (low strain rates).

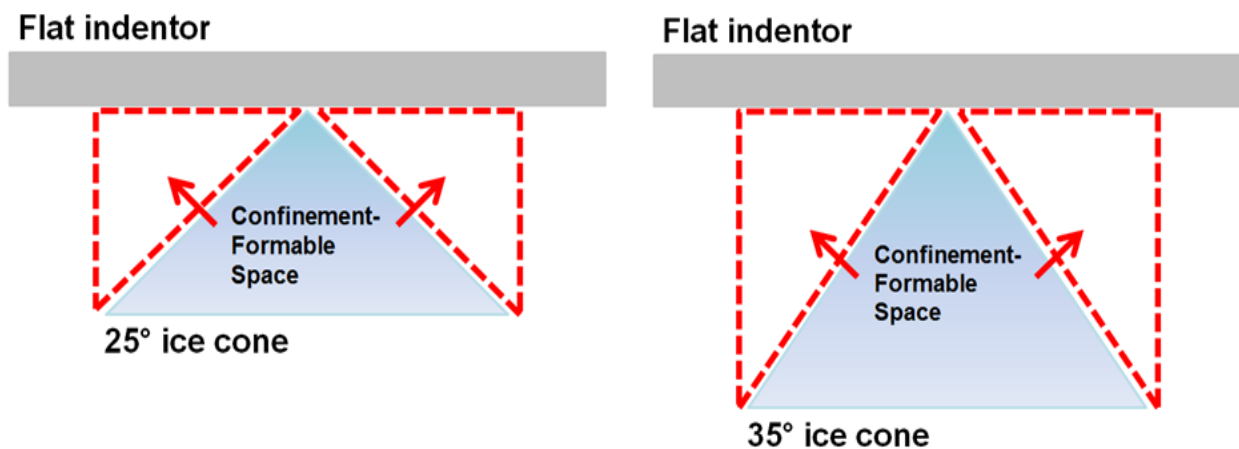


Figure 5-15: Comparison of confinement-formable space between ice and indenter (flat indenter)

The difference becomes more significant in the case of concave-shaped indenter. Figure 5-16 illustrates the space formed between the ice and the wedge-shaped indenter due to the different cone angles. As illustrated in Figure 5-16, the difference in the area of confinement formed by crushed ice obviously varied between the 10° and 20° wedge-shaped indenter. For this reason,

larger ice loads were measured using the 20° wedge indenter, as shown in previous force-displacement history comparison (since it needs to be pushed out against more restrictive shapes).

Unlike the case of the flat indenter, the effect of confinement provided by the shape of indenter cannot be ignored. There are no restraints provided along the wedge length; therefore, the crushed ice can be removed without any restriction. However, in the case of the conical indenter, crushed ice will be trapped in all directions because of the indenter shape. Consequently, the largest loads were measured against the conical indenter, regardless of cone angles or test speeds.

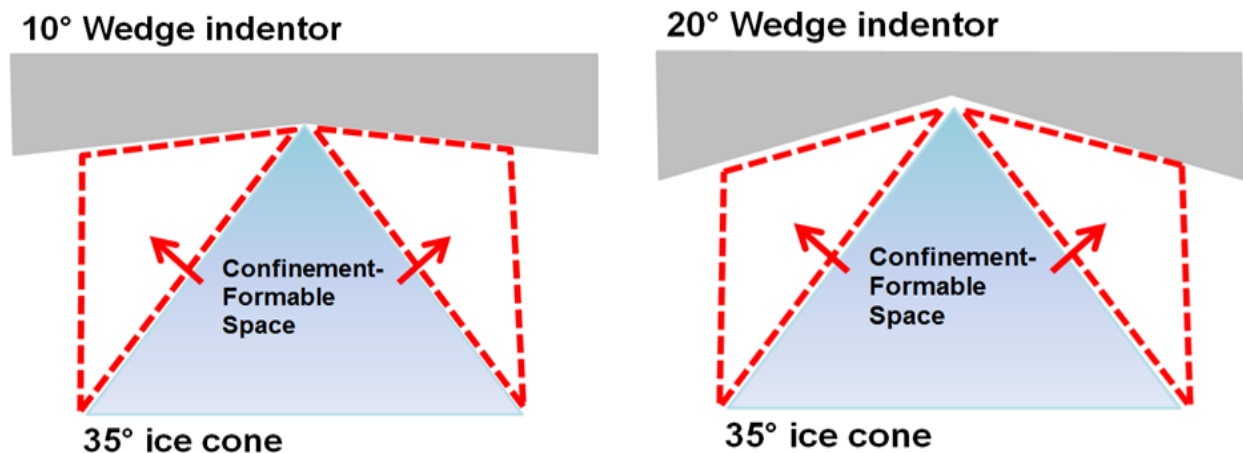


Figure 5-16: Comparison of confinement-formable space between ice and indenter
(wedge indenter)

5.3.2. Verification of suitability of applying a linear relationship: Pressure-Area relationship perspective

As discussed earlier, a linear relationship was adopted to derive the regression equation for the convenience of analysis, utilizing the force-displacement curve obtained through experiments. The derived force comparison convinced the validity of applying the linear relationship. In this discussion, a further verification of using the linear relationship is discussed, followed by considering pressure-area relationship

5.3.2.1. Definition of Cone-Shaped Ice Parameter

A fundamental parameters which applied in this study are as follows (see Figure 5-17). Through each defined parameter, the nominal contact area regarding a crushing distance (δ) can be derived as Equation (5-4).

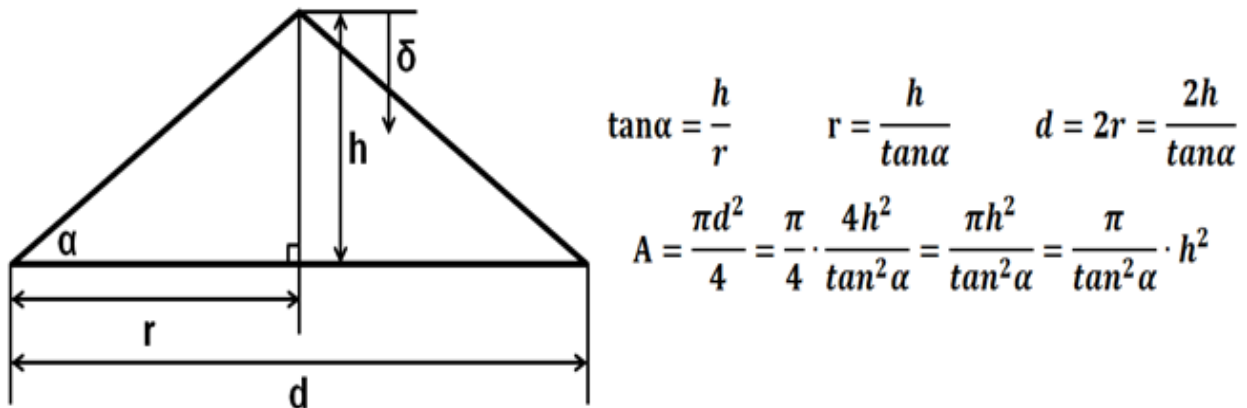


Figure 5-17: Definition of cone-shaped ice parameter

$$A \approx h^2 \approx \delta^2 \quad \rightarrow \quad \delta \approx \sqrt{A} \quad (5-4)$$

5.3.2.2. Comparison of Regression Relationship: Linear vs. Exponential

Figure 5-18 shows a general trend of the force-displacement curve (obtained through experiments), and the linear or exponential relationships can be commonly applied to obtain a regression curve (equation).

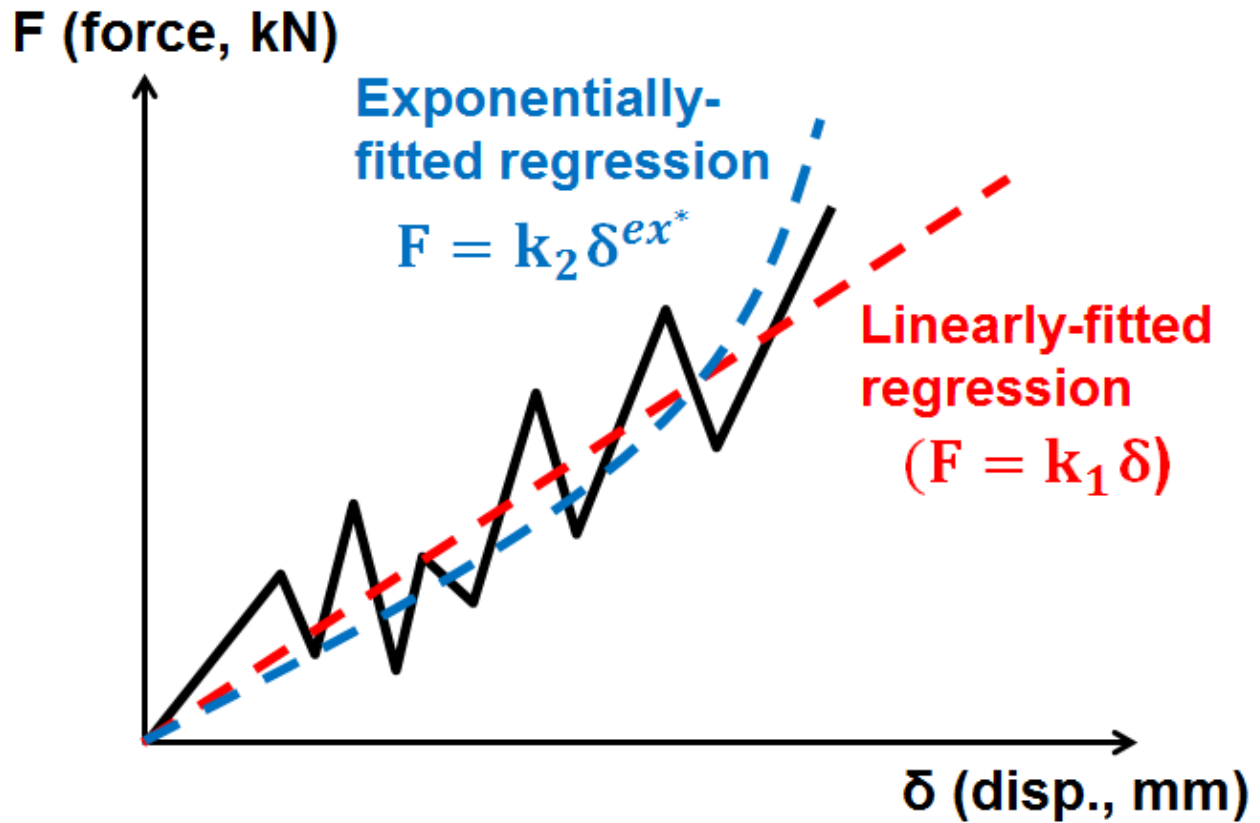


Figure 5-18: Regression fit of force-displacement curve (linear vs. exponential relationship)

Equation (5-4) is applied to derive the definition of each pressure-area relationship, according to each regression relationship (linear and exponential). The following Table 5-15 represents each defined term.

Table 5-15: Definition of force, pressure and exponential term

	Linearly-fitted regression	Exponentially-fitted regression
Force definition	$F = k_1 \delta$	$F = k_2 \delta^{ex^*}$ where, $(ex \geq 1)$
Pressure definition	$P = \frac{F}{A} = \frac{k_1 \delta}{A} \cong \frac{k_1 \sqrt{A}}{A} \cong k_1 A^{-0.5}$	$P = \frac{F}{A} = \frac{k_2 \delta^{ex^*}}{A} \cong \frac{k_2 (\sqrt{A})^{ex^*}}{A}$ $\cong \frac{k_2 A^{0.5ex^*}}{A} \cong k_2 A^{0.5ex^*-1}$
Exponential term (ex)	-0.5 (fixed)	Varies depends on defined ex^*

As shown in Table 5-15, eventually the exponential term, ex , in the pressure-area curve will be a fixed value as ‘-0.5’ if the force-displacement curve is assumed as the linear relationship. In this case, the variation of pressure-area curve depends on k_1 value, but the overall trend (slope) of the curve is already determined by pre-defined regression relationship of the force-displacement curve as linear relationship.

In contrast, behavior of the pressure-area curve will tend to vary according to the defined ‘ ex ’ value when the force-displacement curve is assumed as exponential relationship. Variation of the pressure-area curves are illustrated in Figure 5-19.

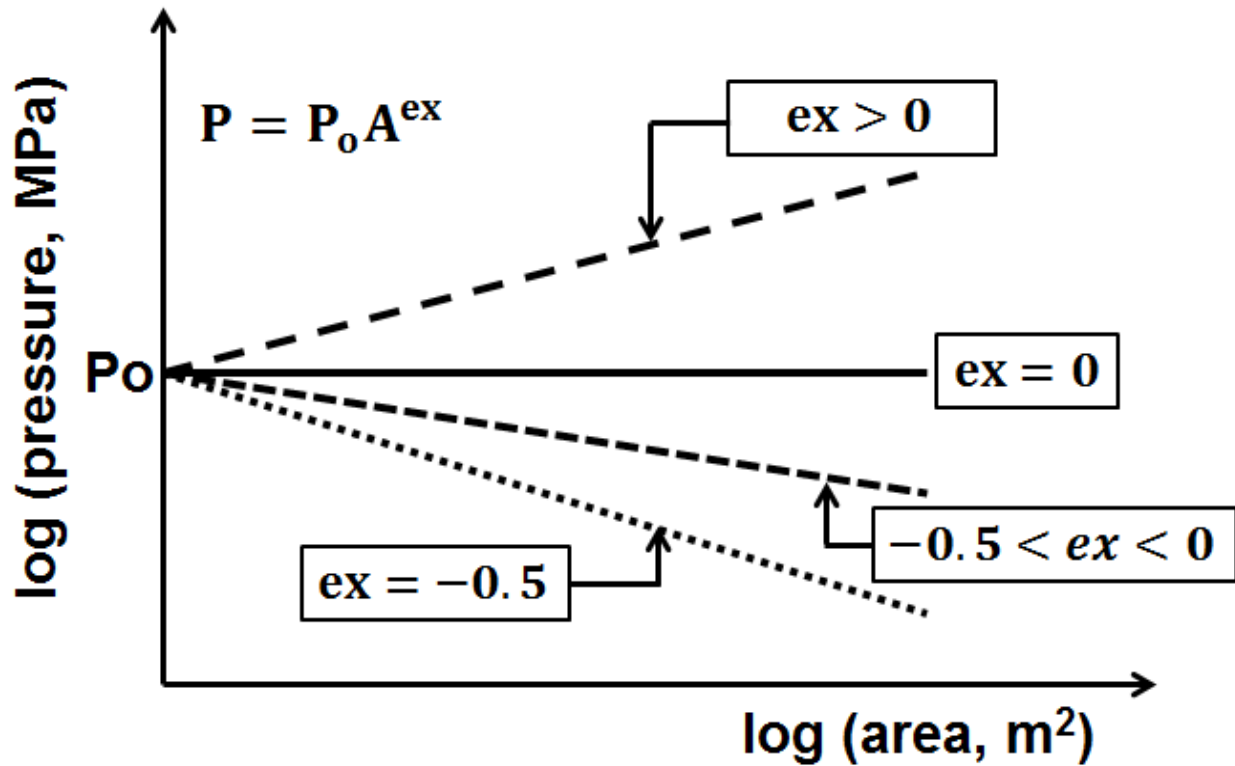


Figure 5-19: Variety behavior of the pressure-area curve depends on ‘ex’

As mentioned earlier, applying the linear relationship means that the exponential term (ex) is fixed as ‘-0.5’. In this case, the exponential term is defined regardless of the experimental results and as a result, the behavior of pressure-area curve may influence. Therefore, an additional validity of the assessment of applying linear relationship is mandatory with respect to the pressure-area relationship.

For this reason, ‘ P_0 ’ and ‘ex’ parameters from a series of pressure-area curves were extracted for diverse test conditions, as presented in Table 5-16. The values of each parameter for each experimental results (‘ P_0 ’ and ‘ex’) are shown in Figure 5-20.

Table 5-16: Test conditions (to extract 'P₀' and 'ex' from pressure-area curve)

	Indenter Shape	Indenter Angle (°)	Cone angle (°)	Test speed (mm/)
Test 1	Flat	-	35	100
Test 2	Flat	-	35	100
Test 3	Flat	-	25	1
Test 4	Flat	-	35	1
Test 5	Wedge	10	35	100
Test 6	Conical	10	35	100
Test 7	Wedge	10	25	100

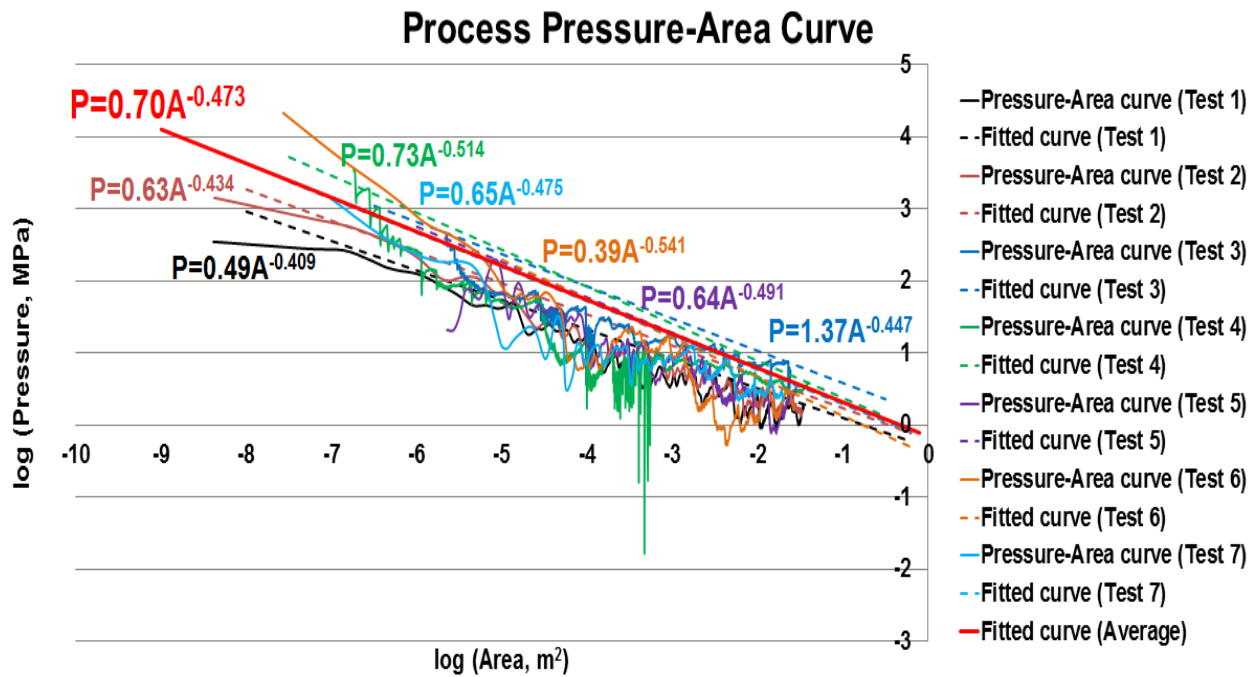


Figure 5-20: Pressure-area curve (including P₀ and ex)

As shown in Figure 5-20, most of the experimental results represented the exponential term, which is 'ex', close to '-0.5'. The values varied between '-0.409' to '-0.541' and the average value was '-0.473' as marked with a bold-red line (which represent the average of test results).

The linear relationship was applied and experimental results were analyzed through this study for the purpose of the simplicity of the regression relationship. However, an assumed value of exponential term, ex , as '-0.5' (applying the linear relationship) showed a close comparison, followed by the experimental results (see Figure 5-20).

Thus, through the analysis of the pressure-area curve with respect to regression relationship confirmed that applying the linear relationship, which gives the exponential term value as '-0.5', may be referred as a reasonable assumption.

Chapter 6 Numerical Analysis

6.1. Overview

This section is aimed to develop a numerical simulation model and determining the material properties of ice that can be applied equally from low to high strain rate testing using LS-DYNA[®]. Validation of the proposed numerical simulation model was verified based on the compressive ice crushing test results performed in a cold room using the 10cm diameter cone-shaped ice specimen, as described earlier by Kim et al. (2012; 2013; 2014). Furthermore, the verification processes for scalability were performed by applying the developed numerical simulation model to larger-scale ice samples, which are 25cm diameter cone-shaped ice specimen against concave (wedge and conical shape) indenter as described in Chapter 4.

6.2. Proposed Ice Model

In this study, the force-displacement history was implemented by applying the modified volumetric strain-stress relationship. To simulate a ‘sawtooth’ pattern during numerical simulations, the ‘maximum principal stress’ failure criterion was added additionally along with the ice model properties as represented in Table 6-1 (Bjerkås, 2002). The tensile cutoff stress, which is the highest tensile stress allowed in the material also considered as material criterion.

Table 6-1: Ice material properties and failure criteria

	Density (kg/m ³)	Young's modulus (GPa)	Poisson ratio	Tensile Cutoff Stress (MPa)	Max. Principal Stress Criteria (MPa)
Ice material 1	900.0	9.0	0.003	35.0	35.0
Ice material 2	900.0	9.0	0.003	15.0	15.0

In the case of two-body contacts, an element eroding option in the *CONTACT_ERODING_NODES_TO_SURFACE was set up to eliminate any element automatically that reached the failure criteria. This add-on option was adopted to reflect the phenomenon of ice spalling events during experiments. Diverse trend of volumetric stress-strain relationships were analyzed to obtain the optimal force-displacement curve. As a result, ‘stepped’ trend was chosen and applied in this study, which showed the most similar results (see Figure 6-1).

The ice model was separated into two different parts (assigned two different Part ID/Material ID during a simulation) to reflect a high pressure zone at the center, which was commonly observed through the physical experiments. Ice model properties for each parts were assigned differently to simulate the high pressure zone (contained in the center of ice model), and the low pressure zone consisting of pulverized ice (the outer parts consisting of lower material property).

Figure 6-3 shows the concept of the numerical simulation model. Ice model's bottom was fixed (6-DOF) to implement the conditions attached to the test equipment. In addition, outer nodes of the ice model had an additional boundary condition to simulate the ice specimen in ice holder. Translational degrees of x and y directions and rotational degrees of x, y and z were fixed. Only z-direction translation was set as free.

The steel plate on top of the universal testing machine (UTM) was moving downward at specific velocity. Two-body contact simulations were performed. The material property of the steel plate was applied as a rigid body because there was no visual deformation of the plate during the tests as well as the steel plate was thick enough to be considered as rigid (see Figure 6-3). A solid element was applied for both steel indenter and ice model during simulations.

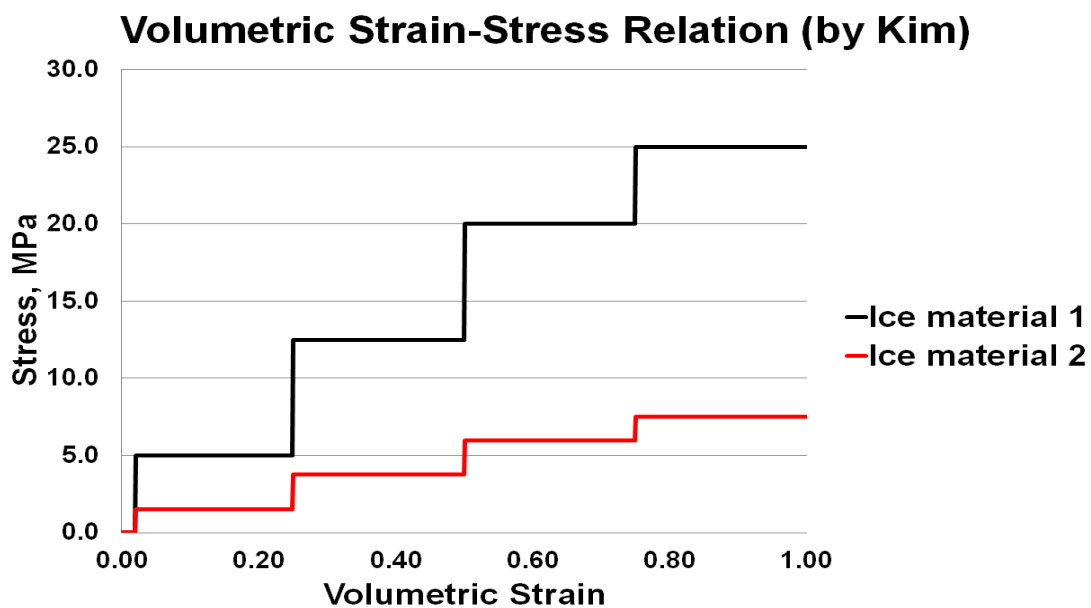


Figure 6-1: Volumetric strain-stress relation of crushable foam (by Kim)

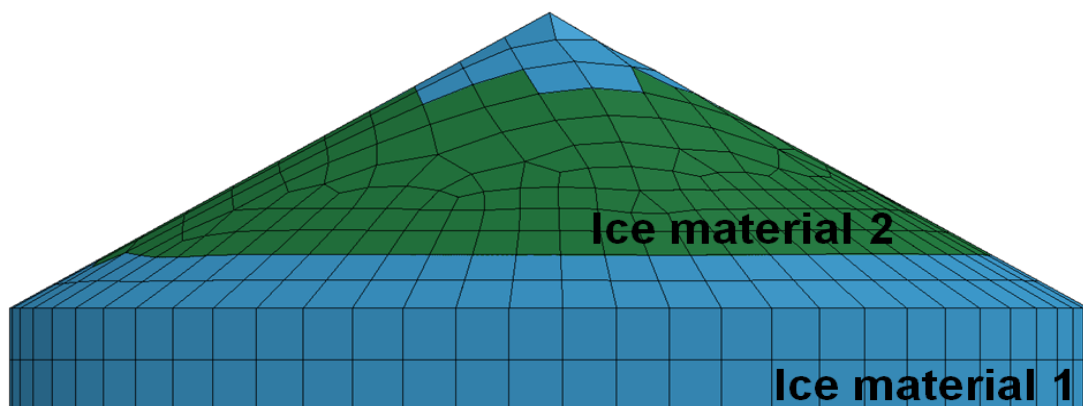


Figure 6-2: Layer of ice model (Blue: Ice material 1, Green: Ice material 2)

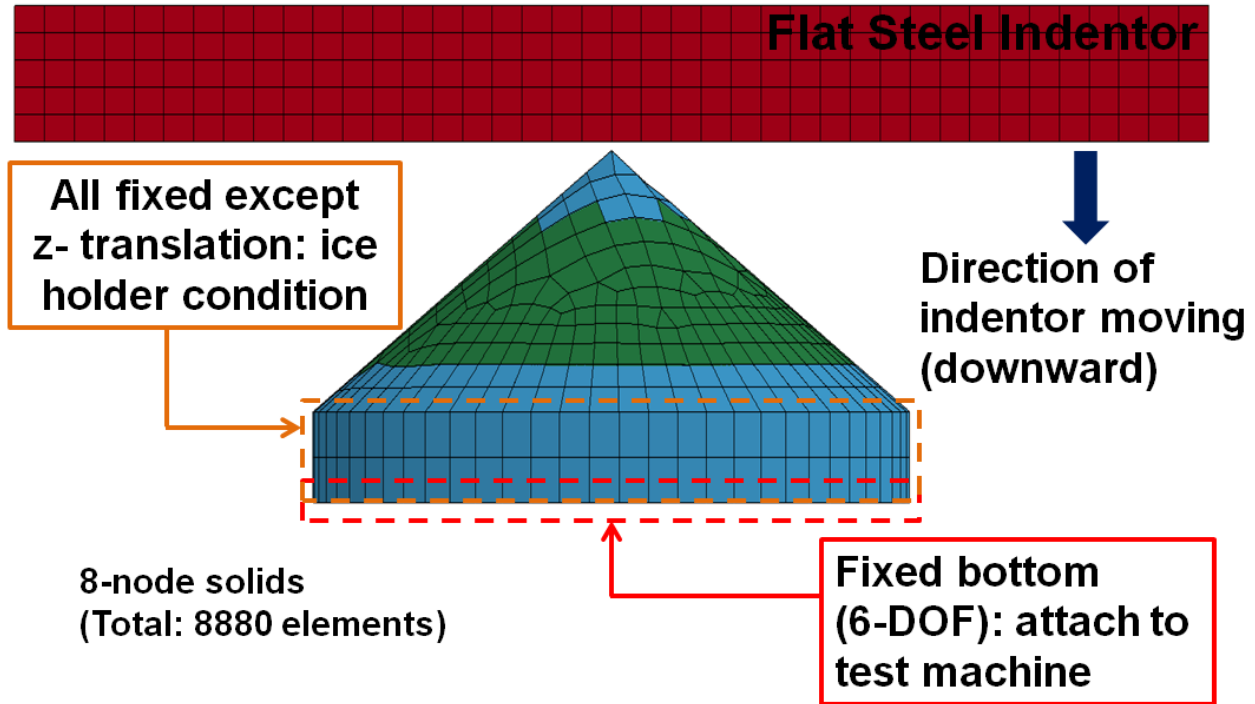


Figure 6-3: Numerical simulation model consists of ice specimen and the steel plate

6.3. Simulation Results

The numerical simulation model developed in this study was verified through the evaluation and comparison with experimental results performed in the laboratory. A 10cm diameter cone-shaped ice samples were chosen for the comparison. Table 6-2 represents the specific experimental conditions. The temperature in a cold room and the grain size of the ice sample were not considered in the numerical simulation model. Figure 6-4 shows test set-up of 30° cone-shaped ice specimen mounted on the universal test machine in a cold room.



Figure 6-4: Test set-up (30° ice cone)

Table 6-2: Test condition (10cm diameter ice cone)

	Cone angle (°)	Test speed (mm/s)	Grain size (mm)	Cold room temp. (°C)
Test 1	30	1	5-10	-5
Test 2	30	100	5-10	-5

6.4. Parametric Study

Sensitivity analysis was performed to determine the values of the principal parameter (i.e. mesh size, material properties of ice, etc.), which may affect the numerical simulation results during the numerical analysis. The parameters that were considered in this study were, 1) mesh size, 2) value of max. principal stress and 3) ratio of high/low pressure region. In the case of Young's modulus and Poisson's ratio, both were verified as not significant parameters in the analysis carried out by Zong (2012).

6.4.1. Mesh Size Sensitivity

Figure 6-5 illustrates the structure of the element composition in steel indenter for the numerical analysis. Height and breadth of each element were identical for ease of interpretation. Unit size of the element was denoted by X_p as shown in Figure 6-5. The width and height of the indenter are denoted by 'b' and 'h', respectively. Then the total number of elements in width and height directions can be calculated by dividing 'b' and 'h' with the unit element size ' X_p '. Number of total elements for width and height were denoted by 'M' and 'N'. In the case of the ice model, an identical unit mesh size was applied during the numerical analysis.

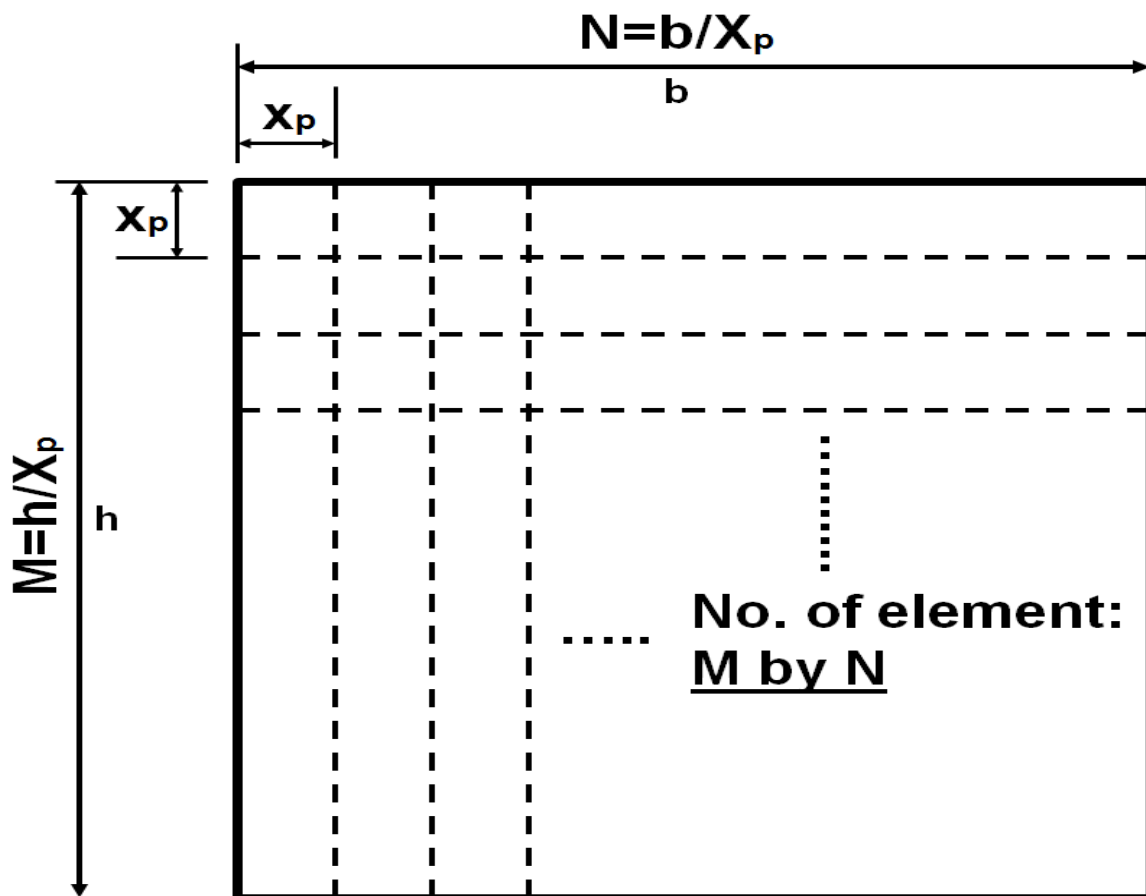


Figure 6-5: Structure of the element composition in indenter part

Different mesh sizes (10.0mm, 8.0mm, 5.0mm, 4.0mm, 2.5mm, 2.0mm) were applied to the identical FE model to explore the mesh size sensitivity in this study. The results of numerical analysis were compared with the experimental results (for Test 2). Figure 6-6 shows the comparison result of the force-displacement curve according to each mesh sizes adopted in this study.

Table 6-3: Mesh size/No. of element comparison (indenter and ice)

	In case of b=200mm, h=200mm					
Element size (mm, unit)	10.0	8.0	5.0	4.0	2.5	2.0
No. of element (M by N)	20 by 20	25 by 25	40 by 40	50 by 50	80 by 80	100 y 100

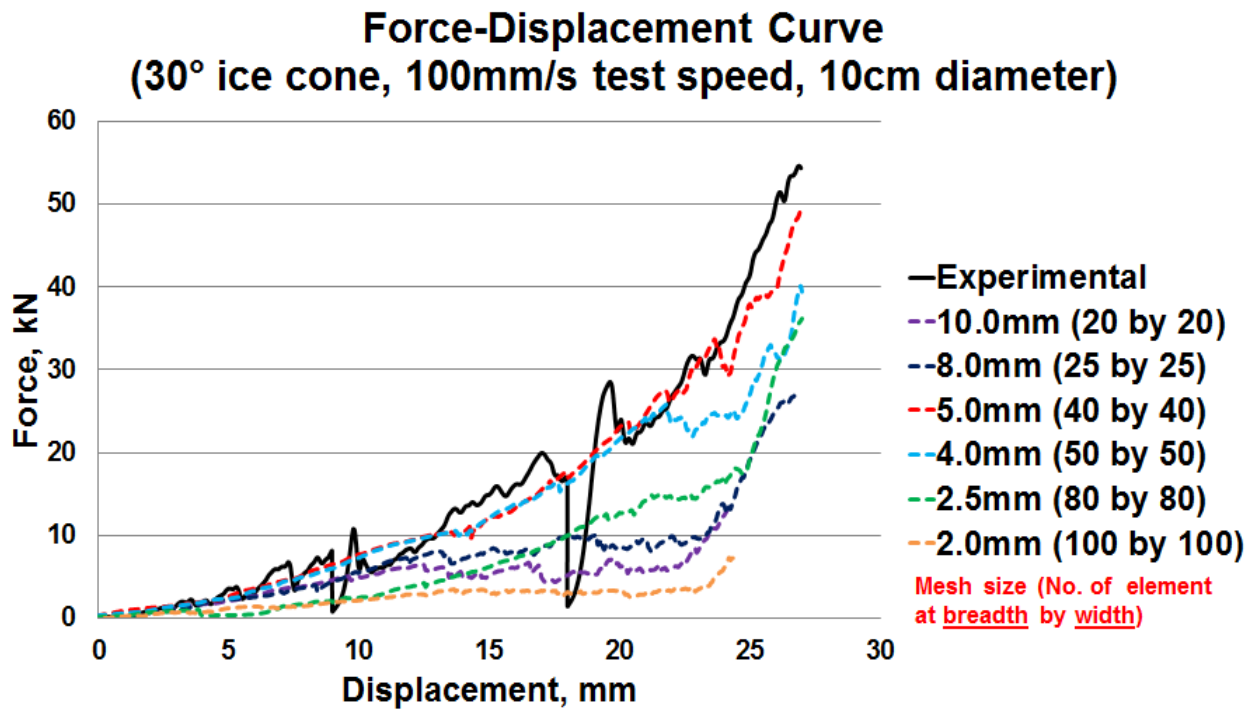


Figure 6-6: Comparison of force-displacement curve by diverse mesh size

Figure 6-6 shows that the results obtained by applying 5.0mm mesh size showed results finest to the experimental results obtained in test 2. If the mesh size was 2.5mm or less, the force magnitude was observed much less (difference was even more clearly shown using 2.0mm mesh size).

6.4.2. Value of Max. Principal Stress (failure criteria) Sensitivity

Figures 6-7 and 6-8 show the comparison results of force-displacement curves according to the difference of failure criteria used in this study. Based on the suggested failure criteria in this study (max. principle stress of ‘ice material 1’ = 35MPa, ‘ice material 2’ = 15MPa), four different percentages of failure criteria were selected for comparison. The force-displacement curve is plotted by each failure criteria to check the sensitivity of failure criteria during the numerical simulation.

As shown in Figures 6-7 and 6-8, the failure criteria which was applied in this study indicated a similar trend compared to the experimental result. In the case of 80% and 90%, the magnitude of forces was reduced, but the overall trend followed very similarly. When the percentage drops as 50%, the magnitude also reduced as 50% level.

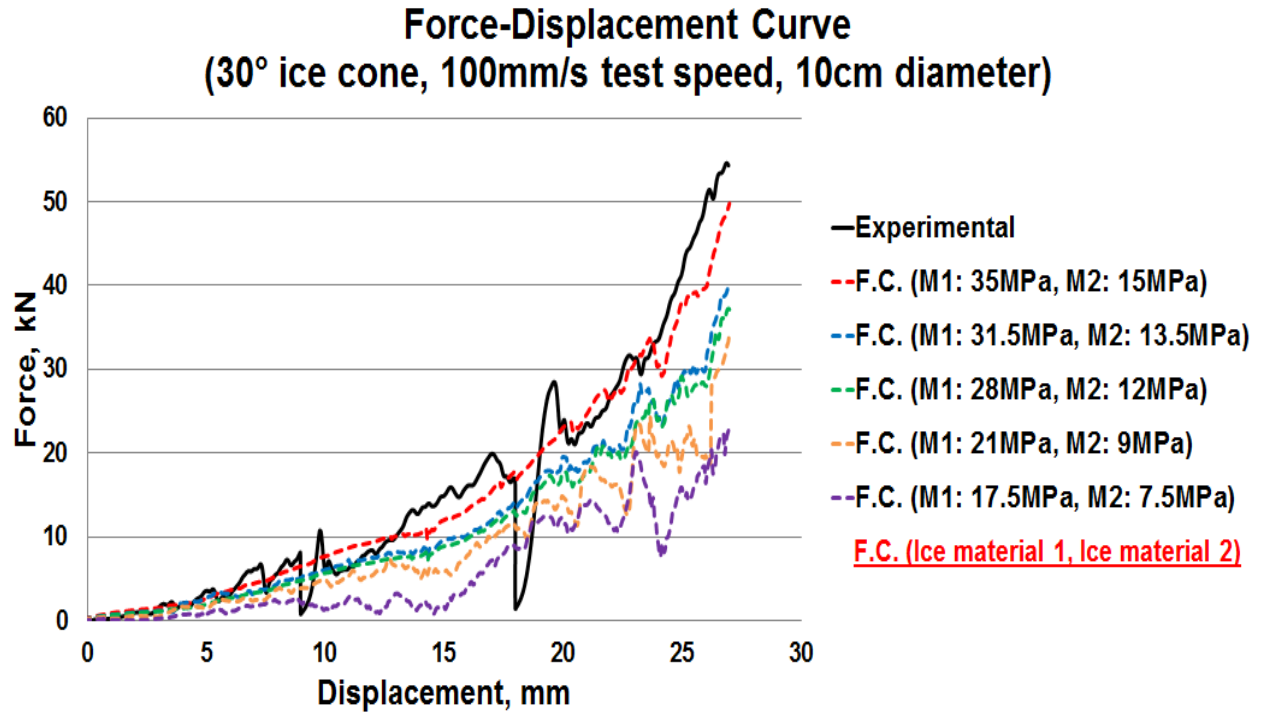


Figure 6-7: Comparison of the force-displacement curve by percentage of failure criteria (F.C)
(100mm/s test speed)

A similar trend was also observed with 1mm/s test speed as shown in Figure 6-8 (overall trend of the curves shown are almost identical to one another, regardless of the percentage of failure criteria used). Only the magnitude seems to decrease linearly as failure criteria varies. Based on the sensitivity analysis of failure criteria, applying the suggested failure criteria in this study is verified as the optimal condition to obtain the best fit.

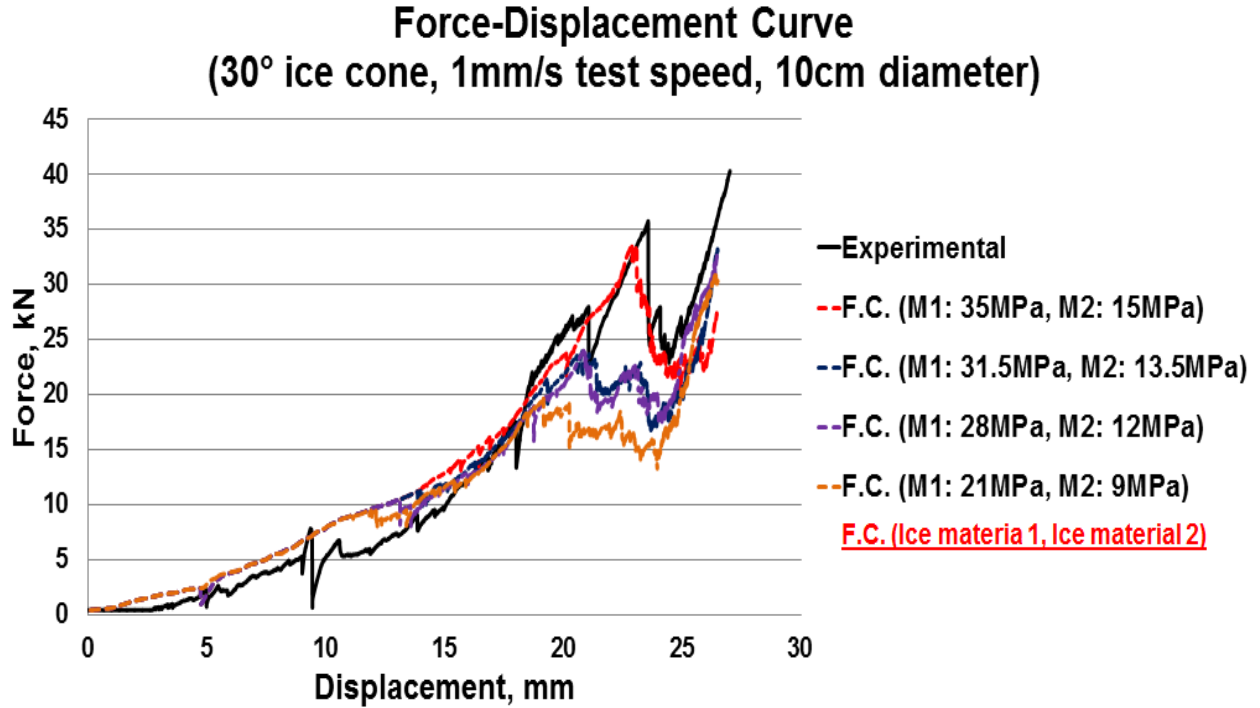


Figure 6-8: Comparison of force-displacement curve by percentage of failure criteria (F.C)

(1mm/s test speed)

6.4.3. Size of HPZ Sensitivity

Gagnon (2010) introduced the concept of applying different ‘layer’ of elements in FE model to simulate the forced-sawtooth pattern, observed in real-ice experiments. As mentioned earlier, a similar methodology was applied in this study that; applying two different layers to simulate the high and low pressure regions. Each layer had different ice material properties to simulate the similar force-displacement curves, which were obtained during the experiments. The definition of each parameter ($H_{ice\ mat_1}$, $H_{ice\ mat_2}$ or $r_{ice\ mat_1}$, $r_{ice\ mat_2}$) for comparison is given in Figures 6-9 and Figure 6-10.

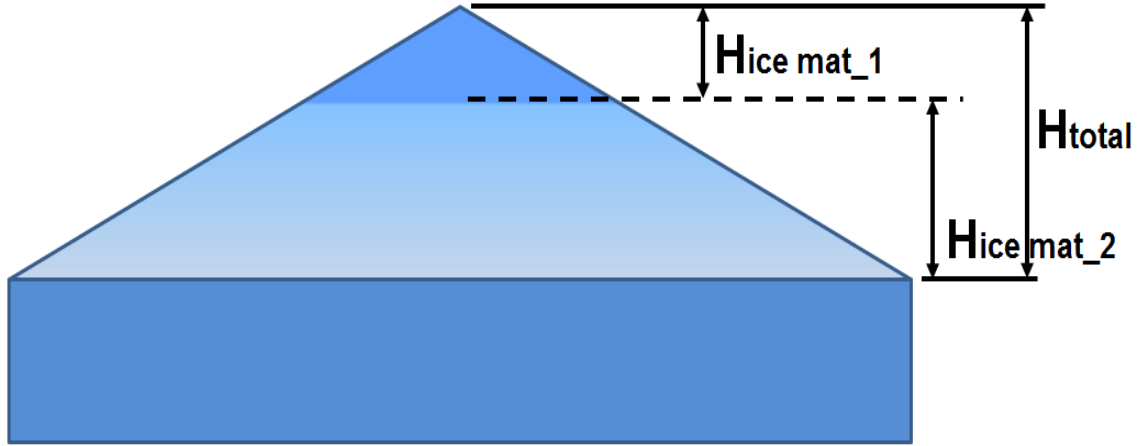


Figure 6-9: Definition of layered ice model (front view)

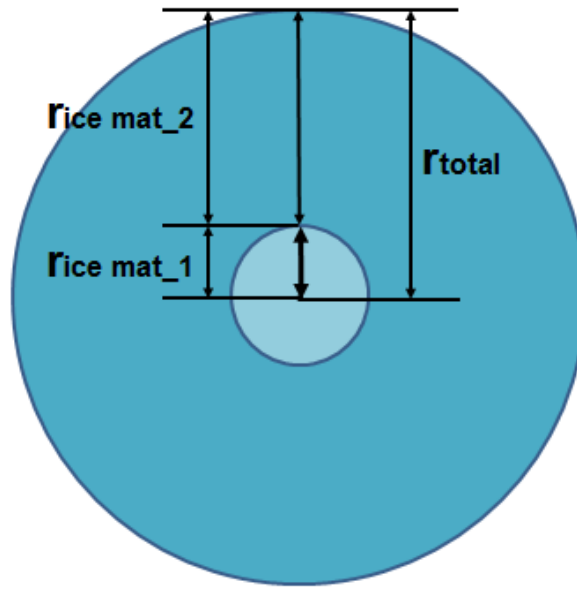


Figure 6-10: Definition of layered of ice model (top view)

Four different ratios were chosen ($H_{ice\ mat_1} : H_{ice\ mat_2} = 0.1 : 0.9, 0.2 : 0.8, 0.3 : 0.7, 0.4 : 0.6$ or $r_{ice\ mat_1} : r_{ice\ mat_2} = 0.1 : 0.9, 0.2 : 0.8, 0.3 : 0.7, 0.4 : 0.6$) to determine the sensitivity of ratios. In general, high pressures were measured from the center of contact between the structure and the ice. Based on this concept, boundary of two separate layers (ice material properties) was set up

from the tip of the ice cone to a particular position (downward direction). ‘ $H_{ice\ mat_1}$ or $r_{ice\ mat_1}$ ’ representing the height/radius of relatively high pressure regions (layer 1, ice material 1). ‘ $H_{ice\ mat_2}$ or $r_{ice\ mat_2}$ ’ representing the portion of the height of relatively low pressure regions (layer 2, ice material 2). H_{total} represents the total height of any ice cone (having different angles), which represents the exposed part of ice sample.

In this study, analyses were performed where the ratios of ‘ $H_{ice\ mat_1} : H_{ice\ mat_2}$ or $r_{ice\ mat_1} : r_{ice\ mat_2}$ ’ were 0.1 : 0.9, 0.2 : 0.8, 0.3 : 0.7, and 0.4 : 0.6 (as represented in Figures 6-11 and 6-12) and the obtained results of force-displacement curves are shown in Figure 6-13.

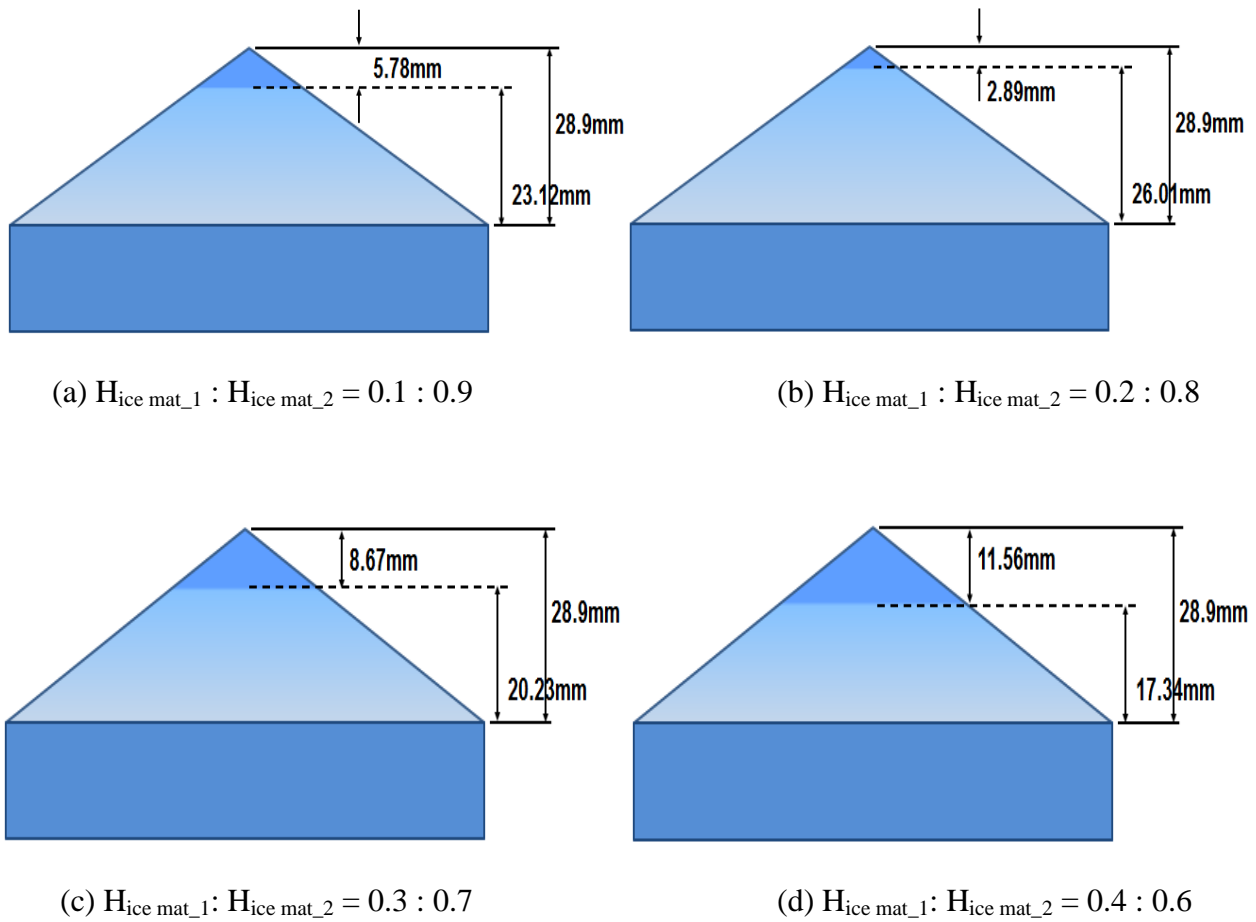
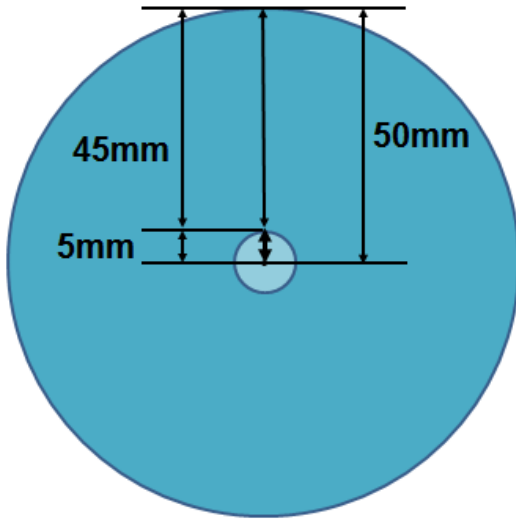
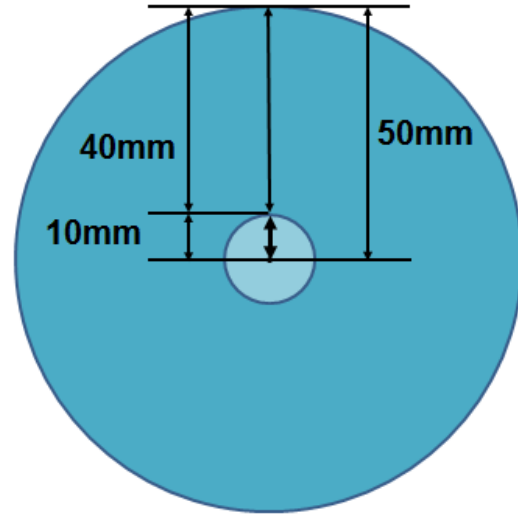


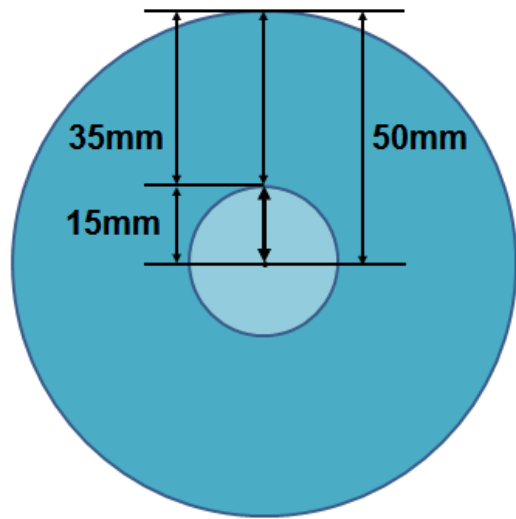
Figure 6-11: Height and Ratio of layered ice model



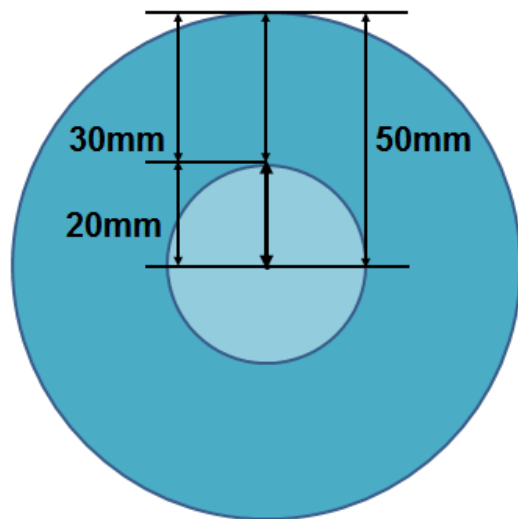
(a) $r_{ice\ mat_1} : r_{ice\ mat_2} = 0.1 : 0.9$



(b) $r_{ice\ mat_1} : r_{ice\ mat_2} = 0.2 : 0.8$



(c) $r_{ice\ mat_1} : r_{ice\ mat_2} = 0.3 : 0.7$



(d) $r_{ice\ mat_1} : r_{ice\ mat_2} = 0.4 : 0.6$

Figure 6-12: Radius and Ratio of layered ice model

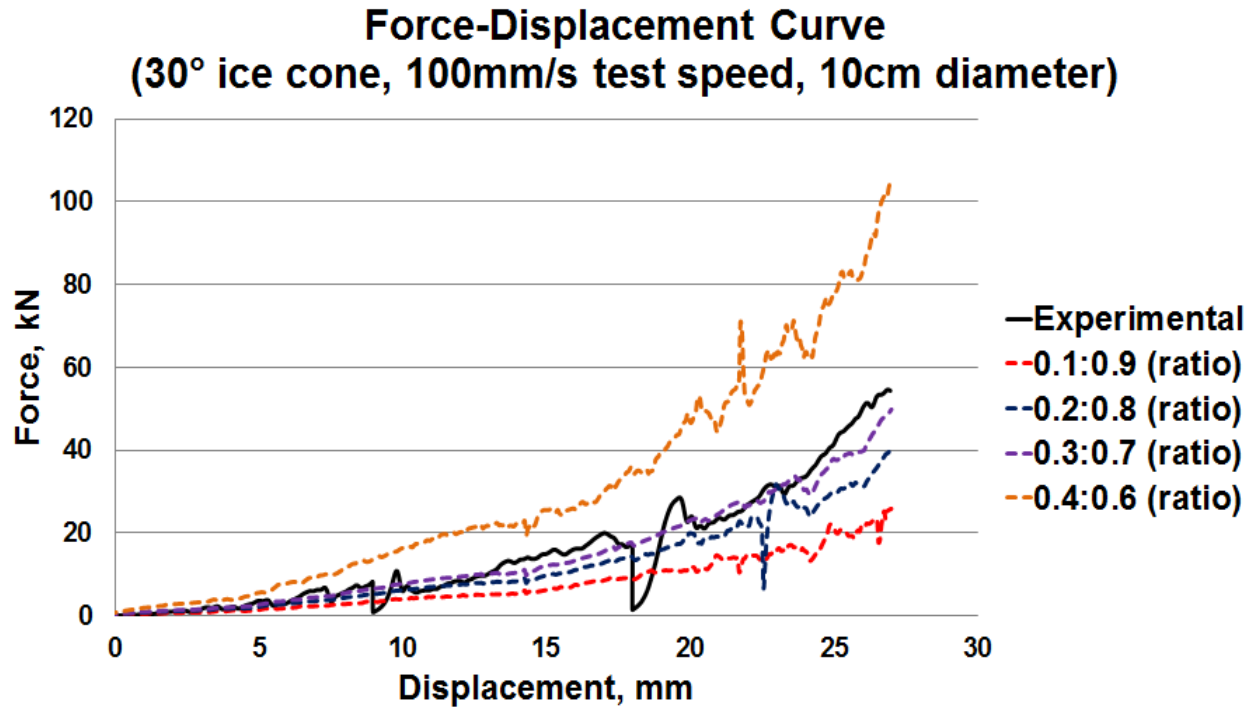


Figure 6-13: Comparison of the force-displacement curve by $H_{ice\ mat_1} : H_{ice\ mat_2}$

($r_{ice\ mat_1} : r_{ice\ mat_2}$) ratio (100mm/s test speed)

As shown in Figure 6-13, obtained trends were similar compared to the experimental results when the $H_{ice\ mat_1} : H_{ice\ mat_2}$ ($r_{ice\ mat_1} : r_{ice\ mat_2}$) ratios were around 0.2 : 0.8 and 0.3 : 0.7. When the high pressure region was relatively small (ratio 0.1 : 0.9), comparison results showed a significant difference (magnitude was about 20-30% lower). On the other hand, obtained results compared to the experimental results was about the twice higher when the high pressure region was over-estimated (ratio 0.4 : 0.6).

Ratios of 0.2 : 0.8 and 0.3 : 0.7 give results closer to the experiments (among the four different conditions). However, there was a sudden load drop for a ratio 0.2 : 0.8, in between 20 - 25mm displacement locations. This phenomenon did not occur for the experimental results. In addition,

magnitude of loads matched even better for the ratio 0.3 : 0.7; in addition, none of the abnormal trends were observe during numerical simulation. Therefore, the optimum ratio of $H_{ice\ mat_1} : H_{ice\ mat_2}$ ($r_{ice\ mat_1} : r_{ice\ mat_2}$) was determined to be 0.3 : 0.7 based on the comparison results. The determined ratio in this section was also applied to the numerical model extended to the 25cm diameter ice sample.

6.5. Results of Numerical Analysis: 10cm Diameter Ice Sample

The main focus of developing a numerical simulation model was to create a model that can be directly applied for different experimental conditions, such as different strain-rates or the size of the ice samples as discussed. In other words, the aim was to create a numerical simulation model that could be used in multiple conditions without any significant modification of ice material properties or simulation conditions. Figures 6-14 and 6-15 shows the comparison results of force-displacement curves between the proposed numerical simulations and experimental results.

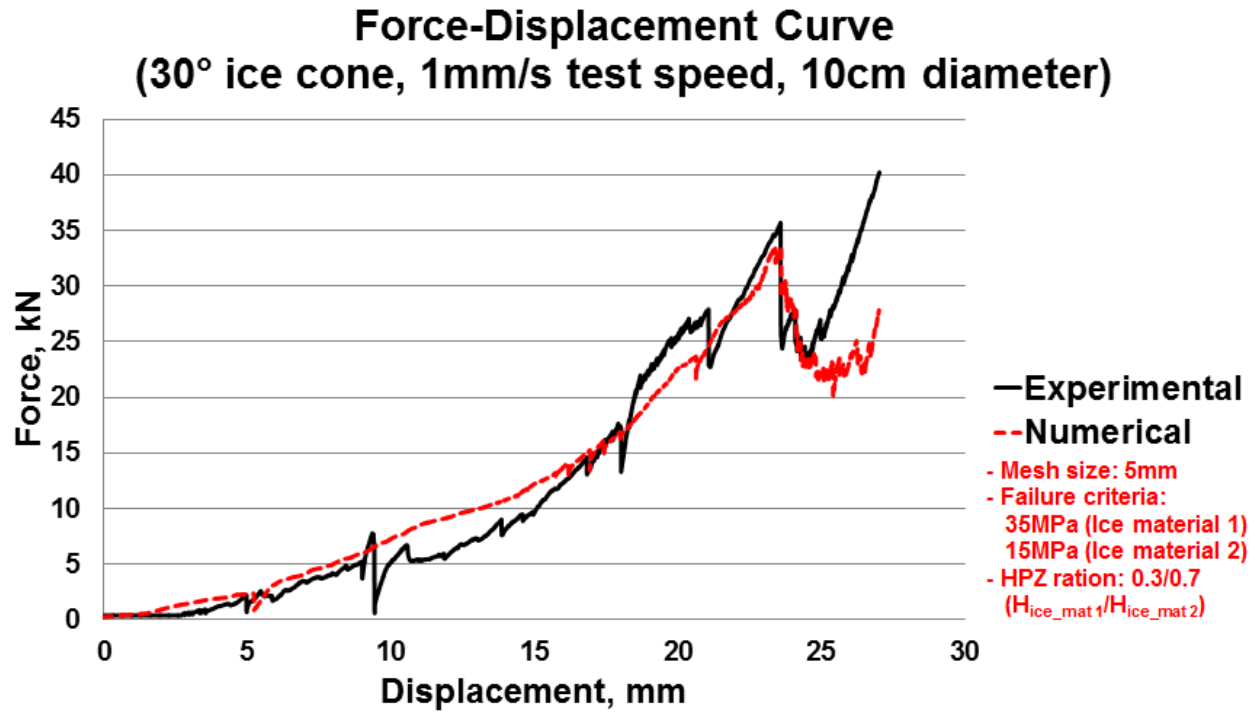


Figure 6-14: Comparison of the force - displacement curve (1mm/s test speed)

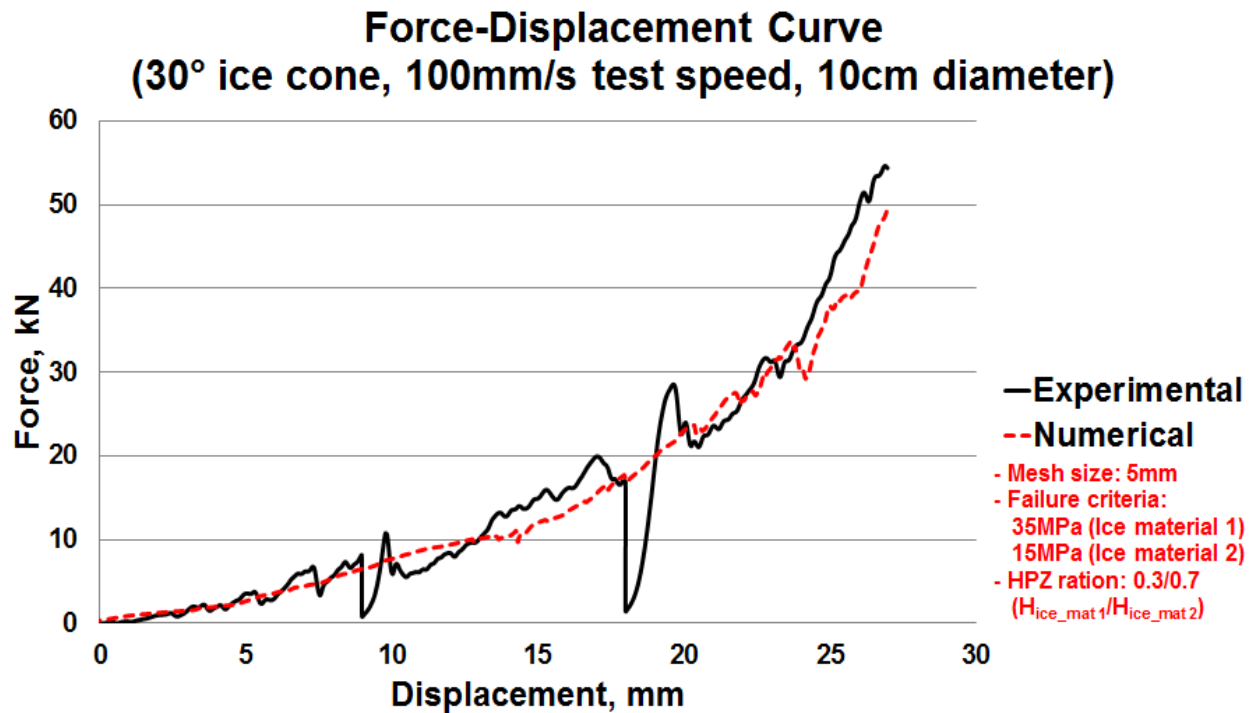


Figure 6-15: Comparison of the force-displacement curve (100mm/s test speed)

As shown in Figures 6-14 and 6-15, similarities between numerical simulations and experimental results can be identified in terms of qualitative and quantitative perspectives.

The low speed test (Figure 6-14) showed a good agreement compared to the high speed test (Figure 6-15) because the typical spalling event occurs more often in the high speed tests than the low speed tests. Therefore, magnitude of ice load variations is relatively small in the low speed tests. The numerical simulations had not represented every spalling event that occurred in experimental results, as shown in the case of the high speed tests in Figure 6-14; however, the overall results of the numerical simulation model have shown similar trends.

As shown in Figure 6-15, the experimental ice loads at certain displacements, at 9.0mm and 18.0mm, vary dramatically from the numerical values. This is due to the fact that experiment was done as ‘stepped’ crushing method instead of ‘straight’ crushing method; hence, the variations in this range (at 9.0mm and 18.0mm in this case) were caused by the discontinuity of the obtained data rather than by the experiment itself (Kim et al., 2012). Therefore, a comparison between numerical simulations and experimental results will become similar qualitatively, if the curve is assumed to be continuous during the tests (as the result of the ‘straight crushing’ method).

Figures 6-16 and 6-17 show the comparison of process pressure-area curves at each test condition. The experimental and numerical simulation results indicated similar trends in both cases.

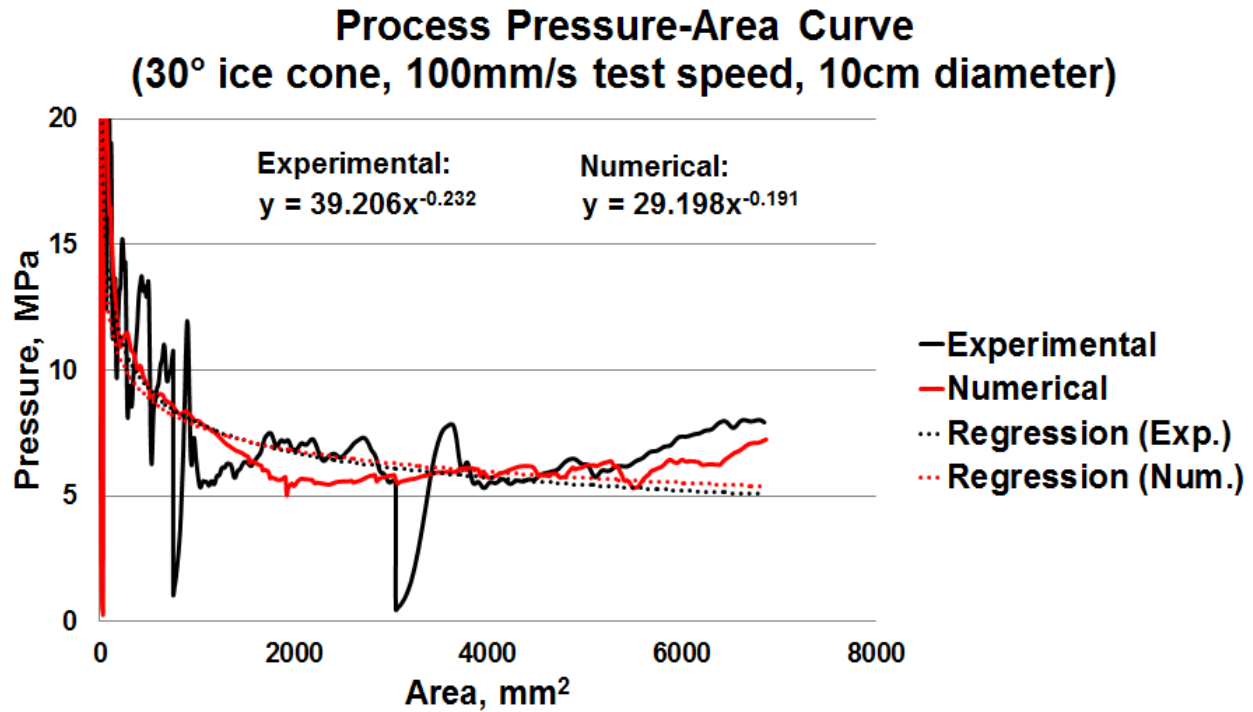


Figure 6-16: Comparison of process pressure-area curves (100mm/s test speed)

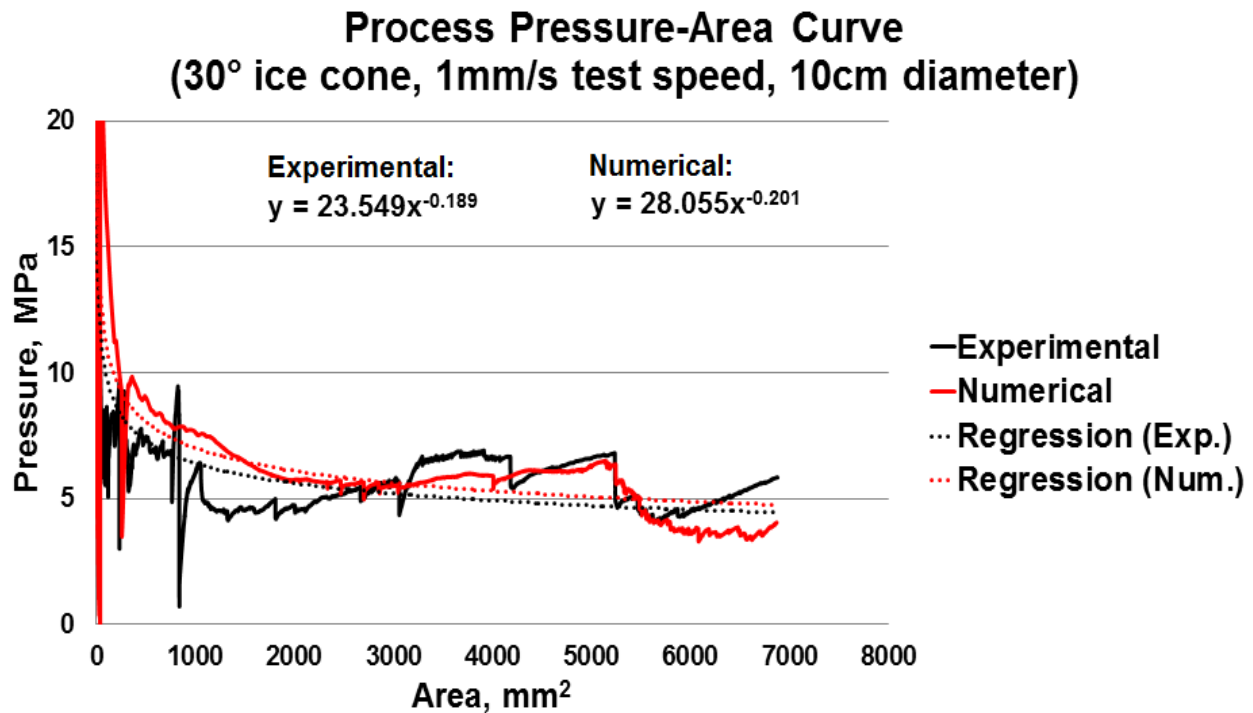
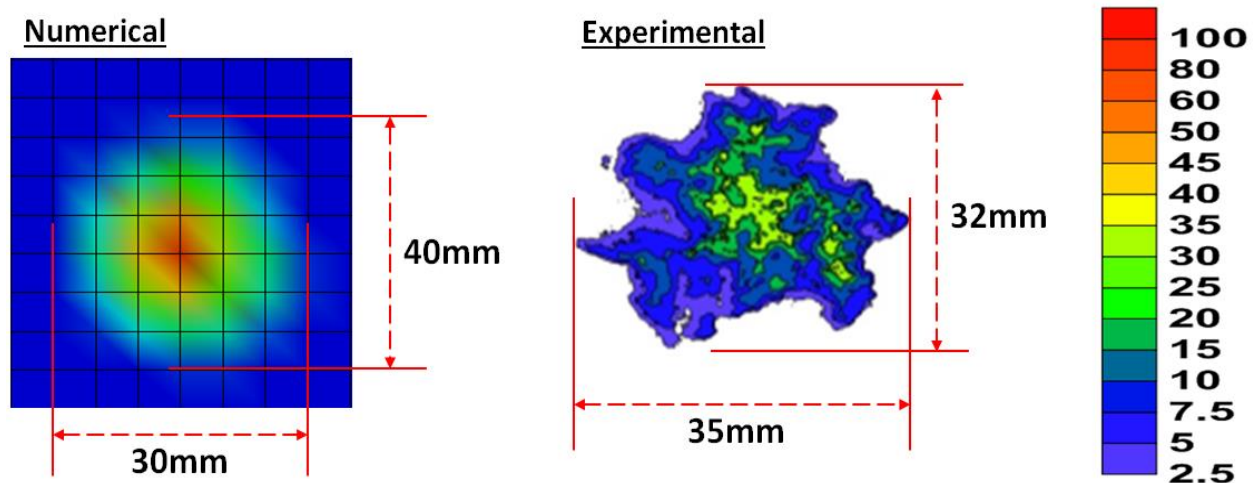


Figure 6-17: Comparison of process pressure-area curves (1mm/s test speed)

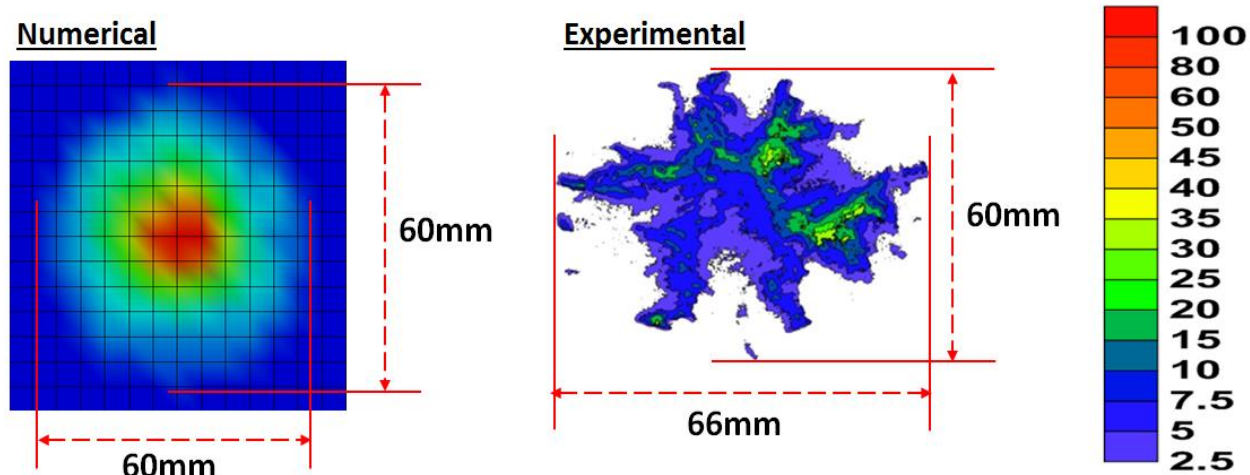
As mentioned earlier, numerical simulation results indicated a good agreement with respect of global loads.

In addition, a comparative assessment of local load was also performed by comparing the spatial pressure distributions in each case. The following Figure 6-18 represents the results of spatial pressure distributions at each designed displacement. The spatial pressure distribution from experiment, plotted in Figure 6-16, was obtained from the results of the pressure measurement film.

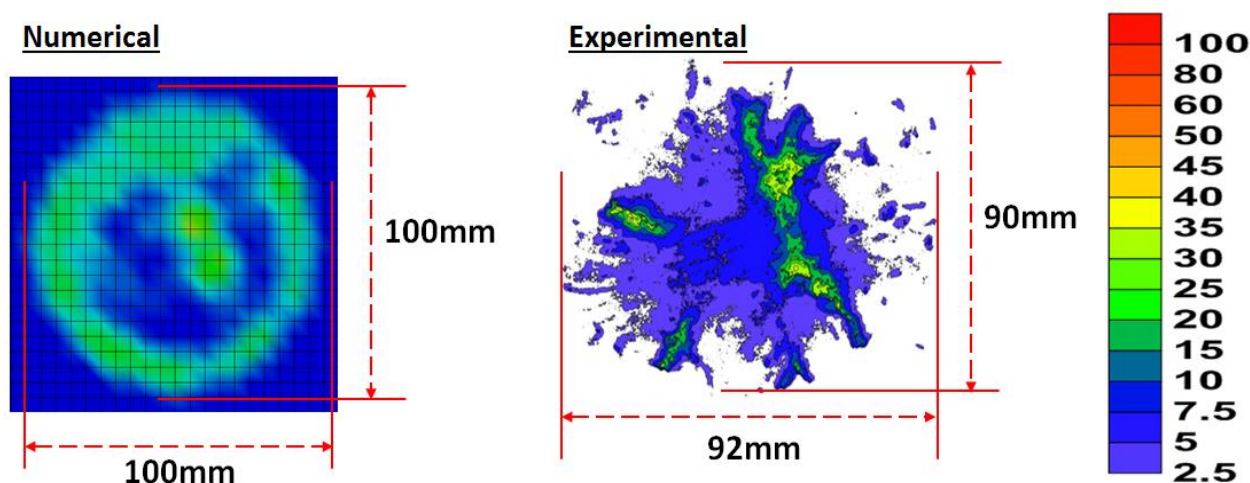
A separate segment set was defined in the numerical simulation on the contact surface (in structure side) to obtain the ‘interface pressure’, and the results are utilized to compare the spatial pressure distributions between the numerical simulations and experimental results.



(a) Spatial pressure distribution at test step 1 (at displacement = 9mm)



(b) Spatial pressure distribution at test step 2 (at displacement = 18mm)



(c) Spatial pressure distribution at test step 3 (at displacement = 27mm)

Figure 6-18: Spatial pressure distribution plots (100mm/s test speed)

As shown in Figure 6-18 (a), a spatial pressure distribution in the first step represented a similar trend. However, differences of spatial pressure distribution between numerical simulation and experimental results became significant as test step progresses. Variation of pressure patterns can be explained in terms of two ways;

1) Behavior of ice such as (a) the timing of spalling events of ice did not coincide between numerical simulations and experimental results and (b) the size of spall was not identical, even though the failure criteria option was applied to simulate spalling events as close as possible. This induced the difference in the shape of the pressure distribution between the numerical simulation and experimental test results.

2) Characteristics of the pressure measurement film itself encouraged the difference as discussed by Kim et al. (2012; 2014), which means that spatial pressure distributions obtained through experiments may have been overestimated by the pressure measurement film. Figures 6-19 and 6-20 represent spatial pressure-area curves at a given data set.

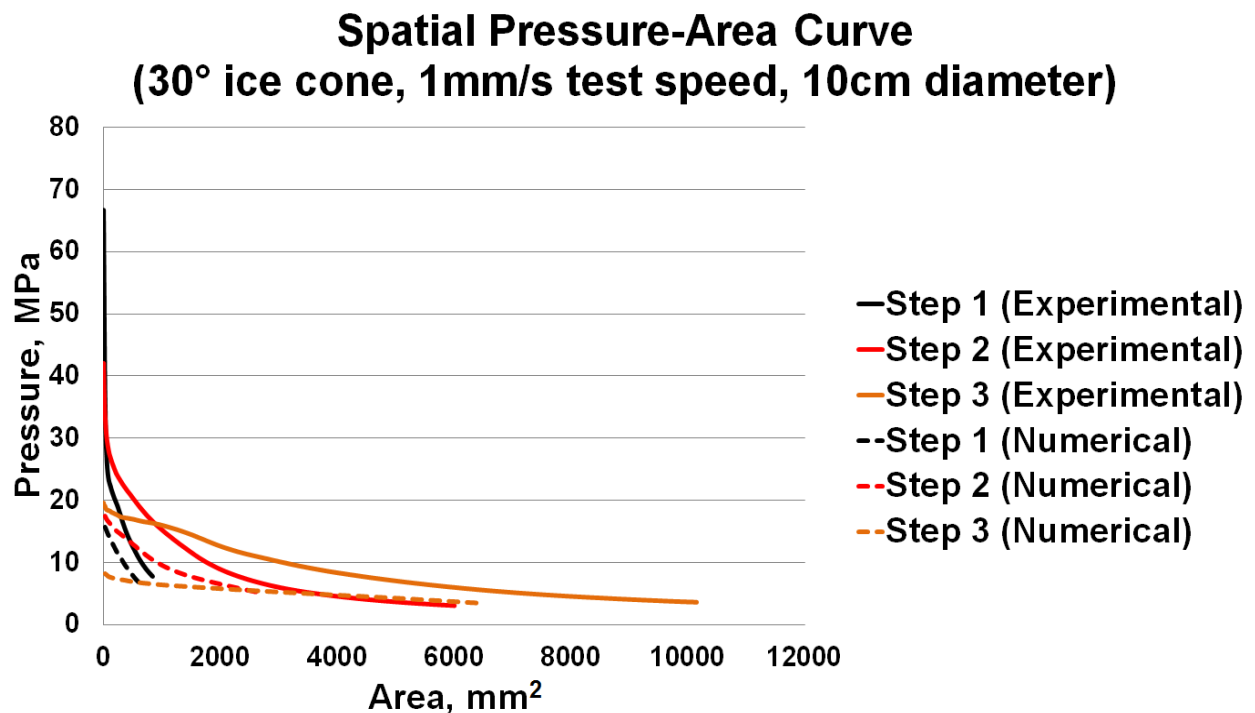


Figure 6-19: Spatial pressure-area curves (1mm/s test speed)

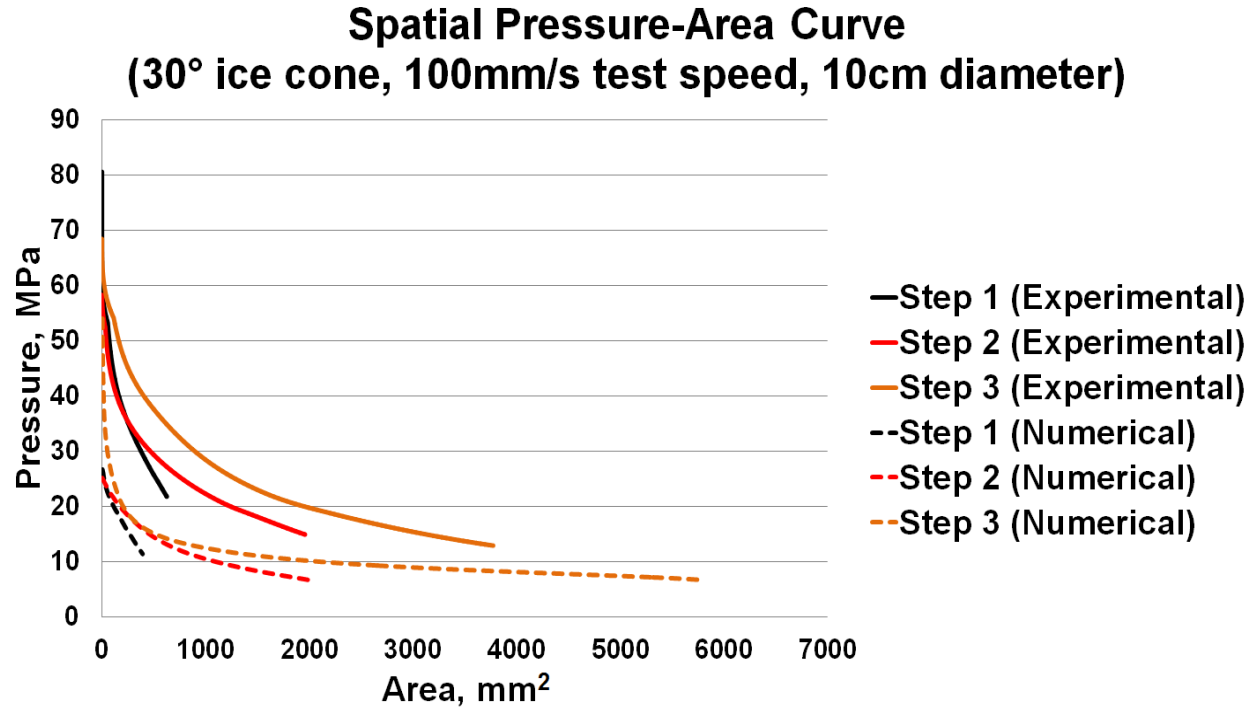


Figure 6-20: Spatial pressure-area curves (100mm/s test speed)

Obtained results from numerical simulations indicated a somewhat lower magnitude as expected. However, results can be similar if the appropriate correction factor is applied. In this specific case, modified spatial pressure-area curves are plotted and showed a good agreement if a correction factor was applied as $\alpha_c = 2.0$ (see Figures 6-21 and 6-22). A further study may require to obtain more specific results.

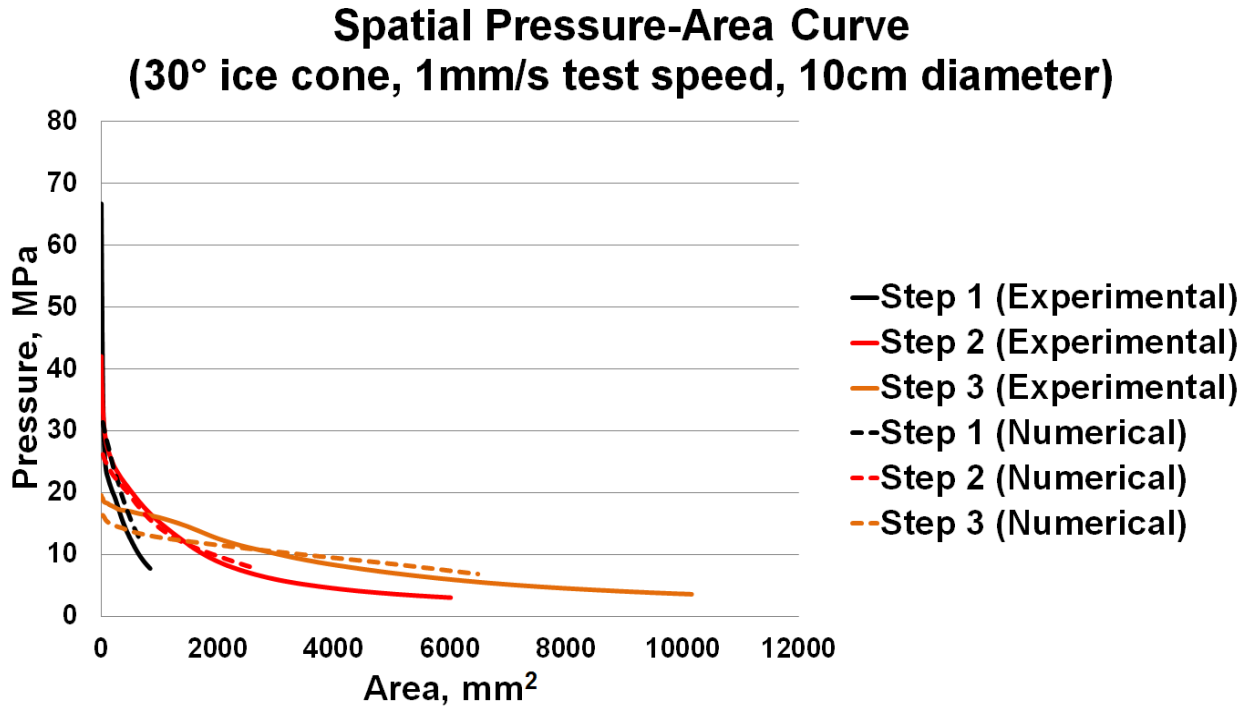


Figure 6-21: Spatial pressure-area curves: Applying correction factor $\alpha = 2.0$ (1mm/s test)

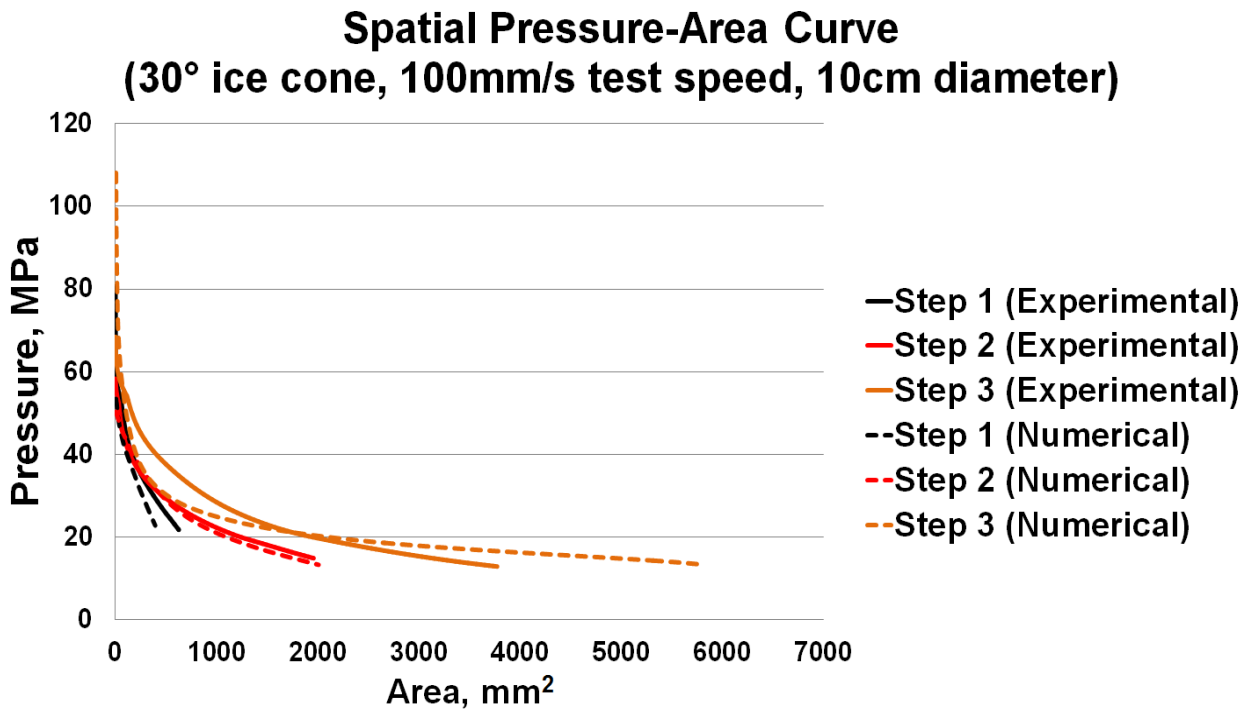


Figure 6-22: Spatial pressure-area curves: Applying correction factor $\alpha = 2.0$ (100mm/s test)

The proposed numerical simulation model was evaluated by comparing the obtained results with those from the experiment and the comparison showed a very good match for global load. In addition, spatial pressure distributions also investigated in terms of the local load and this topic requires in further study.

6.6. Application to Larger Model

As mentioned earlier, verification of the applicability of the developed numerical simulation model to a larger model, was carried out without any modification. Experimental results obtained from a study, which conducted in the laboratory using a 25cm diameter cone-shaped ice specimen, were selected for the comparison purpose (details of test procedure were described in Chapter 4). The results of three types of indenter shape were chosen for verification purposes in this section (see Table 6-4).

Table 6-4: Test condition (25cm diameter ice cone)

	Indenter shape	Indenter angle (°)	Cone angle (°)	Test speed (mm/s)
Test 1	Flat	-	25	1
Test 2	Flat	-	25	100
Test 3	Wedge	10	25	1
Test 4	Conical	10	25	1
Test 5	Wedge	10	25	100
Test 6	Conical	10	25	100

Identical numerical simulation model was applied to evaluate the scalability of results, and the results compared. Force-displacement curves for each experimental and numerical simulation results are shown in Figures 6-23 and 6-24.

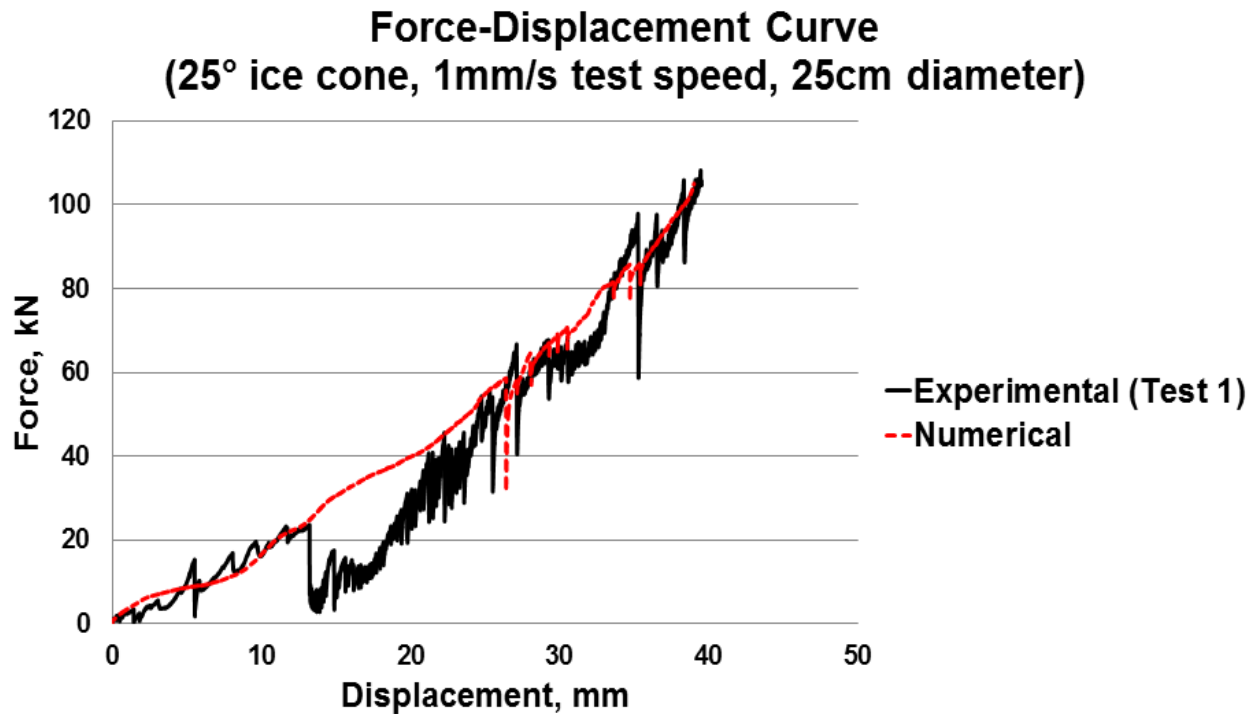


Figure 6-23: Comparison of force-displacement curve on the flat indenter

(Test 1: 25cm ice cone, 1mm/s test speed)

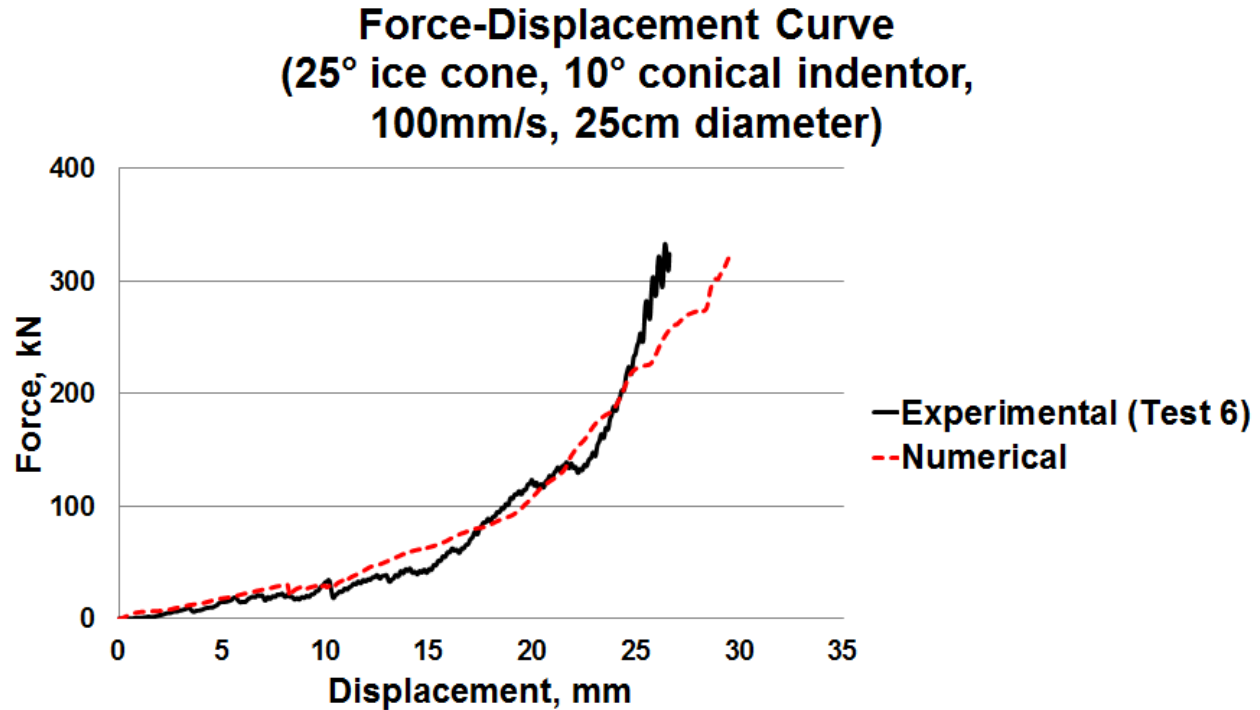


Figure 6-24: Comparison of force-displacement curve on a 10° conical indenter

(Test 6: 25cm ice cone, 100mm/s test speed)

All the detailed spalling events were not captured by the numerical simulation model (compared to small-scale ice cone), unlike experimental result. However, as shown in Figures 6-23 and 6-24, comparison results of the larger ice specimen showed a good agreement in terms of quantitative and qualitative aspects. These results confirmed that the proposed numerical simulation model can be expanded without any specific modification; even the indenter shape was not a simple flat surface.

The behavior of ice as ‘material’ is distinctly different during different strain rate testing. Ductile behavior at low-strain rates and brittle behavior at high strain rates are observed (Schulson, 1990; 1997). In addition, there is somewhat of a ‘transition’ region between these two distinctive

behaviors (Batto and Schulson, 1993). Therefore, the term ‘ice strength’ has to be used carefully in ice mechanics area (Sanderson, 1988). Dillenburg (2012) applied the procedure in which ‘Ice crushing energy (E)’ divided by the ‘Nominal crushed volume (V)’ when used to calculate the compressive ice strength, and gave a valid result. The identical methodology was also adopted in this study to calculate the compressive ice strength between experimental and numerical simulations in this study. The trapezoidal rule of integration was applied to determine the ice crushing energy (E) as represented by Equation (6-1).

$$E = \int_0^{x_{max}} F(x)dx \approx \frac{1}{2} \sum_{i=1}^N (x_i - x_{i-1}) (F(x_i) + F(x_{i-1})) \quad (6-1)$$

Ice crushing energy (E) was obtained on each targeted displacement, and the results were compared. Nominal crushed volume (V) was determined using Equation (6-2).

$$V(x_{max}) = \frac{1}{3} \frac{\pi x_{max}^3}{\tan^2 \alpha} \quad (6-2)$$

Compressive ice strength (σ), at each targeted displacement, can be obtained by dividing the two terms (E and V) calculated by Equation (6-1) and (6-2), as represented by Equation (6-3).

$$\sigma = \frac{E}{V(x_{max})} \quad (6-3)$$

Figure 6-25 represent a comparison of compressive ice strengths using a flat indenter, and the results of experimental and numerical simulation matched well in this case.

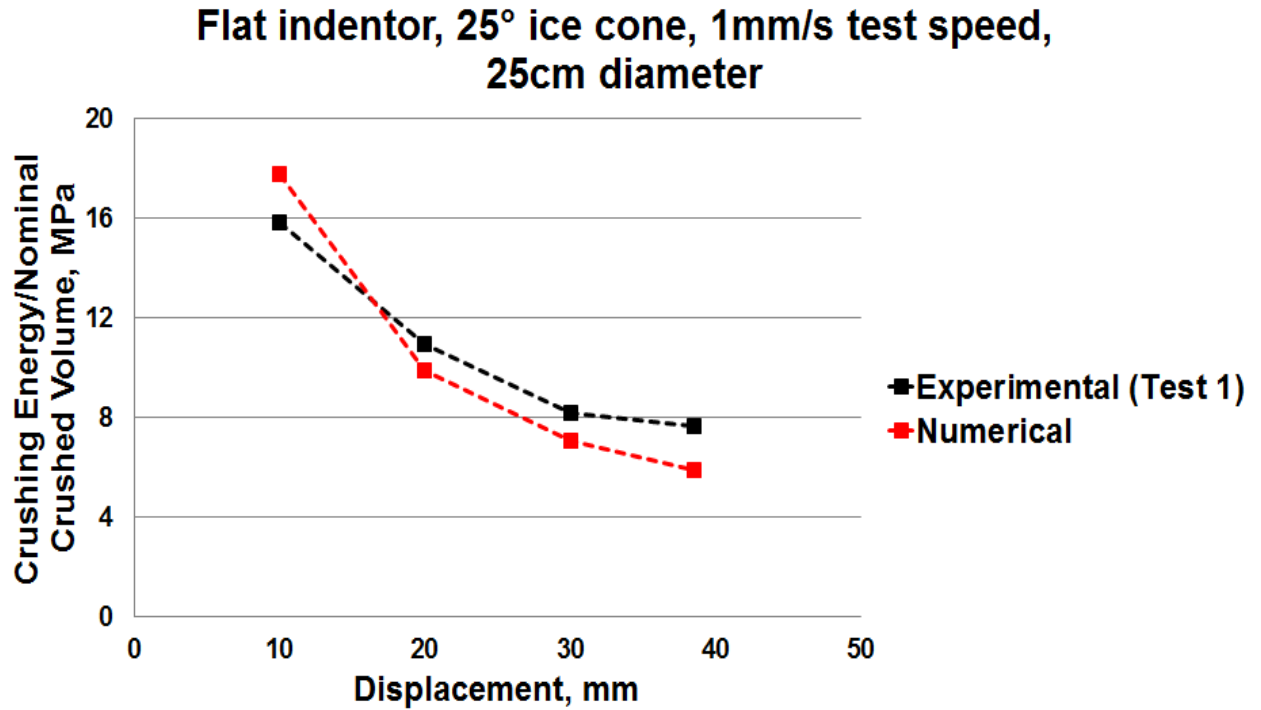


Figure 6-25: Comparison of compressive ice strength on a flat indenter

(Test 1: 25cm ice cone, 1mm/s test speed)

Figures 6-26 and 6-27 represent comparisons of compressive ice strength using the 10° conical and wedge indenter at 1mm/s and 100mm/s test speeds, respectively.

In the case of the 10° conical indenter as shown in Figure 6-26, the overall trend of both curves follows a similar trend through each displacement. However, difference between experimental and numerical simulations was about 24.9% on an average.

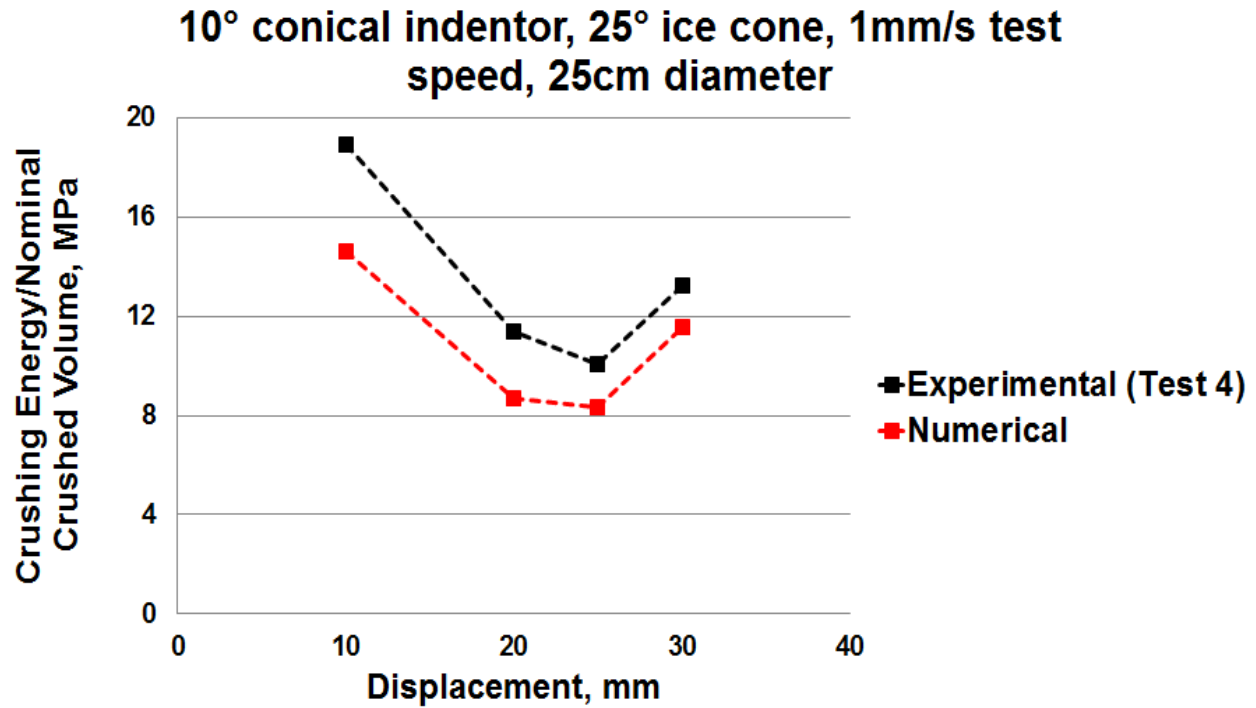


Figure 6-26: Comparison of compressive ice strength on a 10° conical indenter

(Test 4: 25cm ice cone, 1mm/s test speed)

Figure 6-27 shows the result of a 10° wedge indenter case with 100mm/s test speed. As shown in Figure 6-27, overall trend of both curves follows a similar trend at each displacement. The difference between experimental and numerical simulations was less than 5% on an average.

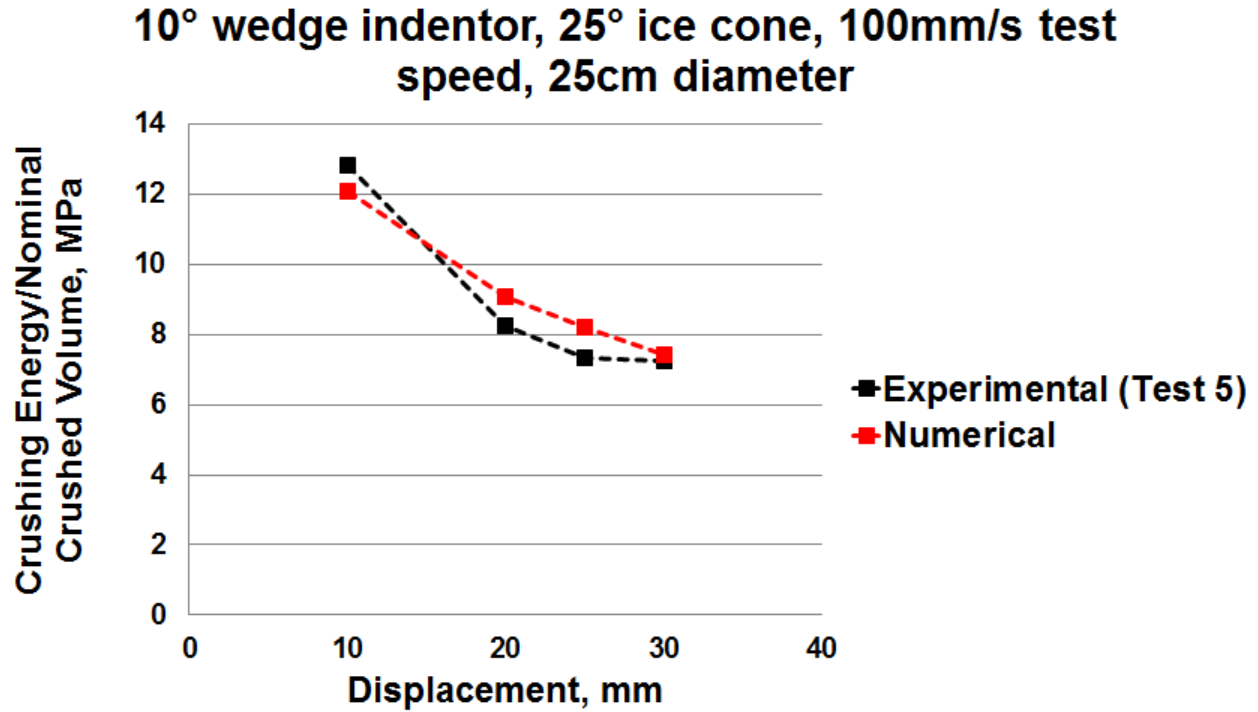


Figure 6-27: Comparison of compressive ice strength on a 10° wedge indenter

(Test 5: 25cm ice cone, 100mm/s test speed)

Comparison of numerical simulation and experimental results (through Figures 6-24 to 6-27) confirmed that the proposed numerical simulation model is fully applicable from the flat as well as to concave-shaped indenters (more results can be found in Appendix I).

First, the size of 10cm-diameter cone-shaped ice sample was adopted to verify the numerical model, and the model was extended to 25cm-diameter size. In this section, the various shapes of contact surface (flat, wedge and conical) were analyzed for the verification purpose and reasonable results could be confirmed. This represents that the scalability of the proposed model was proved without changing the simulation conditions or material properties.

Therefore, the numerical simulation model which meets the primary goal of this study, “numerical model which will be available for the general purpose along with various sizes/shapes of experimental condition without changing the simulation condition”, is developed and verified through comparison of the experimental results.

Chapter 7 Conclusions

This thesis provides the results of investigation on ice-structure interaction studies on non-planar surface through laboratory experiments in a cold room with two different shapes of indenter (wedge and conical) with different angles. A numerical simulation model was developed to predict ice loads acting on the flat and non-planar surface during ice-structure interaction, and the developed simulation model has been validated by experimental results. For the numerical model, the indenter was considered as rigid body and the ice modelled as a crushable foam material with added failure criteria. In this chapter, major findings from the above studies and recommendations for future research are summarized.

With reference to the originally stated research objectives the following outcomes have been achieved:

1. Investigate the effect of surface concavity in influencing ice loads and pressures during ice crushing using a series of systematic experiments on simplified concave shapes. Determine from the experiments if the load/pressure increases and if it does is the increase significant with reference to flat surface cases.

The ice load and pressure has been shown to increase substantially for 3-d (conical) concave shapes and insignificantly for 2D (wedge) concave shapes. This difference is thought to be due to the different levels of ice confinement that can be achieved with the 3D shape over the 2D shape.

2. Adopt procedures, previously developed for using pressure measurement films on a flat surface, to shaped surfaces in order to determine variations in spatial ice crushing pressure as influenced by the shape of the crushing surface.

The pressure film measurement technique has been adapted to non-planar surfaces and the previous procedures used to demonstrate the differences in pressures generated on the concave shapes. It is likely that the techniques developed for this study would work equally well for convex shapes.

3. Develop a numerical model of the ice crushing process against a concave surface that correctly captures both the global load variation and the local and spatial pressure variation as a crushing event proceeds.

The numerical model developed for LS-DYNA[®], using the crushable foam model with modified material properties and a two-layer material showed good agreement with the measured loads and pressures for both flat and concave surfaces. This model is believed to be suitably general to allow extrapolation to other shapes of ice and/or indenting surface.

4. Develop preliminary recommendations as to whether existing standards concerning ice loads on planar surfaces should be modified to account for the concave surfaces that commonly arise in ships subject to denting from ice loads.

The evidence from this study is that 3D concave shapes where ice confinement is increased substantially from flat surface cases can lead to significantly increased ice loads. This indicates that ice loads should be assessed considering the shape of the structure they are bearing on and that flat surface crushing tests do not adequately capture the load characteristics for concave structural shapes.

These conclusions along with some recommendations for follow-on work are discussed in more detail in the following sections.

7.1. Conclusions

7.1.1. Ice Crushing Pressure/Load on Non-Planar Surface

Two different shapes of concave indenter were considered in order to determine the characteristics of ice behavior against on non-planar surface. Wedge and conical-shaped indenters were designed to represent a simplified ‘concave’ shape in ship structure due to accidental dent or existing structural shape. Obtained test results were compared with existing test data against rigid flat indenters. Different shapes/angles of the indenter and ice samples, test speed, and crushing method have been adopted as test conditions. The contact area was defined to plot the process pressure-area curve. Pressure distributions and patterns of each of the test were evaluated using the pressure measurement film. Previously developed procedures were applied successfully to the concave surface indenters without any major modification.

Development of ice loads/pressures influenced by the confinement effect were evaluated. Important conclusions derived from the above study are as follows;

1) Overall, a higher ice load was measured against concave-shaped indenter. This was most evident in the conical indenter as this shape always presented higher ice loads due to the confinement effect provided by crushed ice trapped in the shape. In the case of conical-shaped indenter, the measured ice load was about 2.7 times (on average) greater compared to the flat indenter. Higher ice loads against the conical-shaped indentors imply that there are certain load scenarios that concave-shaped structure will experience higher ice loads compared to the flat structure.

In the case of the wedge-shaped indenter, measured ice loads showed only about 1.01 times (on average) higher load than flat indenters. The wedge-shaped indenter presented a slightly larger ice load for particular cases (generally when the wedge angle was less than 10°), but the results measured in this study were not significant when compared with a conical indenter.

The fact that the wedge-shaped indenter yields almost the same result in terms of global load as a flat indenter indicates that confinement effects can be relatively easily relieved and that shapes that provide an outlet for extruded ice in one or more directions do not suffer from the same degree of load amplification that a shape that fully confines the contact area. This conclusion applies to the load but the pressure distribution for the wedge shape was shown to be different and resulted in areas of higher local pressure than the flat surface case.

Table 7-1: Effect of indenter shape (25° ice cone, 1mm/s test speed)

Indenter shape	Indenter angle (°)	Test Speed (mm/s)	Force (ratio)
Flat	0	1	1.00
Conical	10	1	3.65
Wedge	10	1	1.02

Table 7-2: Effect of indenter shape (25° ice cone, 100mm/s test speed)

Indenter shape	Indenter angle (°)	Test Speed (mm/s)	Force (ratio)
Flat	0	100	1.00
Conical	10	100	2.63
Wedge	10	100	1.01

2) The width and height of the ice crushing pressure pattern were evaluated. Overall, there was no significant difference in pressure width regardless of test conditions. However, height of pressure patterns was affected by test speed (high test speed introduced a wider pressure pattern) due to frequent spalling events during processes.

3) Effect of cone angle, test speed and ice sample shape was evaluated through the analysis. Small cone angles and slow test speeds showed relatively higher ice loads. In addition, cone-shaped ice showed greater ice loads than cylindrical ice samples. It can be seen that the effects of cone angle and ice sample shape were related to the development of confinement.

7.1.2. Numerical Simulation

A valid numerical simulation model has been developed, based on results of small-scale laboratory compressive ice crushing tests in this study. Primarily, a numerical simulation model has been developed to model ice crushing against a flat surface. In addition, evaluations of scalability and compatibility were performed by considering 2.5 times larger-sized ice samples and various indenter shapes for the proposed numerical model. Consequently, the proposed model was determined to be valid through the verification analysis. The conclusions obtained in this study can be summarized as follows;

1) The numerical simulation model of the compressive cone-shaped and cylindrical ice tests were developed using LS-DYNA[®]. An improved crushable foam material property and failure criteria (max. principal stress) were applied to simulate a realistic behavior of the ice crushing processes. Diverse simulation parameters, for example, mesh size, failure criteria, was analyzed to obtain an optimal numerical simulation condition. The applicability of the proposed numerical simulation model was verified from the viewpoint of global load variation. In addition, the global and spatial pressure variations (local load) were also reviewed.

2) The evaluation of the scalability of the proposed numerical simulation model was conducted and validated (expanded to the 25cm diameter cone-shaped ice sample tests). Based on this applicability of the proposed numerical simulation model, a series of numerical simulations can be conducted considering various parameters and variables to investigate the influence of each selected parameter. Comparison of numerical simulation and experimental results confirmed that

the proposed numerical simulation model is fully applicable from the flat as well as to concave-shaped indenters without changing the simulation conditions or material properties.

7.2. Recommendations

7.2.1. Consideration of Structural Shape Effect

The concave-shaped indenter was intended to explore the ice load development during ice-structure interaction when the structure gets deformed to produce a dent prior to experiencing the ice loads. Results of the experimental studies, the numerical simulation and the regression equation developed confirm the fact that, the structure may experience nearly three times higher ice loads with dented structural surface. The occurrence of unexpected dents in structure due to excessive ice load is not a desirable situation in respect of the quality of ship hull.

However, as identified from the results obtained in this study, a structure may experience up to three times higher ice load acting on the structure when the ice load is applied repeatedly against the deformed hull such as in the conical shape (most common deformed shape of the structure generated by external loads). This means that a ship structure may experience a further damage, where already damaged by excessive overload due to the shape effect.

The phenomenon of load increment, caused by structural shape, has not previously been studied. In addition, existing ice class rules do not consider structural shape effect. In this study, the

results obtained through the experiments clearly confirmed that consideration of the structural shape effects should be undertaken.

Therefore, the necessity for taking account of additional ice loads may be induced by structural deformation (shape effect) becomes very important. Consideration is required at the design stage (or update in ice class rules) for ice-going ships that are expected to encounter ice-ship collisions during a service period in terms of risk management.

7.2.2. Ice Crushing Pressure/Load Experiments on Non-Planar Surface

In this study, preliminary results on the effect of formation of ice loads/pressures against a concave surface were examined. However, realistic Arctic regions, associated with ice-structure interaction scenarios, are more extensive and diverse.

In addition, only limited results of test condition were analyzed due to limitations in the experimental environment during this study. Therefore, the following suggestions will enhance the quality of further study and more significant results will be able to reveal on this topic.

1) For more precise assessment regarding the effect of wedge shape indenter, additional tests need to be conducted where the angle of indenter and the ice cone matched. Tightness of the gap between the two bodies will exclude the effect of void space interference between two objects and will maximize the confinement effect.

2) Tests using different indenter shapes and ice sample shapes will be valuable to understand the effect of shapes more precisely. In addition, a large-scale test and numerical simulation (close to a real-scale ice in the Arctic region) will give a better understanding of the size effects.

7.2.3. Numerical Simulation

The following comments will be useful to be considered in future research investigation:

1) Additional consideration of ice model and material properties, such as, different failure criteria, simulation options, would be required in order to obtain more precise results in terms of global and local ice loads. Furthermore, applying and comparison of results by different analysis methods as discussed in the literature review (SPH, CEM) will also be valuable.

2) An ice specimen 2.5 times larger was chosen to conduct verification analysis of scalability in this study, and a good results were obtained. In addition, ice sizes 10 or 20 times larger will also be required (a real scale that can be encountered in the arctic condition) for the verification purposes.

References

- Arora, J.S. and Wang, Q. (2006). 53.134: Structural Design II, *Lecture notes*, Univ. of Iowa, College of Engineering
- Akagawa, S., Saeki, H., Takeuchi, T., Sakai, M., Matsushita, H., Kamio, Z., Terashima, T. and Nakazawa, N. (2001). Medium-Scale Field Ice Indentation Test - Winter 1996-2000 Test Program -. *Proceedings of the 16th International Conference on Port and Ocean Engineering under Arctic Conditions*, August 12-17, Ottawa, ON, Canada, pp 567-576.
- Alfred L. T. (1984). Dynamic Ice Loads on a Ship. *Proceedings of 7th IAHR Ice Symposium*, Hamburg, F.R. Germany, August 25-31, 1984, Vol. 3, pp 227-313.
- Barrette, P., Pond, J., Li, C. and Jordaan, I. (2003). Laboratory-Scale Indentation of Ice. *Report submitted to the National Research Council Canada*, p.77
- Batto, R.A. and Schulson E.M. (1993). On the Ductile-to-Brittle Transition in Ice Under Compression. *Acta Metall Mater*, 41(7):2219–25.
- Bjerkås, M. (2002). Two Failure Criteria in Common Use for Ice-Structure Interaction Simulations. *Project report in "DIB 7989 Non-linear finite element methods-basic principles"*, Norwegian University of Science and Technology (NTNU), p. 18.

- Blanchet, D. and Defranco, S. (2001). Local Ice Pressure Area Curves. *IUTAM Symposium on Scaling Laws in Ice Mechanics and Ice Dynamics*, pp.13-30.
- Bruneau, S., Dillenburg, A. and Ritter, S. (2011). STEPS-RP001-2011 Ice Specimen Fabrication Techniques and Indentation Experiments. *A STePS² Pilot Laboratory Investigation of Ice-Structure Interaction*. Memorial University of Newfoundland, Sustainable Technology for Polar Ships and Structures, St. John's, p.9.
- Bruneau, S. E., Dillenburg, A. K. and Ritter, S. (2012). Ice Sample Production Techniques and Indentation Tests for Laboratory Experiments Simulating Ship Collisions with Ice. *Proceeding of 22nd International Offshore and Polar Engineering Conference*, Rhodes, Greece, June 17-22, pp.1268-1271.
- Bureau Veritas (BV) Rule Notes (2012). *Propulsors in Ice. NR 584 DT R00 E*, July 2012, p.12
- Carney, K.S., Benson, D.J., Bois, P.D. and Lee, R. (2006). A High Strain Rate Model with Failure for Ice in LS-DYNA. *Proceedings of 9th International LS-DYNA Users Conference*, Dearborn, MI, USA June 4-6, pp.15: 1-16.
- Cole, D.M. (1987). Strain-Rate and Grain-Size Effects in Ice. *Journal of Glaciology*, Vol. 33, No. 115, pp.274-280.

- Croasdale, K. (2001). Local Ice Load Data Relevant to Grand Backs Structures. *Report for: National Research Council of Canada (Contract number: 40731), PERD/CHC Report 20-61*, March 2001, p.216.
- Det Norske Veritas (DnV) Classification Notes (2011). *Ice Strengthening of Propulsion Machinery*, No.51.1 (Sec. 8), p.63.
- Daley, C. (1992). Ice Edge Contact and Failure. *Journal of Cold Regions Science and Technology*, Vol. 21, pp. 1-23.
- Daley, C.G. (1994). Compilation of Medium Scale Ice Indentation Test Results and Comparison to ASPPR. *Report by Daley R&E to National Research Council of Canada, Transport Canada*, Report No. TP 12151E, p.46.
- Daley, C.G., Tuhkuri, J., and Riska, K. (1996). Discrete Chaotic Ice Failure Model Incorporating Extrusion Effects. *Report submitted to the National Energy Board by Daley R&E and the Helsinki University of Technology*, Nov.,p.51.
- Daley, C., Tuhkuri, J. and Riska, K. (1998). The Role of Discrete Failures in Local Ice Loads. *Journal of Cold regions science and technology*, Vol. 27, pp. 197-211.

- Daley, C. (1999). Energy Based Ice Collision Forces. *Proceedings of 15th International Conferences on Port and Ocean Engineering under Arctic Conditions*, Espoo, Finland, August 23-27, pp.674-686.
- Daley, C.G. (2002). Application of Plastic Framing Requirements for Polar Ships. *Marine Structures*, 15, pp. 533-542.
- Daley, C.G. (2002). Derivation of Plastic Framing Requirements for Polar Ships. *Marine structures*, 15, pp. 543-559.
- Daley, C. (2004). A Study of the Process-Spatial Link in Ice Pressure-Area Relationships. *NRC PERD/CHC*, Report 7-108, p.57.
- Daley, C. (2007). Reanalysis of Ice Pressure-Area Relationships. *Marine Technology*, Vol. 44, No. 4, pp. 234-244.
- Daley, C. (2010). Sea Ice Engineering: Theory and Application. *Lecture note for EN8674/9096*, Memorial University of Newfoundland, p.154.
- Daley, C. and Kim, H.W. (2010). Ice Collision Forces Considering Structural Deformation. *Proceedings of 29th International Conference on Ocean, Offshore and Arctic Engineering*, Shanghai, China, June 6-11, pp. 817-825.

Delsart, D., Fabis, J. and Vagnot, A., (2011), Ice Impacts Modelling Using Smooth Particle Hydrodynamics Method, *4th European Conference for Aerospace Sciences (EUCASS)*, St. Petersburg, RU, July 4-8.

Dillenburg, A.K. (2012). Rate Dependency in Conical Ice Indenter Failure. *Diplomarbeit by Universität Duisburg-Essen (Master's thesis)*, Report No.:L-015/2012, p.140.

Dorival, O., Metrikine, A.V. and Simone, A. (2008). A Lattice Model to Simulate Ice-Structure Interaction. *Proceedings of the International Conference on Offshore Mechanics and Arctic Engineering*, June 15-20, Estoril, Portugal, pp. 989-996.

Frederking, R. (1998). The Pressure Area Relation in the Definition of Ice Forces. *Proceedings of 8th International Offshore and Polar Engineering Conference*, Montreal, QC, Canada, May 24-29, pp. 431-437.

Frederking, R. (1999). The Local Pressure-Area Relation in Ship Impact with Ice. *Proceedings of 15th International Conferences on Port and Ocean Engineering under Arctic Conditions*, Vol. 2, pp. 687-696.

Frederking, R. (2004). Ice Pressure Variations During Indentation. *Proceedings of 17th International Symposium on Ice*, Saint Petersburg, Russia, June 21-25, pp. 307-314.

Frederking, R. and Sudom, D. (2008). Local Ice Pressure Distributions During 1990 Hobson's Choice Ice Island Multi-Year Ice Indentation Tests. *Proceeding of the 19th IAHR International Symposium on Ice*, Vancouver, BC, Canada, July 6-11, pp. 815-827.

Frederking, R. and Ritch, R. (2009). Ice Pressure Variations During Indentation. *Proceedings of 19th International Offshore and Polar Engineering Conference*, Osaka, Japan, June 21-26, pp. 307-314.

Fujifilm homepage, Retrieved June 15, 2010, from <http://www.fujifilm.com/products/prescale/>

Gagnon, R.E. (1994). Generation of Melt During Crushing Experiments on Freshwater Ice. *Journal of Cold Regions Science and Technology*, Elsevier Science Publishers, 22 (1994) pp.385-398.

Gagnon, R. (2004). Side-Viewing High-Speed Video Observations of Ice Crushing. *Proceedings of 17th International Symposium on Ice*, Saint Petersburg, Russia, June 21-25, pp. 289-298.

Gagnon, R. (2004). Analysis of Laboratory Growler Impact Tests. *Journal of Cold Regions Science and Technology*, Elsevier Science Publishers, Vol. 39, pp. 1-17.

- Gagnon, R. and Derradji-Aouat, A. (2006). First Results of Numerical Simulations of Bergy Bit Collision with the CCGS Terry Fox Icebreaker. *Proceedings of the 18th International Symposium on Ice*, Sapporo, Japan, pp. 9-16.
- Gagnon, R.E. (2007). Results of Numerical Simulations of Growler Impact Tests. *Journal of Cold regions science and technology*, Elsevier Science Publishers , Vol. 49, pp.206-214.
- Gagnon, R. (2008). Analysis of Data from Bergy Bit Impacts Using a Novel Hull-Mounted External Impact Panel. *Journal of Cold Regions Science and Technology*, Elsevier Science Publishers, Vol. 52, pp.50-66.
- Gagnon, R. (2008). A New Impact Panel to Study Bergy Bit/Ship Collisions. *Proceedings of 19th IAHR International Symposium on Ice (Using New Technology to Understand Water-Ice Interaction)*, Vancouver, BC, Canada, July 6-11, pp. 993-1000.
- Gagnon, R., Bugden, A. and Ritch, R. (2009). Preliminary Testing of a New Ice Impact Panel. *Proceedings of the 20th International Conference on Port and Ocean Engineering under Arctic Conditions*, 2009, Lulea, Sweden.
- Gagnon, R.E. (2010). Numerical Rendition on Ice Crushing. *Proceedings of 20th IAHR International Symposium on Ice*, Lahti, Finland, pp. 888-900.

Gagnon, R.E. (2011). A Numerical Model of Ice Crushing Using a Foam Analogue. *Journal of Cold Regions Science and Technology*, Elsevier Science Publishers, 65 (2011) pp.335-350.

Golden Software. Surfer 11 manual, Retrieved January 4, 2013, from: <http://www.goldensoftware.com/products/surfer.shtml>.

Hanninen, S. (2005). Incidents and Accidents in Winter Navigation in the Baltic Sea, Winter 2002-2003. *Research Report No 54, Winter Navigation Research Board, FMA and SMA*, p.44.

Hobson's Choice Ice Test image, Retrieved November 21, 2012, from: <http://www.engr.mun.ca/~jordaen/research/>.

Hilding, D., Forsberg, J. and Gürtner, A. (2011). Simulation of Ice Action Loads on Offshore Structures. *Proceedings of 8th European LS-DYNA Users Conference*, Strasbourg.

IACS. (2011). Requirements Concerning Polar Class. *London: International Association of Classification Societies*.

Izumiyama, K., Takimoto, T. and Uto, S. (2007). Length of Ice Load Patch on a Ship Bow in Level Ice. *Proceedings of 10th International Symposium on Practical Design of Ships and Other Floating Structures*, Houston, TX, USA, October 1-5 (WP 10).

- Johnson, G.R. and Beissel, S.R., (1996), Normalized Smoothed Functions for SPH Impact Computations, *International Journal for Numerical Methods in Engineering*, 39:2725-2741.
- Johnson, G.R. and Hollquist, W.H., (1998), Evaluation of Cylindrical Impact Test data for Constitutive Model Constants, *Journal of Applied Physics*, 64(8):3901-3910.
- Jones, S. J. (1978). Triaxial Testing of Polycrystalline Ice. *Proceedings of the 3rd International Conference on Permafrost*, Edmonton, AB, Canada, Vol. I, pp. 670-674.
- Jones, S. J. (1982). The Confined Compressive Strength of Polycrystalline Ice. *Journal of Glaciology*, Vol. 28, No. 98, pp.171-177.
- Jones, S.J. (1997). High Strain-Rate Compression Tests on Ice. *Journal of Physical Chemistry B*, 101 (32), pp. 6099-6101.
- Jones, S. J. (2006). Comparison of the Strength of Iceberg and Other Freshwater Ice and the Effect of Temperature. *Report Number TR-2006-07*, Institute for Ocean Technology, National Research Council of Canada, p.21.
- Jordaan, I.J. (2001). Mechanics of Ice-Structure Interaction. *Engineering fracture mechanics* Vol. 68, pp. 1923-1960.

- Kim, H.W., Ulan-kvitberg, C. and Daley, C. (2011). Characteristics of Dry, Wetted and Submerged Ice. *Proceedings of 21st International Offshore and Polar Engineering Conference*, Maui, HI, USA, June 19-24, pp. 1056-1063.
- Kim, H.W., Daley, C. and Ulan-kvitberg, C. (2012). Reappraisal of Pressure Distribution Induced by Ice-Structure Interaction Using High-Precision Pressure Measurement Film. *Proceedings of 10th International Conference and Exhibition on Performance of Ships and Structures in Ice*, Banff, AB, Canada, September 17-20, pp. 191-199.
- Kim, H.W. and Daley, C. (2013). Reanalysis of Pressure Patterns and Pressure-Area Curves Considering Resolution of Pressure Measurement film. *Proceedings of 22nd International Conferences on Port and Ocean Engineering under Arctic Conditions*, Espoo, Finland, June 9-13.
- Kim, H.W. and Daley, C. (2013). Characteristics of Ice Crushing Pressure on Non-Planar Surface. *2013 Society of Naval Architects and Marine Engineers Annual Meeting and Expo*, Bellevue, WA, USA, November 6-8.
- Kim, H.W., Ulan-kvitberg, C. and Daley, C. (2014). Evaluation of Spatial Pressure Distribution During Ice-Structure Interaction Using Pressure Indicating Film. *International Journal of Naval Architecture and Ocean Engineering (IJNAOE)*, Vol. 6, Issue 3, DOI: 10.2478/ijnaoe-2013-0199.

- Konuk, I., Gurtner, A. and Yu, S. (2009). Study of Dynamic Ice and Cylindrical Structure Interaction by the Cohesive Element Method. *Proceedings of the 20th International Conference on Port and Ocean Engineering under Arctic Conditions*, June 9-12, 2009, Lulea, Sweden.
- Kujala, P. (1991). Damage Statistics of Ice-Strengthened Ships in the Baltic Sea 1984-1987. *Winter Navigation Research Board, Research Report No. 50, Research Report No 54*, Winter Navigation Research Board, FMA and SMA, p.72.
- Lavoie, M-A, Gakwaya, A. and Nejad Ensan, M., (2008), Application of the SPH Method for Simulation of Aerospace Structures under Impact Loading, 10th International LS-DYNA Users Conference, Dearborn, MI, USA, June 8-10, 9:35-42.
- Li, C. and Jordaan, I. (2006), Study of Spalls During Ice-structure Interaction, *PERD/CHC Report 7-110*.
- Liggins, A.B., Stranart, J. C. E., Finlay, J. B. and Rorabeck, C. H. (1992). Calibration and Manipulation of Data from Fuji Pressure-Sensitive Film. *Experimental Mechanics: Technology Transfer Between High Tech Engineering and Biomechanics* (Clinical Aspects of Biomedecine), Elsevier Science, pp. 61-70.

- Masterson, D.M. and Frederking, R.M.W. (1993). Local Contact Pressures in Ship/Ice and Structure/Ice Interactions. *Journal of Cold Regions Science and Technology*, Elsevier Science Publishers, Vol.21, pp.169-185.
- Masterson, D.M., Frederking, R.M.W., Wright, B., Karna, T. and Maddock, W.P. (2007). A Revised Ice Pressure-Area Curve. *Proceedings of the 19th International Conference on Port and Ocean Engineering under Arctic Conditions*, Dalian, China, June 27-30, pp.305-314.
- Matsuzawa, T., Wako, D. and Izumiyama, K. (2006). Local Ice Load on a Ship with Podded Propulsors. *Proceedings of the 18th IAHR International Symposium on Ice*, pp. 33-40.
- Myhre, S.A. (2011). Analysis of Accidental Iceberg Impacts with Membrane Tank LNG Carriers. *Norwegian University of Science and Technology (Master's thesis)*, p.62.
- Palmer, A.C., Dempsey, J.P. and Masterson, D.M. (2009). A Revised Ice Pressure-Area Curve and a Fracture Mechanics Explanation, *Journal of Cold Regions Science and Technology*, Elsevier Science Publishers, 56 (2009) pp.73-76.
- Pilling, M. (2011). The Influence of Ice Geometry on Indentation Loads - Experimental Setup, Data Acquisition, and Data Analysis. *Work term report submitted to STePS²*, p.105.

- Reddy Gudimetla, P.S., Colbourne, B., Daley, C., Bruneau, S.E and Gagnon, R. (2012). Strength and Pressure Profiles from Conical Ice Crushing Experiments. *Proceedings of 10th International Conference and Exhibition on Performance of Ships and Structures in Ice*, Banff, AB, Canada, September 17-20.
- Ritch, R., Frederking, R., Johnston, M., Browne, R. and Ralph, F. (2008). Local Ice Pressure Measured on a Strain Gauge Panel During the CCGS Terry Fox Bergy bit Impact Study. *Journal of Cold Regions Science and Technology*, Elsevier Science Publishers, Vol.52, 2008, pp.29-49.
- Rolls-Royce. Propulsion PDF. Retrieved December 07, 2012, from: [http:// www.rolls-royce.com/Images/RR-B_Propulsion_0612_singlepages_LR10_250512_tcm92-8664.pdf](http://www.rolls-royce.com/Images/RR-B_Propulsion_0612_singlepages_LR10_250512_tcm92-8664.pdf).
- Sanderson, T.J.O. (1988). Ice Mechanics-Risks to Offshore Structures. *Graham and Trotman*, London, UK.
- Sayed, M. and Frederking, R.M.W. (1992). Two-Dimensional Extrusion of Crushed Ice. Part 1: Experimental, *Journal of Cold Regions Science and Technology*, Elsevier Science Publishers, 21, pp. 25-36.
- Schulson, E.M. (1990). The Brittle Compressive Fracture of Ice. *Acta Metall Mater*, 38(10):1963–76.

- Schulson, E.M. and Buck, S.E. (1995). The Ductile-to-Brittle Transition and Ductile Failure Envelopes of Orthotropic Ice Under Biaxial Compression. *Acta Metallurgica et Materialia*, Volume 43, Issue 10, pp. 3661-3668.
- Schulson, E.M. (1997). The Brittle Failure of Ice Under Compression. *Journal of Phys Chem B*, 101(32):6254–8.
- Schulson, E.M. (2001). Brittle Failure of Ice. *Engineering Fracture Mechanics*, Vol. 68, pp. 1839-1887.
- Shunying, J. and Shewen, L. (2012). Interaction Between Sea Ice/Iceberg and Ship Structures: A review, *Advances in polar science*, Vol. 23, No.4:187-195.
- Sodhi, D.S. (1998). Nonsimultaneous Crushing During Edge Indentation of Freshwater Ice Sheets. *Journal of Cold Regions Science and Technology*, Elsevier Science Publishers, Vol. 27, pp. 179-195.
- Sodhi, D.S., Takeuchi, T., Nakazawa, N., Akagawa, S. and Saeki, H. (1998). Medium-Scale Indentation Tests on Sea Ice at Various Speeds. *Journal of Cold Regions Science and Technology*, Elsevier Science Publishers, Vol. 28, pp. 161-181.
- Sodhi, D.S. (2001). Crushing Failure During Ice-Structure Interaction. *Engineering Fracture Mechanics*, Pergamon , Vol. 68, pp. 1889-1921.

- Sodhi, D.S., Takeuchi, T., Kawamura, M., Nakazawa, N. and Akagawa, S. (2001). Measurement of Ice Forces and Interfacial Pressure During Medium-Scale Indentation Tests in Japan. *Proceedings of the 16th International Conference on Port and Ocean Engineering under Arctic Conditions*, August 12-17, Ottawa, ON, Canada, pp. 617-626.
- Sodhi, D. and Haehnel, R. (2003). Crushing Ice Forces on Structures. *Journal of Cold Regions Engineering*, Elsevier Science Publishers, 17(4), pp. 153-170.
- Sodhi, D.S., Takeuchi, T., Nakazawa, N., Akagawa, S. and Saeki, H. (2006). Ice Pressure Measured During JOIA Indentation Tests. *Proceeding of the 18th IAHR International Symposium in Ice*, Sapporo, Japan, September, pp. 199-206.
- Spencer, P. and Timco, G. (2010). Local Ice Pressures from Flatjacks and Rigid Indetors. *Proceedings of 20th IAHR International Symposium on Ice*, Lahti, Finland, June 14-18, pp. 9-19.
- Takeuchi, T., Kawamura, M., Sakai, M., Nakazawa, N., Terashima, T., Kamio, Z., Matsushita, H., Kurokawa, A., Akagawa, S. and Saeki, H. (2001). Ice Load Equation by Medium Scale Field Indentation Test Data. *Proceedings of the 11th International Offshore and Polar Engineering Conference*, Stavanger, Norway, June 17-22, pp. 713-720.

- Takeuchi, T., Akagawa, S., Nakazawa, N., Sakai, M. and Terashima, T. (2002). Ice Failure Mode and Ice Load Observed in Medium-Scale Field Ice Indentation Test. *Proceedings of the 12th International Offshore and Polar Engineering Conference*, Kitakyushu, Japan, May 26-31, pp. 760-765.
- Timco, G.W. and Weeks, W.F. (2010). A Review of the Engineering Properties of Sea Ice, *Journal of Cold Regions Science and Technology*, Elsevier, Vol. 60, pp. 107-129.
- Tuhkuri, J. (1995). Experimental Observations of the Brittle Failure Process of Ice and Ice-Structure Contact. *Journal of Cold Regions Science and Technology*, Elsevier Science Publishers, Vol. 23, pp.265-278.
- Ulan-kvitberg, C., Kim, H.W. and Daley, C. (2011). Comparison of Pressure-Area Effects for Various Ice and Steel Indenters. *Proceedings of 21st International Offshore and Polar Engineering Conference*, Maui, HI, USA, June 19-24, pp. 1048-1055.
- Ulan-kvitberg, C. (2012). Adapting Pressure Films to Measure Pressure Patterns in Ice-Steel Interaction Experiments. *Memorial University of Newfoundland (Master's thesis)*, p.271.
- Valkonen, J., Izumiyama, K. and Kujala, P. (2007). Measuring of Ice Induced Pressures and Loads on Ships in Model Scale. *Proceedings of 10th International Symposium on Practical Design of Ships and Other Floating Structures*, Houston, TX USA, pp. 1206-1214.

- Weiss, J. and Schulson, E.M. (1995). The Failure of Fresh-Water Granular Ice Under Multiaxial Compressive Loading. *Acta Metallurgica et Materialia*, Volume 43, Issue 6, June 1995, pp. 2303-2315.
- Yu, T., Yuan, Z. and Shan, S. (2010). Research on Simulation Model of Collision Force between Floating Ice and Pier. *World Academy of Science, Engineering and Technology* 61, pp. 371
- Zong, R. (2012). Finite Element Analysis of Ship-Ice Collision Using LS-DYNA. *Memorial University of Newfoundland (Master's thesis, p.192)*.
- Zou, B., Xiao, J. and Jordaan, I.J. (1996), Ice Fracture and Spalling in Ice-Structure Interaction, *Journal of cold regions and science technology* Vol. 24, pp. 213-220.

Appendix A Verification of Stepped Crushing Method

In order to create spatial pressure-area curves using the pressure measurement film, the pressure pattern at a specific instant of a collision needs to be measured. A conventional crushing method (defined as a straight crushing method) cannot sample the pressure pattern during the test therefore; a new approach needs to be adopted. In this study, a ‘stepped’ crushing method was employed. Details regarding the ‘stepped’ crushing method is well described by Kim et al. (2012; 2013; 2014) and Ulan-Kvitberg (2012).

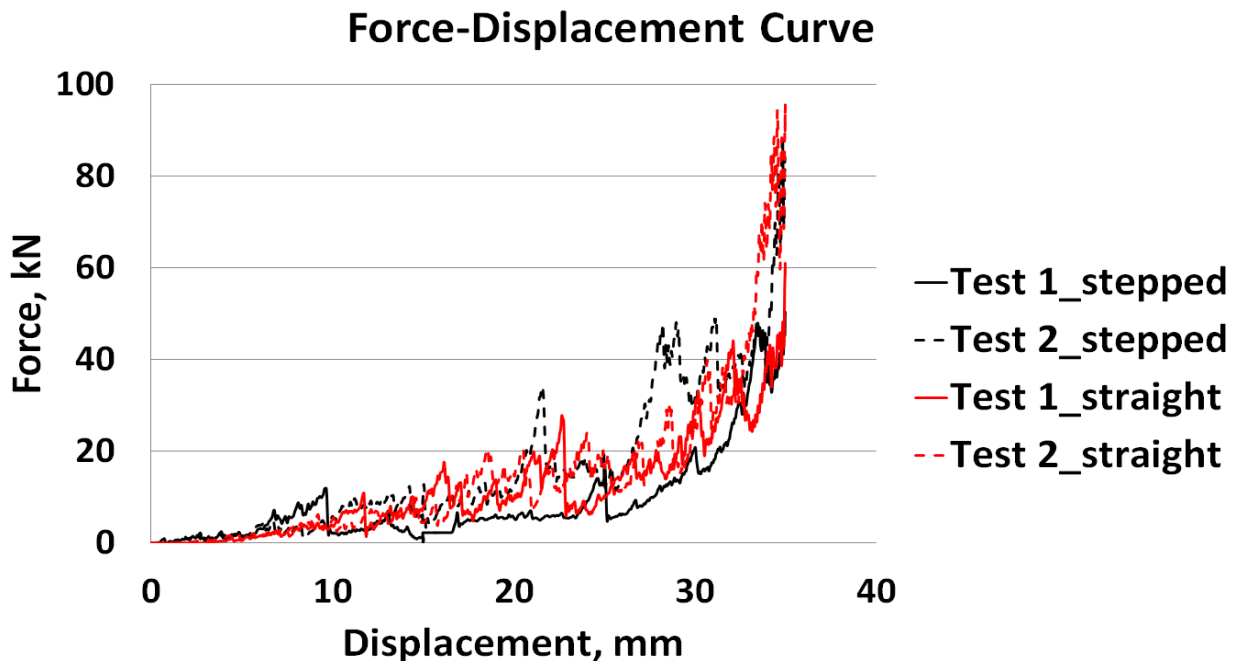
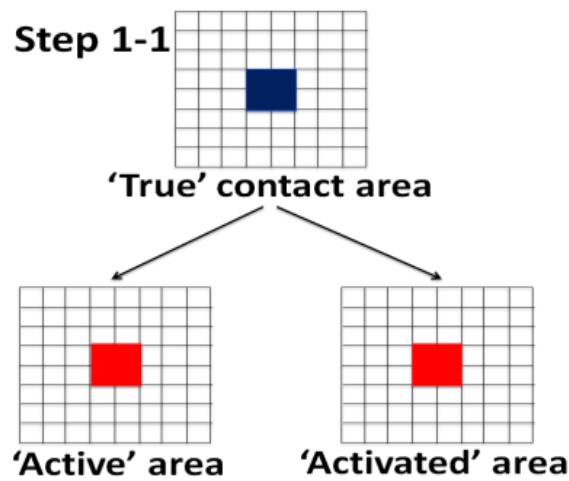


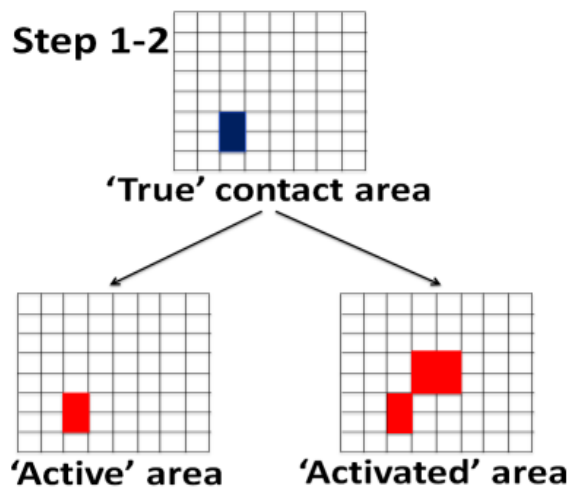
Figure A-1: Comparison of ‘straight’ and ‘stepped’ crushing method (reproduced by Kim)

Appendix B Active vs. Activated Area

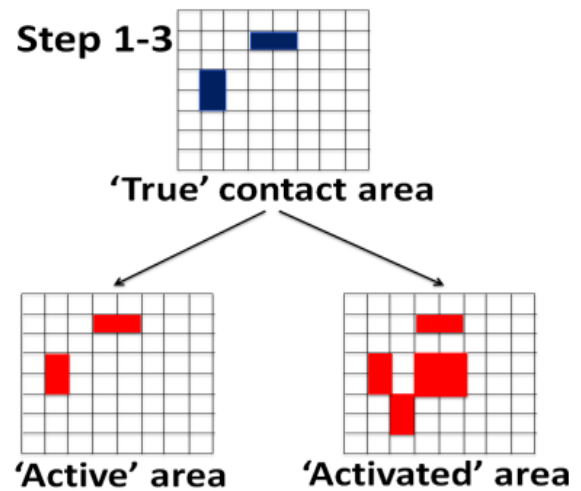
It is important to categorize a clear concept of the obtained pressure patterns (contact area) appearing after experiment using the pressure measurement film. The comparison of the ‘Active’ and ‘Activated’ area is described by Kim et al. (2012; 2014).



(a) Step 1-1



(b) Step 1-2



(c) Step 1-3

Figure B-1: Concept of ‘Active’ and ‘Activated’ area (reproduced by Kim)

Appendix C Verification of Resolution Sensitivity

C.1. Activated Area Comparison

Figures C-1 to C-6 represent the activated area comparison at each crushing steps considering all five different resolutions (pixel size). The total activated area did not differ significantly with varying resolution.

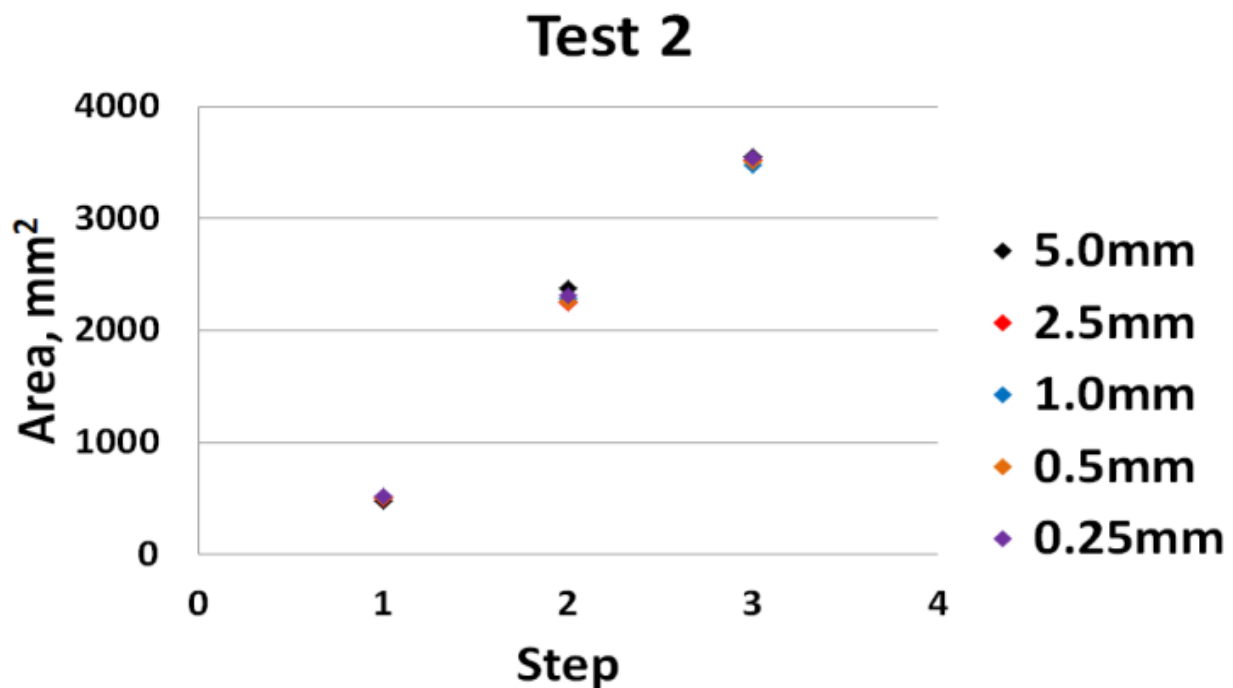


Figure C-1: Comparison of activated area by pixel size (Test 2)

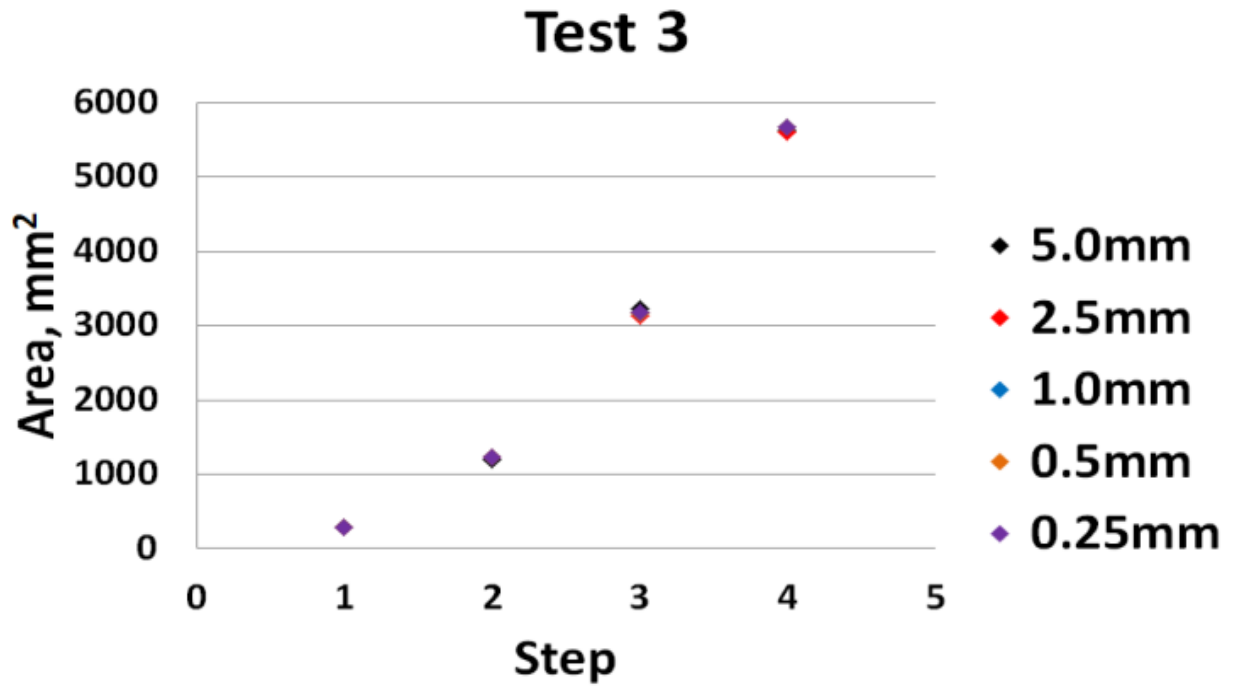


Figure C-1: Comparison of activated area by pixel size (Test 3)

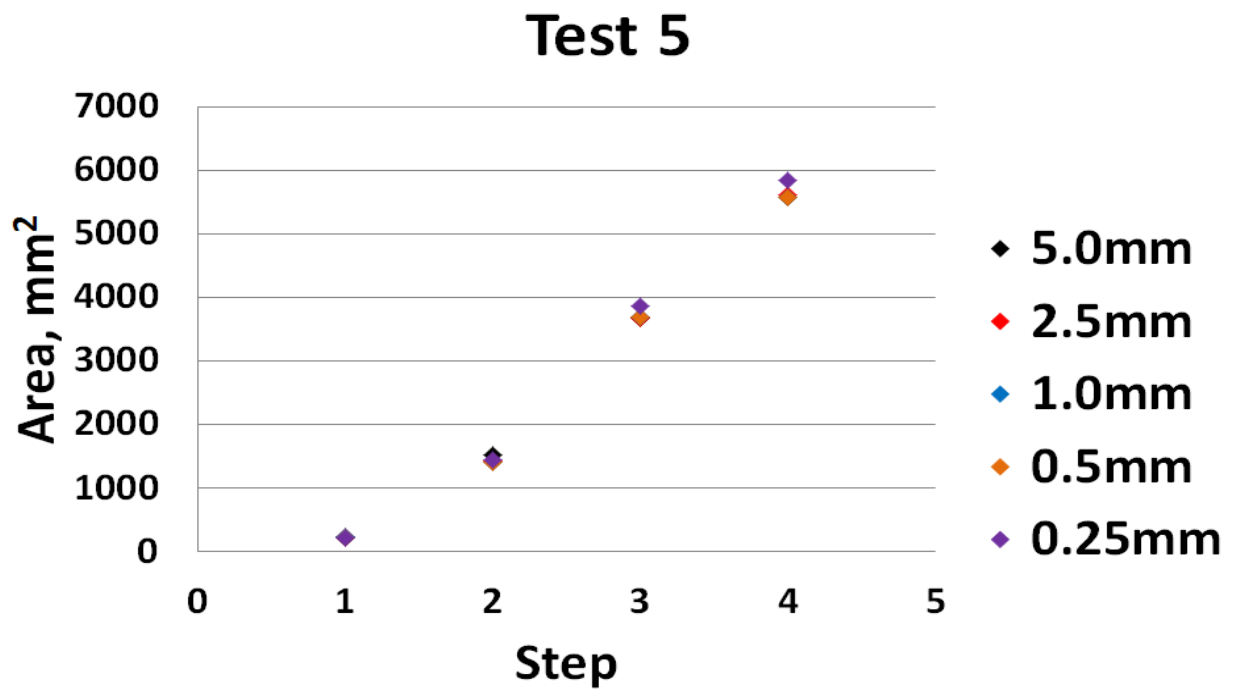


Figure C-3: Comparison of activated area by pixel size (Test 5)

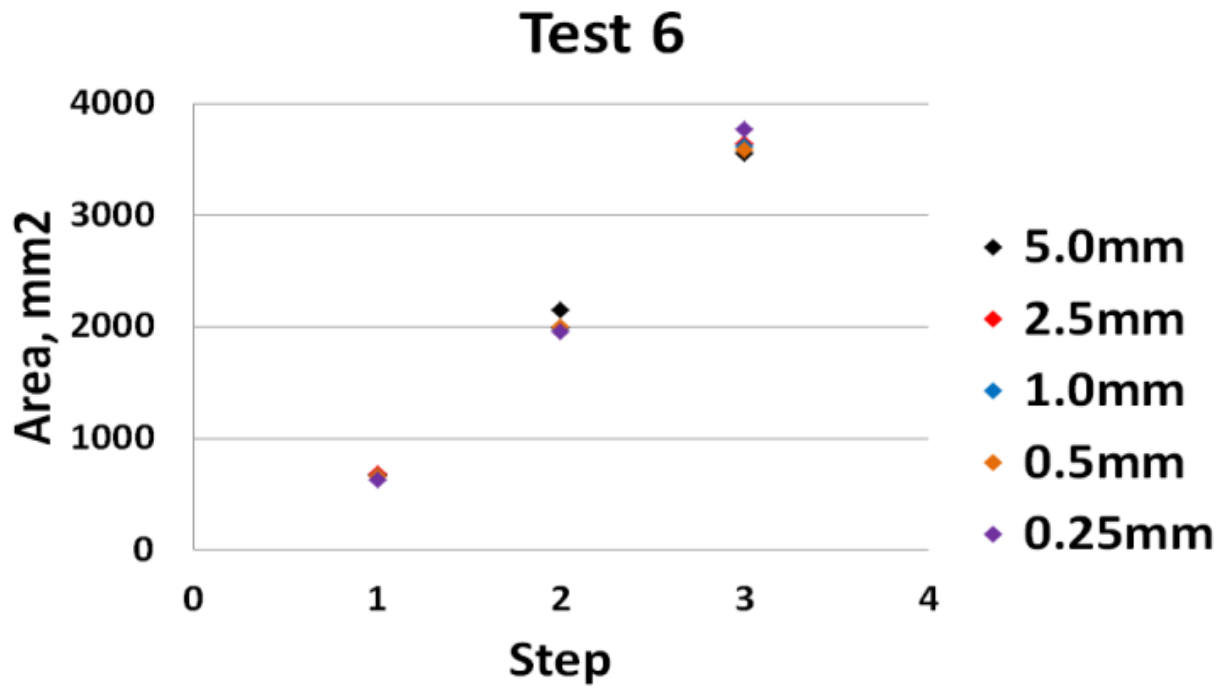


Figure C-4: Comparison of activated area by pixel size (Test 6)

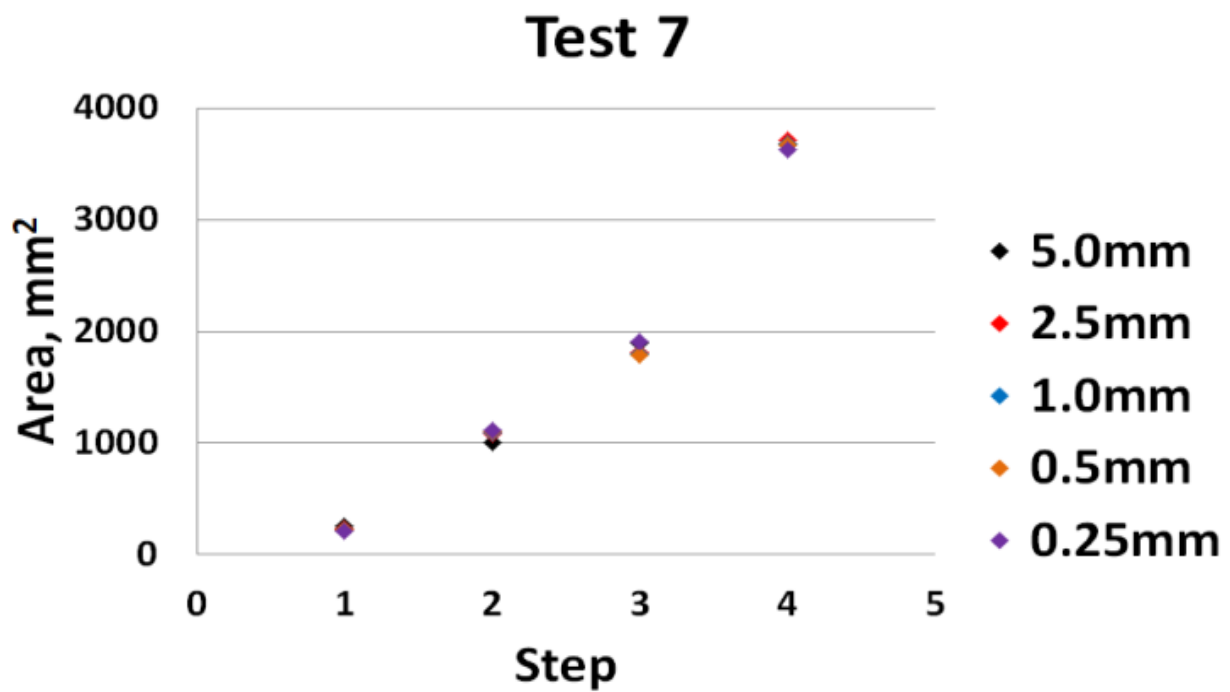


Figure C-5: Comparison of activated area by pixel size (Test 7)

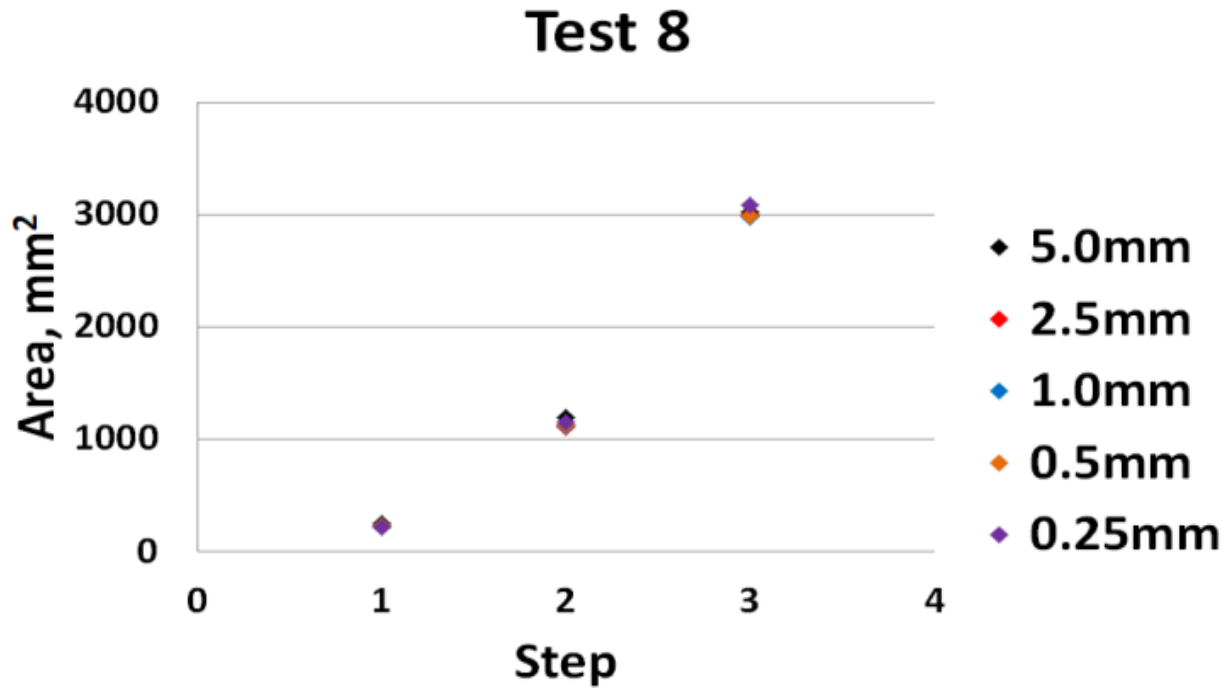


Figure C-6: Comparison of activated area by pixel size (Test 8)

Tables C-1 to C-3 represent the activated area comparison at each crushing step considering all five different resolutions (pixel size). As mentioned, the activated area was not significantly affected by resolution.

Step 1: Test 3 and 4 both satisfied the $\pm 5\%$ analysis criteria. Approximately 37.5% of the obtained results fell outside the $\pm 5\%$ designed range. Only 9.4% fell outside the $\pm 10\%$ designed range.

Table C-1: Results of activated area: Step 1

Pixel size (mm)	Test 1	Test 2	Test 3	Test 4	Test 5	Test 6	Test 7	Test 8
5.0	500.00 (+7.0)	475.00 (-8.2)	275.00 (-3.4)	225.00 (+1.8)	225.00 (+4.0)	675.00 (+8.0)	250.00 (+17.9)	250.00 (+13.6)
2.5	462.50 (-1.0)	500.00 (-3.4)	275.00 (-3.4)	218.75 (-1.1)	231.25 (+6.9)	687.50 (+10.0)	231.25 (+9.0)	225.00 (+2.2)
1.0	472.00 (+1.0)	513.00 (-0.9)	275.00 (-3.4)	221.00 (-0.1)	230.00 (+6.3)	663.00 (+6.1)	219.00 (+3.2)	229.00 (+4.1)
0.5	475.00 (+1.7)	514.50 (-0.6)	279.75 (-1.7)	225.00 (+1.8)	226.50 (+4.7)	664.25 (+6.3)	218.00 (+2.8)	233.50 (+6.1)
0.25	467.25	517.44	284.56	221.13	216.31	624.94	212.13	220.06

Step 2: Tests 1, 2, 4, and 8 satisfied the $\pm 5\%$ analysis criteria. Approximately 21.9% of the obtained results fell outside the $\pm 5\%$ designed range. Only 3.1% fell outside the $\pm 10\%$ designed range. Except the test 4, the majority of the results were within the designed range of $\pm 5\%$ regardless of the resolution.

Table C-2: Results of activated area: Step 2

Pixel size (mm)	Test 1	Test 2	Test 3	Test 4	Test 5	Test 6	Test 7	Test 8
5.0	1900.0 (-1.3)	2375.0 (+2.7)	1200.0 (-2.5)	1000.0 (+9.3)	1525.0 (+5.9)	2150.0 (+9.8)	1000.0 (-10.6)	1200.0 (+4.0)
2.5	1900.0 (-1.3)	2243.8 (-3.0)	1225.0 (-0.4)	968.75 (+5.9)	1418.8 (-1.4)	1987.5 (+1.5)	1081.3 (-3.3)	1106.3 (-4.1)
1.0	1917.0 (-0.4)	2284.0 (-1.2)	1224.0 (-0.5)	970.00 (+6.0)	1407.0 (-2.2)	1994.0 (+1.8)	1093.0 (-2.3)	1118.0 (-3.1)
0.5	1920.8 (-0.2)	2263.0 (-2.1)	1231.8 (+0.1)	968.25 (+5.8)	1409.5 (-2.1)	1999.8 (+2.1)	1103.0 (-1.4)	1126.0 (-2.4)
0.25	1924.5	2312.4	1230.4	914.94	1439.4	1958.3	1118.6	1153.7

Step 4: Tests 3, 5, and 7 satisfied the $\pm 5\%$ analysis criteria. Approximately 18.8% of the obtained results fell outside the $\pm 5\%$ designed range. None of the results fell outside the $\pm 10\%$ designed range. This indicates that the sensitivity of resolution decreases when the activated area (as test step progress) is increased.

Table C-3: Results of activated area: Step 4

Pixel size (mm)	Test 3	Test 4	Test 5	Test 7
5.0	5625.0 (-0.7)	2675.0 (-2.9)	5575.0 (-4.6)	3675.0 (+1.1)
2.5	5606.3 (-1.0)	2550.0 (-7.5)	5618.8 (-3.9)	3712.5 (+2.2)
1.0	5671.0 (+0.1)	2505.0 (-9.1)	5573.0 (-4.6)	3679.0 (+1.2)
0.5	5673.3 (+0.2)	2529.3 (-8.2)	5583.8 (-4.5)	3675.8 (+1.2)
0.25	5663.4	2756.1	5844.6	3633.0

C.2. Total Force Comparison

Figures C-7 to C-12 show a comparison of the total load at each step of the tests at the varying resolutions. In contrast to the comparison of the activated area, the calculated total load represents a higher sensitivity to resolution.

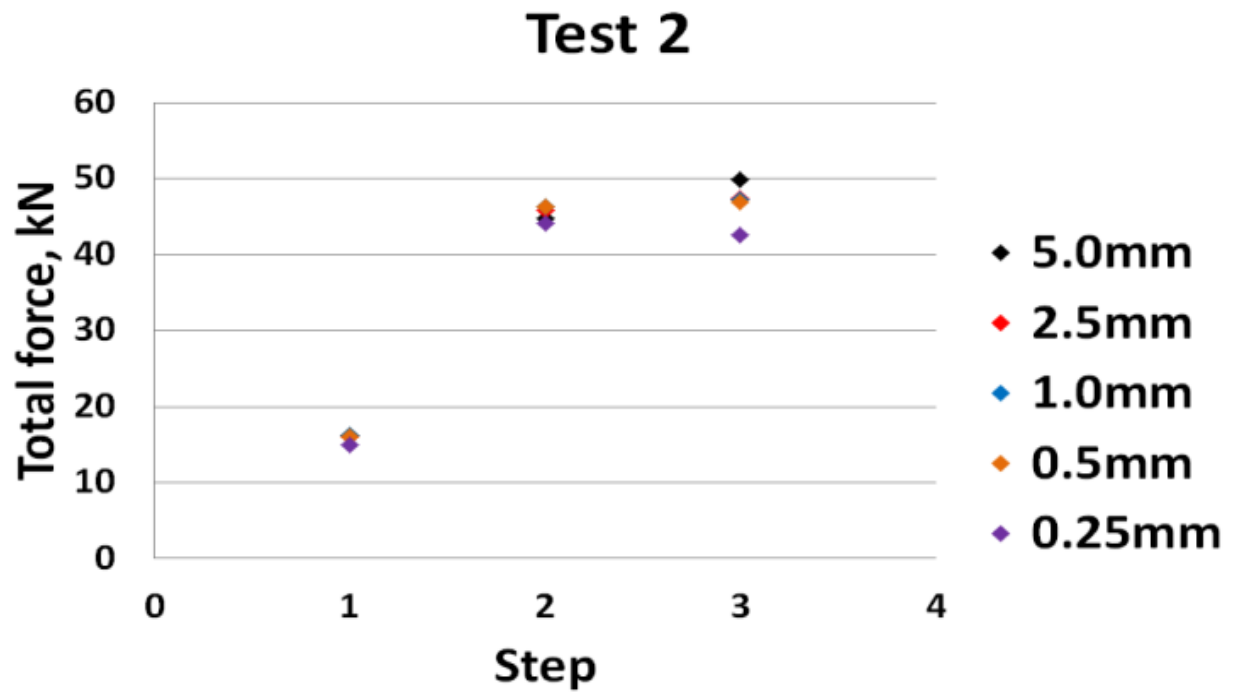


Figure C-7: Comparison of total force by pixel size (Test 2)

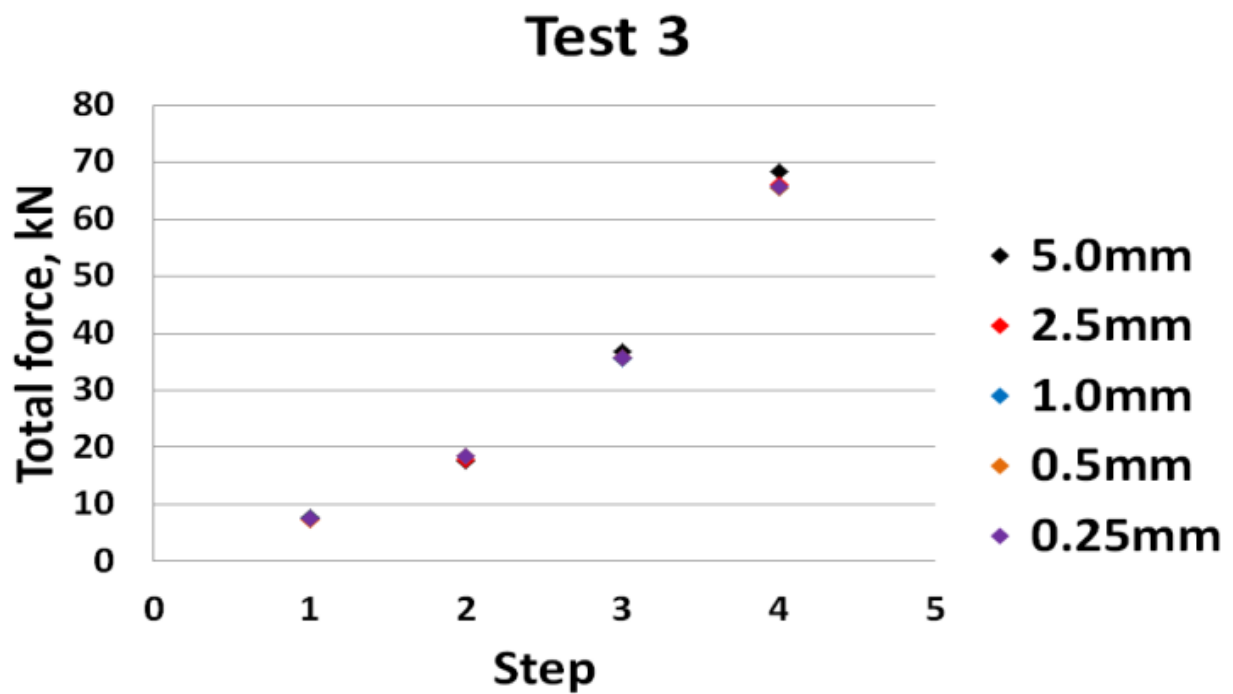


Figure C-8: Comparison of total force by pixel size (Test 3)

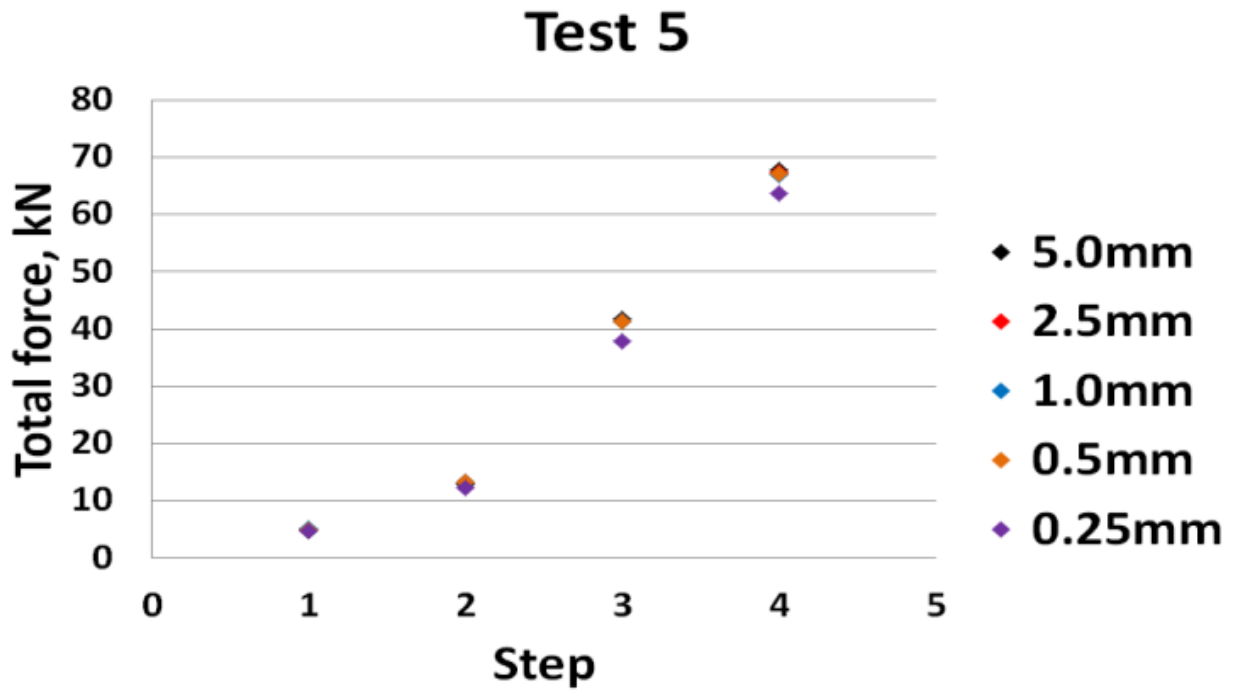


Figure C-9: Comparison of total force by pixel size (Test 5)

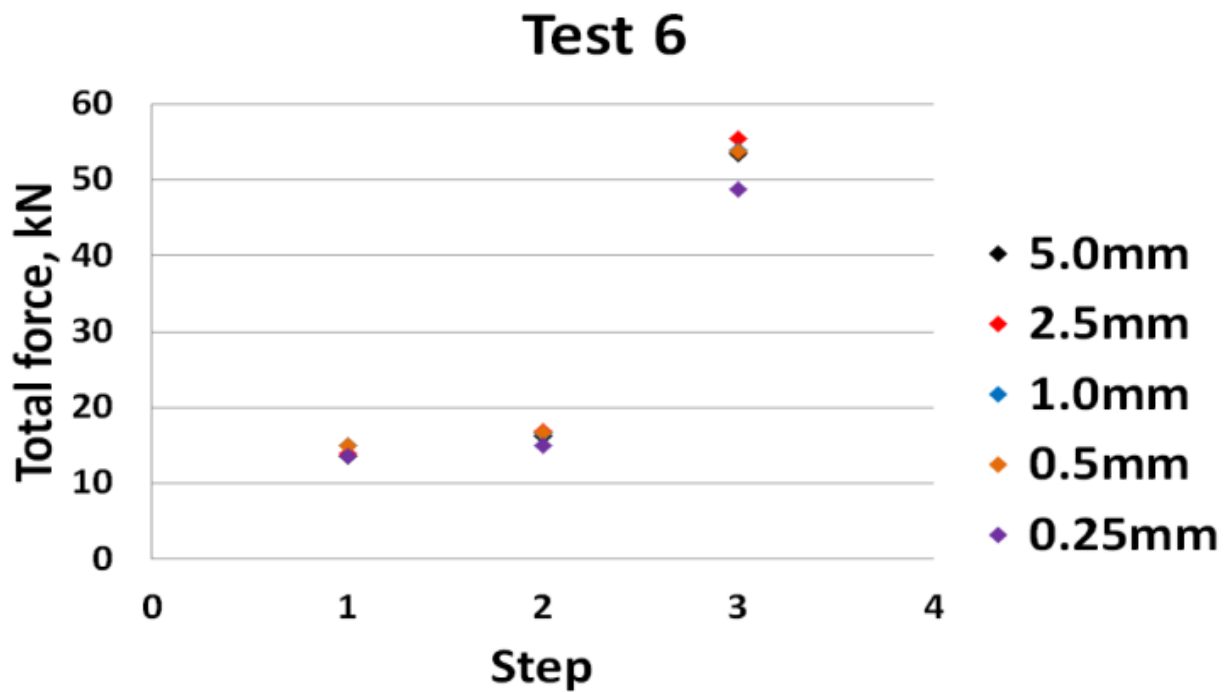


Figure C-10: Comparison of total force by pixel size (Test 6)

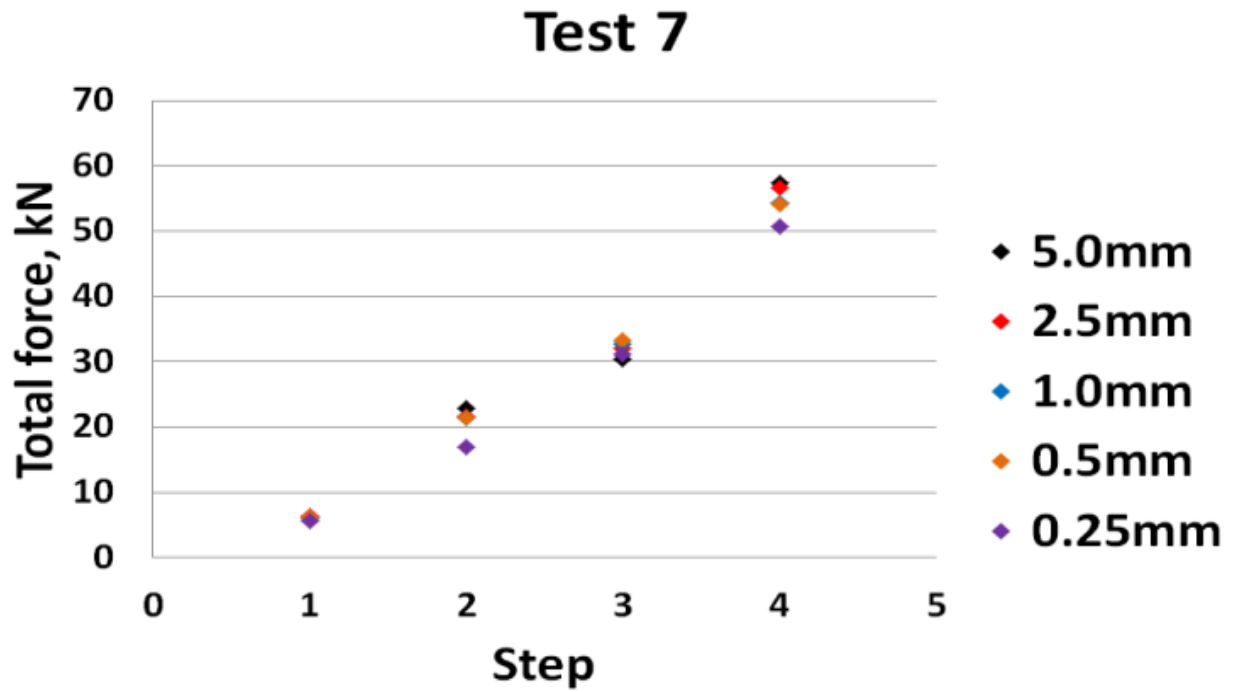


Figure C-11: Comparison of total force by pixel size (Test 7)

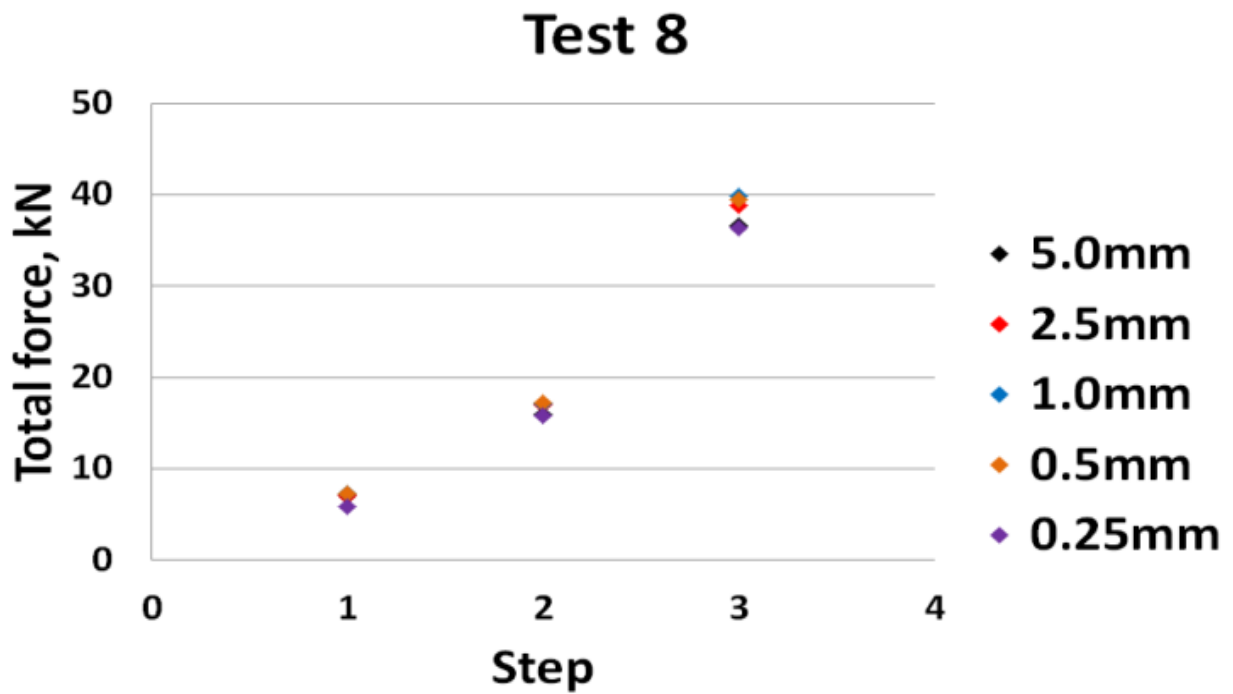


Figure C-12: Comparison of total force by pixel size (Test 8)

Tables C-4 and C-5 show a comparison of the total load at each step of the tests at varying resolutions. Again, the calculated total load shows that it is highly sensitive to resolution, compared to the activated area. Comparative tables for each step offer a more detailed look at the data and are shown in Tables C-4 and C-5.

Step 2: 71.9% of the results fell outside of the $\pm 5\%$ designed range. 40.6% fell outside of the $\pm 10\%$ designed range. Tests 1, 4, 5, 6 and 7 fell outside the $\pm 5\%$ range regardless of the pixel size, while Tests 1 and 7 fell outside of the specified $\pm 10\%$ range. A little improvement was observed in resolution sensitivity for expanding contact area, but it was not significant.

Table C-4: Results of total force: Step 2

Pixel size (mm)	Test 1	Test 2	Test 3	Test 4	Test 5	Test 6	Test 7	Test 8
5.0	36.01 (+10.7)	44.70 (+1.1)	17.68 (-4.2)	24.51 (-15.3)	12.82 (+5.1)	16.18 (+8.3)	22.85 (+34.6)	15.90 (+0.3)
2.5	36.12 (+11.1)	45.86 (+3.8)	17.77 (-3.7)	30.48 (+5.3)	13.26 (+8.7)	16.79 (+12.4)	21.54 (+26.9)	17.04 (+7.4)
1.0	35.98 (+10.6)	46.25 (+4.7)	18.45 (-0.1)	31.84 (+10.0)	13.22 (+8.4)	16.57 (+10.9)	21.45 (+26.3)	17.16 (+8.2)
0.5	36.15 (+11.1)	46.26 (+4.7)	18.41 (-0.2)	31.51 (+8.9)	13.33 (+9.3)	16.74 (+12.0)	21.41 (+26.1)	17.25 (+8.8)
0.25	32.52	44.19	18.46	28.94	12.20	14.94	16.98	15.86

Step 3: 75.0% of the results fell outside of the $\pm 5\%$ designed range while 25.0% fell outside of the $\pm 10\%$ designed range. This indicates an improvement from step 1 to step 4, although the improvement was not significant compared to the activated area case.

Table C-5: Results of total force: Step 3

Pixel size (mm)	Test 1	Test 2	Test 3	Test 4	Test 5	Test 6	Test 7	Test 8
5.0	45.70 (+9.0)	49.84 (+17.0)	36.86 (+2.8)	27.50 (+0.9)	41.71 (+10.3)	53.36 (+9.4)	30.36 (-2.6)	36.63 (+0.5)
2.5	44.36 (+5.8)	47.40 (+11.2)	35.58 (-0.8)	29.34 (+7.7)	41.35 (+9.4)	55.46 (+13.7)	32.14 (+3.1)	38.85 (+6.6)
1.0	44.75 (+6.8)	47.22 (+10.8)	35.58 (0.0)	29.29 (+7.5)	41.25 (+9.1)	53.85 (+10.4)	32.80 (+5.2)	39.92 (+9.5)
0.5	44.45 (+6.1)	46.96 (+10.2)	35.70 (-0.4)	29.65 (+8.8)	41.29 (+9.2)	53.77 (+10.2)	33.30 (+6.8)	39.47 (+8.3)
0.25	41.91	42.61	35.85	27.25	37.81	48.79	31.17	36.45

C.3. Pressure Distribution Comparison

Figures C-13 to C-38 show the pressure distributions for each step of the test. As shown in the main text, 5.0 mm and 2.5mm pixel size does not give an adequate representation of the pressure pattern. According to the list of Figures C-13 to C-38, it is confirmed that 1.0 mm pixel size give a better representation of detailed pressure distribution.

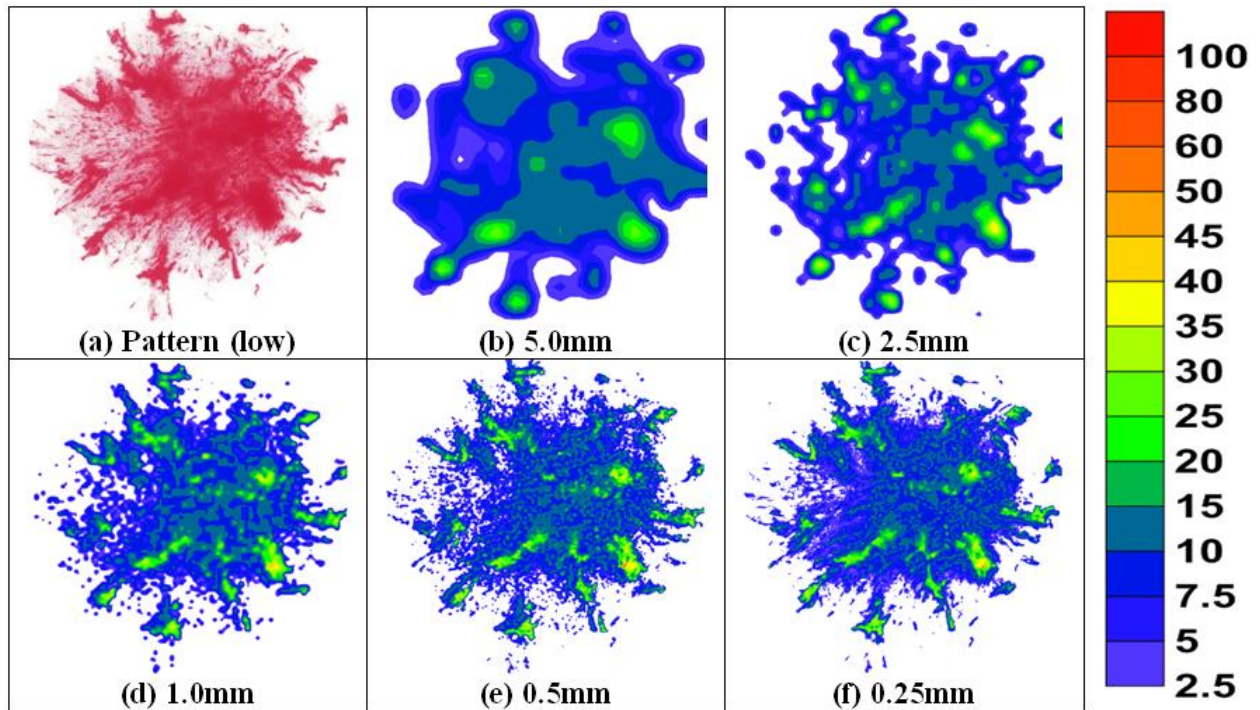


Figure C-13: Pressure distribution of Test 1-Step 3

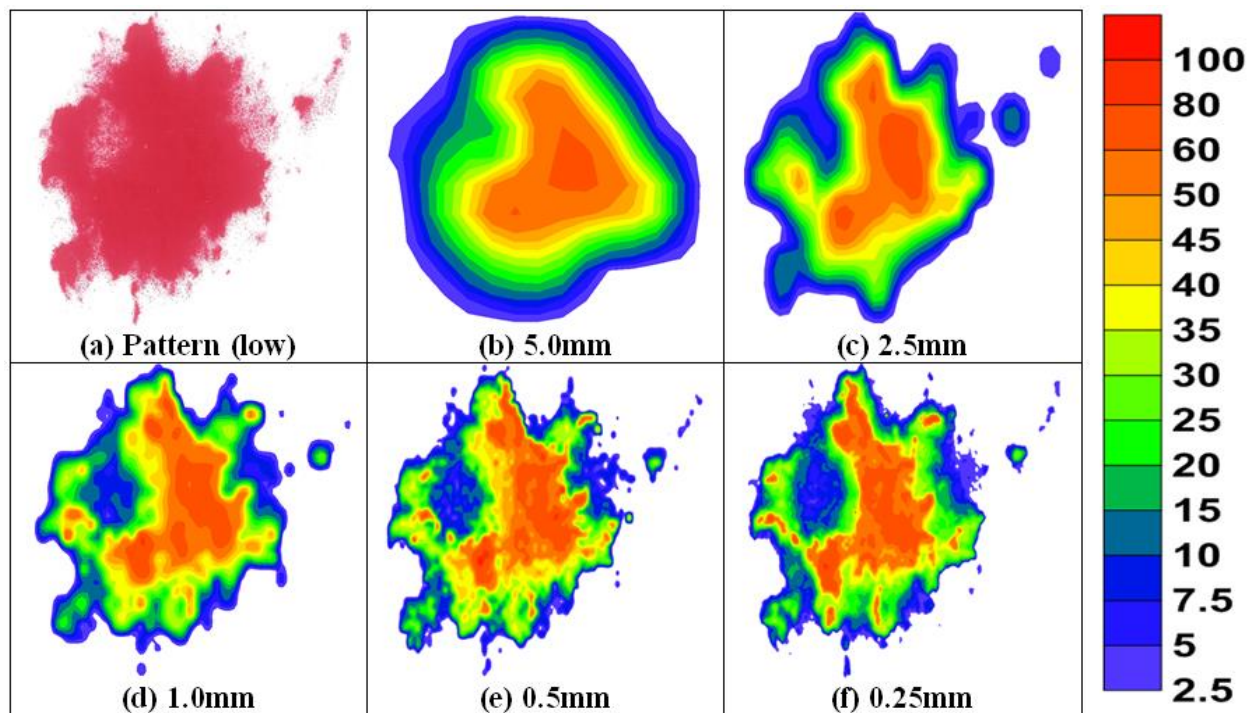


Figure C-14: Pressure distribution of Test 2-Step 1

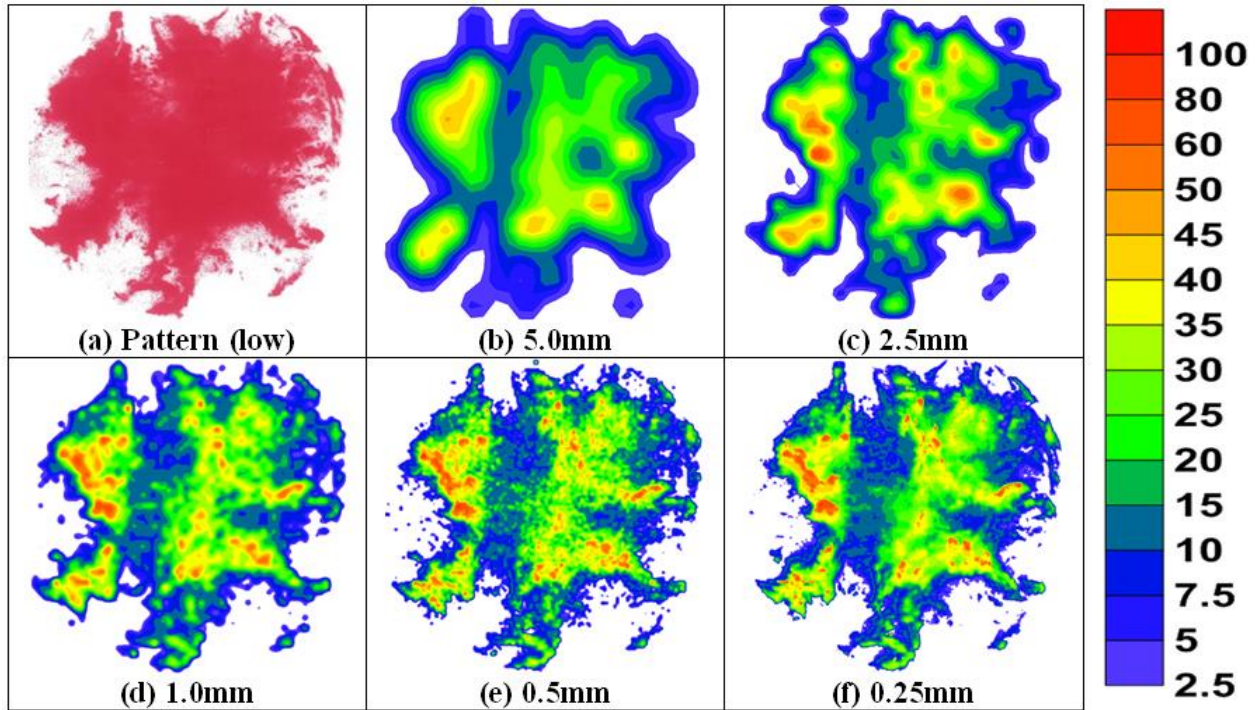


Figure C-15: Pressure distribution of Test 2-Step 2

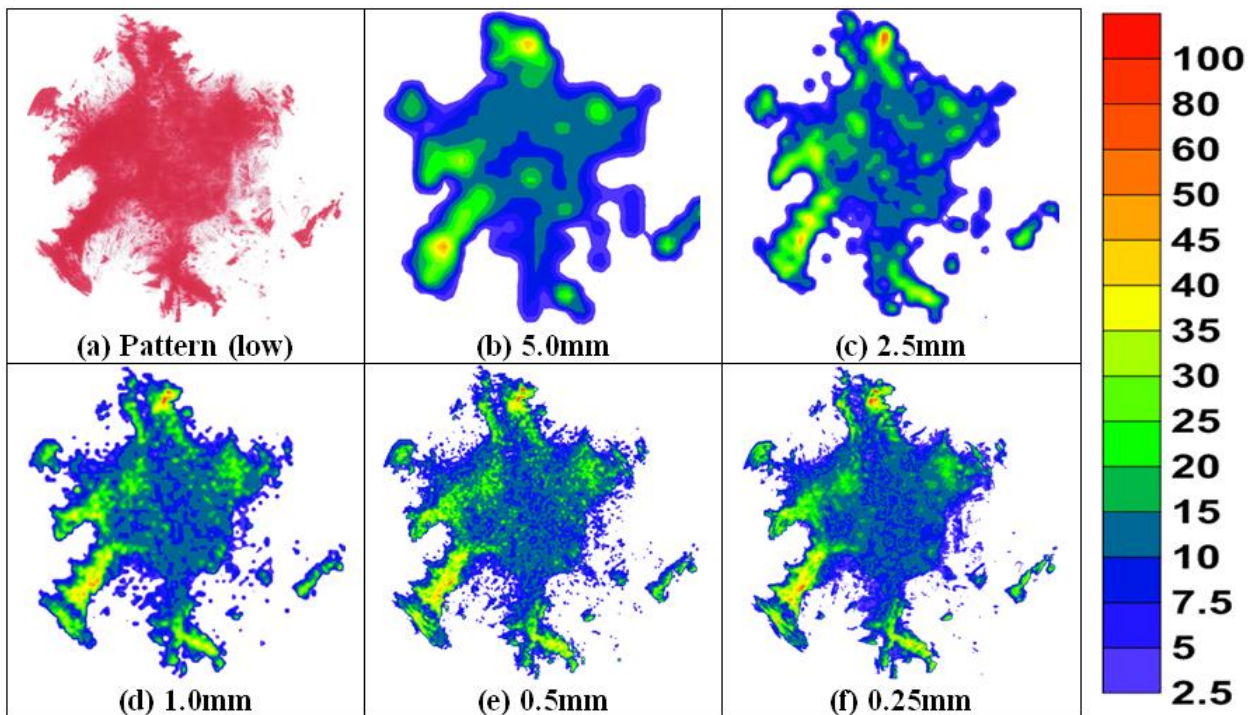


Figure C-16: Pressure distribution of Test 2-Step 3

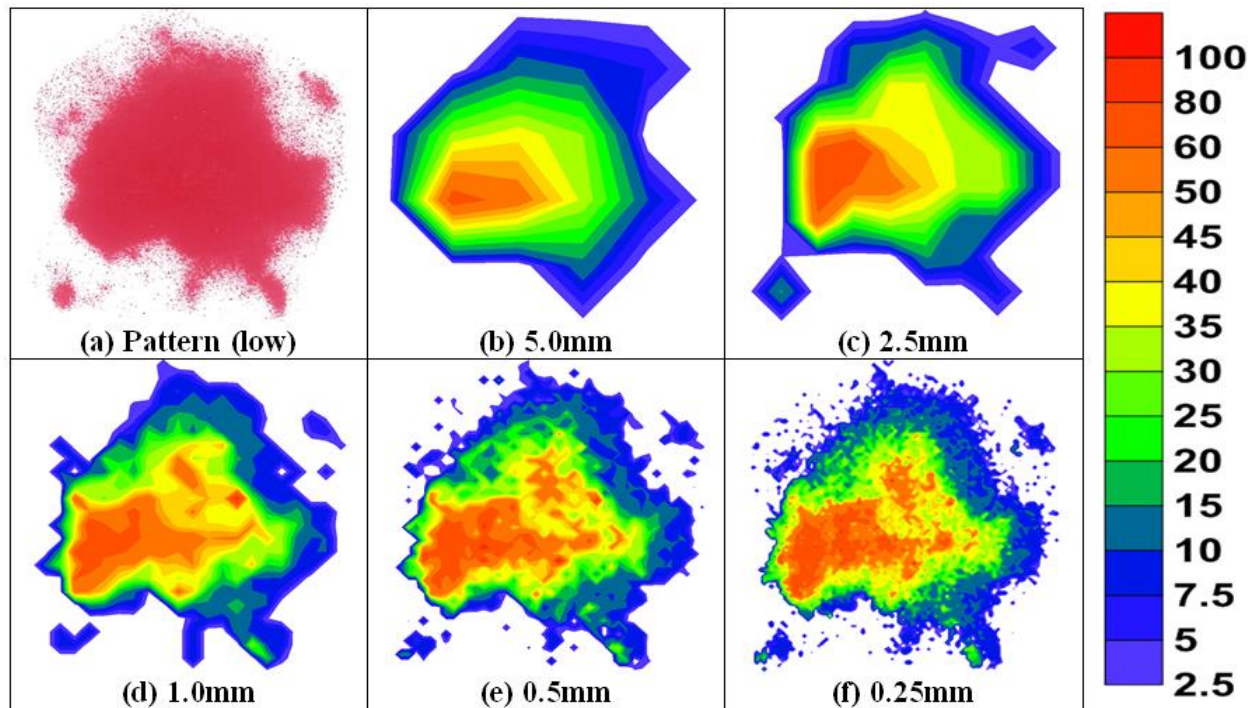


Figure C-17: Pressure distribution of Test 3-Step 1

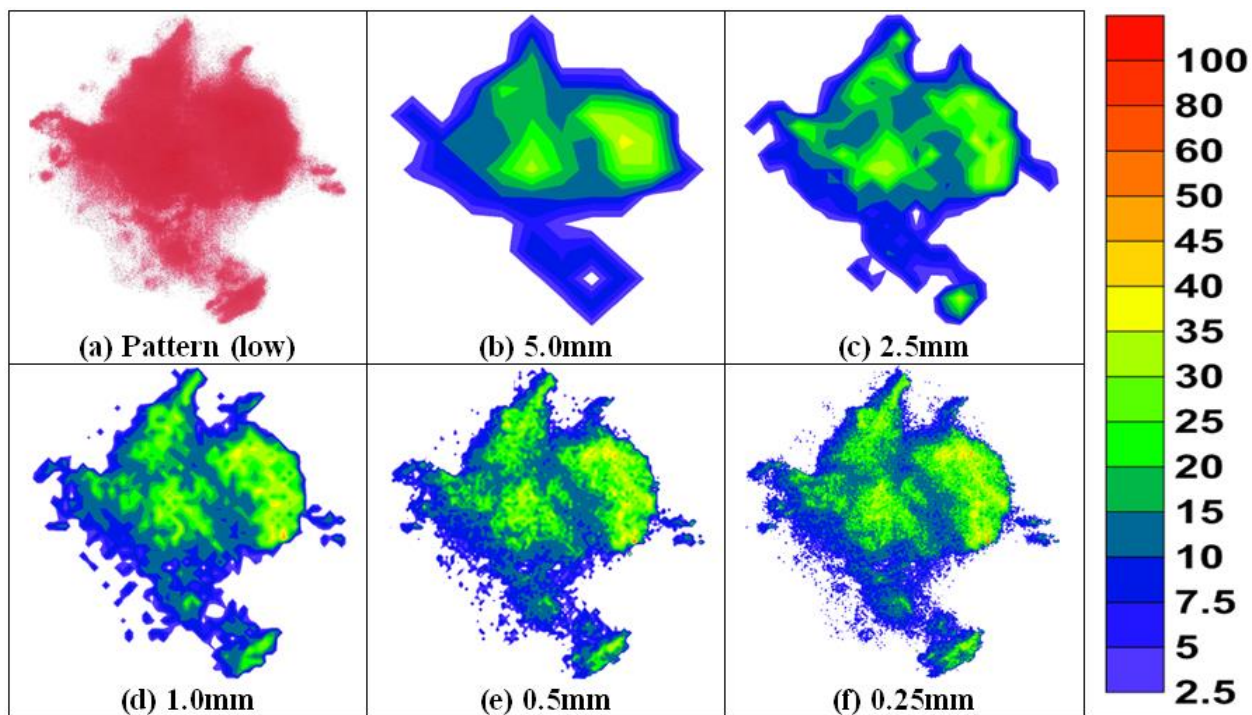


Figure C-18: Pressure distribution of Test 3-Step 2

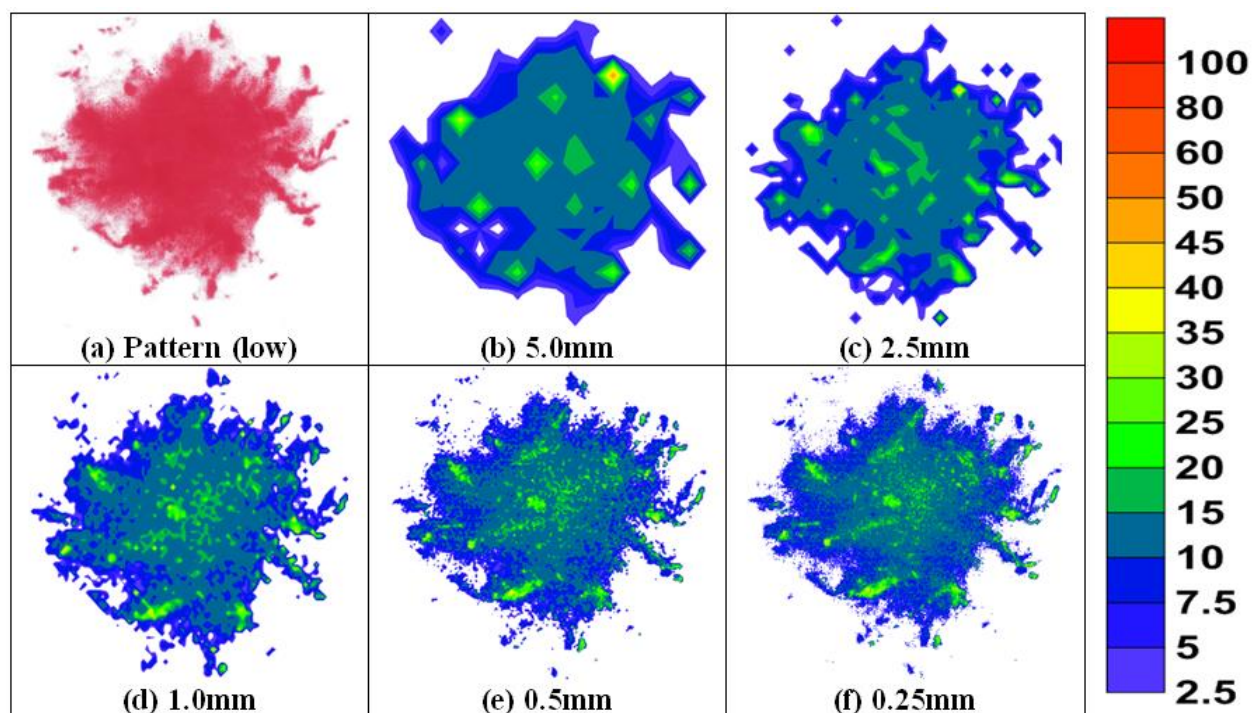


Figure C-19: Pressure distribution of Test 3-Step 3

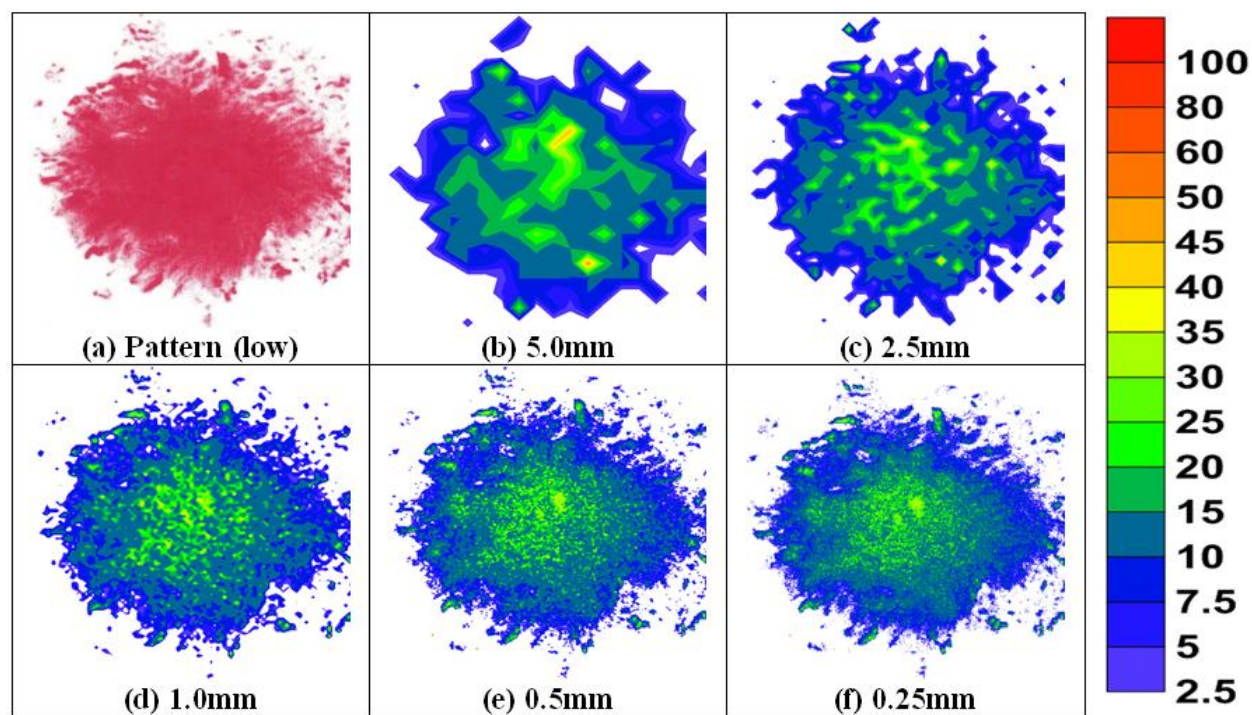


Figure C-20: Pressure distribution of Test 3-Step 4

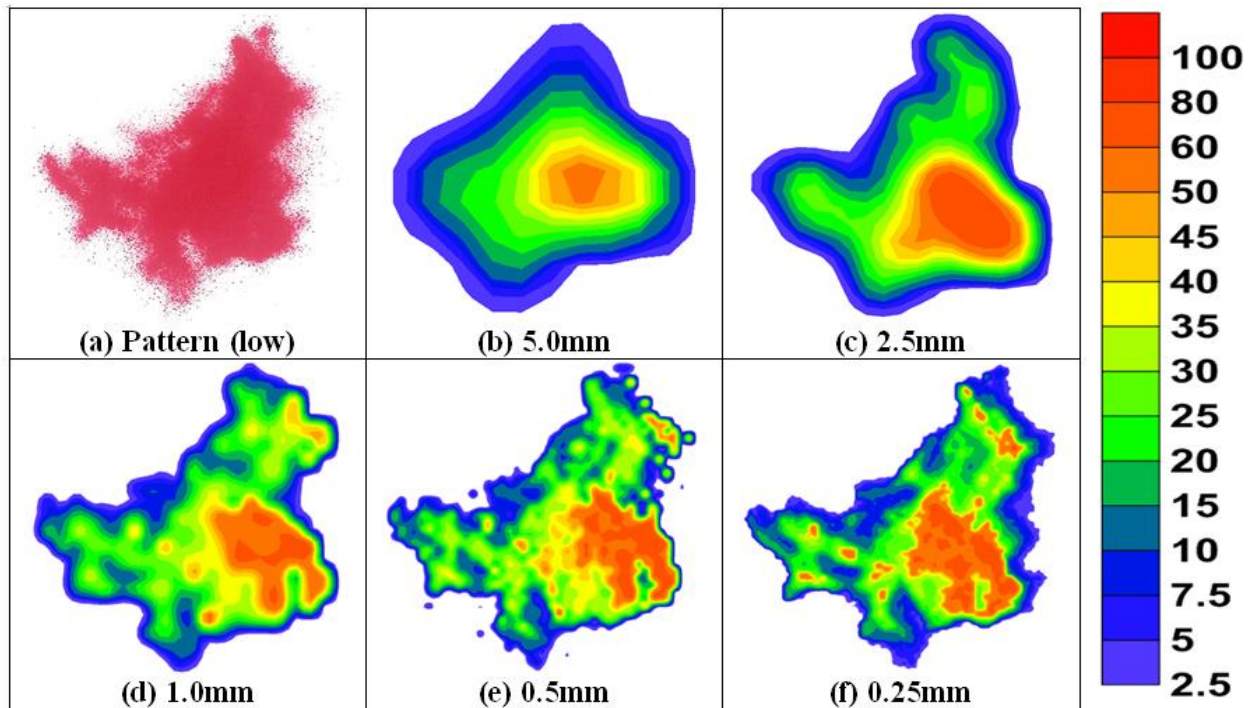


Figure C-21: Pressure distribution of Test 4-Step 1

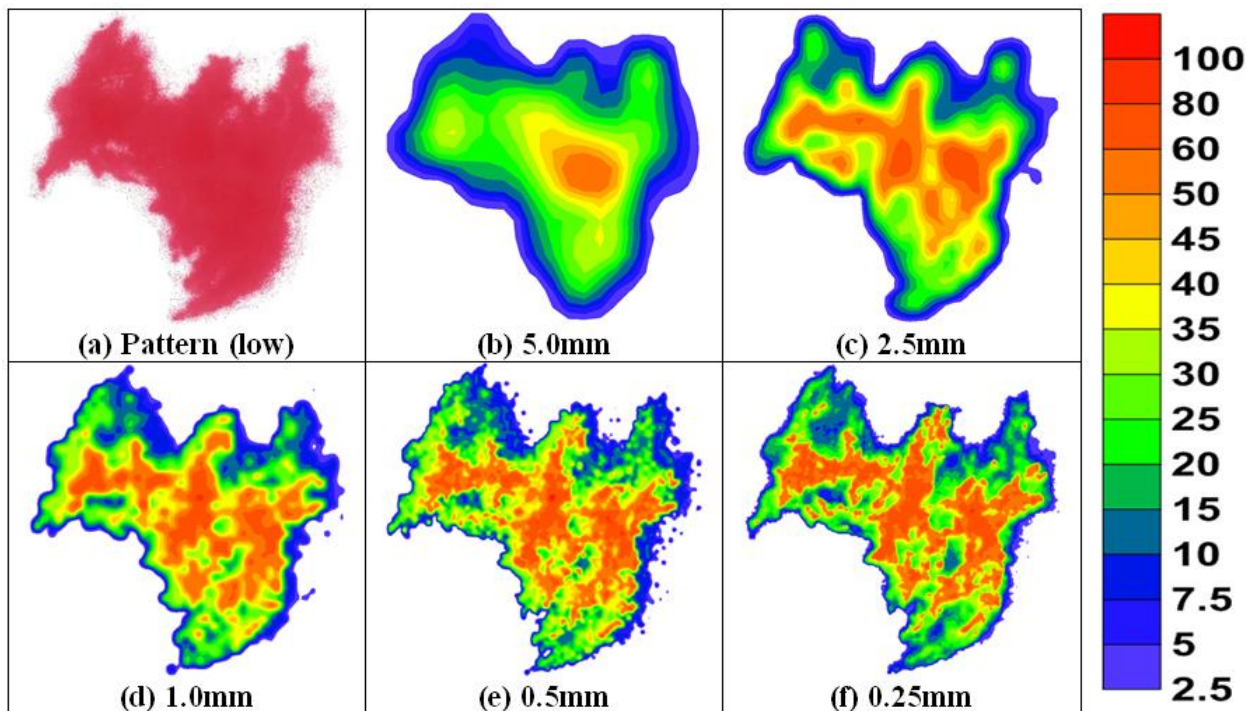


Figure C-22: Pressure distribution of Test 4-Step 2

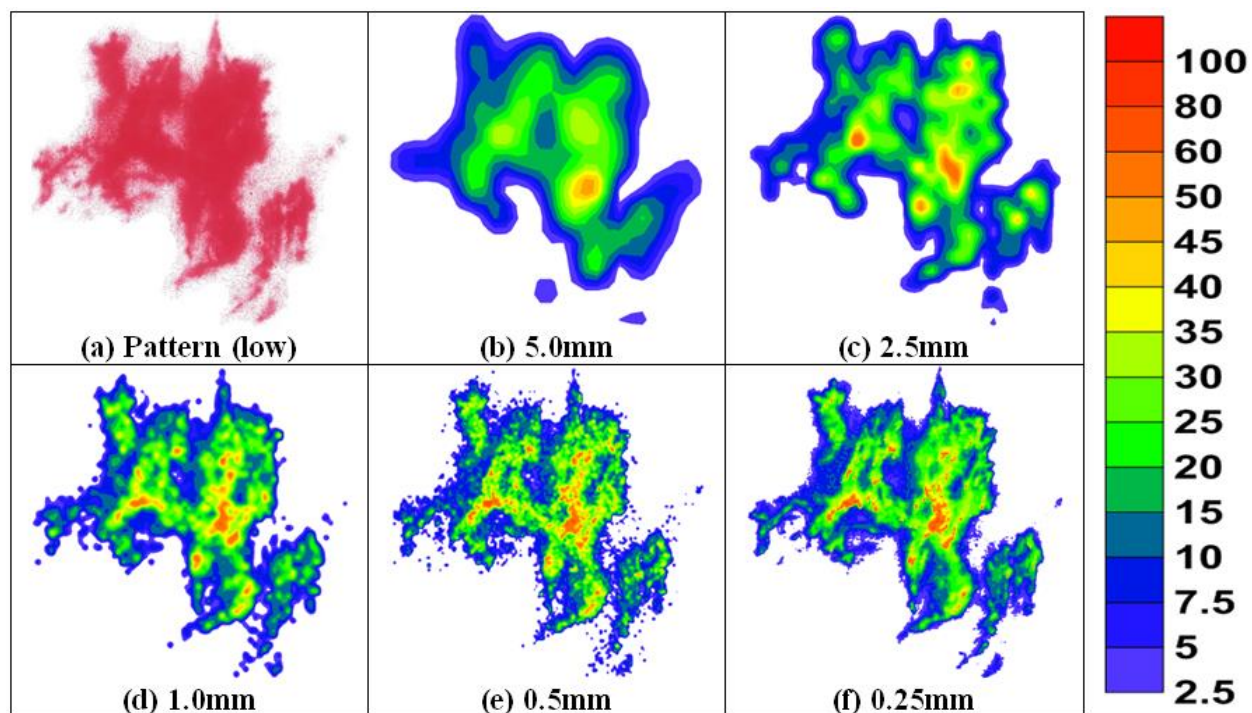


Figure C-23: Pressure distribution of Test 4-Step 3

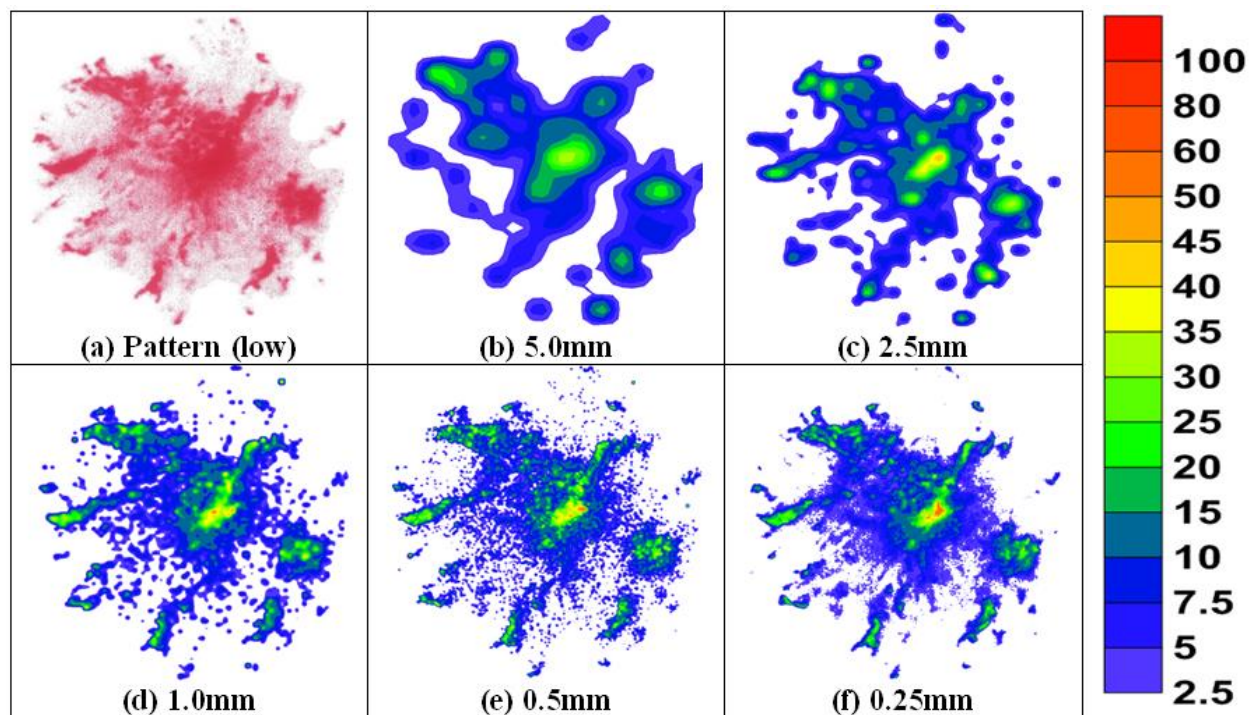


Figure C-24: Pressure distribution of Test 4-Step 4

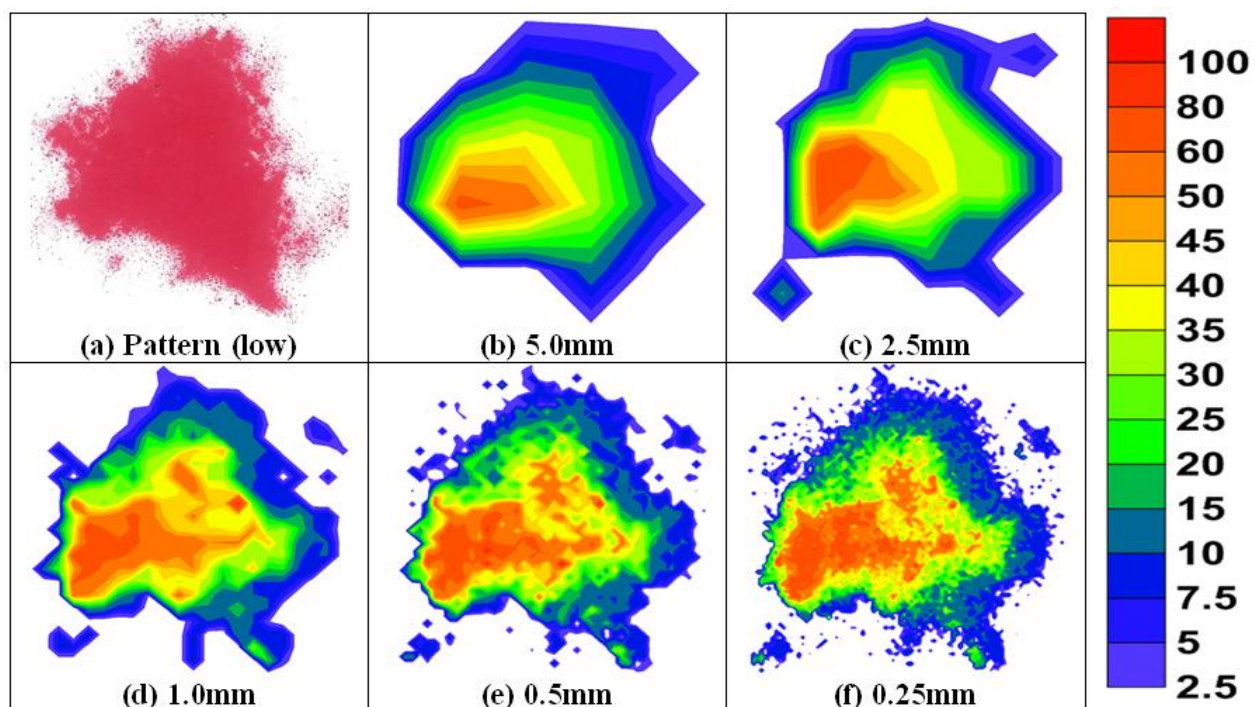


Figure C-25: Pressure distribution of Test 5-Step 1

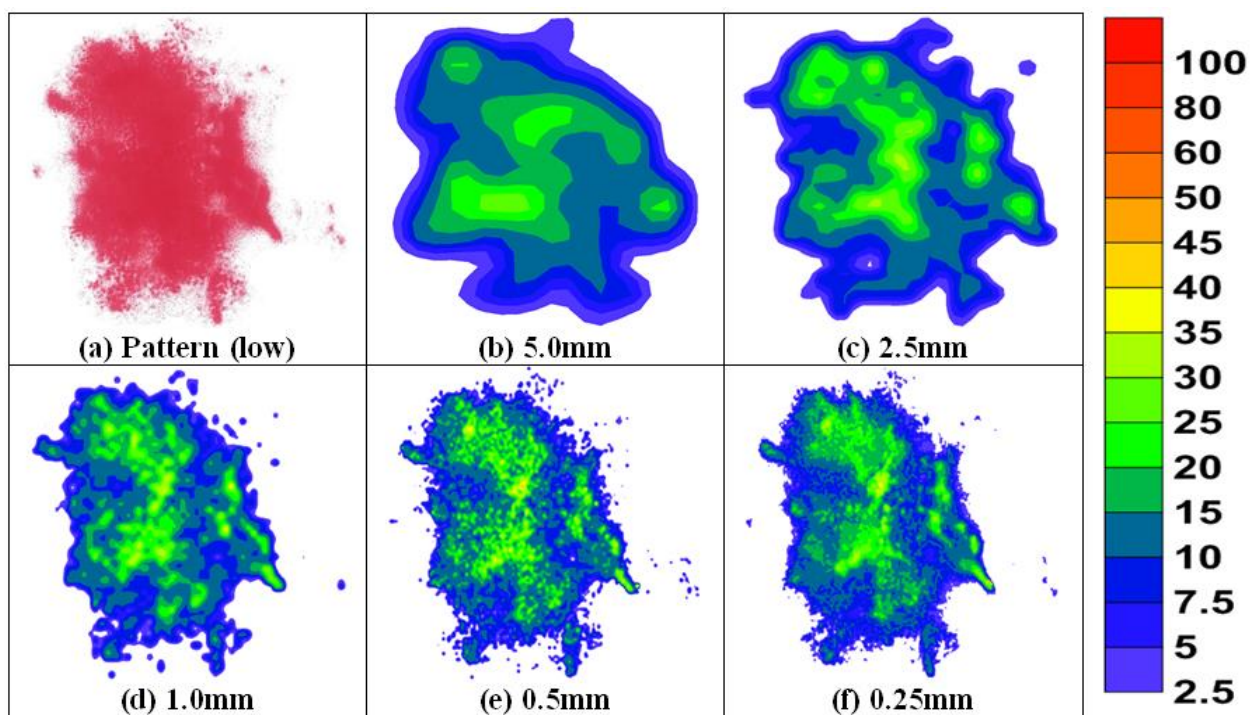


Figure C-26: Pressure distribution of Test 5-Step 2

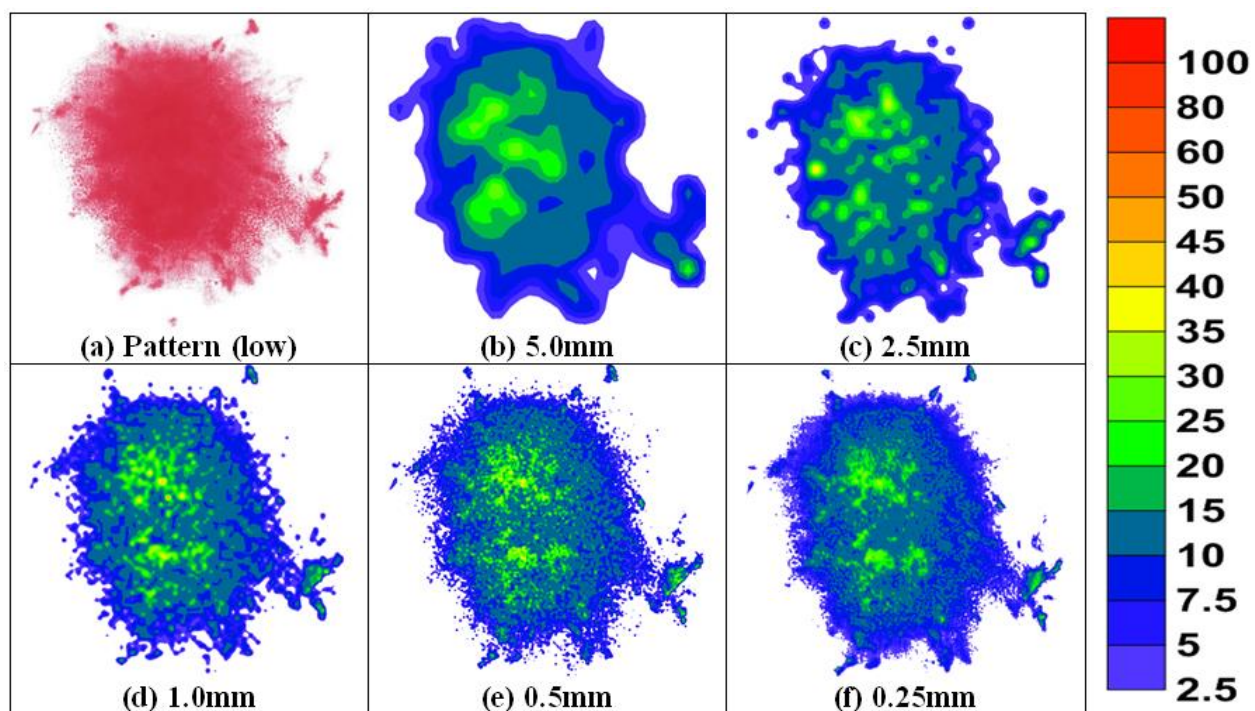


Figure C-27: Pressure distribution of Test 5-Step 3

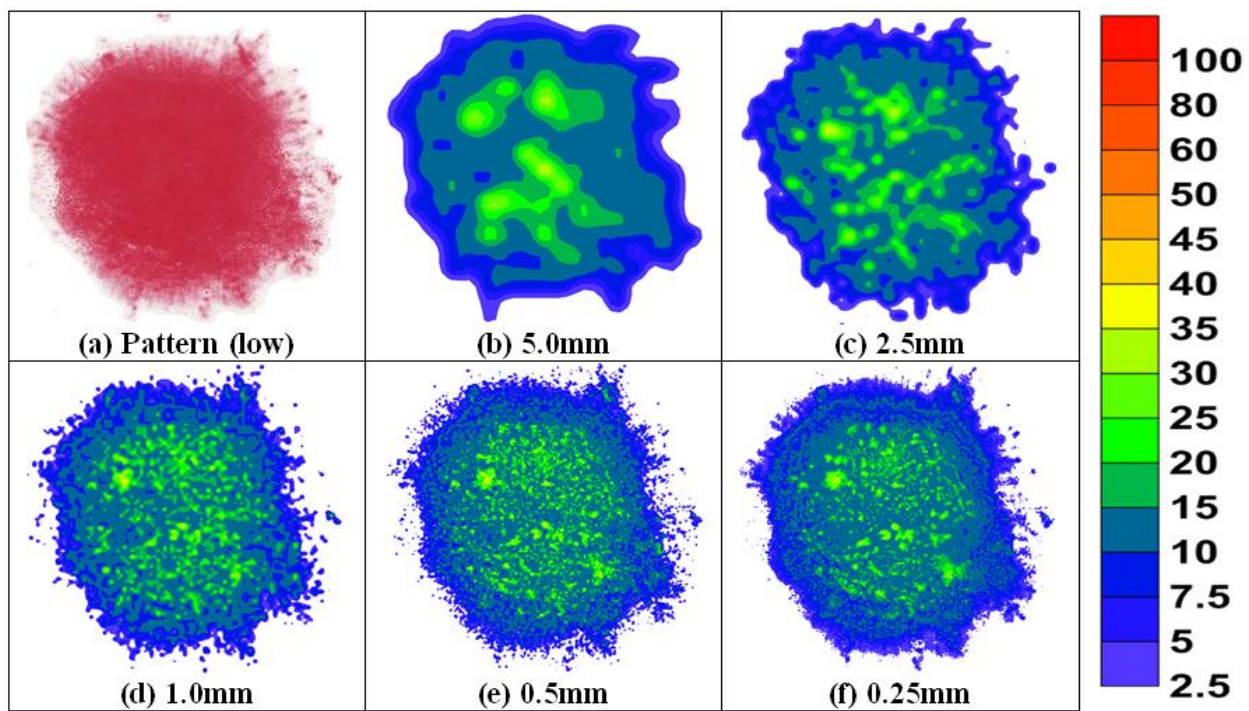


Figure C-28: Pressure distribution of Test 5-Step 4

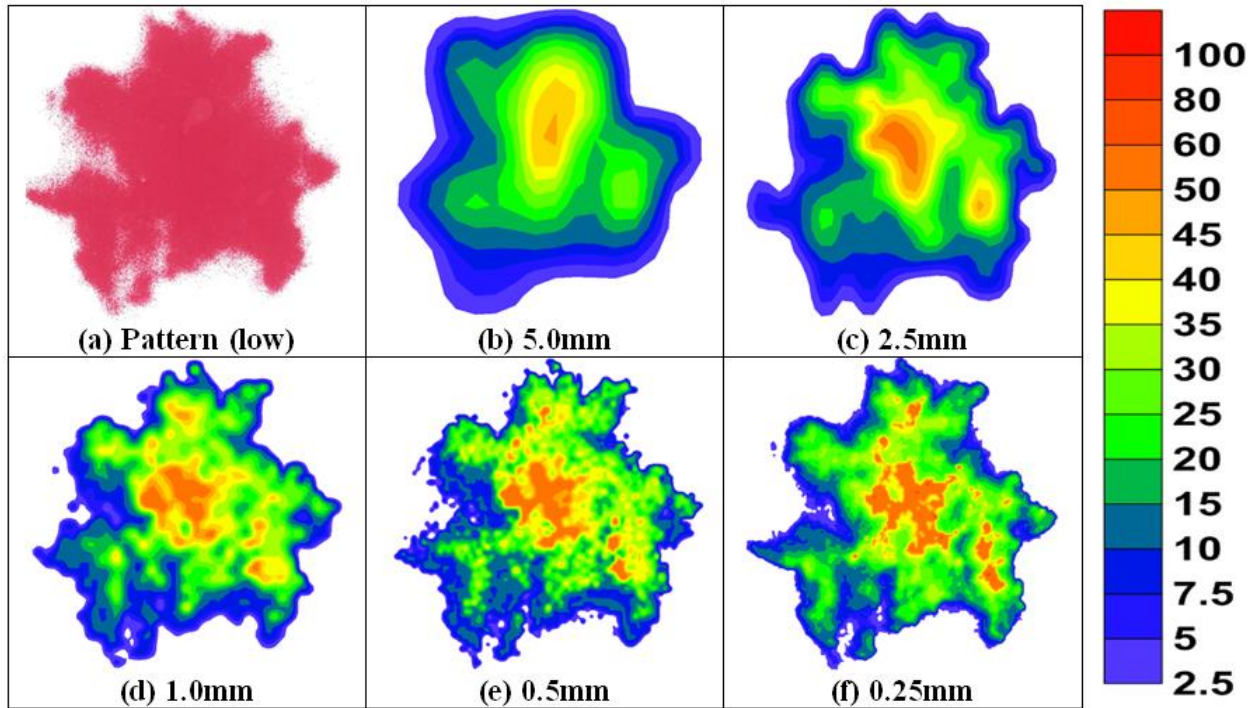


Figure C-29: Pressure distribution of Test 6-Step 1

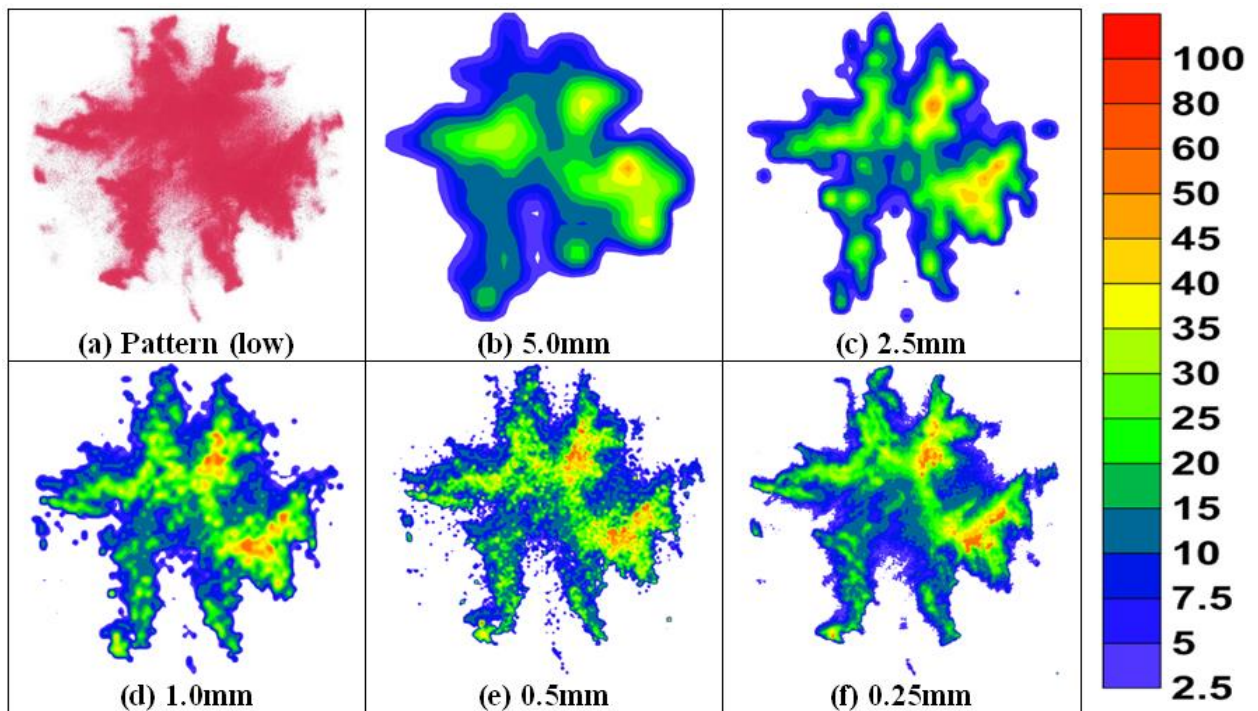


Figure C-30: Pressure distribution of Test 6-Step 2

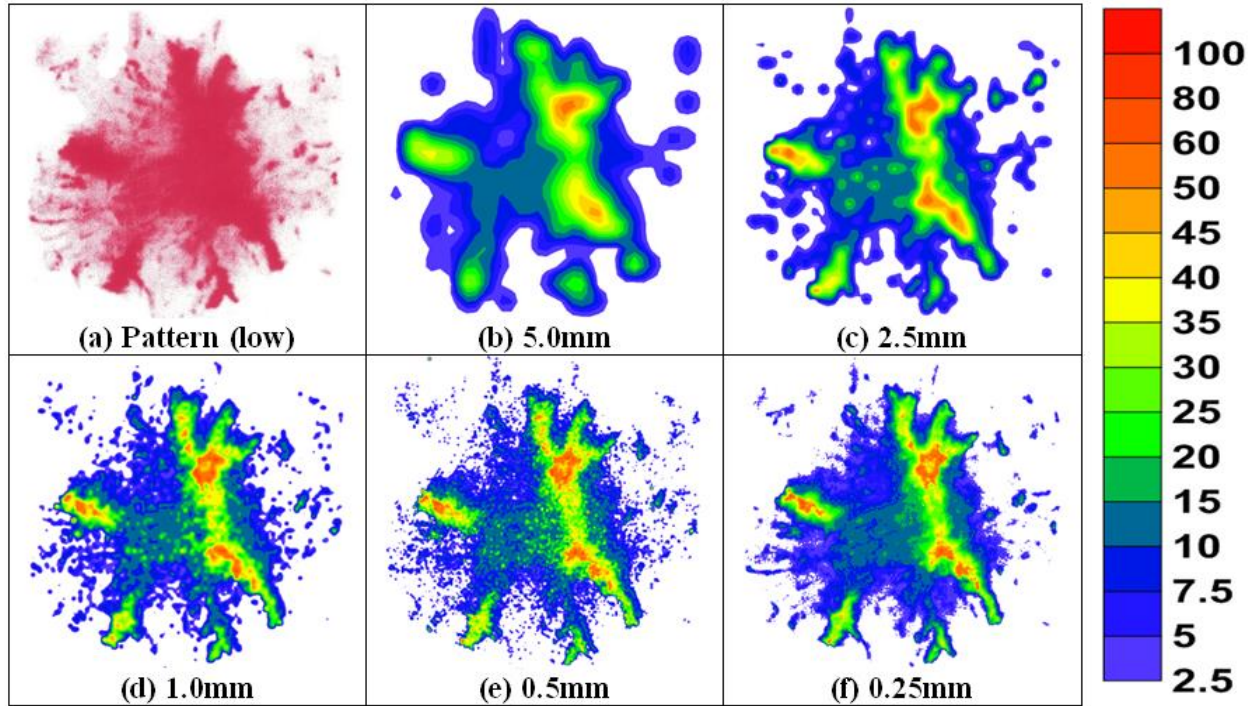


Figure C-31: Pressure distribution of Test 6-Step 3

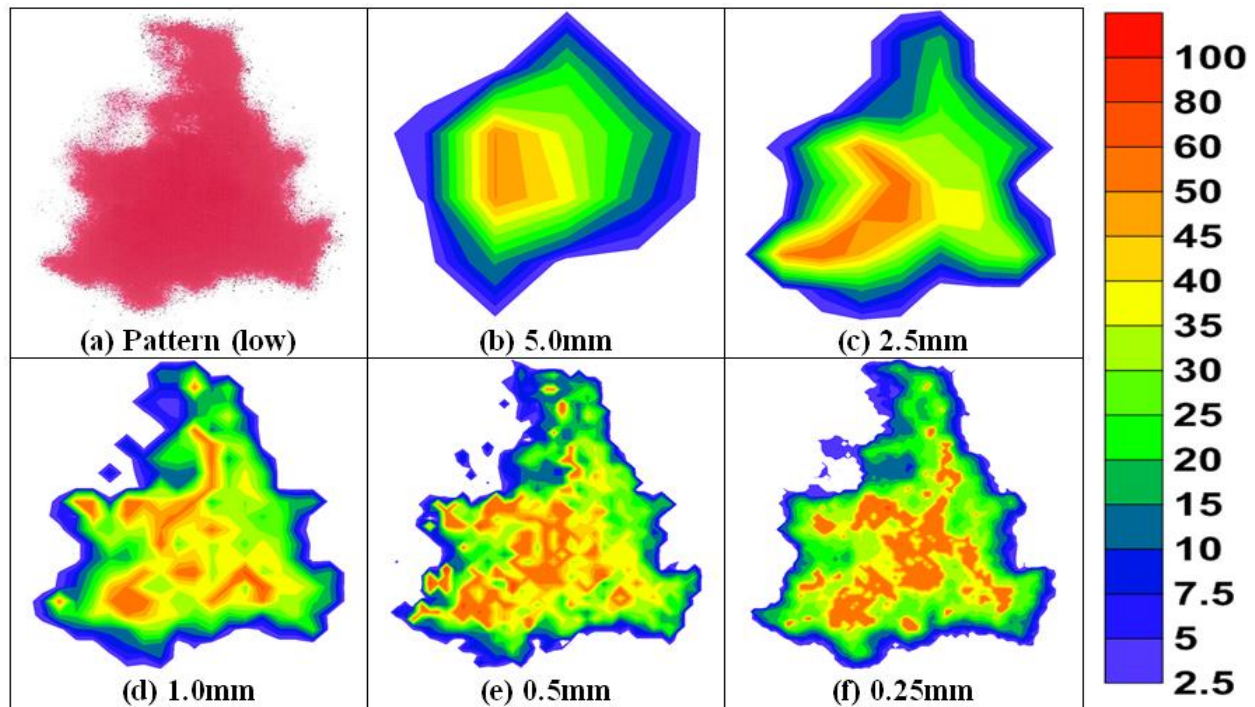


Figure C-32: Pressure distribution of Test 7-Step 1

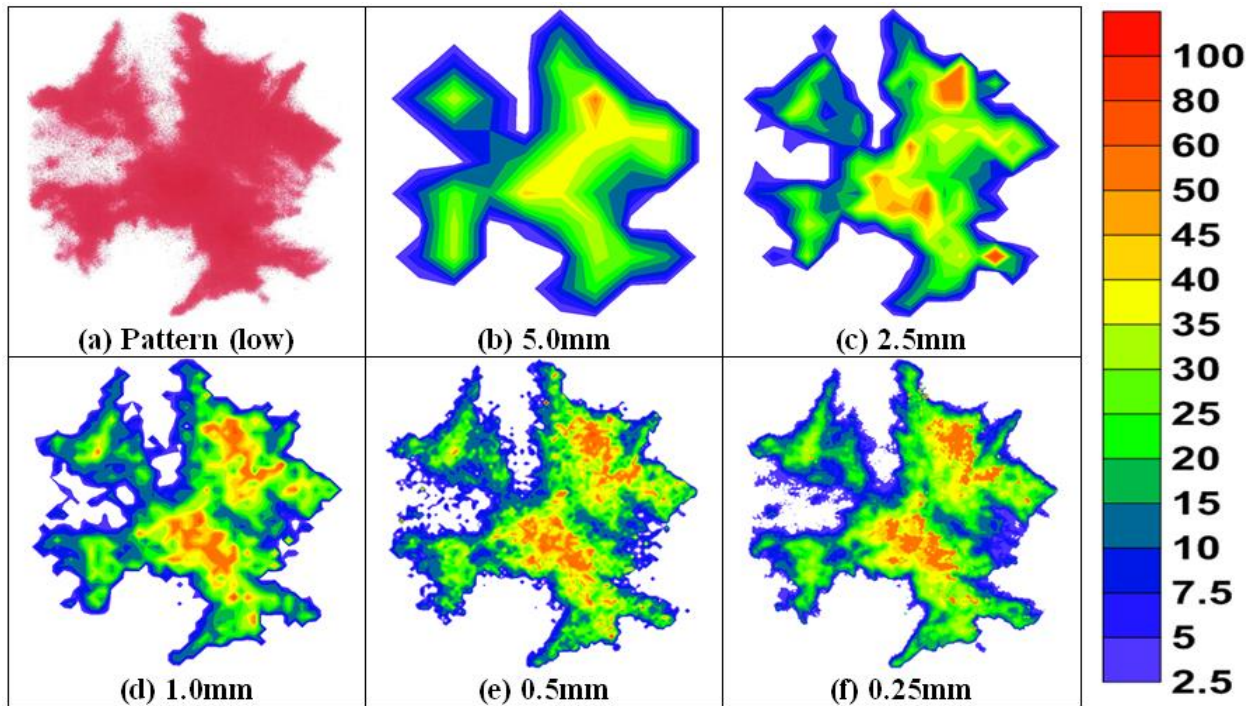


Figure C-33: Pressure distribution of Test 7-Step 2

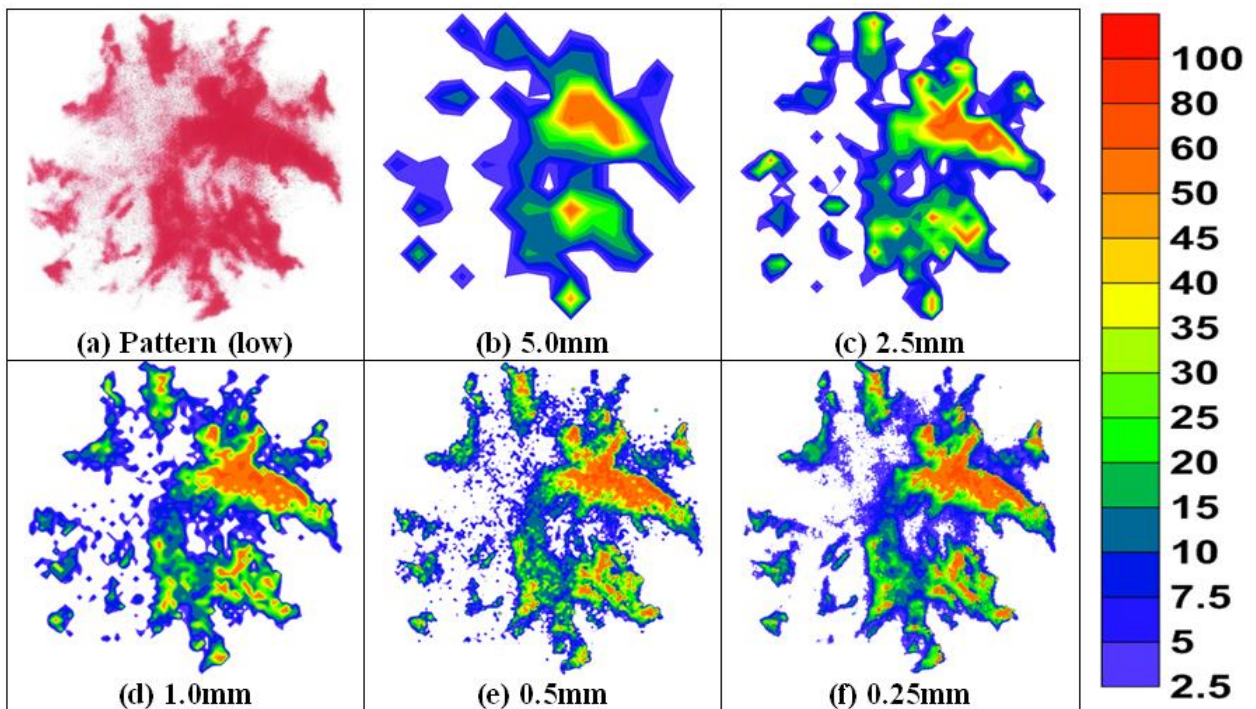


Figure C-34: Pressure distribution of Test 7-Step 3

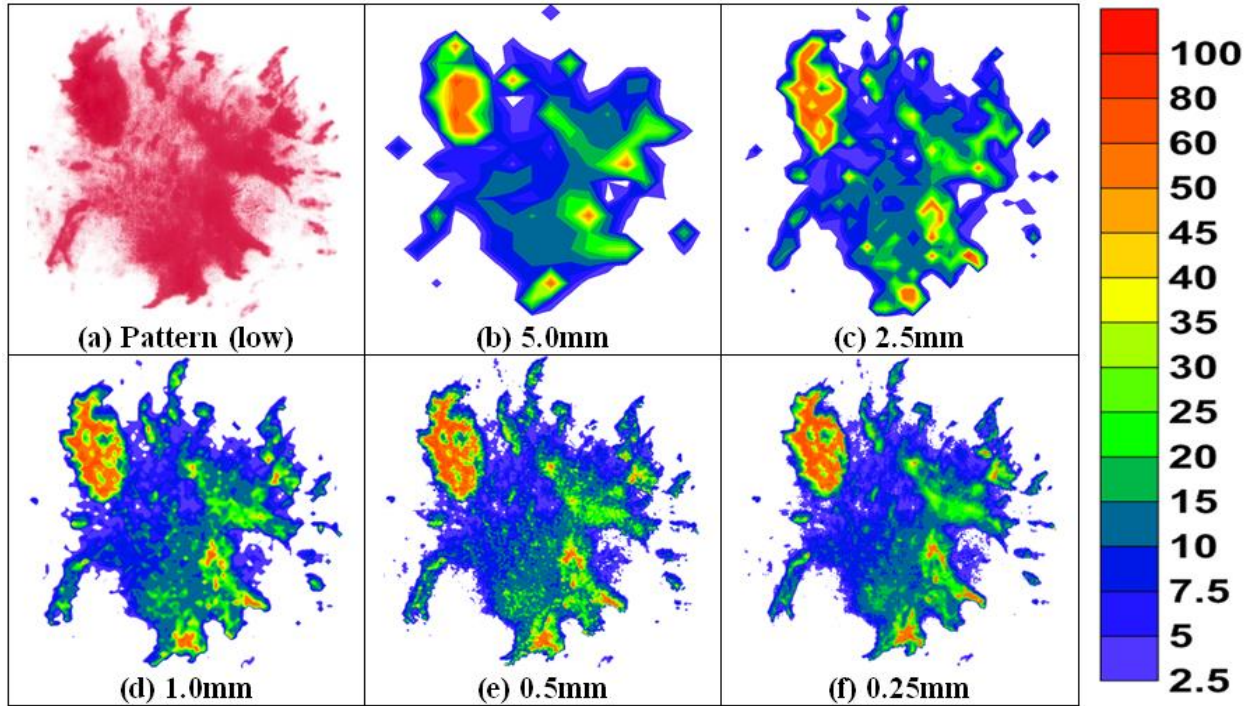


Figure C-35: Pressure distribution of Test 7-Step 4

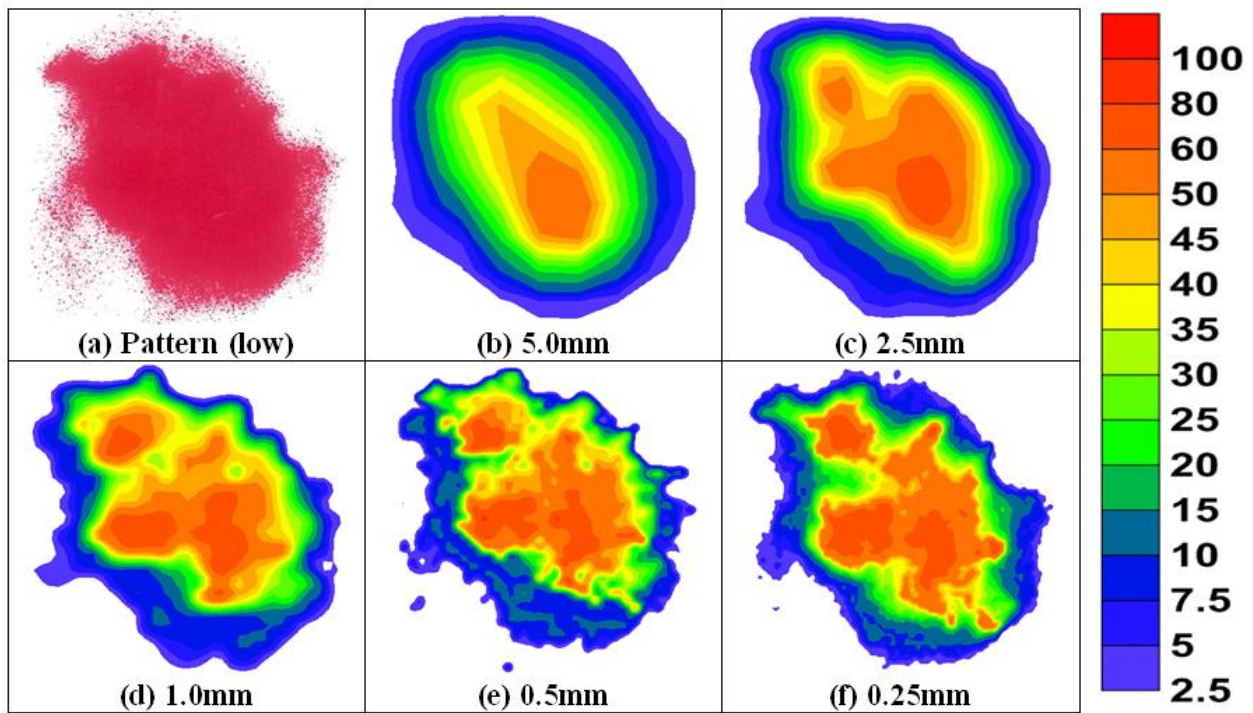


Figure C-36: Pressure distribution of Test 8-Step 1

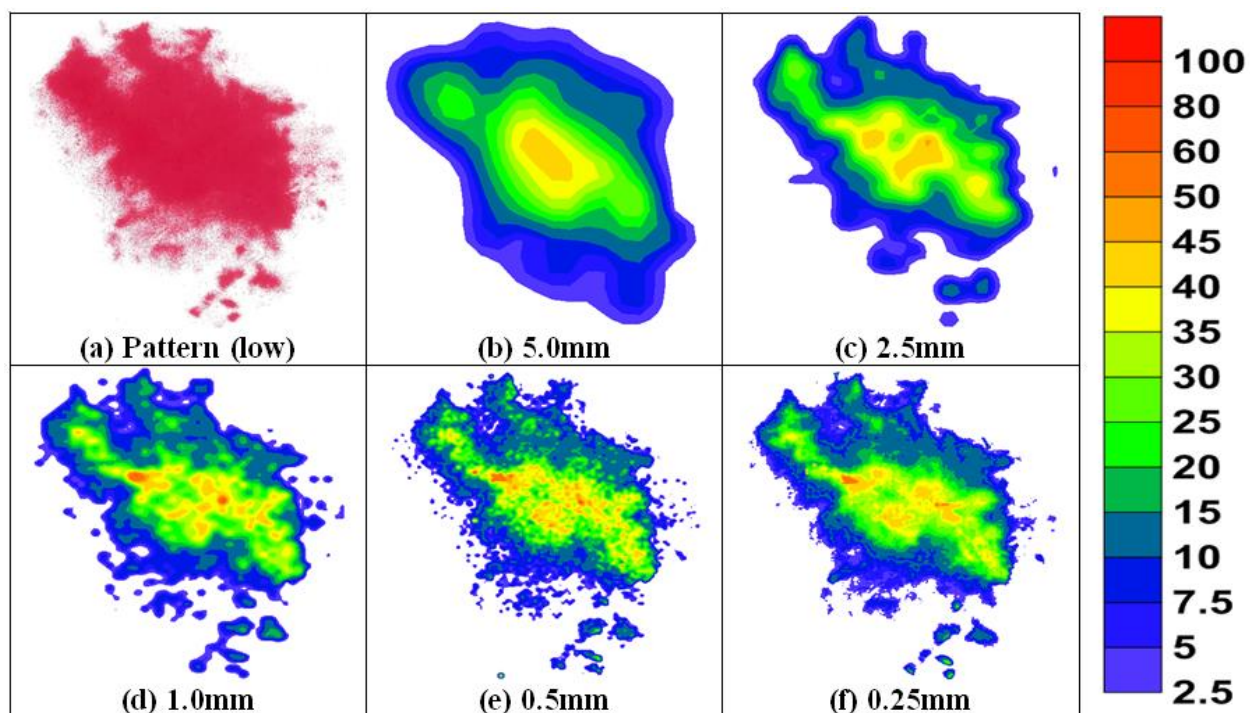


Figure C-37: Pressure distribution of Test 8-Step 2

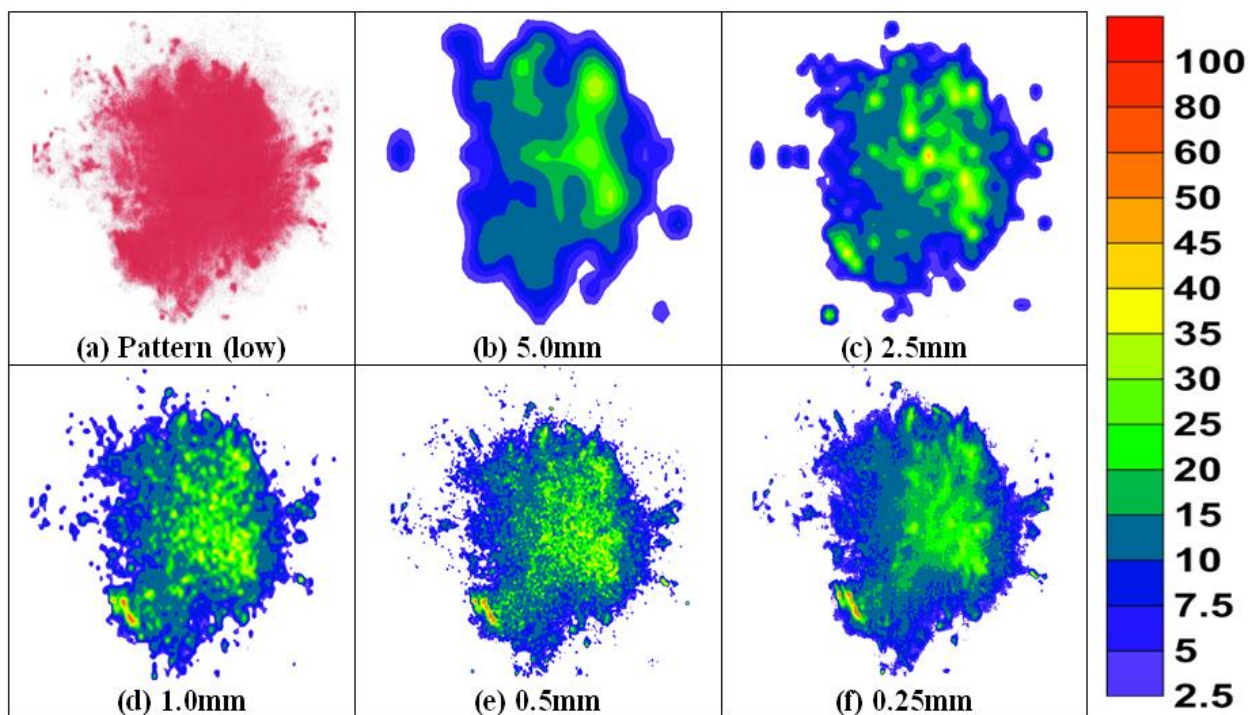


Figure C-38: Pressure distribution of Test 8-Step 3

Appendix D Comparison of Defined Contact Area

Comparison of ‘Nominal’ and ‘Projected’ contact areas between each test parameters (shape/angle of indenter, shape/angle of the ice sample) are shown in Figures D-1 to D-5.

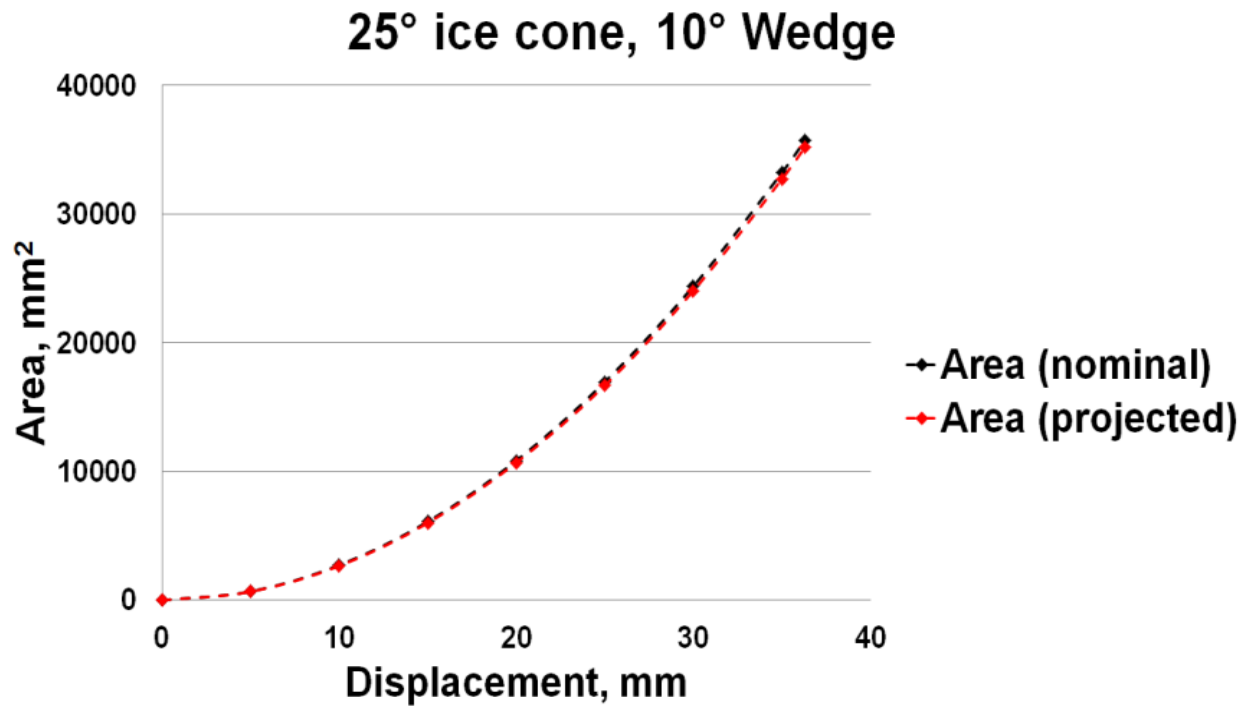


Figure D-1: Comparison of $A_{\text{nom.}}$ vs. $A_{\text{proj.}}$ (25° ice cone, 20° wedge indenter)

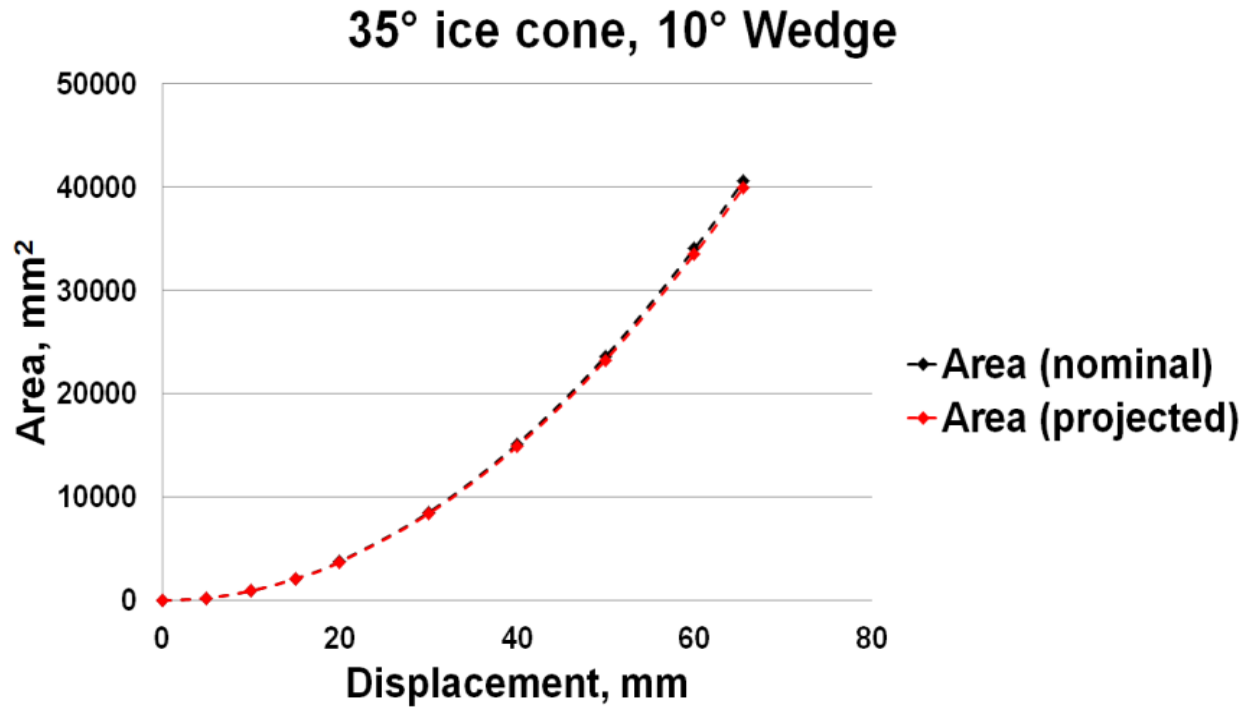


Figure D-2: Comparison of $A_{\text{nom.}}$ vs. $A_{\text{proj.}}$ (35° ice cone, 10° wedge indenter)

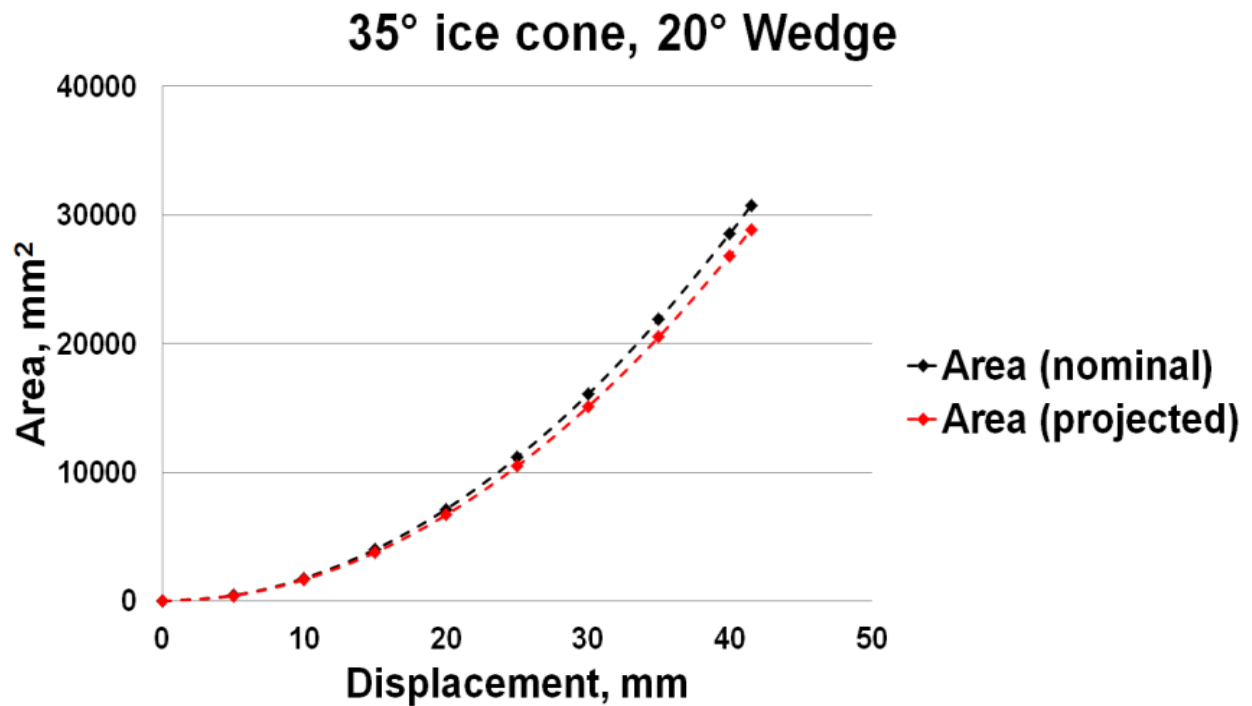


Figure D-3: Comparison of $A_{\text{nom.}}$ vs. $A_{\text{proj.}}$ (35° ice cone, 20° wedge indenter)

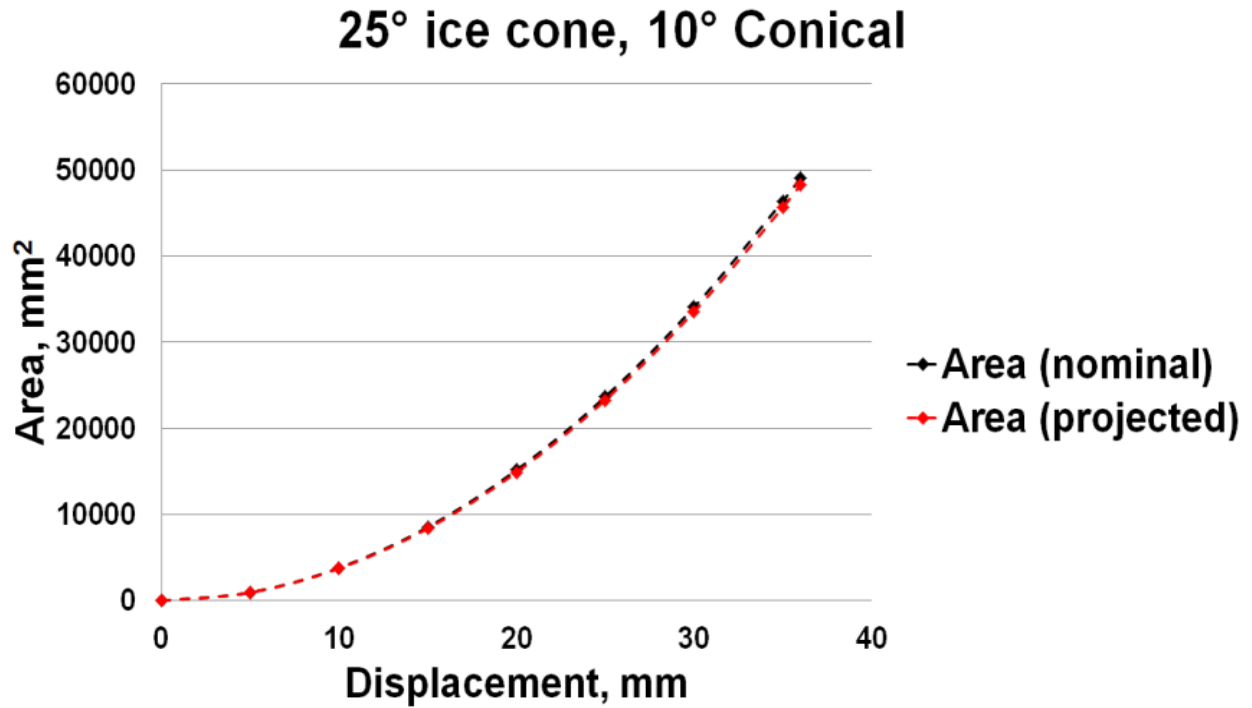


Figure D-4: Comparison of $A_{nom.}$ vs. $A_{proj.}$ (25° ice cone, 10° conical indenter)

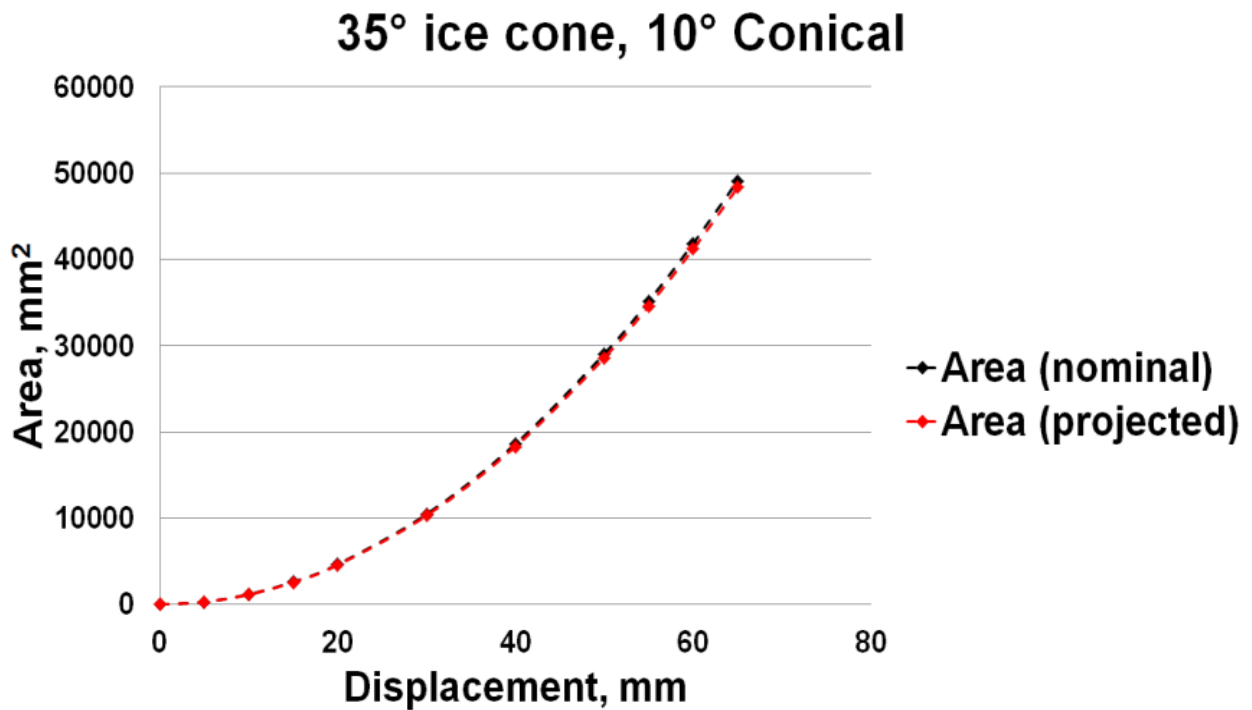


Figure D-5: Comparison of $A_{nom.}$ vs. $A_{proj.}$ (35° ice cone, 10° conical indenter)

Appendix E Force-Displacement History/ Process Pressure-Area Curve/Compressive Ice Strength Comparison

Force-displacement history, process pressure-area curve and compressive ice strength depending on the test speed and the cone angle/cylindrical ice were compared, followed by each test condition.

E.1. 35° Ice Cone, 1mm/s Test Speed

Force-displacement curve: 10° conical indenter test showed a higher load compared to the flat and 10°/20° wedge indenter test. 20° wedge indenter gave a higher load at first (displacement up to 25mm); however, a load against flat indenter showed relatively higher loads than a 10° wedge indenter, after this displacement.

Process pressure-area curve: 10° conical indenter showed a higher pressure level compared to the other indenter. 10°/20° wedge indenter showed a much lower pressure level than a flat indenter case.

Compressive ice strength: 10° conical indenter showed the largest values in overall contact area.

The compressive ice strength of 10° wedge indenter was lower than flat indenter.

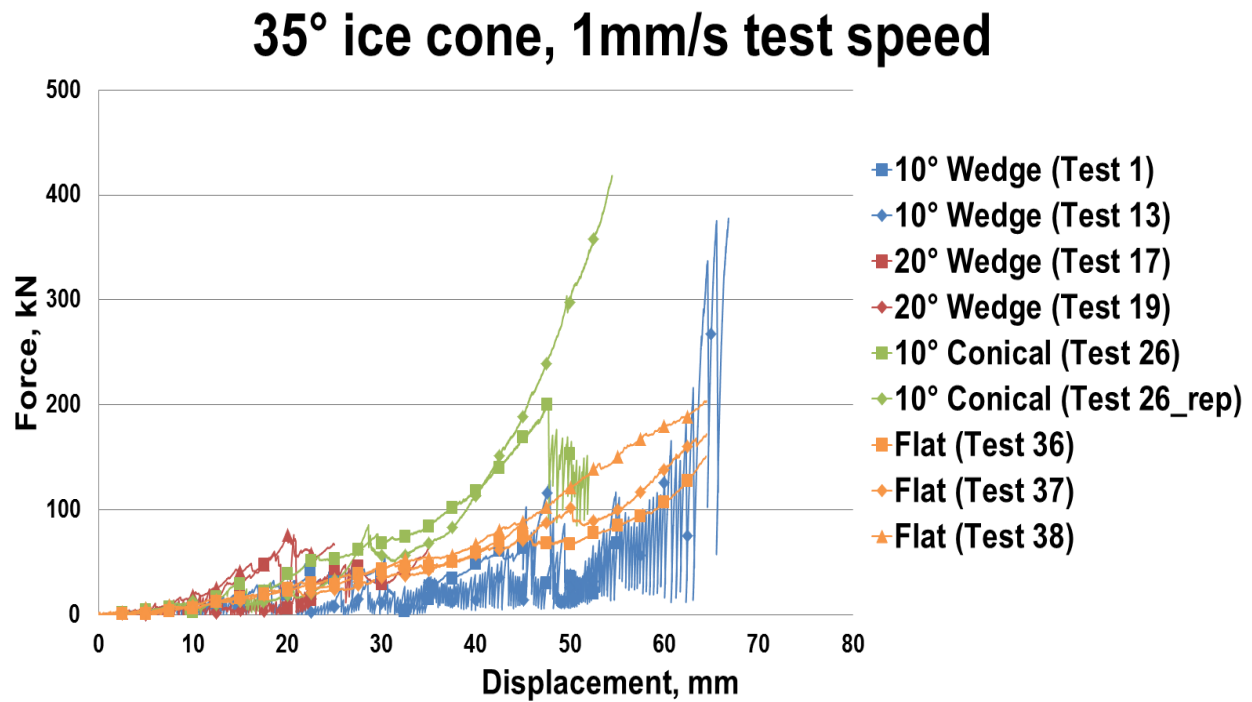


Figure E-1: Force-displacement history (35° ice cone, 1mm/s test speed)

35° ice cone, 1mm/s test speed

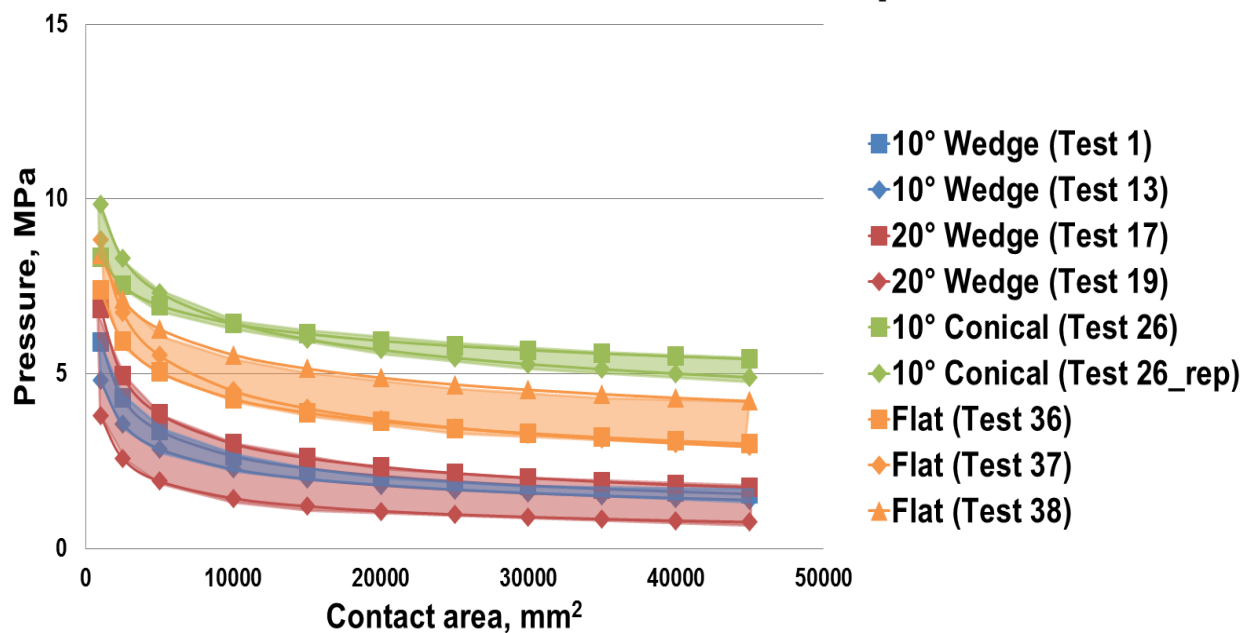


Figure E-2: Process pressure-area curve (35° ice cone, 1mm/s test speed)

35° ice cone, 1mm/s test speed

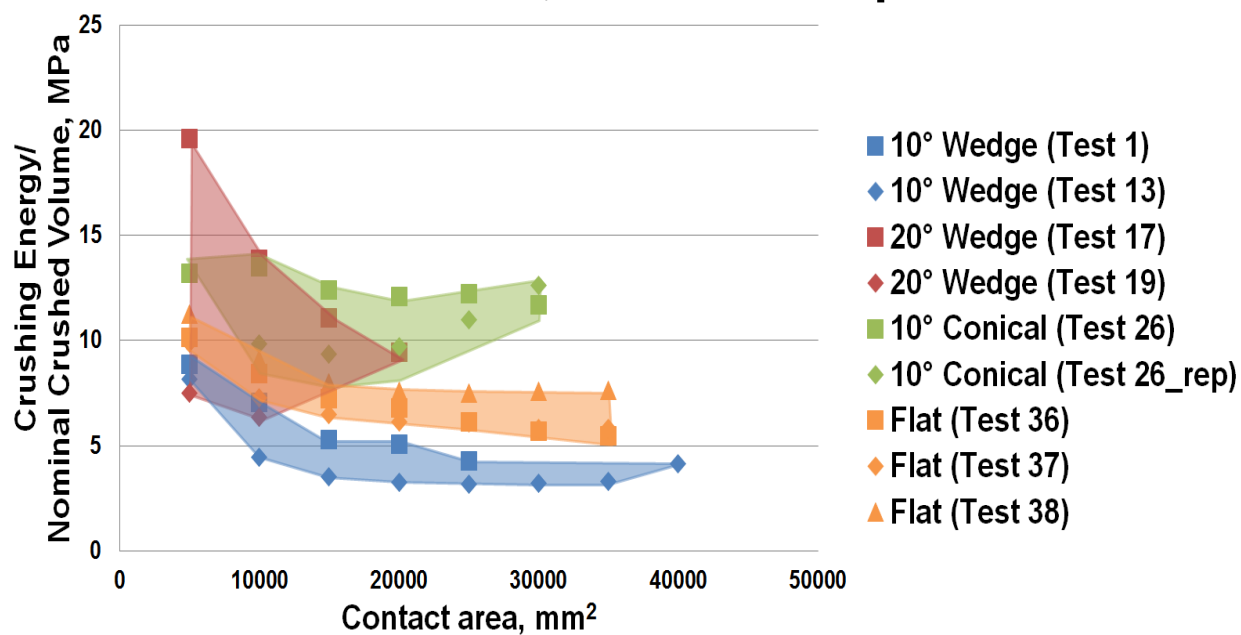


Figure E-3: Compressive ice strength (35° ice cone, 1mm/s test speed)

E.2. 35° Ice Cone, 100mm/s Test Speed

Force-displacement curve: Unlike the previous results, the level of force showed almost identical trends regardless of indenter shape and angle.

Process pressure-area curve: An overall trend of process pressure-area curve was also similar for all indenter shapes and angles.

Compressive ice strength: Similar to the previous results, slightly higher loads were measured using 20° wedge indenter, during the first stage. The results were almost identically for other indenter cases.

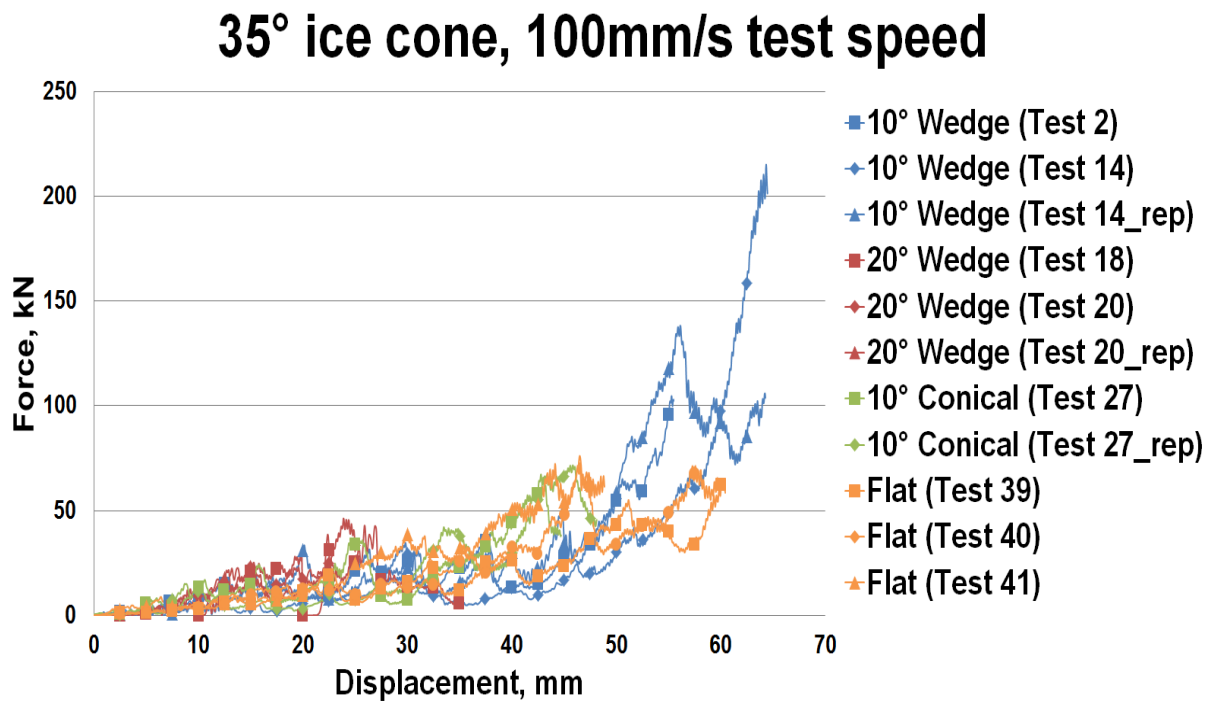


Figure E-4: Force-displacement history (35° ice cone, 100mm/s test speed)

35° ice cone, 100mm/s test speed

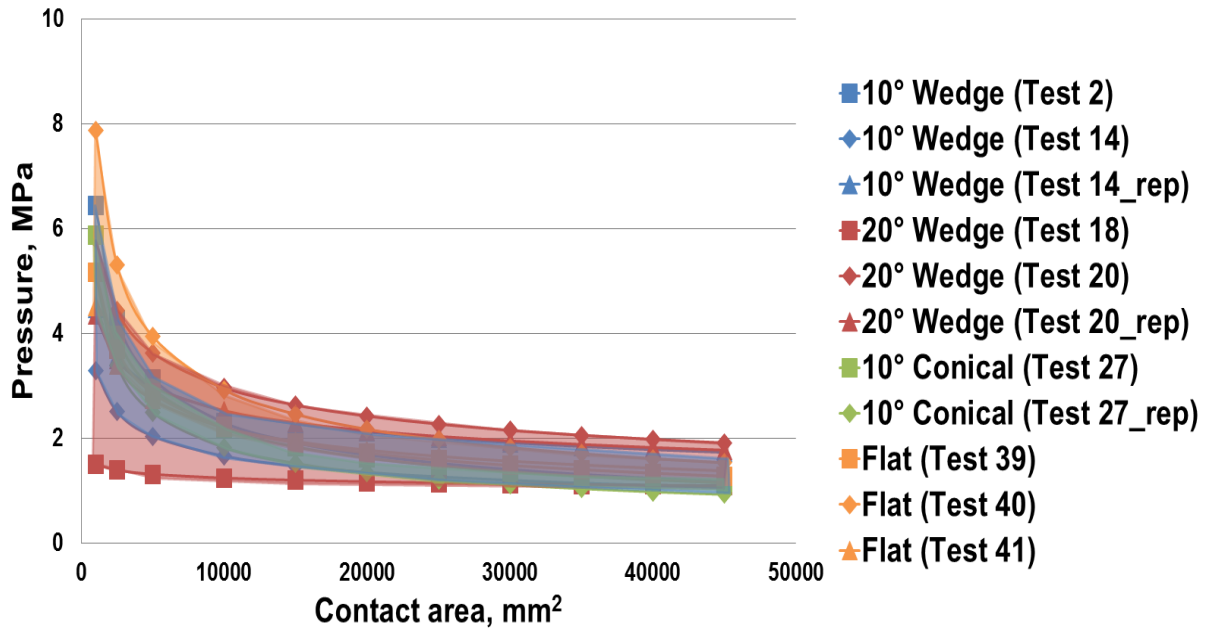


Figure E-5: Process pressure-area curve (35° ice cone, 100mm/s test speed)

35° ice cone, 100mm/s test speed

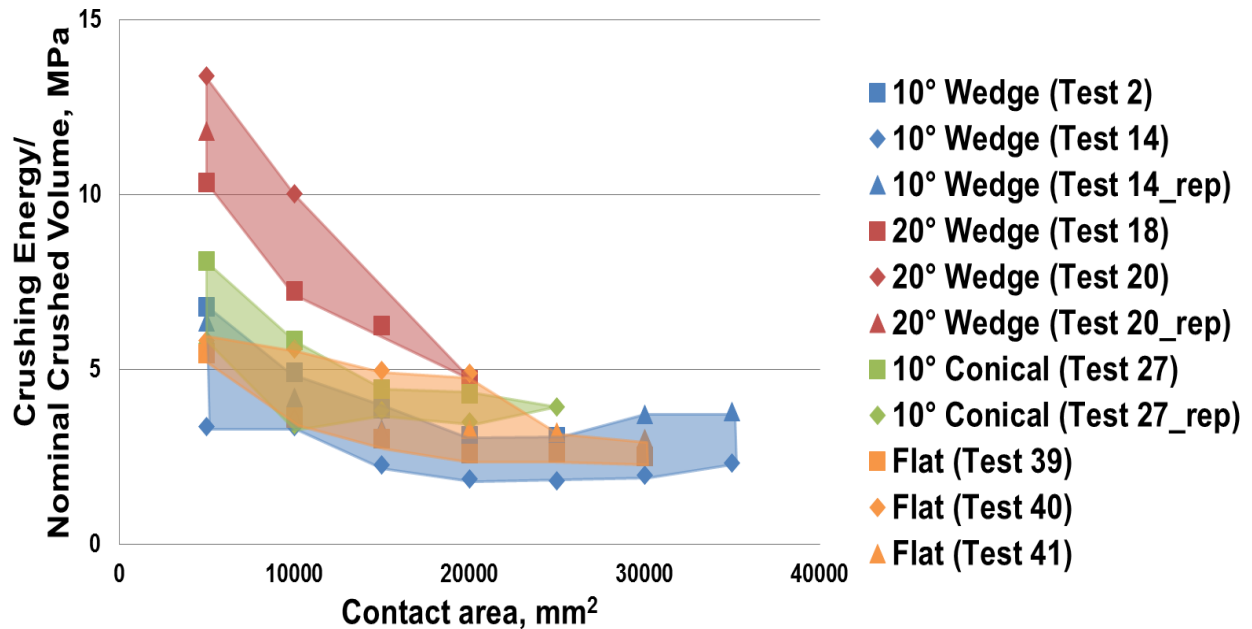


Figure E-6: Compressive ice strength (35° ice cone, 100mm/s test speed)

E.3. Cylindrical Ice, 100mm/s Test Speed

Force-displacement curves: Magnitude of load was similar regardless of the indenter angle, and the location of peak force occurrence was at the maximum depth of the indenter as discussed in the test. In the case of 10° & 20° wedge indenters, the maximum depth and the time of the peak force was nearly identical to the 1mm/s test case. In addition, the position of the peak force in case of 30° wedge indenter was around ~88% of the maximum depth.

Process pressure-area curve: No significant effect of indenter angle was observed similar to 1mm/s tests. However, the pressure against 30° wedge indenter was higher than 10° and 20° wedge indenter.

Compressive ice strength: Magnitude and the overall trends of compressive ice strengths were also identical when compared with 1mm/s test case (1/50 magnitude scale).

Cylindrical ice, 100mm/s test speed

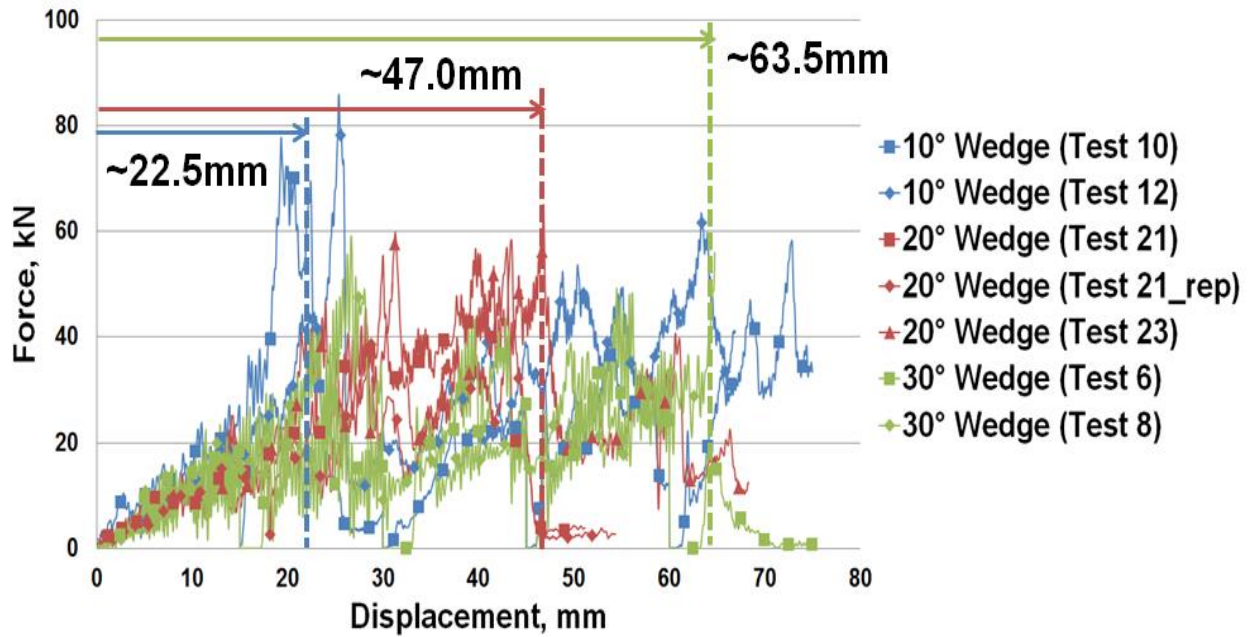


Figure E-7: Force-displacement history (cylindrical ice, 100mm/s test speed)

Cylindrical ice, 100mm/s test speed

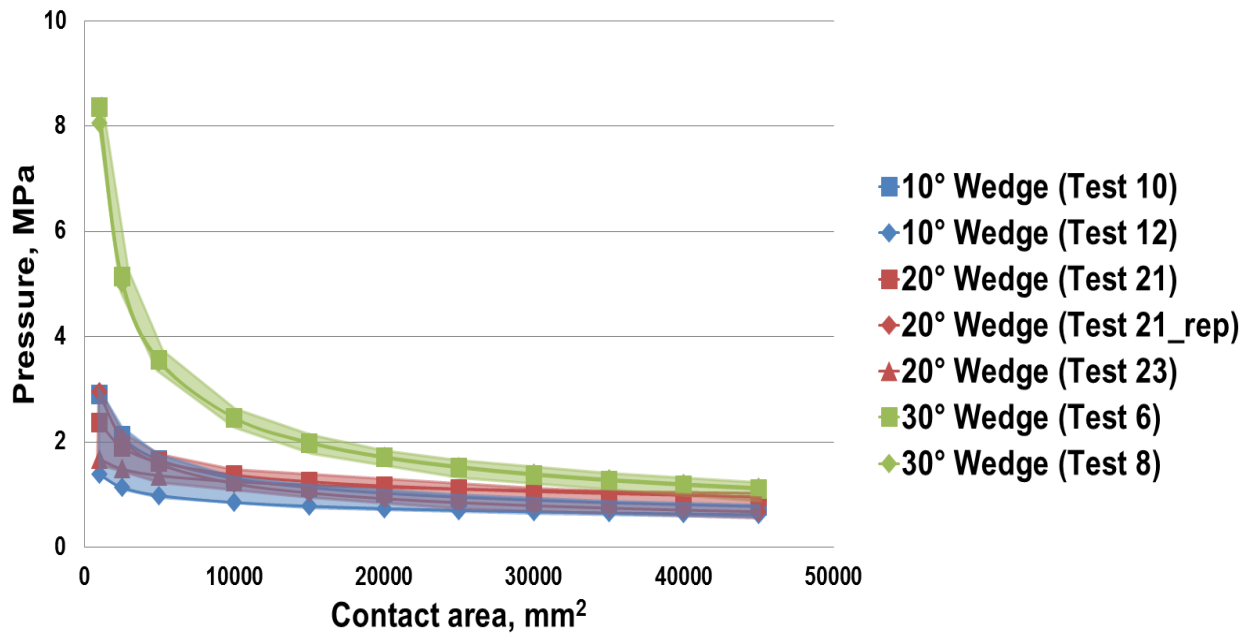


Figure E-8: Process pressure-area curve (cylindrical ice, 100mm/s test speed)

Cylindrical ice, 100mm/s test speed

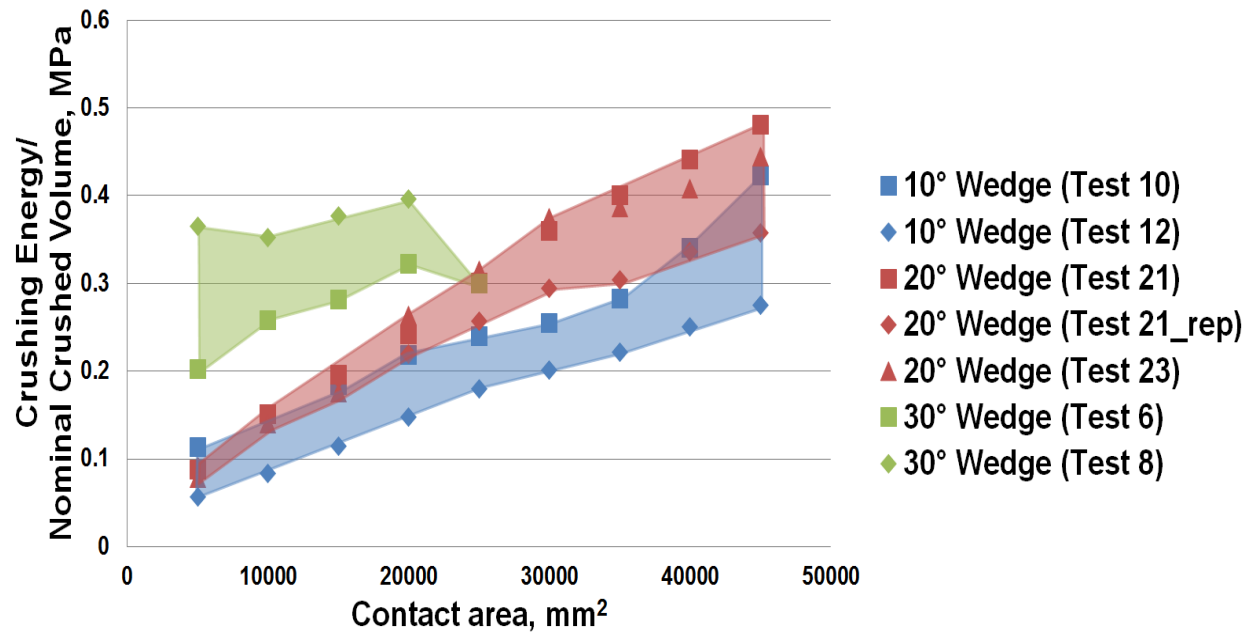


Figure E-9: Compressive ice strength (cylindrical ice, 100mm/s test speed)

Appendix F Pressure Distribution Map

F.1. Pressure Distribution Map: Cone-Shaped Ice Sample

Figures F-1 to F-4 show an obtained pressure distribution for each test using pressure measurement film against wedge-shaped indenter. Cone-shaped ice samples were used.

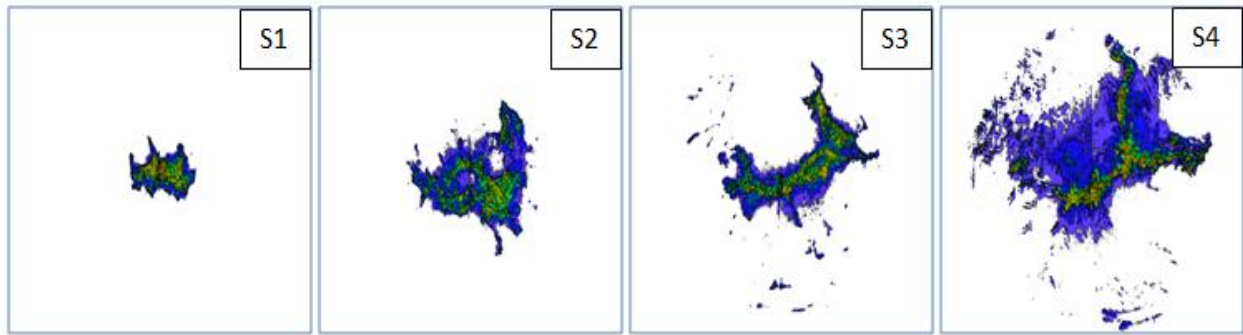


Figure F-1: Pressure distribution map of Test 2

(10° wedge indenter, 35° ice cone, 100mm/s test speed)

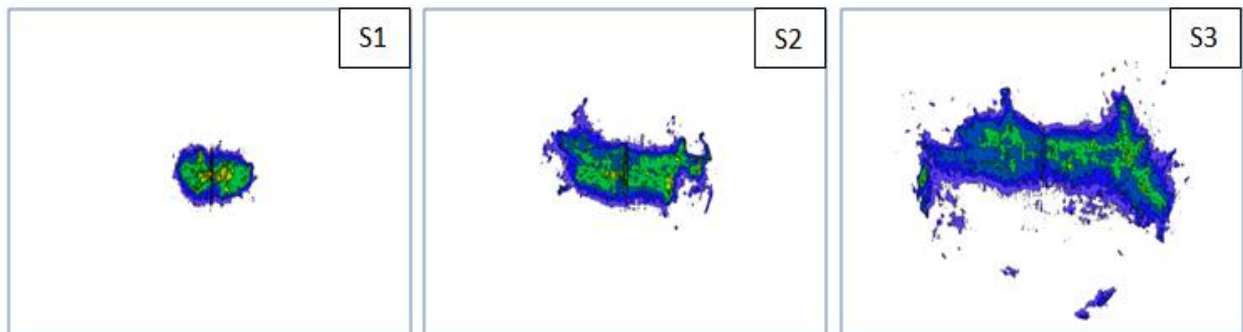


Figure F-2: Pressure distribution map of Test 3

(10° wedge indenter, 25° ice cone, 1mm/s test speed)

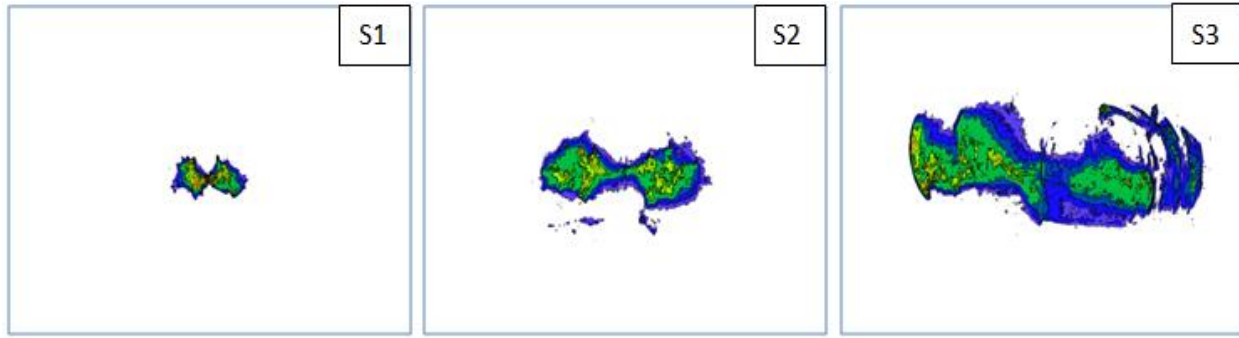


Figure F-3: Pressure distribution map of test 17
(20° wedge indenter, 35° ice cone, 1mm/s test speed)



Figure F-4: Pressure distribution map of test 18
(20° wedge indenter, 35° ice cone, 100mm/s test speed)

F.2. Pressure Distribution Map: Cylindrical Ice Sample

Figures F-5 and F-6 indicate that the pressure pattern developed from the outer to inner location as ice penetrated into the wedge-shaped indenter. The effect of test speed was not significant using the cylindrical ice samples.

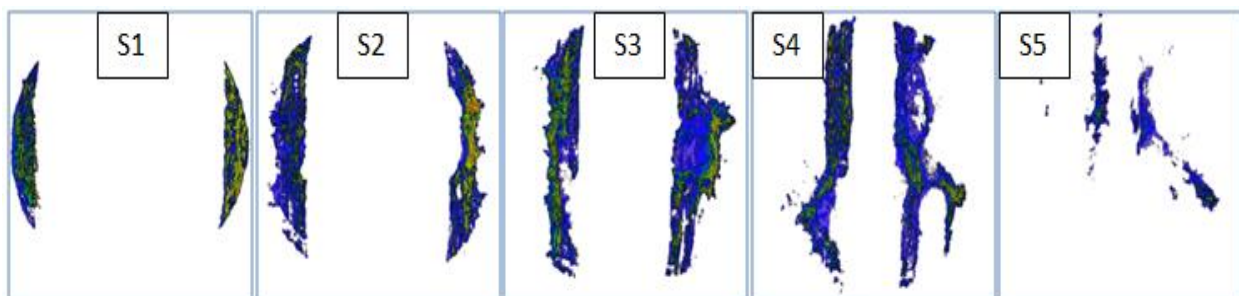


Figure F-5: Pressure distribution map of test 6
(30° wedge, cylindrical ice, 100mm/s test speed)

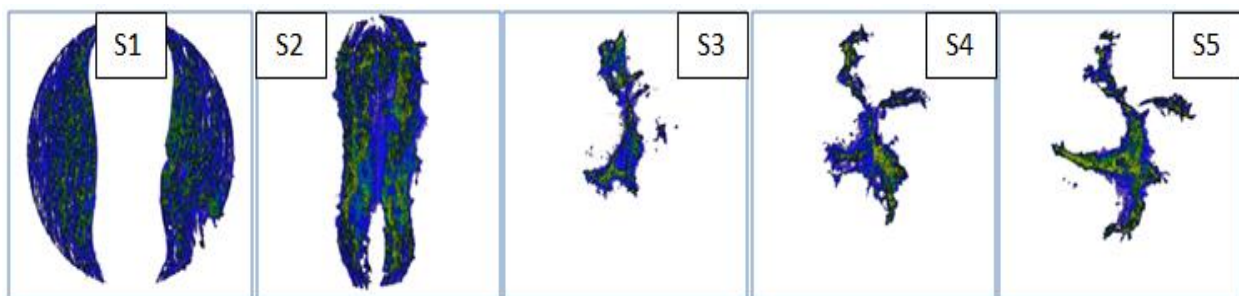


Figure F-6: Pressure distribution map of test 10
(10° wedge, cylindrical ice, 100mm/s test speed)

Appendix G Spatial Pressure-Area Curve

(25cm Diameter Ice Sample)

Figures G-1 to G-6 show the spatial pressure-area curve for each test. Process pressure-area curves were plotted as black-bold line. Spatial pressure-area curves for each step were plotted as colored-dotted line. The curve labeled as ‘PPA (Process Pressure-Area) trend’ on the graph was the connection of the end points of spatial pressure-area curve at each step.

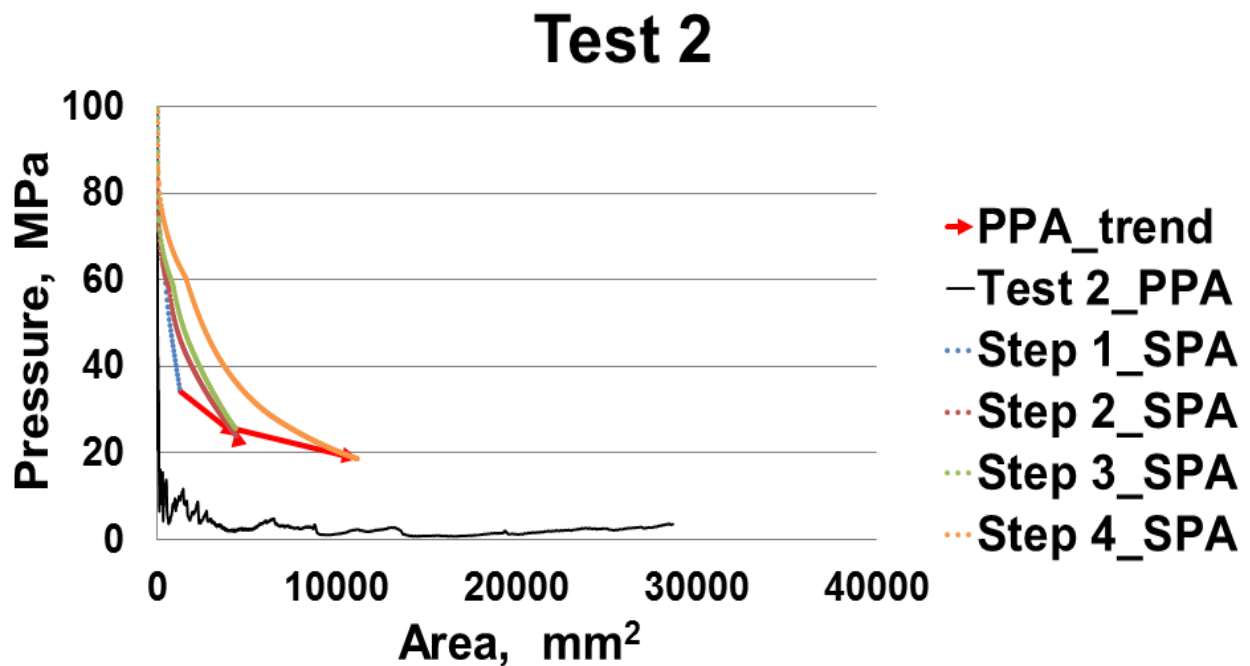


Figure G-1: Spatial pressure-area curve of Test 2
(10° wedge, 35° ice cone, 100mm/s test speed)

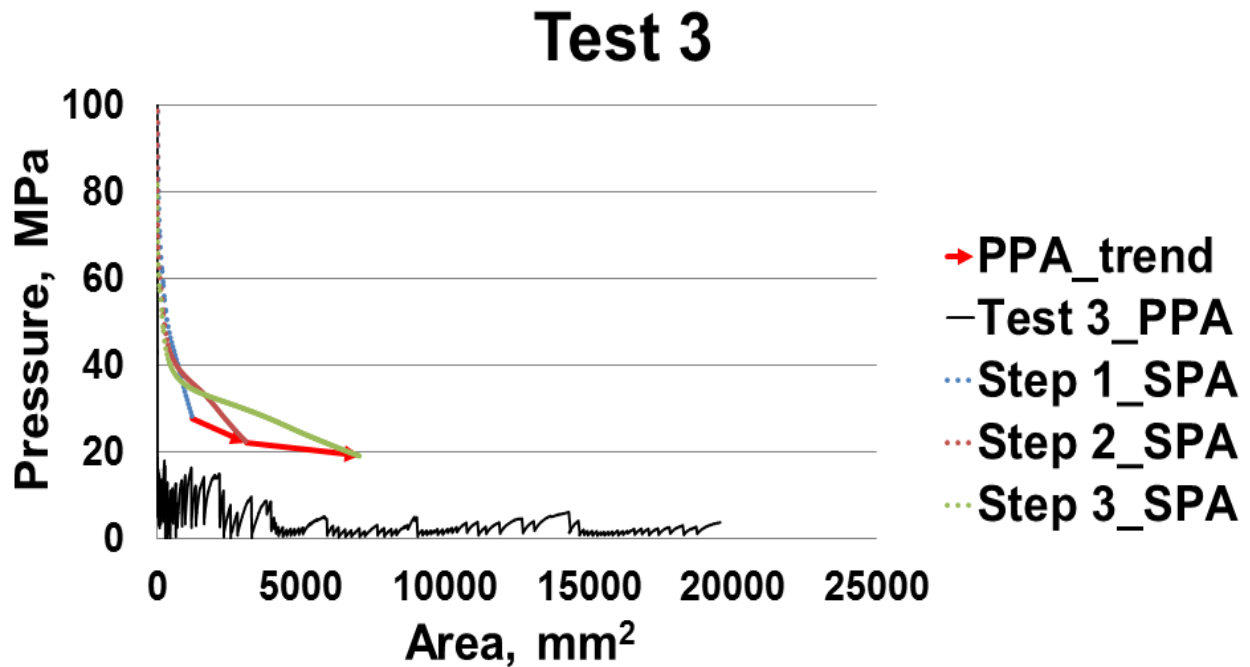


Figure G-2: Spatial pressure-area curve of Test 3

(10° wedge, 25° ice cone, 1mm/s test speed)

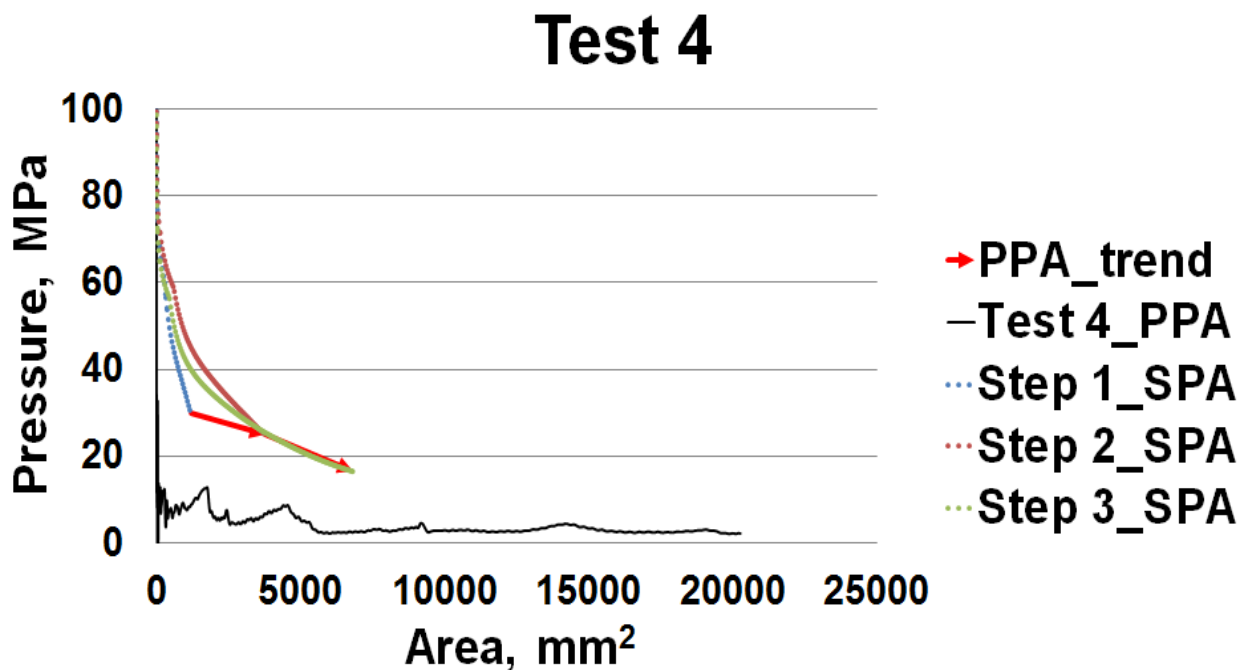


Figure G-3: Spatial pressure-area curve of Test 4

(10° wedge, 25° ice cone, 100mm/s test speed)

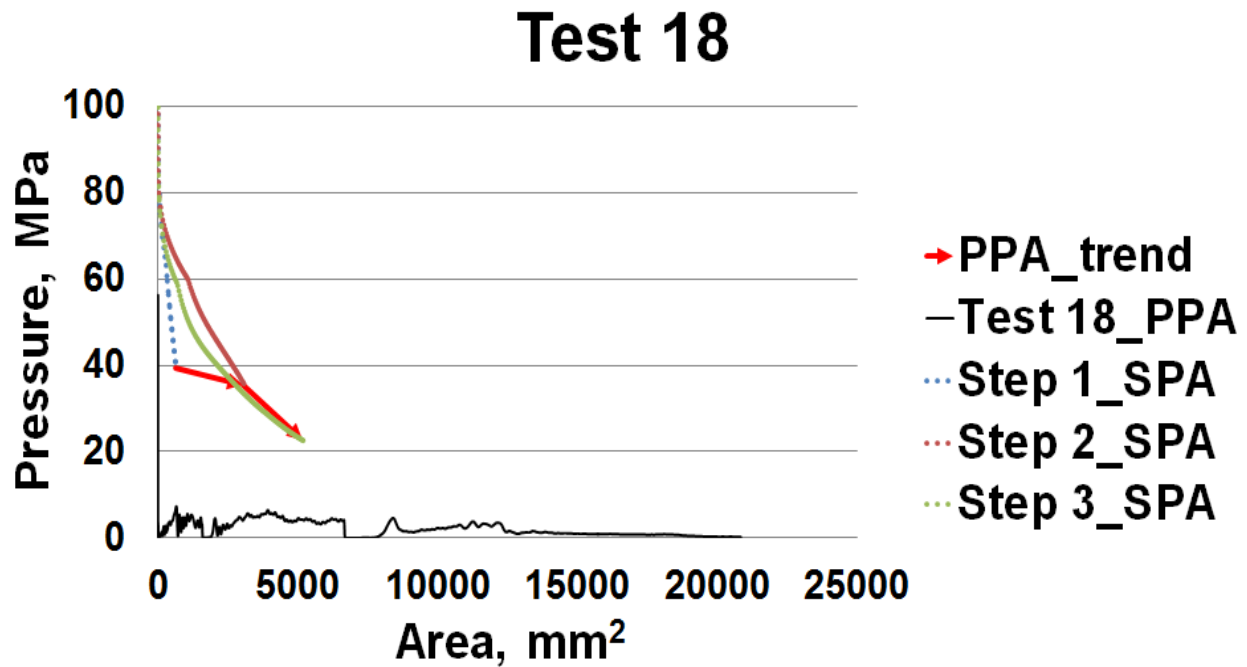


Figure G-4: Spatial pressure-area curve of Test 18

(20° wedge, 35° ice cone, 100mm/s test speed)

The results of 'PPA trend' using cylindrical ice samples tend to have more complexity as shown in Figures G-5 and G-6, because of the reduction of the contact area as the test step progresses in the case of cylindrical ice samples.

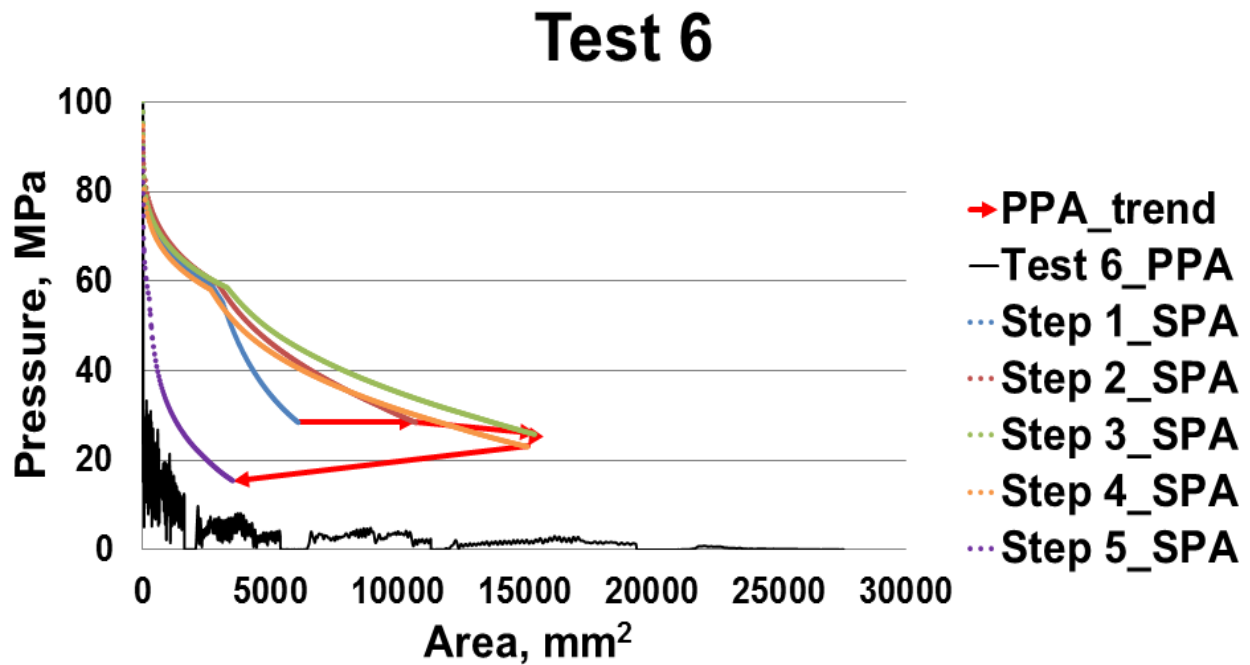


Figure G-5: Spatial pressure-area curve of Test 6

(30° wedge, cylindrical ice, 100mm/s test speed)

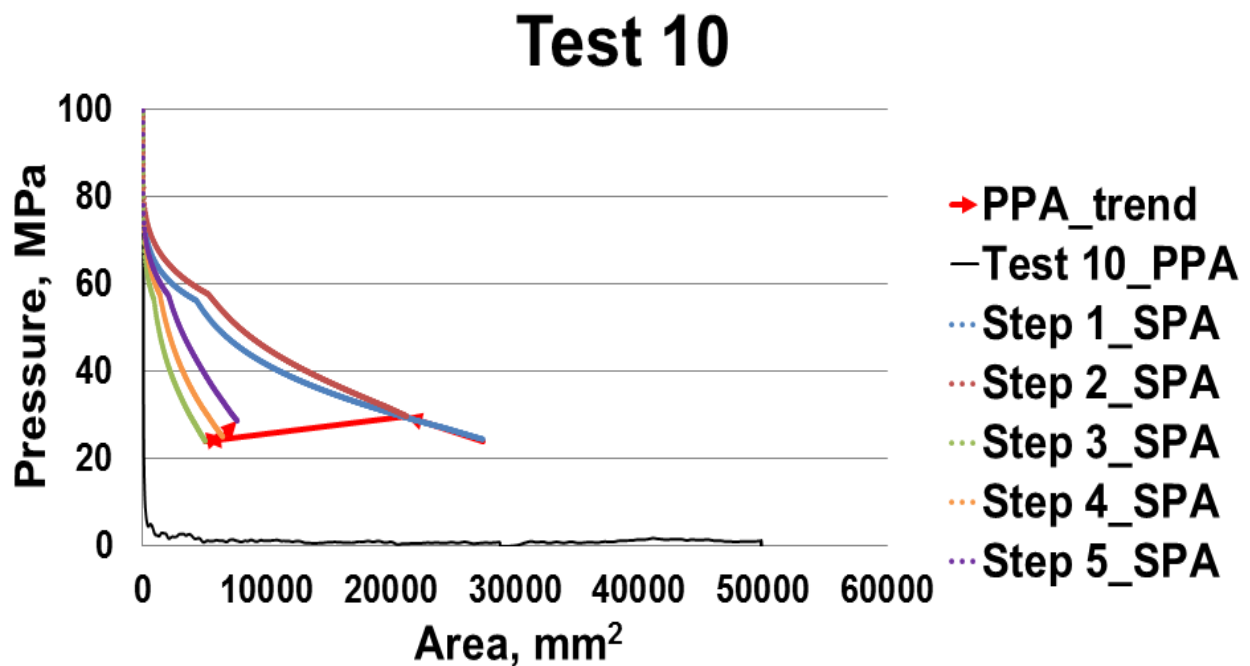


Figure G-6: Spatial pressure-area curve of Test 10

(10° wedge, cylindrical ice, 100mm/s test speed)

Appendix H Contact Area/Pressure comparison: Flat vs. Concave Shape Indenter

H.1. Results of Test against a Flat Indenter

Table H-1 shows the results of an earlier study using a flat indenter.

Table H-1: Results of using 10cm diameter ice cone test against flat indenter

(a) Test 2 (30° ice cone, 1mm/s test speed)

Step no. (Disp.)	Nominal contact area (mm ²)	Nominal pressure (MPa)	Activated contact area (mm ²)	Activated pressure (MPa)	A _{act} /A _{nom} . (%)	P _{act} /P _{nom} . (%)
1 (9mm)	763.41	4.48	517.44	28.77	67.78	641.47
2 (18mm)	3053.63	7.25	2312.38	19.11	75.73	263.69
3 (27mm)	6870.67	2.06	3539.38	12.04	51.51	583.66
				Avg.	65.01	496.27

(b) Test 4 (50° ice cone, 1mm/s test speed)

Step no. (Disp.)	Nominal contact area (mm ²)	Nominal pressure (MPa)	Activated contact area (mm ²)	Activated pressure (MPa)	A _{act} /A _{nom} . (%)	P _{act} /P _{nom} . (%)
1 (15mm)	497.69	5.08	221.13	24.91	44.43	490.23
2 (30mm)	1990.76	6.95	914.94	31.63	45.96	455.29
3 (45mm)	4479.21	7.94	1715.94	15.88	38.31	200.07
4 (55mm)	6691.17	11.23	2756.13	7.76	41.19	69.09
				Avg.	42.47	303.67

(c) Test 5 (50° ice cone, 100mm/s test speed)

Step no. (Disp.)	Nominal contact area (mm ²)	Nominal pressure (MPa)	Activated contact area (mm ²)	Activated pressure (MPa)	A _{act} /A _{nom} . (%)	P _{act} /P _{nom} . (%)
1 (15mm)	497.69	1.63	216.31	21.60	43.46	1324.81
2 (30mm)	1990.76	3.15	1439.38	12.20	72.30	387.02
3 (45mm)	4479.21	2.01	3865.94	9.78	86.31	487.52
4 (55mm)	6691.17	1.72	5844.63	10.91	87.35	635.54
				Avg.	72.36	708.72

(d) Test 6 (30° ice cone, 100mm/s test speed)

Step no. (Disp.)	Nominal contact area (mm ²)	Nominal pressure (MPa)	Activated contact area (mm ²)	Activated pressure (MPa)	A _{act} /A _{nom} . (%)	P _{act} /P _{nom} . (%)
1 (9mm)	763.41	1.26	624.94	21.91	81.86	1732.75
2 (18mm)	3053.63	0.47	1958.31	14.94	64.13	3157.82
3 (27mm)	6870.67	7.93	3773.31	12.93	54.92	163.01
				Avg.	66.97	1684.53

(e) Test 7 (50° ice cone, 100mm/s test speed)

Step no. (Disp.)	Nominal contact area (mm ²)	Nominal pressure (MPa)	Activated contact area (mm ²)	Activated pressure (MPa)	A _{act} /A _{nom} . (%)	P _{act} /P _{nom} . (%)
1 (15mm)	497.69	3.01	212.13	26.39	42.62	877.19
2 (30mm)	1990.76	2.62	1118.56	19.98	56.19	763.14
3 (45mm)	4479.21	1.19	1909.88	16.32	42.64	1376.51
4 (55mm)	6691.17	3.86	3633.88	13.96	54.31	361.84
				Avg.	48.94	844.67

(f) Test 8 (30° ice cone, 1mm/s test speed)

Step no. (Disp.)	Nominal contact area (mm ²)	Nominal pressure (MPa)	Activated contact area (mm ²)	Activated pressure (MPa)	A _{act} /A _{nom} . (%)	P _{act} /P _{nom} . (%)
1 (9mm)	763.41	6.37	220.06	29.60	28.83	464.99
2 (18mm)	3053.63	5.53	1153.69	15.86	37.78	287.02
3 (27mm)	6870.67	5.80	3088.56	11.80	44.95	203.57
				Avg.	37.19	318.53

H.2. 25cm Diameter Ice Sample Test against a concave shape indenter

The difference of the contact area and pressure were even more increased using concave-shaped indenter as shown in Table H-2. The average ratio of the contact area showed a value of 42.5% (on average) and the pressure difference was about 5-40 times higher.

Table H-2: Results of using 25cm diameter ice cone test against concave shape indenter

(b) Test 2 (10° wedge, 35° ice cone, 100mm/s)

Step No. (Disp.)	Nominal contact area (mm ²)	Nominal pressure (MPa)	Activated contact area (mm ²)	Activated pressure (MPa)	A _{act} /A _{nom.} (%)	P _{act} /P _{nom.} (%)
1 (15mm)	2097.61	6.43	1265.44	34.32	60.33	938.60
2 (30mm)	8383.06	3.08	4430.56	23.83	52.85	1716.03
3 (45mm)	18856.35	1.45	4392.63	25.52	23.30	1604.80
4 (55mm)	28165.11	3.40	11164.56	18.63	39.64	1165.36
				Avg.	44.03	1356.20

(c) Test 3 (10° wedge, 25° ice cone, 1mm/s)

Step No. (Disp.)	Nominal contact area (mm ²)	Nominal pressure (MPa)	Activated contact area (mm ²)	Activated pressure (MPa)	A _{act} /A _{nom.} (%)	P _{act} /P _{nom.} (%)
1 (9mm)	2177.61	3.77	1226.13	27.82	56.31	738.37
2 (18mm)	8688.23	3.10	3110.44	22.24	35.80	717.6
3 (27mm)	19531.86	3.73	7035.38	19.06	36.02	511.56
				Avg.	42.71	655.76

(d) Test 4 (10° wedge, 25° ice cone, 100mm/s)

Step No. (Disp.)	Nominal contact area (mm ²)	Nominal pressure (MPa)	Activated contact area (mm ²)	Activated pressure (MPa)	A _{act} /A _{nom.} (%)	P _{act} /P _{nom.} (%)
1 (9mm)	2177.61	5.44	1195.13	29.86	54.88	549.38
2 (18mm)	8688.23	3.38	3756.38	25.05	43.24	741.23
3 (27mm)	19531.86	2.33	6821.75	16.49	34.93	708.25
				Avg.	44.35	666.29

(e) Test 17 (20° wedge, 35° ice cone, 1mm/s)

Step No. (Disp.)	Nominal contact area (mm ²)	Nominal pressure (MPa)	Activated contact area (mm ²)	Activated pressure (MPa)	A _{act} /A _{nom.} (%)	P _{act} /P _{nom.} (%)
1 (10mm)	1677.39	4.10	787.25	34.23	46.93	835.52
2 (20mm)	6708.78	0.81	3391.25	27.90	50.55	3462.13
3 (35mm)	20544.62	3.08	9226.94	24.60	44.91	799.28
				Avg.	47.46	1698.97

The difference became larger in case of the cylindrical ice test as shown in Table H-3. There was no big difference about the contact area. Otherwise, the pressure difference up to 300 times (a specific cases only) was observed (Test 10).

Table H-3: Results of using cylindrical ice test against concave shape indenter

(a) Test 5 (30° wedge, cylindrical ice, 1mm/s)

Step No (Disp.)	Nominal contact area (mm ²)	Nominal pressure (MPa)	Activated contact area (mm ²)	Activated pressure (MPa)	A _{act} /A _{nom.} (%)	P _{act} /P _{nom.} (%)
1 (15mm)	7251.11	10.31	6652.19	36.31	91.74	352.02
2 (30mm)	16976.55	2.31	12911.69	26.18	76.06	1134.24
3 (45mm)	29176.31	3.97	12567.63	24.97	43.07	628.37
4 (60mm)	43850.40	0.76	17417.94	18.99	39.72	2504.73
5 (75mm)	57630.00	0.53	13030.63	17.03	22.61	3198.46
				Avg.	54.64	1563.56

(d) Test 10 (10° wedge, cylindrical ice, 100mm/s)

Step No (Disp.)	Nominal area (mm ²)	Nominal pressure (MPa)	Activated contact area (mm ²)	Activated pressure (MPa)	A _{act} /A _{nom} . (%)	P _{act} /P _{nom} . (%)
1 (15mm)	28774.43	0.93	27416.25	24.52	95.28	2638.88
2 (30mm)	49828.00	0.02	21260.31	29.82	42.67	149113.44
3 (45mm)	49828.00	0.50	5025.44	24.11	10.09	4829.51
4 (60mm)	49828.00	0.23	6452.25	25.08	12.95	10947.52
5 (75mm)	49828.00	0.67	7599.31	28.76	15.25	4290.33
				Avg.	35.25	34363.94

Appendix I Results of Numerical Analysis:

25cm Diameter Ice Sample

I.1. Force-Displacement Curve

Figures I-1 to I-3 shows the comparison results of force-displacement curve between the proposed numerical simulation model and experimental results for different test conditions.

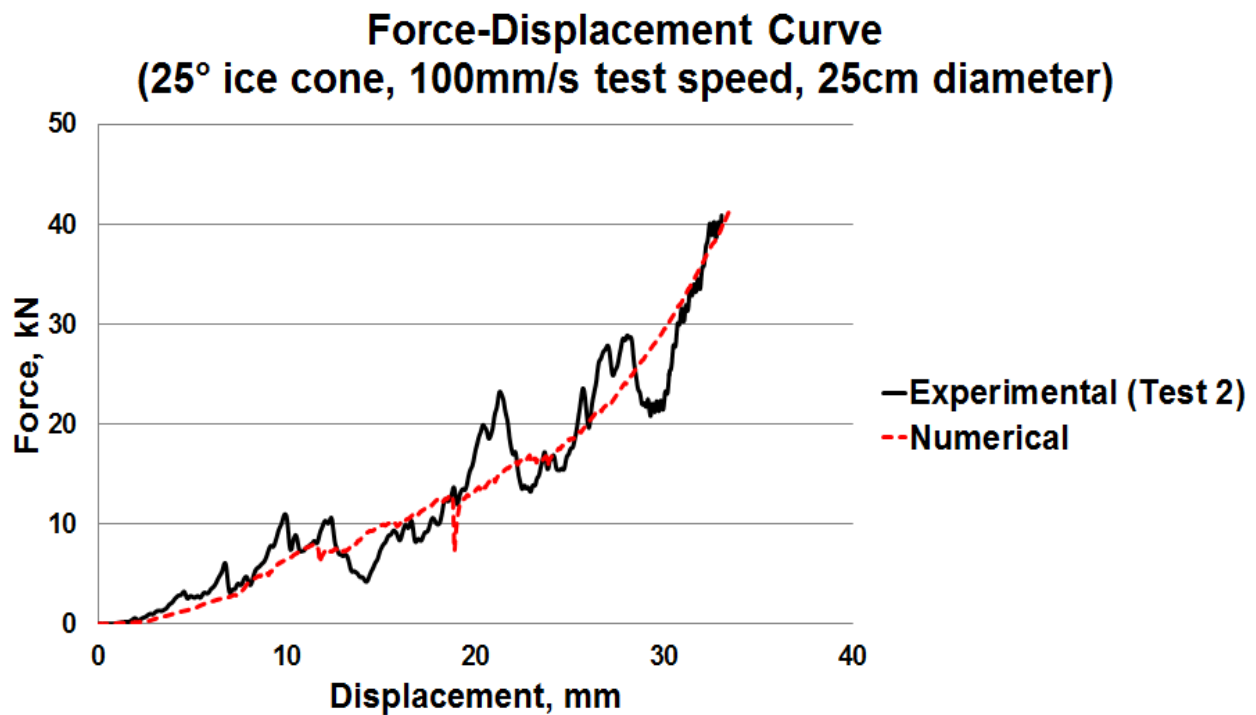


Figure I-1: Comparison of force-displacement curve (25cm ice cone, 100mm/s test speed)

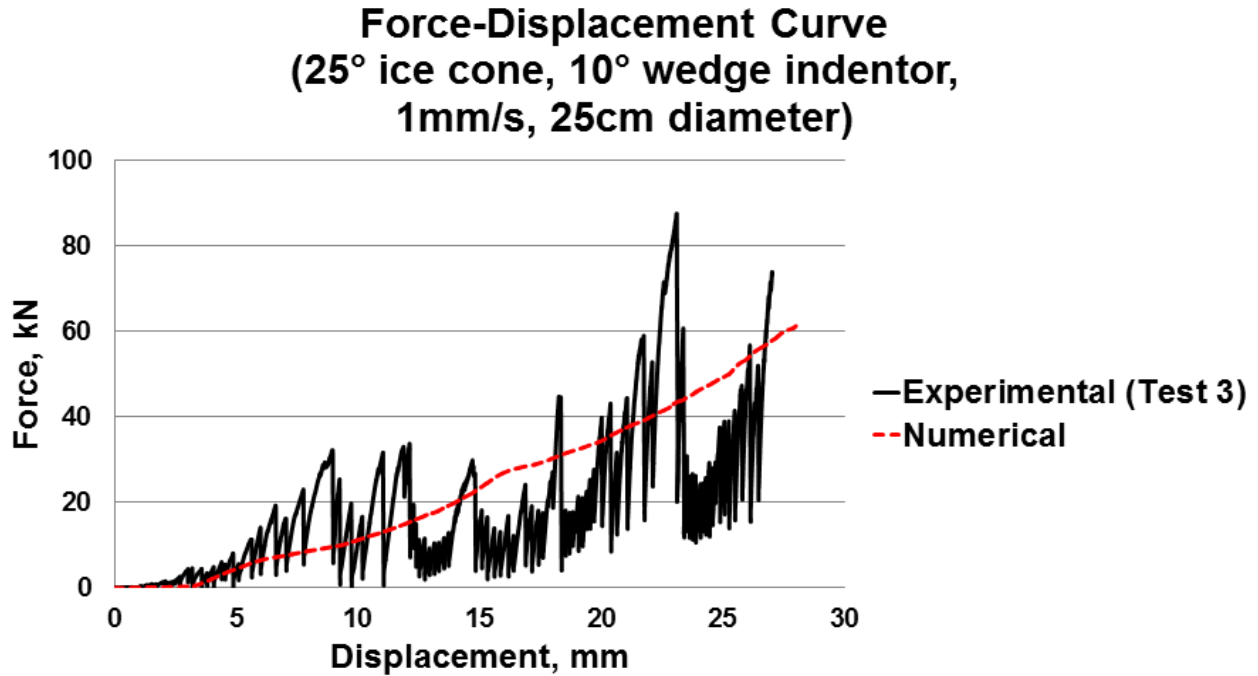


Figure I-2: Comparison of force-displacement curve on a 10° wedge indenter
(25cm ice cone, 1mm/s test speed)

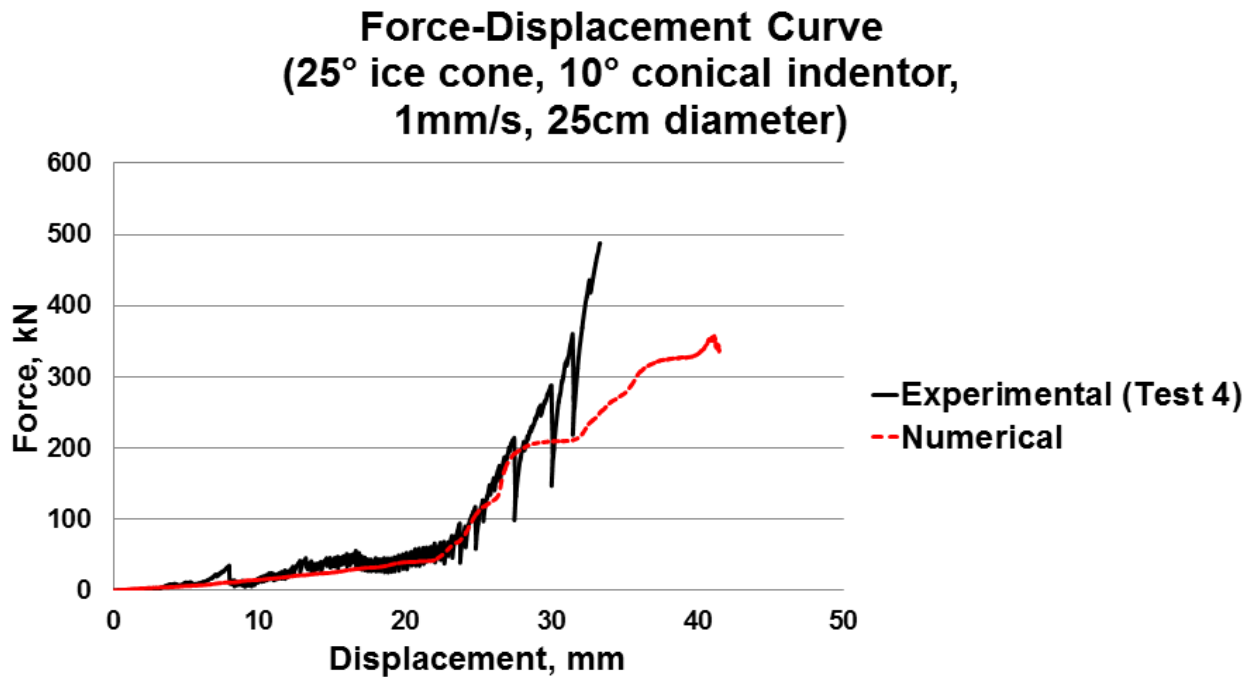


Figure I-3: Comparison of force-displacement curve on a 10° conical indenter
(25cm ice cone, 1mm/s test speed)

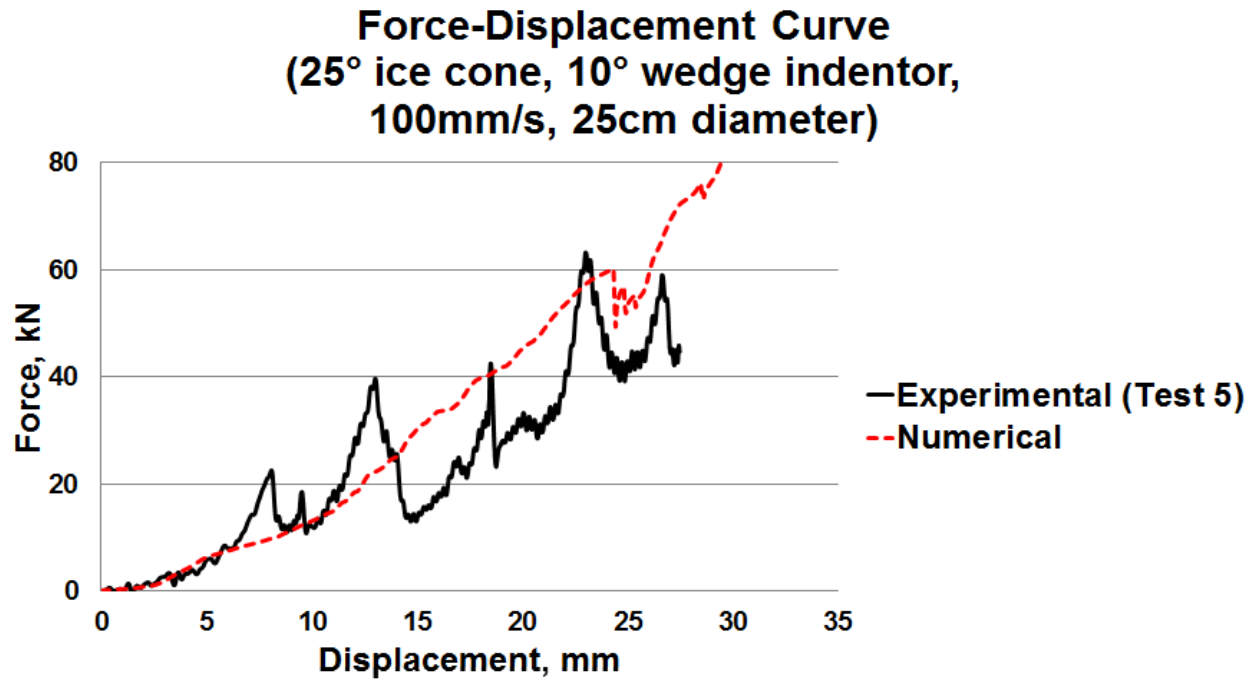


Figure I-4: Comparison of force-displacement curve on a 10° wedge indenter
(25cm ice cone, 100mm/s test speed)

I.2. Compressive Ice Strength

Figures I-4 to I-6 represents a comparison of compressive ice strengths using a flat indenter and concave shape indenter.

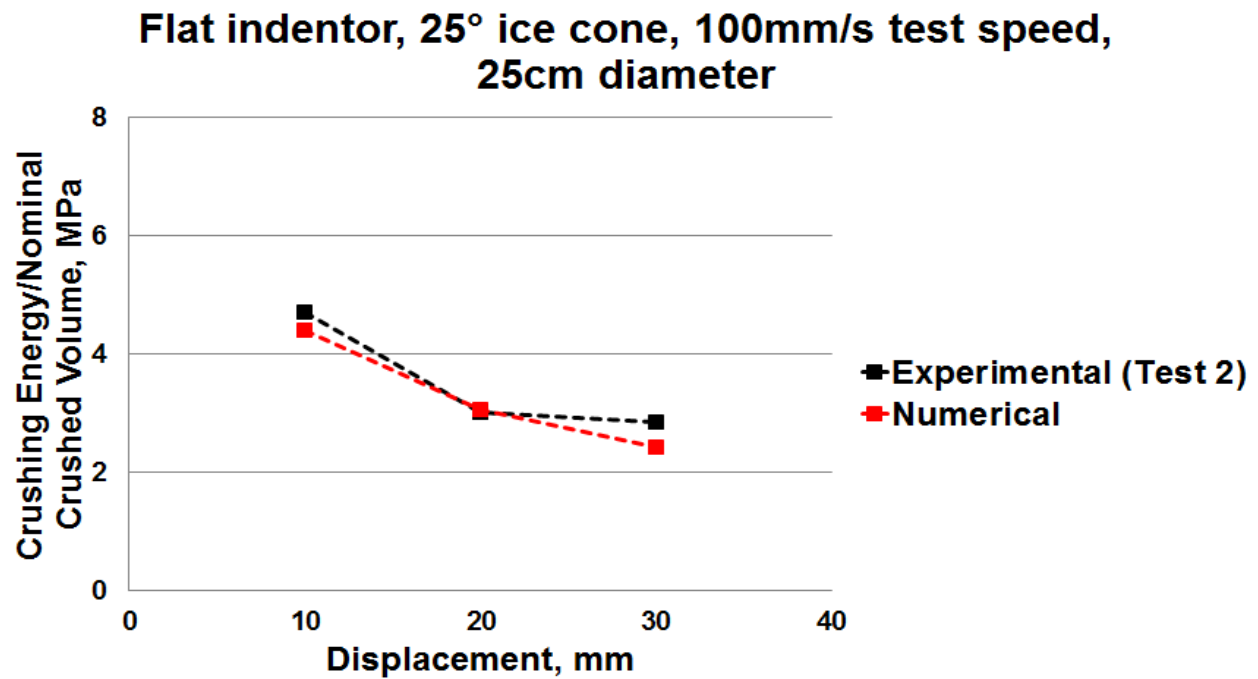


Figure I-5: Comparison of compressive ice strength on a flat indenter
(25cm ice cone, 100mm/s test speed)

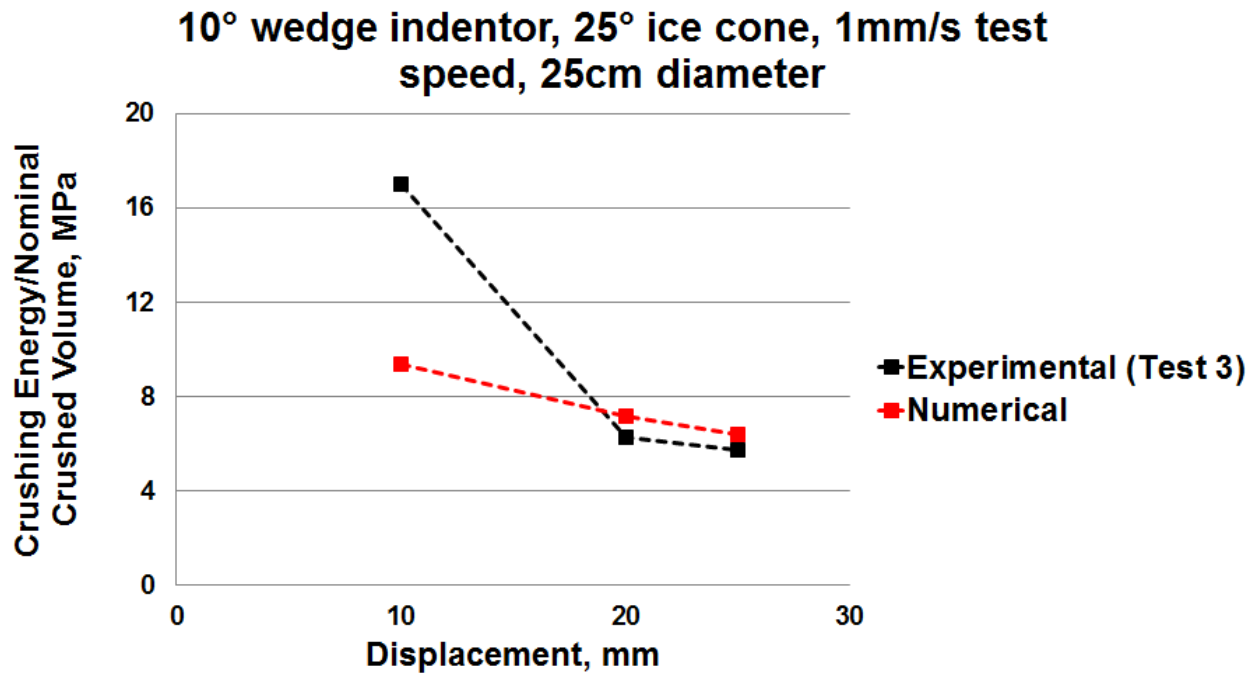


Figure I-6: Comparison of compressive ice strength on a 10° wedge indenter
(25cm ice cone, 1mm/s test speed)

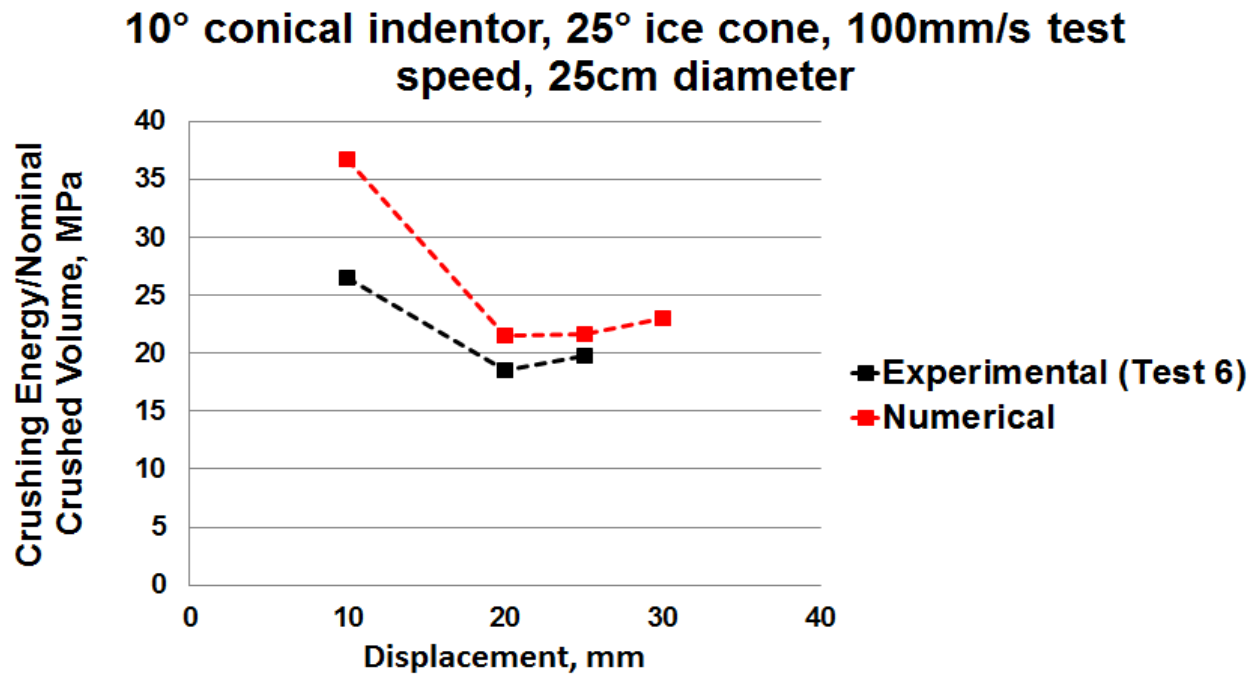


Figure I-7: Comparison of compressive ice strength on a 10° conical indenter
(25cm ice cone, 100mm/s test speed)